Validation and improvment of atmospheric correction methods for ocean colour images in optically complex coastal waters

Clémence Goyens

To cite this version:

Clémence Goyens. Validation and improvment of atmospheric correction methods for ocean colour images in optically complex coastal waters. Oceanography. Université du Littoral Côte d'Opale, 2013. English. NNT : 2013DUNK0401 . tel-01337366

HAL Id: tel-01337366
https://theses.hal.science/tel-01337366

Submitted on 25 Jun 2016

Liberté • Égalité • Fraternité
RÉPUBLIQUE FRANÇAISE

MINISTÈRE DE
L'ENSEIGNEMENT
SUPÉRIEUR ET DE
LA RECHERCHE

UNIVERSITÉ DU LITTORAL CÔTE D'OPALE

Université du Littoral Côte d'Opale

LABORATOIRE D'OCÉANOLOGIE ET DE GÉOSCIENCES

THÈSE
PRÉSENTÉE ET SOUTENUE PUBLIQUEMENT PAR
CLÉMENCE GOYENS

POUR OBTENIR LE GRADE DE DOCTEUR EN SCIENCES-OCÉANOGRAPHIE

VALIDATION ET AMÉLIORATION DES MÉTHODES DE CORRECTION ATMOSPHÉRIQUE POUR LES IMAGES DE LA COULEUR DE L'OCÉAN DANS LES EAUX CÔTIÉRES OPTIQUEMENT COMPLEXES

Rapporteurs	Simon BÉLANGER	UQAR, Canada
	Fréderic MÉLIN	JRC - European Comission, Italy
Membres de jury	François SCHMITT	ULCO - LOG, France
	Kevin RUDDICK	MUMM, Belgium
	Juliette LAMBIN	CNES, France
Directeur de thèse	Hubert LOISEL	ULCO - LOG, France
Co-Directeur de thèse	Cédric JAMET	ULCO - LOG, France

EDSMRE

Ecole Doctorale - 104
Sciences de la Matière, du Rayonnement
et de l'Environnement
Université Lille Nord de France

cnes

Université du Littoral Côte d'Opale

Laboratoire d'Océanologie et de Géosciences

Thesis

presented by

Clémence Goyens

Submitted in partial fulfillment for the requirements for the degree of Doctor in Sciences-Oceanography

Validation and improvement of atmospheric correction methods for ocean colour images in optically complex coastal waters

Reporters	Simon Bélanger	UQAR, Canada
	Fréderic Mélin	JRC - European Comission, Italy
Committee members	François Schmitt	ULCO - LOG, France
	Kevin Ruddick	MUMM, Belgium
	Juliette Lambin	CNES, France
Promoter	Hubert Loisel	ULCO - LOG, France
Co-Promoter	Cédric Jamet	ULCO - LOG, France

Ecole Doctorale - 104
Sciences de la Matière, du Rayonnement
et de l'Environnement
Université Lille Nord de France

Contents

Acknowledgments

First and foremost, I would like to thank my supervisors, Cédric Jamet and Hubert Loisel. Cédric, thank you for your time, motivation and support, even during the tough times of this Ph.D. pursuit. It has been an honour to be one of your first Ph.D. students. I hope you enjoyed the experience. I did. Thanks Hubert for your rare but extremely helpful advises. I enjoyed your contagious and motivational joy and enthusiasm.

I thank the reporters of my dissertation, Simon Bélanger and Frédéric Mélin, and the members of the dissertation committee, Kevin Ruddick, François Schmitt and Juliette Lambin for evaluating this work.

The colleagues of the LOG have also greatly contributed to this work thanks to their good advices, collaboration and friendship. My special thanks go to Xavier, David, Séverine and Vincent who answered most of my questions and helped me out with data classification, processing and analysis.

I'm very grateful to the Remote Sensing and Ecosystem Modelling team of the MUMM who welcomed me during a month in their group and shared their dataset, which has been crucial for my Ph.D. I particularly want to thank Kevin Ruddick for his scientific advice and knowledge and many insightful discussions and suggestions, these have been of great help and interest for my Ph.D. Thanks also to Quinten Vanhellemont for his help with the match-up extraction.

I would like also to acknowledge Thomas Schroeder, with whom I had the chance to discuss and exchange about atmospheric correction ideas; Griet Neukermans, who's love and enthusiasm for research is contagious; all the teachers and students of the Ocean Optics Summer School with whom I had a great time during those three weeks of intense labour and through which I learned immensely about ocean optics; David Doxaran for his advices about the BB9 data; Tim Moore for sharing his good ideas and making me sing atmospheric correction; my thesis committee, Cyril Moulin, Kevin Ruddick and Didier Ramon, for their time and constructive advices; and the researchers and crew of the MV1102 and FG12 sea campaigns.

Special thanks go to the Ocean Biology Processing Group of The NASA for the distribution of the MODIS-Aqua data and the development and support of the SeaDAS Software, as well as to the PIs and maintenance staffs of the AERONET-OC sites used in the present research. The French Spatial Agency (CNES) through the TOSCA program and the "Ministère de l'Enseignement et de la Recherche Française" are also acknowledge for their funding.

I would also like to thank Simon Bélanger and the TAKUVIK team for having shown interest in my research and placing trust in my competencies. During these past three years, I have realised the complexity of the process of atmospheric correction. However, future projects have been planned which appear to be even more ambitious, that is improving AC for high latitudes, ice-contaminated, optically complex, Arctic waters. I'm looking forward to this new challenge. Let me already thank you for welcoming me next year in Quebec.

Finally, a good and strong supportive surrounding is essential to survive a Ph.D. and stay sane while completing it. Therefore, I am very grateful to my colleagues, in particular, Andy (I'm looking after the next RC), Vincent, Xavier, Zied, Natacha, Régis, Séverine, Lucile, Erwan,

and so many others. A very special thank also to all my friends (your calls, “GO GO Clem” messages and emails were very appreciated!!) and my four sisters (especially the oldest one!!), to my two grand-mothers, my parents, and most of all to Sim (who is probably gone be the happiest one to know that I completed my Ph.D).

MERCI! BEDANKT!

Clémence

Abstract

To acquire marine parameters from remote sensing ocean colour data, the sensor-measured signal needs to be corrected for the atmospheric contribution. Indeed, the solar radiation reflected by air molecules and atmospheric aerosols is significant in the sensor bands of interest for ocean colour applications. The removal of the atmospheric contribution is called the atmospheric correction (AC). In open ocean waters, the AC relies on the assumption that the water is totally absorbent in the near infrared (NIR) part of the spectral region, allowing to retrieve the atmospheric contribution and to extrapolate it to the visible spectral range, and thus to determine the marine signal that contains the information on the optical properties of seawaters. However, this assumption is not valid in highly productive and turbid coastal waters. Hence, AC approaches for coastal waters need to rely on alternative assumptions. This Ph.D. thesis has as main objective to validate and improve these AC methods developed for contrasted coastal waters, with a focus on MODIS Aqua images. First, a validation and comparison of existing AC methods, relying on diverse assumptions and methods, is performed. Therefore, four commonly used AC methods are selected, (1) the standard NIR AC approach of NASA, (2) the NIR similarity spectrum AC approach including assumptions of spatial homogeneity in the water and aerosol reflectance, (3) the switching algorithm using the short wave infrared bands for AC in highly turbid waters, (4) an Artificial Neural Network algorithm. With the help of a validation exercise based on *in situ* data and as a function of the water type, several areas of improvement are delineated, including the use of spectral relationships to constrain NIR-modelling schemes. Modified NIR-modelling schemes are suggested for the standard NASA and NIR similarity spectrum AC methods. Both are forced with globally valid spectral relationships. Sensitivity studies and validation exercises, using MODIS-Aqua images in the Eastern English Channel/North Sea and French Guiana waters, are conducted showing that the suggested modified NIR-modelling schemes improve the estimations of the marine signal in contrasted coastal waters.

Résumé

L'acquisition de paramètres marins à partir des données spatiales de la couleur de l'eau nécessite l'élimination de la contribution de l'atmosphère au signal mesuré par le capteur. En effet, la majorité du rayonnement solaire mesuré par les instruments optiques dans les longueurs d'ondes qui intéressent la couleur de l'eau provient de la diffusion par les molécules de l'air et les aérosols atmosphériques. L'élimination de la contribution de l'atmosphère est appelée correction atmosphérique (CA). Pour les eaux claires, les méthodes de CA supposent une réflectance marine nulle dans le proche infra-rouge (PIR). Ceci permet d'estimer la réflectance de l'atmosphère et de l'extrapoler vers les bandes du visible, et donc de déterminer le signal marin qui contient les informations sur les propriétés optiques des eaux marines. Cette hypothèse n'est cependant pas vérifiée pour les eaux turbides, qui représentent la quasi totalité des eaux côtières. Par conséquent, de nombreux algorithmes de CA ont été développés pour les eaux côtières incluant des hypothèses alternatives. L'objectif de ce travail de thèse est de valider et d'améliorer ces méthodes de CA pour les images MODIS Aqua. Pour cela, diverses approches de CA développées pour les eaux côtières ont été comparées et validées: (1) l'algorithme standard de la NASA, (2) le 'NIR similarity spectrum algorithm' qui inclut des hypothèses d'homogénéité spatiale des réflectances marines et atmosphériques, (3) l'algorithme qui utilise les bandes dans l'infrarouge moyen pour la CA dans les eaux très turbides, et (4) un algorithme utilisant un réseau de neurones artificiels. L'exercice de validation à partir de données *in situ*, et en fonction des types d'eaux, a permis d'identifier différentes pistes d'amélioration pour l'estimation du signal marin. L'une d'entre elles comprend l'utilisation de relations spectrales pour forcer les modèles de réflectances marines utilisés par les algorithmes de CA pour estimer le signal marin dans le PIR. Des modifications ont été apportées aux modèles de réflectances marines de l'algorithme standard de la NASA et du 'NIR similarity spectrum algorithm'. Chacun des modèles a été forcé avec des relations spectrales préalablement validées grâce à des données globales. Une étude de sensibilité et une validation de ces algorithmes modifiés à partir de données MODIS-Aqua dans la Manche Orientale/Mer du Nord et la Guyane Française ont démontré que les modifications suggérées amélioraient les estimations du signal marin dans les eaux côtières optiquement complexes.

Introduction

Oceans constitute nearly 70% of Earth's surface and hold an important population of aquatic microscopic plant-like organisms, the so-called phytoplankton. These marine organisms, which represent the first step in the marine food web, act as a biological pump of the atmospheric carbon by taking up carbon dioxide in the surface ocean and producing organic carbon through the process of photosynthesis. Phytoplankton is considered to be responsible of approximately half of the planetary primary production (Field et al., 1998; Behrenfeld et al., 2006) and plays thus a major role in the ecosystem health and global climate processes as it partially regulates the ocean processes acting as a sink and source of carbon and heat. Large scale factors, such as climate, ocean circulation and water temperature variations, as well as changes in the vertical stratification of the water column, affect availability in light and in-water constituents and subsequently phytoplankton growth and distribution (Behrenfeld et al., 2006). Hence, an in-depth understanding of the oceans and these marine populations is essential to explain the global climate and its main changes due to anthropogenic factors. Long-term and global views of phytoplankton abundance are thus crucial and may only be provided by satellite ocean colour data.

Space-borne ocean colour images allow to monitor the oceans with high spatial (between 300 m and 1 km) and temporal (every 2-3 days) resolutions. Through these data, open oceans have been extensively observed and are today relatively well understood. However, this is (still) not the case for coastal waters presenting complex optical properties and high spatio-temporal variability in physical, biological and geological processes. Though, these highly dynamic environments, representing only about 7% of the total ocean surface, are among the most productive natural systems on Earth and encompass important economical and environmental concerns (Nellemann et al., 2009). They produce up to 40% of the marine biomass inventoried today and 50% of the worlds fisheries (Nellemann et al., 2009). Coastal land also accommodates more than half of the worlds human population and is expected to be even more densely populated in the future. This explains the need for frequent accurate high spatial and temporal resolution ocean colour data in coastal waters. This need is even greater since, based upon current scientific evidence, the Intergovernmental Panel on Climate Change predicted a significant increase in the global temperature during the 21st century. Indeed, global warming will create novel challenges for coastal and marine ecosystems that are already stressed by many threats. In Europe, the Marine Strategy Framework Directive, adopted in 2008 as a complement of the European Water Framework Directive, came into force to protect more effectively the marine environment from, among others, the impoverishment and degradation of the biological diversity and the modification of its structure, the disappearance of habitats, the contamination by dangerous and nutritive substances and the repercussions of climate change. To follow these threats and changes and to understand their evolution, substantial effort is required in observations and surveys of the marine waters. This can be achieved using satellite ocean colour images, as water constituents concentration maps, water quality surveys, environmental impact assessments, or potential fishing maps, are all examples of outputs fully or partially derived from these data.

The first satellite dedicated for ocean colour missions was the NASA's Coastal Zone Color Scanner (CZCS), launched in 1978. This satellite, considered as a one-year proof-of-concept, was a lot more profitable than expected and lasted for about 6 years (1986). The success of the CZCS mission was the beginning of a long series of ocean colour satellite missions which revolutionised the view of the marine biomass. Well-known ocean colour sensors are, among others, the Sea-viewing Wide Field-of-view Sensor (SeaWiFS, launched in 1997 and operated till 2010), the POLarization and Directionality of the Earth's Reflectances instruments (POLDER-1 and 2 operating from 1996 to 1997 and from 2002 to 2003, respectively), the still operating Moderate Resolution Imaging Spectroradiometers Terra (MODIS-Terra, launched in 1999) and Aqua (MODIS-Aqua, launched in 2002), the Medium Resolution Imaging Spectrometer (MERIS, launched in 2002 and operated till 2012), the Geostationary Ocean Color Imager (GOCI, launched in 2010 and being the first ocean colour sensor on a geostationary orbit), the Hyperspectral Imager for Coastal Oceans (HICO, launched in 2009), and the recently launched Visible Infrared Imager Radiometer Suite (VIIRS, launched in 2011).

The principal concept of ocean colour relies on the fact that the nature and concentration of the water constituents affect the absorption and scattering of the incoming light and, subsequently, the colour of the ocean. Variations in the colour of the water thus reflects variations in inorganic, organic, particulate and dissolved materials present in the water. For instance, remote sensing ocean colour images can depict variations in total chlorophyll pigment concentration (Chl), which preferentially absorbs red and blue light and scatters in the green spectral region. Since Chl is used by phytoplankton to produce carbon photosynthesis, remote sensing estimations of Chl concentrations are used as a proxy to evaluate the global phytoplankton biomass and as input for models predicting primary productivity.

The processing of space-borne measurements to obtain information on the water column is however not a trivial task. Indeed, a significant fraction of the sensor measured signal does not carry any information about the water column and its constituents. About 90% of the sensor measured visible reflectance originates from sunlight reflected by air molecules and atmospheric aerosols. This percentage further increases in the near infra-red spectral bands. Accordingly, to obtain accurate water signal measurements, and consequently accurate ocean colour derived products, the contribution of the atmosphere needs to be removed. This process is called atmospheric correction (AC). Unfortunately, despite the significant progress in ocean colour products since the launch of the CZCS satellite, AC remains a difficult task. The acquisition of accurate ocean colour data is even more challenging in coastal waters where the sensor measured signal is affected by additional and diverse artefacts such as adjacency effects from nearby land, whitecaps from breaking waves, bottom reflectance over shallow waters, absorbing and non-absorbing aerosols from anthropogenic origin.

Initially for the CZCS AC method, it was assumed that sea-water was totally absorbent in the red spectral region allowing to derive the aerosol contribution in this spectral domain (referred to as the black pixel assumption). With the launch of the second generation satellite sensors (e.g., SeaWiFS, MERIS, MODIS), supplied by additional near infra-red (NIR) spectral bands, the black pixel assumption was applied to the NIR spectral domain. However, in the red and NIR spectral domain, the black pixel assumption breaks down in highly productive or turbid coastal waters (Siegel et al., 2000). The application of the black pixel assumption in such waters results in an overestimation of the aerosol contribution and, subsequently, in an underestimation of the water reflectance. Hence, the black pixel assumption performs well in open ocean waters (optically dominated by limited concentrations of algal particles), but generally fails in turbid or highly productive waters.

This Ph.D. study focusses on the removal of the atmospheric contribution in optically complex coastal waters requiring alternative assumptions to account for non-zero water leaving reflectance in the NIR spectral region.

For the past ten years, numerous AC methods have been suggested for turbid and highly productive coastal waters. Some approaches attempt to model the water signal in the NIR spectral region (e.g., Arnone et al., 1998; Moore et al., 1999; Siegel et al., 2000; Ruddick et al., 2000; Stumpf et al., 2003; Ruddick et al., 2006; Bailey et al., 2010) or applied the black pixel assumption to short-wave infra-red (SWIR) bands (e.g., Wang and Shi, 2005, 2007; Wang et al., 2009). Others are based on different approaches including coupled ocean-atmosphere optimization or inversion methods allowing to consider the aerosol and the water contribution simultaneously and/or the signal over the entire spectral range (e.g., Gordon et al., 1997; Chomko and Gordon, 1998; Chomko et al., 2003; Kuchinke et al., 2009a,b; Jamet et al., 2005; Brajard et al., 2006a; Doerffer and Schiller, 2007; Schroeder et al., 2007; Doeffer and Schiller, 2008; Brajard et al., 2012). However, as suggested by numerous studies (e.g., Zibordi et al., 2004b, 2006b; Mélin et al., 2005, 2007; Feng et al., 2008; Zibordi et al., 2009b; Mélin et al., 2011, 2013; Banzon et al., 2009; Jamet et al., 2011; Dogliotti et al., 2011), AC remains a critical step in the processing chain of the satellite ocean colour images and improvement is still required. This brings us to the motivations of the present Ph.D. study, that is to validate and improve AC methods for satellite ocean colour images in optically complex coastal waters. The first objective of this thesis is to conduct a comprehensive validation of commonly used AC algorithms developed for turbid coastal waters and with a focus on MODIS Aqua images. Therefore, four AC methods, presenting very different assumptions and/or approaches to compensate for water signal in the NIR spectral domain, have been selected. Results and conclusions of this validation are expected to highlight the impact of the different assumptions on the performance of the AC and to aid movement towards possible approaches to further improve AC, which is the second objective of this work.

The present manuscript is organized as follows:

The first chapter introduces the ocean colour concept and describes how incoming light is attenuated as it travels down and upward in the water column. Chapter 1 also includes a short description of the optical water type classification methods and, among others, the classification scheme of Vantrepotte et al. (2012) which is used in this work to evaluate the limitations of the AC methods as a function of the water type.

Chapter 2 focusses on the AC processes and briefly describes the radiative transfer equation and aerosol models and products used for the AC of ocean colour images. A short overview of the turbid water AC methods developed and published in the literature is also given followed by a comprehensive description of the classic black pixel assumption AC algorithm and the four turbid water MODIS Aqua AC methods validated in Chapter 4 (Ruddick et al., 2000, 2006; Bailey et al., 2010; Schroeder et al., 2007; Wang et al., 2009).

Chapter 3 details the MODIS Aqua and *in situ* data used for the validation and improvement of the AC methods. This chapter also illustrates the difficulty to acquire valid and accurate *in situ* data by means of two closure exercises. The first closure exercise is part of a work resulting from a cruise campaign (to which I had the chance to participate) across the southern Atlantic and Pacific ocean. This work has been submitted recently to a peer-reviewed journal (Rudorff et al., 2013). The second closure exercise is part of an on-line available report (Arellano et al., 2011) conducted together with other Ph.D. students during the International Ocean Optics Summer School in July 2011 at the Darling Marine Centre (Maine, USA).

Next, in Chapter 4, a global validation and inter-comparison exercise of the four turbid water MODIS Aqua AC methods is conducted. This work resulted in a published paper (Goyens et al., 2013c) included in Chapter 4 together with some complementary results. This global validation gives rise to several ideas of possible improvements for AC which brings us to Chapter 5. Indeed, in Chapter 5, the potential of spectral relationships to improve the STD and MUMM NIR-modelling schemes is investigated. Spectral relationships are defined in this work as relations between the water signal at two or more wavelengths, reflecting the spectral dependence of the marine signal itself.

Chapter 5 includes two published papers. The first one reviews and validates red and NIR spectral relationships encountered in the literature (Goyens et al., 2013a), and the second one investigates the performances of the spectral relationship-forced NIR-modelling schemes based on sensitivity studies (Goyens et al., 2013b). In addition to the papers, three complementary studies are conducted. First, additional red-NIR and blue-green spectral relationships are suggested. Second, I attempt to confirm the empirically retrieved spectral relationships with a theoretical basis in order to investigate if the relationships satisfy all water types. Third, two additional modified NIR-modelling schemes are suggested and validated.

In the last chapter, the newly suggested STD and MUMM-based NIR-modelling schemes are evaluated with *in situ*-satellite match-up pairs. Several case studies are discussed including a visual analysis of the resulting ocean colour images.

Finally, general conclusion and perspectives are outlined.

- Chapter 1 -

Ocean colour

1.1 SEAWATER CONSTITUENTS AND OCEAN COLOUR

The principal concept of ocean colour relies on the fact that the nature and concentration of the water constituents affect the absorption and scattering of the incoming light and, subsequently, the colour of the ocean. Variations in the water optical properties thus reflect variations in in-water constituents. In seawater the most important coloured water constituents are phytoplankton, suspended particulate matter (SPM), including inorganic and organic particles, coloured dissolved organic matter (CDOM) and the water itself, including dissolved salt particles and air bubbles. Phytoplankton concentrations are usually derived from the main optically active phytoplankton pigment, chlorophyll a (Chl_a).

Figure 1.1 illustrates the variations in ocean colour according to the in-water constituents. For instance, Chl_a pigments significantly increase blue and red light absorption and backscatter only a very small amount of visible light resulting in greenish water colours (Fig. 1.1). In turbid waters, backscattering appears to be more important and increases with an increase in SPM concentrations, especially in the red and near infra-red (NIR) spectral domain. Accordingly, water masses dominated by SPM appear more brownish (Fig. 1.1). In CDOM dominated waters, significant absorption in the visible spectral domain results in very dark water colours.

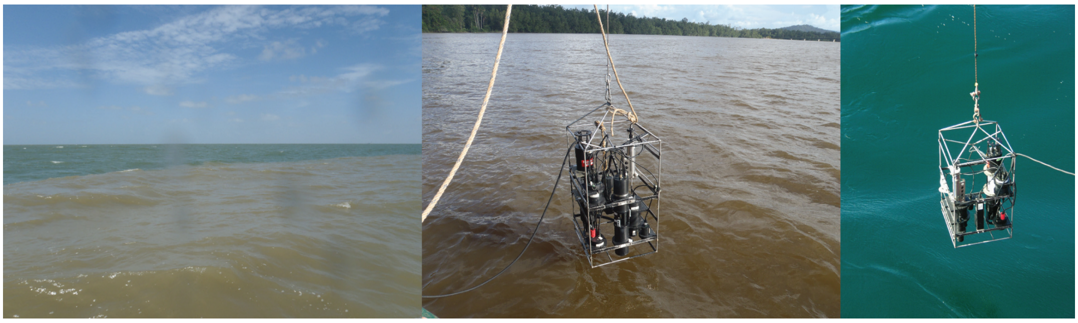

Figure 1.1: *Different water colours reflect variations in in-water constituents and concentrations. Turbid plume penetrating ocean waters dominated by phytoplankton along the coastal region of French Guiana (left). In situ water sensors over brownish water masses dominated by high SPM concentrations in French Guiana (centre) and over phytoplankton dominated greenish water masses in the Southern Atlantic Ocean (right).*

In marine optics, water masses are described by two categories of water optical properties, the Inherent and Apparent Optical Properties (IOPs and AOPs, respectively). Light absorption and scattering by the water column, independent of variations in the ambient light field, are described by the IOPs. These are thus exclusively determined by the nature and the concentrations of the constituents present in the water column and the water itself (Preisendorfer, 1961). Beside absorption and scattering, IOPs also include the volume scattering phase function, the refraction index, the beam attenuation coefficient and the single-scattering albedo. IOPs are briefly described in the next section (Section 1.2).

The AOPs are the properties determined by the angular distribution of the incoming light field as well as by the concentration and nature of the in-water constituents. AOPs depend thus both on the medium (described by the IOPs) and on the ambient light field. Common AOPs are, among others, the diffuse attenuation coefficient, the remote sensing reflectance and the water-leaving reflectance or radiance. Ideally, AOPs should vary only slightly with external environmental changes, but enough from one water body to the next to be useful in characterizing the different optical properties of the two water bodies (Mobley, 1994). AOPs are further described in Section 1.3.

IOPs and AOPs are closely related and need to be both investigated to understand the optical processes determining the ocean colour. Linking AOPs and IOPs is possible with the use of radiative transfer theory inversion algorithms, allowing to derive bio-geochemical parameters from remotely sensed marine reflectances. Section 1.4 shortly describes the link between IOPs and AOPs.

Finally, in the last section of this chapter the concept of optical water type classification is discussed. Optical water type classification schemes separate water masses according to their optical properties, for instance, based on the information provided by their remote sensing reflectance spectra (Moore et al., 2001; Lubac and Loisel, 2007; Moore et al., 2009; Vantrepotte et al., 2012). This is particularly relevant to interpret ocean colour remote sensing signals, especially in optically complex waters where biological processes significantly vary in space and over time and where both IOPs and AOPs are influenced by multiple and non-exclusive biological, chemical and physical processes. In the present PhD project, such a classification scheme is used to evaluate the performance of the atmospheric correction methods as a function of the optical water type, explaining the need to introduce the concept of optical water type classification in this introductory chapter.

1.2 INHERENT OPTICAL PROPERTIES

When light penetrates a volume of seawater, photons can either be absorbed and/or scattered by the water particles and molecules. Considering a small volume of water of thickness Δr, illuminated by a collimated beam of monochromatic light of spectral radiant power at a wavelength λ, $\Phi_\mathrm{i}(\lambda)$ (W nm^{-1}) (Fig. 1.2), some part the incident power $\Phi_\mathrm{i}(\lambda)$ will be absorbed within the volume of water, $\Phi_\mathrm{a}(\lambda)$, while another part, $\Phi_\mathrm{s}(\lambda, \psi)$, will be scattered out of the beam at an angle ψ.

The remaining power $\Phi_\mathrm{t}(\lambda)$ is transmitted through the volume with no change in direction. When no photons undergo a change in wavelength during the scattering process (i.e., in absence of inelastic scattering, see later for more details), energy is conserved so that:

$$\Phi_i(\lambda) = \Phi_a(\lambda) + \Phi_s(\lambda) + \Phi_t(\lambda) \tag{1.1}$$

We can thus define the absorptance, $A(\lambda)$, and scatterance, $B(\lambda)$, as the fraction of incident power that is absorbed within the volume, and, as the fractional part of the incident power that is scattered out of the beam into all directions, respectively (Mobley et al., 2011):

$$A(\lambda) = \frac{\Phi_a(\lambda)}{\Phi_i(\lambda)} \tag{1.2}$$

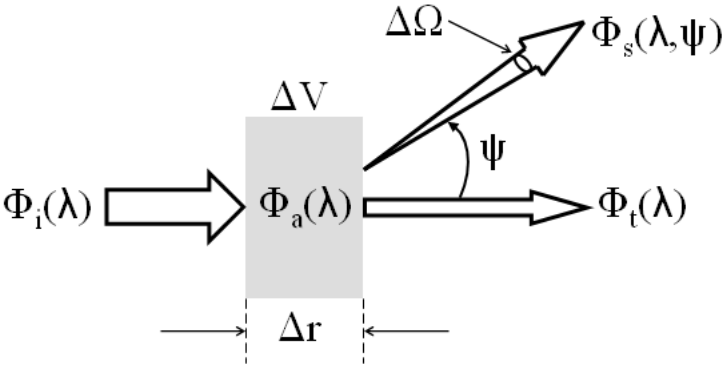

Figure 1.2: *Schematic representation of the process of absorption, scattering and transmission (after Mobley et al. (2011))*

$$B(\lambda) = \frac{\Phi_s(\lambda)}{\Phi_i(\lambda)} \tag{1.3}$$

The absorption coefficient, $a(\lambda)$, and the total scattering coefficient, $b(\lambda)$, are then defined as the spectral absorptance and scatterance per unit path-length in the medium, respectively:

$$a(\lambda) = \lim_{\Delta r \to 0} \frac{\Delta A(\lambda)}{\Delta r} = \frac{dA(\lambda)}{dr} \tag{1.4}$$

$$b(\lambda) = \lim_{\Delta r \to 0} \frac{\Delta B(\lambda)}{\Delta r} = \frac{dB(\lambda)}{dr} \tag{1.5}$$

The sum of $a(\lambda)$ and $b(\lambda)$ is the total volume attenuation coefficient $c(\lambda)$, defining the rate of incoming light, at a given wavelength λ, attenuated by the water mass per unit of path-length (here in m^{-1}). Hence $a(\lambda)$ describes the amount of photons converted into other forms of energy (e.g., heat, chemical energy) while $b(\lambda)$ describes the amount of photons redirected into a range of directions at the same wavelength as the incident photons (elastic scattering). Another secondary scattering process is the inelastic scattering which redirect photons with a different wavelength (i.e., different frequency and energy). Most common inelastic scattering processes in ocean optics are the fluorescence emissions from CDOM and phytoplankton pigments and the Raman scattering process by the water molecules. The former is more significant in coastal waters while the latter gets more important in oligotrophic waters. For simplicity most ocean colour models define reflected radiation in absence of inelastic scattering. Note however that such processes may be significant in certain cases (see for instance the impact of Raman Scattering on in-water *in situ* measurements in Section 3.3.3.1 and in Loisel and Stramski (2000)).

Because $b(\lambda)$ results from a change in the propagation of the photons, it is thus the integration of the volume scattering function, $\beta(\psi)$ (in $\mathrm{m}^{-1}\ \mathrm{sr}^{-1}$), over all solid angles, with ψ being the scattering angle. However, satellite remote sensing only records the reflected light field. Therefore, in ocean colour models, the backscattering coefficient, $b_b(\lambda)$ (in m^{-1}), is often used. $b_b(\lambda)$ is defined as the integration of $\beta(\psi)$ over all backward directions.

For seawater, $a(\lambda)$ and $b_b(\lambda)$ (or $b(\lambda)$) can be written as an addition of the contribution of the different optically significant in-water constituents, namely, phytoplankton, non-algal-particles, CDOM and the water itself (denoted with the subscripts Φ, NAP, CDOM and w, respectively) (Eqs.(1.6) and (1.7)). According to the particular wavelength dependencies of the constituents and their concentrations, the different components will contribute more or less to $a(\lambda)$ and $b_b(\lambda)$. Because the scattering by algal and non-algal particles are spectrally similar, these are often combined as the scattering of particulate material (denoted with the subscripts p).

$$a(\lambda) = a_w(\lambda) + a_\Phi(\lambda) + a_{NAP}(\lambda) + a_{CDOM}(\lambda) \tag{1.6}$$

$$b_b(\lambda) = b_{bw}(\lambda) + b_{bp}(\lambda) \tag{1.7}$$

1.3 Apparent optical properties

Remote sensing reflectance, $R_{rs}(\lambda)$, and water-leaving radiance, $L_w(\lambda, \psi, \theta, \theta_0)$, or reflectance, $\rho_w(\lambda)$, are common AOPs derived from satellite and *in situ* measurements and are used to estimate the optical properties of the seawater. To understand the definition of these AOPs it is necessary to first define the sea-surface irradiance reflectance, $R(\lambda)$. $R(\lambda)$ is the ratio of the down-welling irradiance, $E_d(z, \lambda)$, and the up-welling irradiance, $E_u(z, \lambda)$ (expressed in W m^{-2}) (Fig. 1.3). The former is the amount of incoming light incident on the upper face of a unit of sea-surface at depth z and wavelength λ. The latter is the amount of light at wavelength λ on the lower face of the unit area at depth z. The rate of decrease in $E_d(z, \lambda)$ and $E_u(z, \lambda)$ with depth are defined as the diffuse attenuation coefficient for downwelling irradiance, $K_d(z, \lambda)$, and for upwelling irradiance, $K_u(z, \lambda)$, respectively (expressed in m^{-1}).

Both $E_u(z, \lambda)$ and $E_d(z, \lambda)$ significantly vary according to factors external to the water body which are not directly related to the incident light field (e.g., cloud cover, wind speed and sea surface roughness). However, per definition, $R(\lambda)$ is a ratio of irradiance quantities partly cancelling the impact of these external factors.

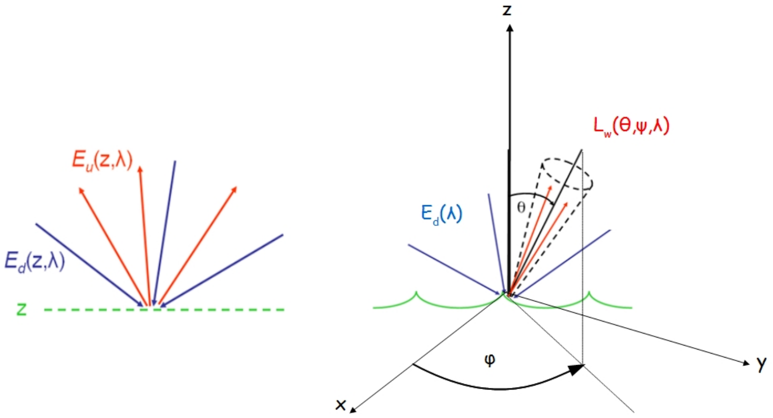

Figure 1.3: *Illustration of light rays contributing to the irradiance reflectance $R(\lambda)$ (left) and to the remote sensing reflectance, $R_{rs}(\lambda)$ (right) (picture adapted from Mobley et al. (2011)).*

In satellite remote sensing, the sensor detects only the fraction of $E_u(z, \lambda)$ in the viewing direction θ and ψ (Fig. 1.3), namely, the radiance $L(z, \lambda, \psi, \theta, \theta_0)$ (expressed in W m^{-2} sr^{-1} and with θ_0 being the sun angle and ψ the azimuthal angular distance from the sun's direction). $L(z, \lambda, \psi, \theta)$ is thus the scattered light flux leaving a surface at depth z in the direction ψ and θ per unit solid angle, $d\omega$, and per unit area. When evaluated just above the sea-surface, $L(z, \lambda, \psi, \theta, \theta_0)$ becomes the water-leaving reflectance $L_w(\lambda, \psi, \theta, \theta_0)$. With the sun at zenith and a nadir viewing instrument, in absence of atmospheric loss and considering the earth at a mean distance from the sun, the water-leaving radiance $L_w(\lambda, \psi, \theta, \theta_0)$ is called the normalized water leaving radiance $L_{wn}(\lambda)$ (Gordon and Clark, 1981; Morel and Gentili, 1996; Morel et al., 2002) (sometimes referred to as the exact normalized water-leaving reflectance). An operational definition of the normalized water leaving radiance is also used in ocean colour remote sensing. This latter definition consists to divide the measured radiance by the actual irradiance at sea level, $E_d^+(\lambda)$ and to multiply it by the solar irradiance at the top op the atmosphere for a mean sun-earth distance, $F_0(\lambda)$. With this operational definition, the water-leaving radiance is thus normalized for the illumination conditions, however, only partly since the measured radiance $L_w(\lambda, \psi, \theta, \theta_0)$ is not isotropic and will change in response to variations in illumination conditions (including solar and viewing angles) in combination with the inherent optical properties of the water. To remove this bi-directional effect, and thus produce the exact normalized water-leaving reflectance, a correction factor need to be applied according to the illumination and environmental conditions (including the sun and viewing angles, sea state and IOPs).

The water-leaving reflectance quantities are also often converted into remote sensing reflectance, $R_{rs}(\lambda)$ (expressed in sr^{-1}), or normalized water-leaving reflectance, $\rho_{wn}(\lambda)$ (dimensionless). These are the standard input to most models deriving bio-geochemical products.

For most ocean colour AOPs the depth z is defined just above or below the sea-surface. For brevity, except when necessary for clarity, the z argument is therefore omitted or replaced by a plus or minus symbol, for quantities measured just above or below sea-surface, respectively. The notation n for $\rho_{wn}(\lambda)$ is also dropped in this manuscript such that $\rho_w(\lambda)$ indicates the normalized water-leaving reflectance.

$\rho_w(\lambda)$, $R_{rs}(\lambda)$, $L_w(\lambda, \theta, \phi, \theta_0)$ and $L_{wn}(\lambda)$ are related to each other as follows:

$$\begin{aligned}
\rho_w(\lambda) &= \pi \frac{L_w(\lambda, \psi, \theta, \theta_0)}{E_d^+(\lambda) brdf(\theta, \theta_0, \psi, \tau_a, W, IOP)} && (1.8)\\
&= \pi \frac{L_w(\lambda, \psi, \theta, \theta_0)}{F_0(\lambda) t_0(\lambda) cos\theta_0 brdf(\theta, \theta_0, \psi, \tau_a, W, IOP)} && (1.9)\\
&= \pi \frac{L_{wn}(\lambda)}{F_0(\lambda)} = \pi R_{rs}(\lambda) && (1.10)
\end{aligned}$$

with $t_0(\lambda)$ being the atmospheric diffuse transmittance in the incident direction θ_0 (θ_0 is the solar zenith angle), and $brdf(\theta, \theta_0, \psi, \tau_a, W, IOP)$ is the bi-directional effect correction which depends on the viewing angles θ and ϕ, the illumination conditions (with θ_0 and the aerosol optical thickness τ_a) and environmental conditions (including the sea state W and IOPs).

To link AOPs and IOPs it is necessary to convert reflectance, radiance and irradiance quantities from just below to just above the sea surface, and inversely. These quantities differ from each other because above-water measurements includes corrections for air-water interface effects while these corrections are not applied to in-water measurements. When both above- and in-water measurements are made with the same azimuth angle, subsurface up-welling water radiance in the direction θ' just beneath the sea-surface, $L_u^-(\lambda, \psi, \theta', \theta_0)$, can be interpolated to above-water radiance in the direction θ as follows (Gordon and Morel, 1983; Morel and Gentili, 1996; Mobley, 1999):

$$L_w(\lambda, \psi, \theta, \theta_0) = L_u^-(\lambda, \psi, \theta', \theta_0) \frac{1 - \rho_f(\theta', \theta)}{n(\lambda)^2} \tag{1.11}$$

with $n(\lambda)$ being the refraction index of the water and $\rho_f(\lambda, \theta, \theta')$, the Fresnel reflectance of the surface as seen from the water side. For $n(\lambda)$ equal to 1.34 and $\rho_f(\lambda, \theta', \theta)$ equal to 0.021, and assuming a low spectral variation for both $n(\lambda)$ and $\rho_f(\lambda, \theta', \theta)$ (hereafter referred to as n and $\rho_f(\theta', \theta)$), the ratio $(1 - \rho_f(\theta', \theta))/(n^2)$ is often approximated by 0.544 (Austin, 1980; Mobley, 1999).

Similarly, above and below down-welling irradiance, $E_d(\lambda)$ and $E_d^-(\lambda)$, respectively, are related to each other as follows (Morel and Gentili, 1996):

$$E_d(\lambda) = E_d^-(\lambda)\frac{1-\bar{r}R^-(\lambda)}{1-\bar{\rho}(\theta,\theta')} \tag{1.12}$$

with $\bar{r}$ being the coefficient of reflection of the up-welling irradiance from water to air, and $\bar{\rho}(\theta,\theta')$, the reflection coefficient for down-welling irradiance from air to water. $R^-(\lambda)$ denotes the subsurface irradiance. It is a similar quantity as the above mentioned $R(\lambda)$ but it is measured just below the sea-surface and is defined as the ratio $E_u^-(\lambda)/E_d^-(\lambda)$, with $E_u^-(\lambda)$ being the up-welling irradiance just below the surface.

Given Eq.(1.11) and Eq.(1.12), $R_{rs}(\lambda)$ can be written in terms of below water remote sensing reflectance, $r_{rs}(\lambda)$, as follows:

$$R_{rs}(\lambda) = \Re\frac{L_u^-(\lambda,\psi,\theta',\theta_0)}{E_d^-(\lambda)} = \Re r_{rs}(\lambda) \tag{1.13}$$

with $\Re$ being

$$\Re = \frac{1-\rho_f(\theta',\theta)}{n^2}\frac{1-\bar{\rho}(\theta,\theta')}{1-\bar{r}R^-(\lambda)} \tag{1.14}$$

$\Re$ takes into account the reflection and refraction effects at the air-sea interface. If the incident light is nearly normal to the mean sea surface, $1-\rho_f(\theta',\theta)$ and $1-\bar{\rho}(\theta',\theta)$ are the transmittance from sea to air and from air to sea, $t(s,a)$ and $t(a,s)$, respectively. Morel and Gentili (1996) summarized the different possible ranges for the above quantities as follows: (1) $t(a,s)$ is 0.957 and varies slightly ($\approx 3\%$) with sun elevation and atmospheric turbidity, (2) $\bar{r}$, the coefficient of reflection of the up-welling irradiance from water to air, is 0.489 and varies only slightly with $R^-(\lambda)$, and, (3) $R^-(\lambda)$ is considered to vary between 0 and 6%. Hence, assuming a mean $R^-(\lambda)$ of 3%, the term $1-\bar{r}R^-(\lambda)$ equals 0.985. The largest uncertainty relies on $t(s,a)$ which is highly dependent on the sea state and consequently on the wind speed. Considering a perfectly flat sea, and thus very low wind speed, and an incident angle nearly normal to the mean sea-surface, $t(a,s)$ can be set equal to 0.979. Accordingly, $\Re$ can be estimated as ≈ 0.529. This approximation was also found to be valid for highly turbid waters dominated by suspended sediments (Doxaran et al., 2002).

Lee et al. (1998a) suggested to rewrite Eq.(1.13) as follows:

$$R_{rs}(\lambda) = \frac{t(a,s)t(s,a)}{n^2}\frac{R^-(\lambda)}{(1-\bar{r}R^-(\lambda))Q^-(\lambda,\theta',\psi)} \tag{1.15}$$

with $Q^-(\lambda,\theta',\psi)$ being the bidirectional function, defined as the ratio $E_u^-(\lambda)/L_u^-(\lambda,\psi,\theta,\theta_0)$. Accordingly, the ratio $R^-(\lambda)/Q^-(\lambda,\theta',\psi)$ equals $r_{rs}(\lambda)$. $R_{rs}(\lambda)$ can thus be related to $r_{rs}(\lambda)$ as follows:

$$R_{rs}(\lambda) = \frac{t(s,a)t(a,s)}{n^2}\frac{r_{rs}(\lambda)}{(1-\bar{r}Q^-(\lambda,\theta',\psi)r_{rs}(\lambda))} \tag{1.16}$$

If the term $\bar{r}Q^-(\lambda,\theta',\psi)r_{rs}(\lambda)$ is ignored, the relation between $R_{rs}(\lambda)$ and $r_{rs}(\lambda)$ becomes a constant ratio (as approximated by Morel and Gentili (1996) and Doxaran et al. (2002) when considering a perfectly flat sea and nearly normal incident angle). However, according to Lee et al. (1998a) the term $\bar{r}Q^-(\lambda,\theta',\psi)r_{rs}(\lambda)$ might be important, especially in turbid and shallow waters.

Based on radiative transfer simulations (RTE, see Section 2.2) performed with the HydroLight model (Mobley, 1989; Mobley and Sundman, 2008), it was found that the factor

$t(s,a)t(a,s)/n^2$ equals 0.52 and $\bar{r}Q^{-}(\lambda,\theta',\psi)$ equals 1.7 for a nadir viewing sensor and optically deep waters (Lee et al., 1998a,b, 2002). Accordingly, the conversion between above and below remote sensing water leaving reflectance can be approximated by:

$$R_{rs}(\lambda) = \frac{0.52 r_{rs}(\lambda)}{(1 - 1.7 r_{rs}(\lambda))} \tag{1.17}$$

and inversely

$$r_{rs}(\lambda) = \frac{R_{rs}(\lambda)}{(0.52 + 1.7 R_{rs}(\lambda))}. \tag{1.18}$$

1.4 LINK BETWEEN IOPS AND AOPS

As mentioned earlier, AOPs depend on the distribution of the light field as well as on the medium. IOPs and AOPs are thus closely related and the reflectance at the sea-surface can be written as a function of $a(\lambda)$ and $b(\lambda)$ (Gordon et al., 1975; Morel and Prieur, 1977; Gordon and Morel, 1983; Gordon et al., 1988). Based on a Monte Carlo study, Gordon et al. (1975) modelled $r_{rs}(\lambda)$ with a polynomial function of $a(\lambda)$ and $b(\lambda)$. Because the first term of the polynomial largely dominates, the polynomial function is simplified as follows:

$$r_{rs}(\lambda) = C\frac{b_b(\lambda)}{a(\lambda) + b_b(\lambda)} \tag{1.19}$$

where C depends on, among other things, the solar zenith angle. This relation was further investigated (Morel and Prieur, 1977; Gordon and Morel, 1983; Gordon et al., 1988) leading to the conclusion that the remote sensing reflectance, $R_{rs}(\lambda)$, at the sea surface, can be expressed as a function of the IOPs $a(\lambda)$ and $b_b(\lambda)$, as follows:

$$R_{rs}(\lambda) = \Re\frac{f_0(\lambda)}{Q_0(\lambda)}\frac{b_b(\lambda)}{a(\lambda) + b_b(\lambda)} \tag{1.20}$$

where $f(\lambda,\theta_0,\phi,IOP)$ is a dimensionless coefficient reflecting the magnitude of the upward flux depending on the solar zenith angle, the optical properties of the sea-water and the wavelength λ. It relates the irradiance reflectance to the inherent optical properties. $f_0(\lambda)$ denotes the particular case when the sun is at zenith ($\theta_0 = 0$). $Q(\lambda,\theta,\theta_0,\phi,IOP)$ is, as defined above, the bidirectional function expressing the non-isotropic character of the light field. It defines the direction of the upward flux. $Q_0(\lambda)$ denotes the particular case when the sun is at zenith and with a nadir viewing instrument. The ratio $f(\lambda,\theta_0,\phi,IOP)/Q(\lambda,\theta,\theta_0,\phi,IOP)$ accounts thus for the spectrally-dependent, non-isotropic structure of the subsurface light field, which is not addressed in other bidirectional reflectance corrections, and depends on sensor and solar zenith angles, their relative azimuth angle, and in-water constituents. $Q(\lambda,\theta,\theta_0,\phi,IOP)$ is minimal for nadir radiances (ranging from 3.2 to 3.9, Morel and Gentili (1996)) and increases with an increase in Chl_a concentrations. The strongest variations in $Q(\lambda,\theta,\theta_0,\phi,IOP)$ according to the sun angle, are observed in the red spectral region (≈ 670 nm) (Morel and Gentili, 1996). However, since $f(\lambda,\theta,IOP)$ and $Q(\lambda,\theta,\theta_0,\phi,IOP)$ follow similar trends with changing sun angles, the sensitivity of the ratio to sun zenith angles is significantly reduced. Typical values for the ratio $f(\lambda,\theta_0,\phi,IOP)/Q(\lambda,\theta,\theta_0,\phi,IOP)$ ranges from 0.08 to 0.12 sr^{-1} with mean values of approximately 0.11 sr^{-1} (Gordon et al., 1988) and 0.13 sr^{-1} in sediment dominated waters (Loisel and Morel, 2001). Except for very low Chl_a concentrations, where the wavelength dependence of $f(\lambda,\theta_0,\phi,IOP)/Q(\lambda,\theta,\theta_0,\phi,IOP)$ is more pronounced in the green and red region of the spectrum due to the contribution of Raman scattering, the spectral dependence of the $f(\lambda,\theta_0,\phi,IOP)/Q(\lambda,\theta,\theta_0,\phi,IOP)$ ratio is considered as relatively small (Loisel and Morel, 2001; Morel et al., 2002; Doxaran et al., 2003; Ruddick et al., 2006).

Note that, unlike IOPs, AOPs can only be measured in the field, because they depend on the ambient radiance distribution found in the water body itself. This explains the need of radiative transfer models such as HydroLight (Mobley, 1989; Mobley and Sundman, 2008) to relate *in situ* IOPs measurements with modelled AOPs which in turn allows to invert the satellite measured AOPs to determine the IOPs and subsequently the nature and concentration of the in-water constituents.

1.5 OPTICAL WATER TYPE CLASSIFICATION SCHEMES

Ocean colour may be influenced by multiple and non-exclusive biological, chemical and physical processes. Hence, distinctive water masses may present nearly similar reflectance spectra, which significantly increases the difficulty to interpret the water signal. Therefore, optical water type classification schemes have been developed to differentiate water masses based on a well defined optical property or a combination of different optical properties (e.g., Jerlov, 1951; Morel and Prieur, 1977; Moore et al., 2001; Lubac and Loisel, 2007; Moore et al., 2009; Vantrepotte et al., 2012). Optical water type classification also represent a valuable way to improve the retrieval of marine parameters by applying class-specific bio-optical algorithms (Loisel et al., 2010; Wozniak et al., 2010; Vantrepotte et al., 2012). In this thesis, a classification of the water masses was also performed to compare the performance of the atmospheric correction methods as a function of the optical water type.

A quantitative classification method was already suggested in the 1950s by Jerlov (1951) who classified oceanic water types according to their optical attenuation properties. Later, Morel and Prieur (1977) used the ratio of Chl_a concentration to scattering coefficient as basis to discriminate water masses dominated by phytoplankton and their associated materials (living or inanimate, particulate or dissolved) (the so-called Case 1 waters) from all other water types (the so-called Case 2 waters). Hence, the latter represents optically complex waters dominated by diverse and multiple in-water constituents with distinctive refractive indices, shapes and sizes resulting in large optical variability. Such varying conditions make it impossible to derive general rules for Case 2 waters. Some authors suggested therefore to make a difference between two extreme situations, namely yellow-substance-dominated and sediment-dominated Case 2 waters (e.g., Bricaud and Morel, 1987; Loisel and Morel, 2001; Morel and Belanger, 2006). The classification method of Morel and Prieur (1977) was useful in the past to aid movement towards the first generation of inversion models. However, nowadays it is considered as an oversimplified and artificial classification scheme (Mobley et al., 2004; Siegel et al., 2005a,b).

An alternative way to separate different optical water types was adopted by Moore et al. (2001, 2009) who identified the degree of membership of each satellite pixel to a given optical water type based on the information provided by their remote sensing reflectance spectra. The authors used therefore a fuzzy logic approach (D'Alimonte et al., 2003). This fuzzy allocation allows to avoid an artificial distinction between Case 1 and Case 2 waters (Morel and Prieur, 1977) and to depict the optical variability encountered in coastal environments.

Lately, Vantrepotte et al. (2012) suggested a similar classification scheme as Moore et al. (2001, 2009) but classified the water masses according to their marine reflectance shape rather than according to their absolute remote sensing reflectance spectra. Therefore, the authors normalized the reflectance spectra by their integrated value prior to data classification. As observed earlier by Lubac and Loisel (2007), the shape of the water reflectance allows to emphasise the nature of the dominant optically significant constituents rather than the clarity of the water column. Hence, a classification scheme based on the spectral reflectance shape is particularly relevant for coastal waters where the magnitude of the reflectance spectra is usually correlated with the relative amount of SPM and not with the type of water optically significant constituents. This is also the reason why the classification scheme of Vantrepotte et al. (2012) is used in the present PhD project to evaluate the performance of the optically complex water atmospheric correction methods as a function of the water type (see later in Chapters 2, 4 and 6).

Vantrepotte et al. (2012) identified four optical coastal water classes and associated them with bio-optical environments: (1) a class dominated by small particles and a high proportion of detrital matter (referred to as Class 1), (2) a class mainly influenced by particulate matter of biological origin with only a low fraction of mineral particles (referred to as Class 2), (3) a class with high loads of particulate matter mainly of mineral origin (referred to as Class 3), and (4) a mixed class presenting high loads of CDOM concentrations and phytoplankton blooms (referred to as Class 4). Next, the authors used a novelty detection technique (D'Alimonte et al., 2003; Mélin et al., 2011) to investigate the belonging of the satellite remote sensing reflectance spectra to the different *in situ* derived optical classes. To illustrate this classification method, Fig. 1.4 shows the normalized reflectance spectra of the *in situ* LOG dataset (detailed in Section 3.3.2.1) classified according to the classification scheme of Vantrepotte et al. (2012). The class-specific spectral shapes are clearly observable. Figure 1.4 also shows the average spectra per class (note that the number of spectra differs for each class). These results are comparable with the results presented by Vantrepotte et al. (2012).

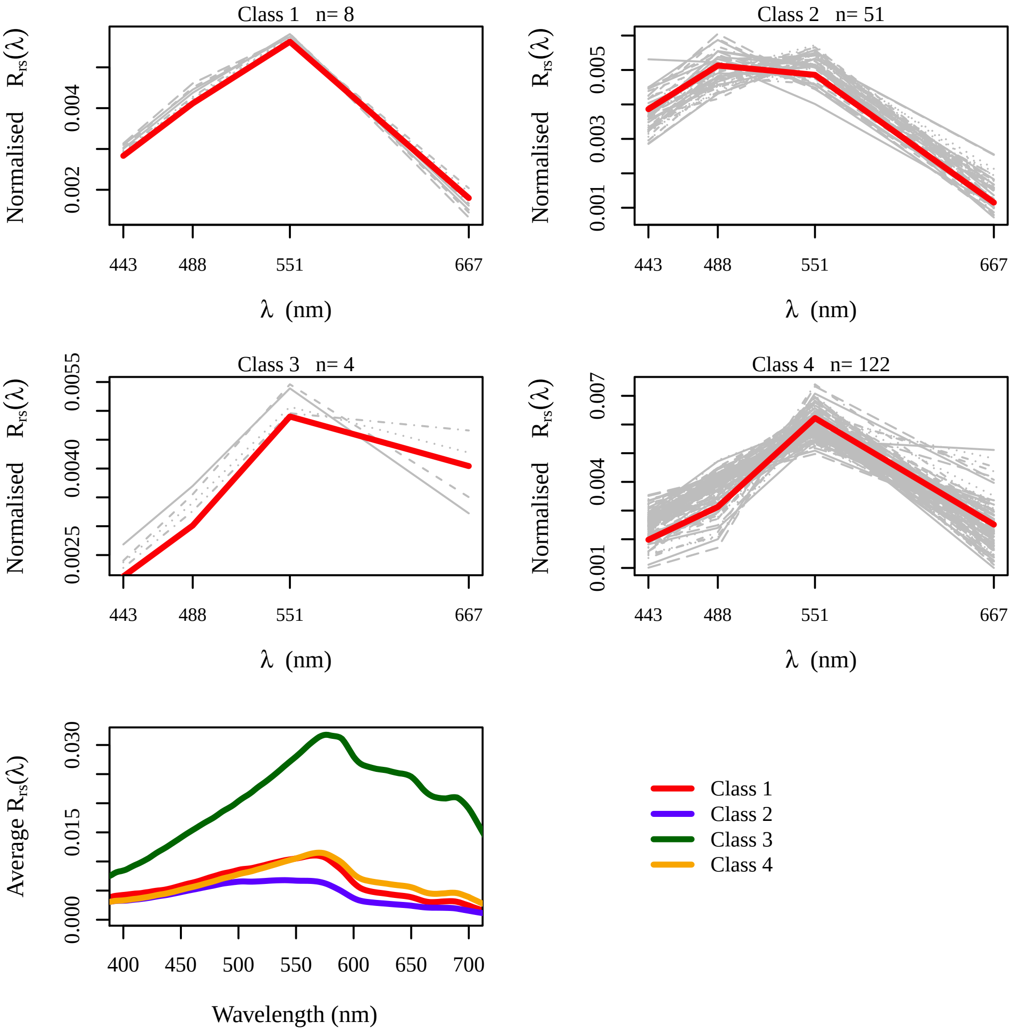

Figure 1.4: *Normalized and averaged reflectance spectra according to the classification scheme of Vantrepotte et al. (2012) applied to the LOG database (Section 3.3.2.1).*

- Chapter 2 -

Atmospheric correction

This chapter describes the concept of atmospheric correction (AC) for ocean colour satellite images. First, the sensor measured signal is defined and analysed. To understand how the contribution of the atmosphere to the sensor measured signal is estimated, it is also essential to briefly discuss the aerosol models and products, used in ocean colour remote sensing, and the radiative transfer equation. Next, a review of the existing AC methods is given followed by a detailed description of the turbid water AC methods evaluated, and eventually improved, in this PhD research.

2.1 Top of atmosphere measured reflectance

Satellite remote sensors measure the top of the atmosphere (TOA) radiance, $L_t^{TOA}(\lambda)$. As represented in Fig. 2.1, $L_t^{TOA}(\lambda)$ can be partitioned in several components and when normalized by the downwelling irradiance at the TOA ($E_d^{TOA}(\lambda)$) and multiplied by π (Eq.(1.10)), the decomposition of the sensor-measured signal can be written in terms of reflectance (Gordon and Wang, 1994; Gordon, 1997):

$$\rho_t^{TOA}(\lambda) = \rho_r^{TOA}(\lambda) + \rho_a^{TOA}(\lambda) + \rho_{ra}^{TOA}(\lambda) + \rho_{wc}^{TOA}(\lambda) + \rho_g^{TOA}(\lambda) + \rho_w^{TOA}(\lambda) \tag{2.1}$$

$\rho_t^{TOA}(\lambda)$ represents the reflectance derived from the sensor measured signal and $\rho_r^{TOA}(\lambda)$, $\rho_a^{TOA}(\lambda)$ and $\rho_{ra}^{TOA}(\lambda)$, the contribution of the atmosphere, i.e., the sunlight scattered by the air molecules in absence of aerosols (Rayleigh scattering), by the aerosols in absence of air (aerosol or Mie scattering) and by the coupling between both air and aerosol molecules, respectively. $\rho_{wc}^{TOA}(\lambda)$ is the reflectance related to the white-caps, $\rho_g^{TOA}(\lambda)$ to the glitter, and $\rho_w^{TOA}(\lambda)$ to the ocean, when transmitted to the top of the atmosphere. To retrieve the normalized water-leaving reflectance at the water surface ($\rho_w(\lambda)$), $\rho_w^{TOA}(\lambda)$ needs to be corrected for the diffuse atmospheric transmittance along the sun-to-sea ($t_v(\lambda)$) and sea-to-sensor ($t_0(\lambda)$) optical path. The analytical definition of the diffuse atmospheric transmittance is the following (Wang, 1999):

$$t_{v,0}(\lambda) = exp\left[-\frac{\frac{\tau_r(\lambda)}{2} + \tau_{oz}(\lambda)}{\mu_{v,0}}\right] * exp\left[\frac{(1-\omega_a(\lambda)F_a(\lambda))\tau_a(\lambda)}{\mu_{v,0}}\right] \tag{2.2}$$

where $\omega_a(\lambda)$ is the aerosol single-scattering albedo, $\mu_{v,0}$ is the cosine of the angle in the sun or sea direction, and $\tau_r(\lambda)$, $\tau_{oz}(\lambda)$ and $\tau_a(\lambda)$ are the Rayleigh, ozone and aerosol optical thickness, respectively. $F_a(\lambda)$ is related to the aerosol scattering phase function $P_a(\Theta,\lambda)$ as follows Wang (1999):

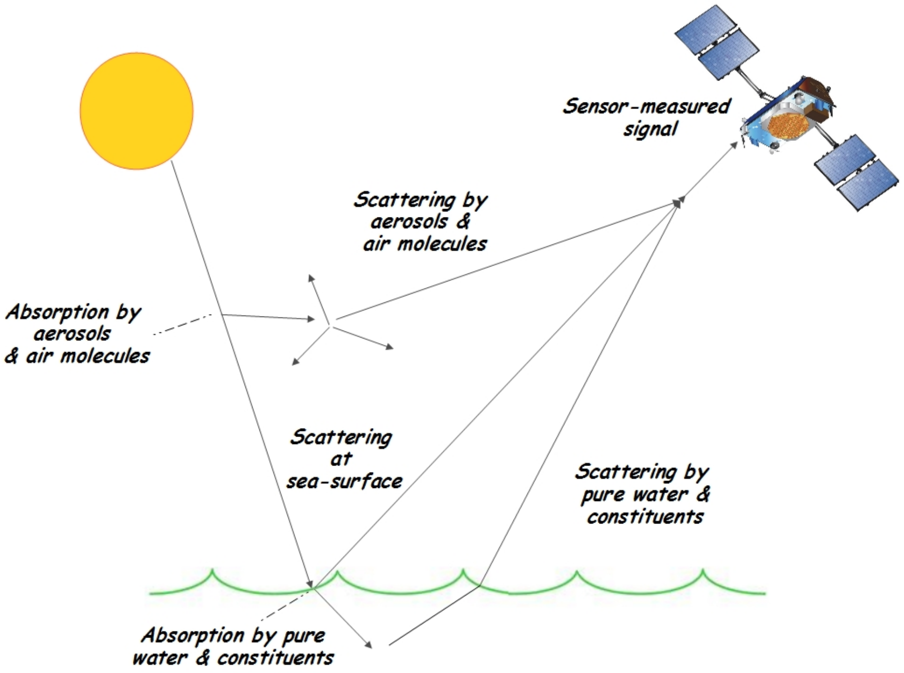

Figure 2.1: *Schematic representation of the light path through water and atmosphere.*

$$F_a(\lambda) = \frac{1}{4\pi}\int_0^1\int_0^{2\pi} P_a(\Theta,\lambda)d\mu_{v,0}d\phi \tag{2.3}$$

In the context of the AC, it may also be useful to mention the formal definitions of $t_v(\lambda)$ and $t_0(\lambda)$. These are (Yang and Gordon, 1997; IOCCG, 2010):

$$t_v(\lambda) = \frac{L_w^{TOA}(\lambda)}{L_w(\lambda)} \tag{2.4}$$

$$t_0(\lambda) = \frac{E_d(\lambda)}{E_d^{TOA}(\lambda)} \tag{2.5}$$

Hence, according to Eq.(1.10), (2.4) and (2.5), $\rho_w^{TOA}(\lambda)$ is related to $\rho_w(\lambda)$ as follows:

$$\rho_w^{TOA}(\lambda) = \pi\frac{L_w^{TOA}(\lambda)}{E_d^{TOA}(\lambda)} = \pi\frac{t_0(\lambda)t_v(\lambda)L_w(\lambda)}{E_d(\lambda)} = t_v(\lambda)t_0(\lambda)\rho_w(\lambda) \tag{2.6}$$

and Eq.(2.1) can be rewritten as:

$$\rho_t^{TOA}(\lambda) = \rho_r^{TOA}(\lambda) + \rho_a^{TOA}(\lambda) + \rho_{ra}^{TOA}(\lambda) + \rho_{wc}^{TOA}(\lambda) + \rho_g^{TOA}(\lambda) + t_v(\lambda)t_0(\lambda)\rho_w(\lambda) \tag{2.7}$$

.

Both $\rho_g^{TOA}(\lambda)$ and $\rho_{wc}^{TOA}(\lambda)$ can be modelled for a given sun and sensor zenith angle (Cox and Munk, 1954) and a given wind speed (Frouin et al., 1996), respectively. During pre-processing, $\rho_t^{TOA}(\lambda)$ is corrected for gas absorption, Rayleigh scattering, white-caps and glitter (Gordon, 1997). This term is referred to as the Rayleigh corrected reflectance, $\rho_{rc}^{TOA}(\lambda)$:

$$\rho_{rc}^{TOA}(\lambda) = \rho_t^{TOA}(\lambda) - \rho_r^{TOA}(\lambda) - \rho_{wc}^{TOA}(\lambda) - \rho_g^{TOA}(\lambda) \tag{2.8}$$

$$= \rho_a^{TOA}(\lambda) + \rho_{ra}^{TOA}(\lambda) + t_v(\lambda)t_0(\lambda)\rho_w(\lambda) \tag{2.9}$$

Accordingly, if the optical properties and concentration of the aerosols are known along their vertical distribution, the quantities $\rho_a^{TOA}(\lambda)$, $\rho_{ra}^{TOA}(\lambda)$, $t_0(\lambda)$ and $t_v(\lambda)$ can be estimated and the parameter of interest $\rho_w(\lambda)$ can be retrieved from the TOA sensor measured signal. However, aerosol concentrations and their optical properties may be highly variable and the aerosol radiance varies over similar magnitude ranges as $\rho_w(\lambda)$. Hence, it is not possible to determine the terms $\rho_a^{TOA}(\lambda)$ and $\rho_{ra}^{TOA}(\lambda)$ a priori without appropriate models for aerosol optical properties and some additional assumptions. AC methods (as defined in this manuscript) have thus as main goal to correctly select the aerosol model and, subsequently, $\rho_a^{TOA}(\lambda)$ and $\rho_{ra}^{TOA}(\lambda)$, in the aim to retrieve $\rho_w(\lambda)$.

2.2 AEROSOL MODELS AND PRODUCTS USED IN OCEAN COLOUR REMOTE SENSING

To ease the retrieval of the aerosol reflectance and optical properties, aerosols are often classified into groups based on their origin and size properties. Shettle and Fenn (1979), for instance, suggested tropospheric models with aerosols from rural and urban origin, and maritime models with aerosols from oceanic and continental origin. Each model is characterized by their volume size distribution, which is based on a combination of two log-normal distributions for fine and coarse particles, respectively (Fig. 2.2):

$$\frac{dV(r)}{dln\ r} = \sum_{i=1}^{2}\left[\frac{V_i}{\sqrt{2\pi}\sigma_i}\right] exp\left(-\frac{(ln\ r - ln\ r_i)^2}{2\sigma_i^2}\right) \tag{2.10}$$

where V_i is the volume of the particles and r is the geometric radius of the unit of volume. r_i and σ_i stand for the geometric mean and standard deviation of the radius of the i-th distribution, respectively. The approximation by a combination of two log-normal distributions is illustrated in Fig. 2.2 which shows an example of aerosol volume size distributions developed based on Sun-photometer data from different maritime Aerosol Robotic Network sites (Sayer et al., 2012).

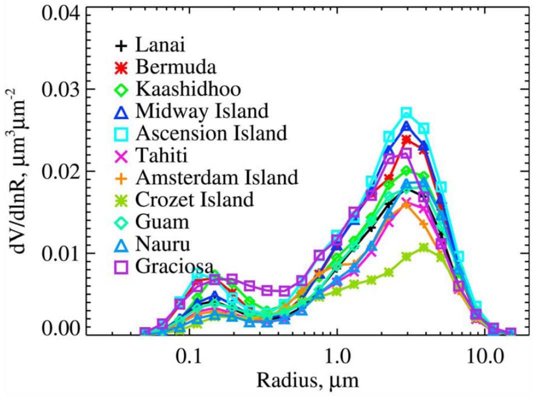

Figure 2.2: *Aerosol volume size distribution based on Sun-photometer data from maritime Aerosol Robotic Network stations (Sayer et al., 2012).*

Shettle and Fenn (1979) observed a dependence of the mean radius and standard deviation to the relative humidity (RH). The authors suggested therefore distinctive aerosol parameters and associated refractive indices, $m(\lambda)$, for the different aerosol models and at different levels of relative humidity. For the processing of SeaWiFS and MODIS Aqua ocean colour images, the aerosol models suggested by Shettle and Fenn (1979) were further extended by Gordon and Wang (1994) to include beside tropospheric and maritime aerosols, also coastal aerosols. The latter are expected to occur near the coast and include half of the fraction of sea salt compared to the maritime models. With the reprocessing of SeaWiFS in 2000, the oceanic aerosol model with 99% RH from Shettle and Fenn (1979) was also added as a candidate model while the tropospheric aerosol model with 70% RH was excluded (McClain et al., 2000). Although these models have been used until the reprocessing of 2009 for SeaWiFS and MODIS Aqua, they are considered as a simplification and generalized version of typical conditions (Shettle and Fenn, 1979; Gordon and Wang, 1994). Moreover, these aerosol particles are considered homogeneous and spherical, for simplification to resolve the radiative transfer equation (Section 2.3), as suggested in the Mie theory (Mie, 1908). Therefore, since 2009, the standard processing of SeaWiFS and MODIS images includes a more realistic suite of aerosol models (Ahmad et al., 2010), derived from ground-based measurements provided by eleven open ocean and coastal sites from the AERONET network (Holben et al., 1998). Ahmad et al. (2010) defined 80 aerosol models characterized by 8 levels of atmospheric RH and each level of RH includes 10 levels of relative concentration of fine- and coarse-mode particles (from 0.0 to 0.95). Fine-mode aerosols are assumed to be from continental origin and all absorbing, while coarse-mode aerosols are oceanic in nature (sea-salt particles) and non-absorbing (Ahmad et al., 2010). Hence, over open ocean, the scattering process is dominated by a high fraction of coarse-mode aerosols (about 80%) and only a small fraction of fine-mode aerosols (about 20%). With these new 80 aerosol models, Ahmad et al. (2010) showed a better agreement between the satellite retrieved aerosol properties (i.e., $\tau(\lambda)$) and the *in situ* AERONET aerosol data.

2.3 RADIATIVE TRANSFER EQUATION

The radiative transfer equation (RTE) describes the propagation of light through a medium taking into account how it is attenuated while passing through the medium (including absorption, elastic and inelastic scattering and emission). In the context of AC the medium is the atmospheric layer between ocean surface and satellite sensor and the RTE is used to construct, for each aerosol model and for a range of sensor wavelengths and sun and viewing geometries, lookup tables for computing the aerosol reflectances (i.e. $\rho_a(\lambda)$ and $\rho_{ra}(\lambda)$).

Therefore, the atmospheric layer between ocean surface and satellite is assumed to be vertically stratified and made up of two plane parallel and described by (Mobley, 1994; Mobley et al., 2011):

1. Its extinction coefficient at a given wavelength and as a function of the altitude, $c(dr, \lambda)$
2. The associated scattering phase function $P(\theta, \phi \rightarrow \theta_v, \phi_v, \lambda)$, describing the probability that the incoming radiation reaching the medium, with a direction described by the angles θ and ϕ, is scattered in the direction θ_v and ϕ_v.
3. The single-scattering albedo $\omega_0(dr, \lambda)$, equal to the ratio $b(dr, \lambda)/c(dr, \lambda)$.

The loss of photons, when the light propagates through a distance dr due to absorption and elastic scattering to other directions, is proportional to the incoming radiance and can be written as:

$$-c(dr, \lambda)L(dr, \theta, \phi, \lambda) \tag{2.11}$$

The process accounting for elastic scattering from all other directions into the viewing direction is function of the incident radiance, the solid angle of the incident radiance and the volume scattering phase function for all scattering angles, $p(\theta, \phi \rightarrow \theta_v, \phi_v, \lambda)$. $p(\theta, \phi \rightarrow \theta_v, \phi_v, \lambda)$ describes the angular distribution of the scattered photons within the medium and is related to the scattering phase function $P(\theta, \phi \rightarrow \theta_v, \phi_v, \lambda)$ as follows:

$$p(\theta, \phi \rightarrow \theta_v, \phi_v, \lambda) = b(dr, \lambda)\frac{P(\theta, \phi \rightarrow \theta_v, \phi_v, \lambda)}{4\pi} \tag{2.12}$$

When considering the scattering coming from all directions, the scattered radiance is integrated over all scattering angles. This is:

$$dL(r + dr, \theta, \phi, \lambda) = \int_0^{2\pi}\int_0^{\pi} L(dr, \theta, \phi, \lambda)p(\theta, \phi \rightarrow \theta_v, \phi_v, \lambda)sin\theta d\theta d\phi \tag{2.13}$$

When ignoring inelastic scattering and polarization, the RTE describing the variation of the incoming radiance becomes:

$$\begin{aligned}\frac{dL(dr, \theta_v, \phi_v, \lambda)}{dr} &= -c(dr, \lambda)L(dr, \theta_v, \phi_v, \lambda) \\ &\quad + \int_0^{2\pi}\int_0^{\pi} L(dr, \theta, \phi, \lambda)p(\theta, \phi \rightarrow \theta_v, \phi_v, \lambda)sin\theta d\theta d\phi\end{aligned} \tag{2.14}$$

It is often more convenient to use a coordinate system with the depth z being normal to the sea surface (Mobley et al., 2011). Assuming a horizontally homogeneous atmosphere, dr becomes $dz/cos\theta$. For AC, the nondimensional optical depth, $\tau(\lambda)$, is often used as the space variable, with $cos\theta$ as the direction variable. $\tau(\lambda)$ is defined as the attenuation coefficient $c(dz, \lambda)$ integrated over the atmospheric depth z.

$$\tau(\lambda) = \int_h^{\infty} c(z, \lambda)dz \tag{2.15}$$

Recalling the definition of $\omega_0(\lambda)$ and Eq.(2.12) and (2.15), Eq.(2.14) becomes:

$$cos\theta\frac{dL(\theta_v, \phi_v, \lambda)}{d\tau(\lambda)} = -L(\theta_v, \phi_v, \lambda) + \frac{\omega_0(\lambda)}{4\pi}\int_0^{2\pi}\int_{-1}^{1} L(\theta, \phi, \lambda)P(\theta, \phi \rightarrow \theta_v, \phi_v, \lambda)dcos\theta d\phi \tag{2.16}$$

According to Eq.(2.16), any two atmospheres radiated with the same incident light flux and with similar $\omega_0(\lambda)$ and $P(\theta, \phi \rightarrow \theta_s, \phi_s, \lambda)$, will have the same radiance distribution $L(\theta_s, \phi_s, \lambda)$ at a given optical depth $\tau(\lambda)$.

The RTE can be easily derived but no analytical solution exists since it involves both an integral and derivative of the radiance. However, when single scattering only is assumed (provided that the optical thickness of the atmosphere is $<< 1$ (Gordon and Wang, 1994) and denoted by $\rho_{as}(\lambda)$), a numerical approximation of the RTE is found and atmospheric radiance can be estimated as follows:

$$\rho_{as}(\lambda) = \frac{\omega_a(\lambda)\tau_a(\lambda)p_a(\theta, \phi \rightarrow \theta_v, \phi_v, \lambda)}{4cos\theta_0 cos\theta_v} \tag{2.17}$$

with $p_a(\theta, \phi \rightarrow \theta_v, \phi_v, \lambda)$ being function of the scattering phase function and the Fresnel reflectance of the interface for a given angle θ, $r(\theta)$ (Gordon and Wang, 1994).

$$p_a(\theta, \phi \rightarrow \theta_v, \phi_v, \lambda) = P(\theta^-, \lambda) + [r(\theta_v) + r(\theta)]P(\theta^-, \lambda) \tag{2.18}$$

$$cos(\theta^{\pm}) = \pm cos(\theta)cos(\theta_v) - sin(\theta)sin(\theta_v)cos(\phi_v - \phi) \tag{2.19}$$

Expression (2.17) is used to estimate at each wavelength and for a given scan geometry, both $\rho_a(\lambda)$ and $\rho_r(\lambda)$ according to the three variables $\omega_x(\lambda)$, $p_x(\theta, \phi \rightarrow \theta_s, \phi_s, \lambda)$ and $\tau_x(\lambda)$ (with x being a or r).

2.4 AC METHODS FOR SECOND GENERATION OCEAN COLOUR SATELLITE IMAGES

In the past, since most studies focussed on open ocean waters, classic AC approaches were based on the so-called black pixel assumption. This assumption supposes that the seawater absorbs all incoming light in a given spectral range allowing to determine the aerosol properties in this part of the spectral region. Knowing the aerosol properties, the atmospheric contribution can be extrapolated to other wavelengths. With the first generation of ocean colour sensors (e.g., CZCS), it was assumed that seawater becomes totally absorbent in the red region of the spectrum (Gordon, 1978). Later, with the NIR sensors aboard the second generation ocean colour satellites (e.g., SeaWiFS, MERIS and MODIS), the NIR bands were used for the AC. The black pixel assumption AC algorithm, initially developed for the AC method of SeaWiFS, has extensively been described by Gordon and Wang (1994) and therefore, often referred as the GW94 AC algorithm. However, the black pixel assumption is verified in open ocean waters ($Chl_a < 2$ mg m^2, according to Siegel et al. (2000)), for which the optical properties are mainly driven by phytoplankton and co-varying biological constituents, but not in highly productive or optically complex waters where significant concentrations of algal and non-algal particles scatter and absorb light in the NIR spectral region (Siegel et al., 2000; IOCCG, 2000). Applying the black pixel assumption for the AC in such water masses may result in significant errors on the retrieved $\rho_w(\lambda)$. Considering zero $\rho_w(\lambda)$ in the NIR will tend to overestimate the aerosol contribution and subsequently induce negative $\rho_w(\lambda)$ estimations. Numerous studies already recognised that the AC algorithm relying on the black pixel assumption was not applicable in optically more complex and highly productive waters and suggested AC methods with alternative assumptions (e.g, Moore et al., 1999; Siegel et al., 2000; Ruddick et al., 2000; Stumpf et al., 2003; Ruddick et al., 2006; Doerffer and Schiller, 2007; Schroeder et al., 2007; Kuchinke et al., 2009a; Wang et al., 2009; Bailey et al., 2010; Brajard et al., 2012; Shanmugam, 2012; Wang et al., 2012). Several approaches are GW94-based AC methods. Accordingly, it is essential to first describe the initial GW94 AC algorithm.

2.4.1 The black pixel assumption GW94 AC algorithm

The GW94 AC algorithm relying on the black pixel assumption uses the spectral information at two wavelengths in the NIR spectral domain (e.g., at 748 and 869 nm for MODIS Aqua) and defines a parameter, $\epsilon(\lambda, \lambda_0)$, the aerosol reflectance ratio. Per definition and according to Eq.(2.17), $\epsilon(\lambda, \lambda_0)$, with λ_0 being a reference wavelength in the NIR spectral domain, can be written as follows:

$$\epsilon(\lambda, \lambda_0) = \frac{\rho_{as}(\lambda)}{\rho_{as}(\lambda_0)} = \frac{\omega_a(\lambda)\tau_a(\lambda)p_a(\theta, \phi \to \theta_v, \phi_v, \lambda)}{\omega_a(\lambda_0)\tau_a(\lambda_0)p_a(\theta, \phi \to \theta_v, \phi_v, \lambda_0)} \tag{2.20}$$

If $p_a(\theta_0, \phi_0 \to \theta_v, \phi_v, \lambda)$ and $\omega_a(\lambda)$ are considered as spectrally independent, $\epsilon(\lambda, \lambda_0)$ is independent of the scattering angle and can be approximated by the optical thickness ratio as follows (Gordon et al., 1983):

$$\epsilon(\lambda, \lambda_0) = \left(\frac{\lambda}{\lambda_0}\right)^{-\alpha(\lambda,\lambda_0)} \approx \frac{\tau_a(\lambda)}{\tau_a(\lambda_0)} \tag{2.21}$$

Latter, to better approximate $\epsilon(\lambda, \lambda_0)$ and to increase the separability between the aerosol models, Gordon and Wang (1994) and Gordon (1997) suggested to replace Eq.(2.21) by an exponential function of the form $e^{c(\lambda_0 - \lambda)}$, with c being a constant depending on the aerosol model, the viewing geometry and the relative humidity.

The approximation for $\epsilon(\lambda, \lambda_0)$ includes thus the following assumptions on the aerosol properties: (1) assuming single scattering, the spectral aerosol reflectance $\rho_a(\lambda)$ is proportional to the aerosol optical thickness, (2) the spectral ratio of the optical thickness follows an Ångström's law, and (3) the aerosol reflectance ratio, $\epsilon(\lambda, \lambda_0)$, is related to the Ångström exponent, $\alpha(\lambda, \lambda_0)$ (also often denoted by $\eta(\lambda, \lambda_0)$, Chapter 4 and 6), a parameter relating the aerosol particle size to the aerosol optical model spectral dependence. $\alpha(\lambda, \lambda_0)$ is independent of the viewing and solar geometry and is computed from the spectral variation of $\tau_a(\lambda)$ between two wavelengths (Eq.(2.21)). The Ångström exponent is usually large for very small aerosols (e.g., sulphates from polluted areas) and low for aerosols containing large particles (e.g., sea-salt, oceanic aerosols or desert dust) (Shettle and Fenn, 1979; Gordon and Wang, 1994; Thieuleux et al., 2005). Towards open ocean waters where oceanic aerosol models are encountered, $\alpha(\lambda, \lambda_0)$ tends to decrease, while over coastal regions, where a larger proportion of continental or tropospheric aerosols are located, $\alpha(\lambda, \lambda_0)$ increases. $\alpha(\lambda, \lambda_0)$ also decreases with an increase in RH. Table 2.1 gives the Ångström exponents, retrieved from the ratio of $\tau_a(\lambda)$ at 510 and 865 nm, corresponding to the 12 aerosol models derived from the oceanic and tropospheric lognormal modes of Shettle and Fenn (1979) and the added coastal aerosol models suggested by Gordon and Wang (1994).

Table 2.1: *Characteristics of the 12 aerosol models derived from the oceanic and tropospheric lognormal modes of Shettle and Fenn (1979) and the coastal aerosol models suggested by Gordon and Wang (1994).*

Model	Type	Relative humidity (%)	% oceanic mode	% tropospheric mode	$\alpha(443, 865)$
O99	Oceanic	99	100	0	-0.08
M99	Maritime	99	1	99	0.10
C99	Coastal	99	0.5	99.5	0.41
M90	Maritime	90	1	99	0.22
C90	Coastal	90	0.5	99.5	0.50
M70	Maritime	70	1	99	0.23
M50	Maritime	50	1	99	0.40
C70	Coastal	70	0.5	99.5	0.64
C50	Coastal	50	0.5	99.5	0.74
T99	Tropospheric	99	0	100	1.08
T90	Tropospheric	90	0	100	1.28
T50	Tropospheric	50	0	100	1.41

Fig. 2.3 illustrates the spectral variations in $\epsilon(\lambda, \lambda_0)$ developed for the AC of SeaWiFS with λ_0 at 865 nm and for the 12 aerosol models, with a viewing angle θ of 45° and with the sun at zenith. As seen in this figure, $\epsilon(\lambda, \lambda_0)$ varies as a function of the aerosol models and RH. Its spectral dependency decreases with an increase in RH (i.e., an increase in particle size due to swelling).

When the estimated $\epsilon(\lambda, \lambda_0)$ falls in between two models, a weighting function is used to account for both models. This allows to include a wider range of atmospheric compositions and to avoid discontinuity between neighbouring pixels in the retrieved parameters due to abrupt changes in the selected aerosol model.

When the optical thickness of the atmosphere is relatively low ($\tau(\lambda_{NIR}) < 0.05$, Gordon (1997)), the atmospheric reflectance is well approximated by single scattering aerosol and Rayleigh reflectance (i.e., $\rho_{ra}(\lambda)$ is ignored in Eq.(2.9), single scattering approximation). In contrast when $\tau(\lambda)$ increases, the single scattering approximation is no longer valid (Gordon and Wang, 1994). To account for multiple scattering, Gordon and Wang (1994) estimated with RTE simulations, for each aerosol model and each scan geometry, the relationship between $\rho_a(\lambda) + \rho_{ra}(\lambda)$ and $\rho_{as}(\lambda)$.

As outlined in Fig. 2.4, the GW94 AC algorithm can be summarized as follows: For two bands in the NIR spectral region, λ_i and λ_j, $\rho_{rc}(\lambda)$ is estimated assuming $\rho_w(\lambda_{NIR})$ being negligible. Next, $\rho_{as}(\lambda_i)$ and $\rho_{as}(\lambda_j)$ are retrieved from $\rho_{rc}(\lambda_i)$ and $\rho_{rc}(\lambda_j)$, respectively, using

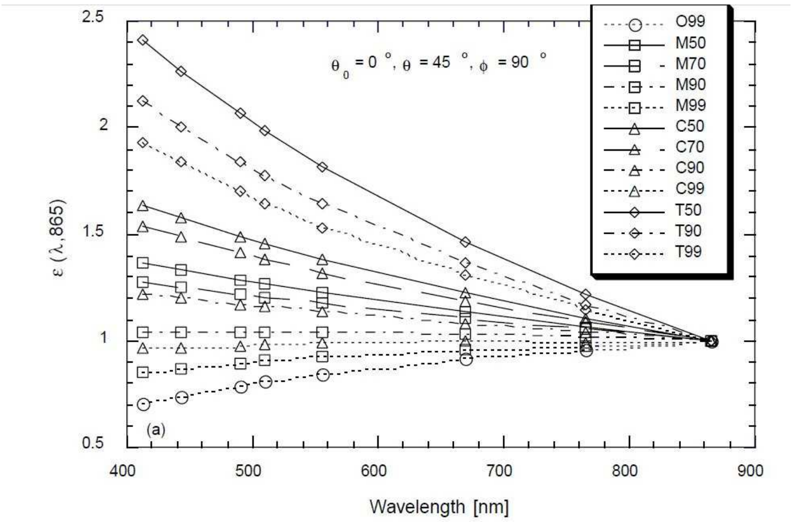

Figure 2.3: *$\epsilon(\lambda, 865)$ as a function of λ with $\theta_v = 45°$ and the sun at zenith ($\theta_0 = 0°$) for the 12 candidate aerosol models. Figure taken from McClain et al. (2000).*

computed look-up tables including the relations between $\rho_a(\lambda) + \rho_{ra}(\lambda)$ and $\rho_{as}(\lambda)$. For each pixel, the ratio $\epsilon(\lambda_i, \lambda_j)$ is thus estimated and two candidate aerosol models are selected. $\epsilon(\lambda, \lambda_j)$ can then be extrapolated from the NIR to any wavelength in the visible, between the pair of candidate aerosol models and the associated $\rho_{as}(\lambda)$ is determined. $\rho_a(\lambda) + \rho_{ra}(\lambda)$ can then be retrieved with the look-up tables as suggested by Gordon and Wang (1994) and Eq.(2.9) can be solved to obtain $\rho_w(\lambda)$.

2.4.2 Atmospheric correction for optically complex waters

To bypass the erroneous application of the black pixel assumption in highly productive or optically complex waters, numerous alternative AC methods have been developed. Some of these attempt to extent the GW94 AC algorithm by modelling the non-zero NIR $\rho_w(\lambda)$ based on estimated geophysical parameters, such as SPM (Moore et al., 1999; Aiken and Moore, 2000; Lavender et al., 2005) or Chl_a (Siegel et al., 2000) or based on spectral relationships and assumptions on the diffuse attenuation coefficient (Wang et al., 2012). A NIR-modelling scheme is also used in the NASA standard AC algorithm (hereafter referred to as STD) including a bio-optical model to retrieve the IOPs in the red bands and extrapolate these to the NIR spectral domain to obtain $\rho_w(NIR)$ (Arnone et al., 1998; Stumpf et al., 2003; Bailey et al., 2010). This AC method is detailed in the next section.

Other AC approaches, such as the AC methods suggested by Hu et al. (2000) and Ruddick et al. (2000, 2006), assume spatial homogeneity in aerosol reflectance allowing to extrapolate over the area of interest the aerosol model selected from nearby pixels where the black pixel assumption is verified. Ruddick et al. (2000, 2006) also suggested to force the AC method with a constant NIR water reflectance ratio to account for the water contribution in the NIR spectral region. This approach, hereafter referred to as the NIR Similarity Spectrum algorithm ('SIMIL' by Goyens et al. (2013c)) or MUMM AC method, is detailed in Section 2.4.2.2.

With the addition of Short-Wave Infra-red (SWIR) bands on the MODIS Aqua sensor, Wang and Shi (2005) also suggested to extent the GW94 AC algorithm using the SWIR spectral domain to retrieve the aerosol properties. Indeed, in the SWIR spectral region, even very turbid waters are strongly absorbent. However, since such bands are often developed for atmospheric and land applications, the signal-to-noise-ratio is often to low to ensure accurate remote sensing derived products for ocean colour applications (Wang, 2007). Wang and Shi (2007) suggested therefore a switching NIR-SWIR AC method combining the STD and SWIR AC approaches.

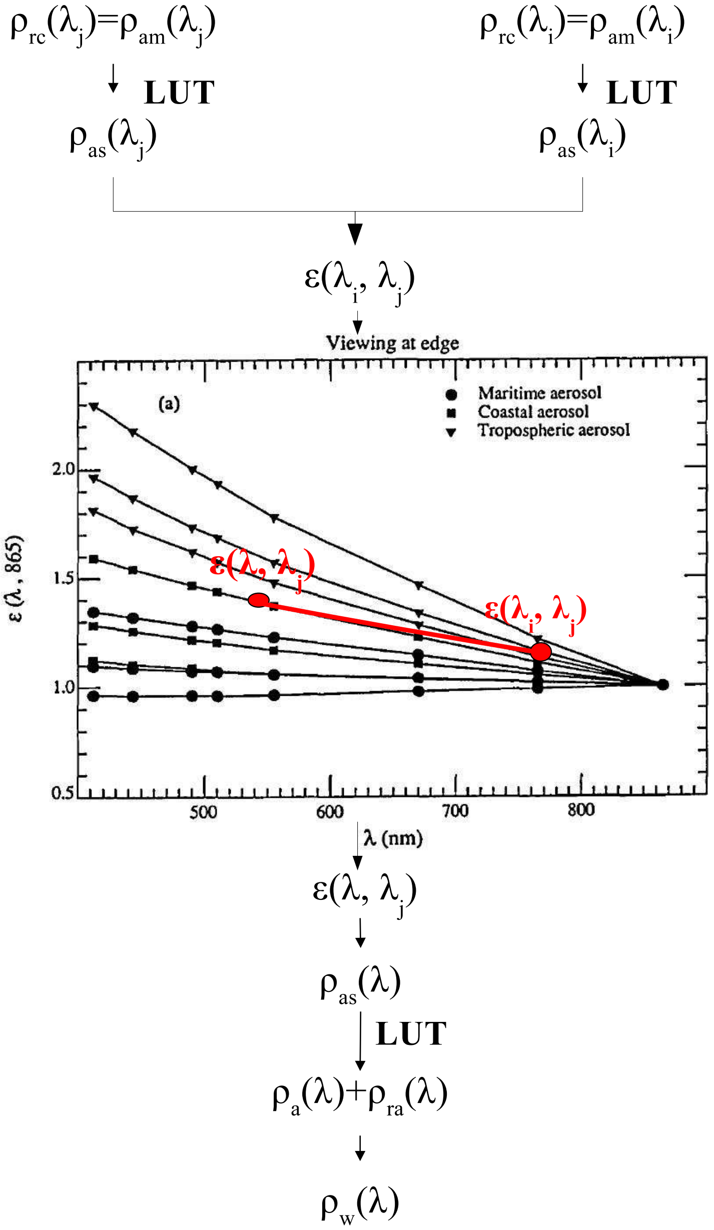

Figure 2.4: *Schematic sketch of the GW94 AC algorithm suggested by Gordon and Wang (1994). 'LUT' stands for look-up tables and λ_i and λ_j indicate the two NIR reference bands.*

This switching method was later revised by Wang et al. (2009) to further improve $\rho_w(\lambda)$ retrievals. The updated NIR-SWIR AC method is described in Section 2.4.2.3.

These GW94-based AC algorithms solve the ocean and atmosphere components separately and only consider the NIR region of the spectrum to retrieve the aerosol properties. However, as shown in Fig. 2.3, a small uncertainty in the retrieved aerosol properties in the NIR spectral region (e.g., $\epsilon(\lambda, \lambda_0)$) may lead to the selection of an inappropriate aerosol model and thus result in a large uncertainty in the estimated aerosol contribution in the visible region. Moreover, the presence of absorbing aerosols can not be detected when considering solely the NIR spectral region where absorbing and non-absorbing aerosols show similar behaviours (Nobileau and Antoine, 2005). Therefore, several AC approaches were suggested including coupled ocean-atmosphere optimization or inversion methods allowing to consider the aerosol and the water contribution simultaneously and, eventually, the signal over the entire spectral range (including the visible range where absorbing aerosols are possibly identified (Moulin et al., 2001a; Chomko et al., 2003; Nobileau and Antoine, 2005)). Commonly used coupled ocean-atmosphere optimization or inversion methods are the spectral matching and optimization AC approaches as well as the neural network-based AC algorithms.

The spectral matching method (Gordon et al., 1997) requires a large set of simulated $\rho_t^{TOA}(\lambda)$ resulting from a combination of NIR aerosol optical thickness values, $\tau_a(\lambda)$, and Chl_a concentrations and a scattering related parameter, b^0. Each $\tau_a(\lambda)$ value is associated with a given aerosol model allowing the estimations of $\rho_a(\lambda)$ and $\rho_{ra}(\lambda)$, while the Chl_a and b^0 values are used as input to the semi-empirical bio-optical model (Gordon et al., 1988) to provide estimations of $\rho_w(\lambda)$. The percent deviation of the simulated and measured $\rho_t^{TOA}(\lambda)$ is then calculated over the entire spectrum and the lowest percent deviation is used to select the model parameters $\tau_a(\lambda)$, Chl_a and b^0. $\rho_w(\lambda)$ is then retrieved at each wavelength. Such AC methods have been successfully applied over absorbing aerosol atmospheres (Moulin et al., 2001c,b; Banzon et al., 2004).

The spectral optimization AC algorithm was first suggested by Chomko and Gordon (1998). This algorithm is similar to the spectral matching algorithm but replaces the set of realistic aerosol models by a simple one-parameter Junge distributed collection of spherical particles and varying wavelength-independent complex refractive index. This implies that such AC methods are only valid for non-absorbing aerosols or when the aerosol absorption index is independent of wavelength (e.g., black carbon) (Chomko et al., 2003). The algorithm of Chomko and Gordon (1998) was later improved by Chomko et al. (2003) by including the Garver-Siegel-Maritorena ocean bio-optical model to simulate $\rho_w(\lambda)$. More recently, Kuchinke et al. (2009a) extended the method to turbid waters by replacing the bio-optical model used to estimate $\rho_w(\lambda)$. Another variation of the spectral optimization AC algorithm was also suggested by Jamet et al. (2005) and later updated by Brajard et al. (2006a,b, 2012). The authors replace the discrete look-up tables from the procedure of Chomko and Gordon (1998) by a neural network regression (Multi-Layer Perceptrons).

The use of neural-networks also appeared to be useful to invert the $\rho^{TOA}(\lambda)$ signal into $\rho_w(\lambda)$ including complex relationships between these two variables (Doerffer and Schiller, 2007; Schroeder et al., 2007; Doeffer and Schiller, 2008). In this study, the neural-network based AC algorithm of Schroeder et al. (2007) adapted for MODIS Aqua bands, is described in Section 2.4.2.4.

2.4.2.1 The standard NASA AC method: a GW94-based algorithm iterating over a NIR-modeling scheme using a bio-optical model ('STD')

The NIR-modeling scheme of the NASA standard AC method (STD) was initially developed for the AC of SeaWiFS by Stumpf et al. (2003), and later revised by Bailey et al. (2010), to extent the GW94 AC algorithm to turbid waters. This NIR-modeling scheme includes an iterative bio-optical model to retrieve $\rho_w(\lambda_{NIR})$. Here, the latest revision of the STD algorithm (as included in the SeaWiFS Data Analysis System (SeaDAS) version 6.4), including the aerosol models suggested by Ahmad et al. (2010), is briefly reviewed. This AC approach relies on the fact that non-zero $\rho_w(NIR)$ can be reconstructed from $\rho_w(\lambda)$ in the red bands assuming a power-law function to express the spectral dependence of the particulate backscattering $b_{bp}(\lambda)$.

A schematic overview of the algorithm is given in Fig. 2.5. First, the STD AC method assumes zero $\rho_w(\lambda)$ in the NIR (i.e., black pixel assumption) resulting in a first guess in $\rho_w(\lambda)$ for the entire spectral range. Estimations of $\rho_w(\lambda)$ at 443, 488 and 547 nm are then used as inputs for the bio-optical model 'MODIS Chl_a OC3 algorithm' (O'Reilly et al., 2000) to estimate the concentration of Chl_a. If the estimated Chl_a concentration is greater than 0.7 mg m^{-3}, a linear regression is used to retrieve, from the estimated Chl_a, the absorption coefficient for particles and dissolved material in the red (Werdell and Bailey, 2005; Bailey et al., 2010), $a_{pg}(\lambda_{red})$ (with minimum and maximum values of 0 and 0.5 m^{-1}, respectively).

$$a_{pg}(\lambda_{red}) = e^{0.9389 * log(Chl_a) - 3.7589} \tag{2.22}$$

Knowing the pure water absorption $a_w(\lambda_{red})$ (Pope and Fry, 1997; Kou et al., 1993), the total absorption coefficient $a(\lambda_{red})$ is estimated as the sum of $a_w(\lambda)$ and $a_{pg}(\lambda)$. According to Eq.(1.20), if both $R_{rs}(\lambda)$ and $a(\lambda)$ are known, $b_{bp}(\lambda)$ can be obtained as follows:

$$b_{bp}(\lambda) = \left[\frac{r_{rs}(\lambda)}{\frac{f}{Q}} * a(\lambda)/(1 - \frac{r_{rs}(\lambda)}{\frac{f}{Q}}) \right] - b_{bw}(\lambda) \tag{2.23}$$

with $r_{rs}(\lambda)$ being the water reflectance measured just below the surface and $b_{bw}(\lambda)$, the pure water back-scattering coefficient (Smith and Baker, 1981). The ratio f/Q is derived from the work of Morel and Gentili (1996) and is function of wavelength, illumination and viewing geometry, and Chl_a concentration.

Next, assuming a power-law spectral dependency of $b_{bp}(\lambda)$, $b_{bp}(\lambda_{NIR})$ can be estimated from $b_{bp}(\lambda_{red})$:

$$b_{bp}(\lambda) = b_{bp}(\lambda_0) \left[\frac{\lambda_0}{\lambda} \right]^{\eta_{b_b}} \tag{2.24}$$

with η_{b_b} being the spectral slope. In very clear waters, η_{b_b} approaches 4 and decreases down to 0 with an increase in turbidity (Loisel et al., 2006). To retrieve η_{b_b}, Lee et al. (2010b) suggested an empirical relation between η_{b_b} and the reflectance ratio $r_{rs}(443)/r_{rs}(555)$:

$$\eta_{b_b} = 2 - 2.4e^{-0.9\frac{r_{rs}(443)}{r_{rs}(555)}} \tag{2.25}$$

Given Eq.(2.24) and (2.25), and assuming that $a_{pg}(\lambda)$ is negligible in the NIR spectral domain compared to the pure water absorption $a_w(\lambda)$, we can retrieve the water contribution in the NIR based on Eq.(1.20). The above calculations are performed for two NIR bands (i.e., for MODIS Aqua at 748 and 869 nm) to obtain $\rho_w(\lambda_{NIRi})$ and $\rho_w(\lambda_{NIRj})$. These values are then removed from $\rho_{rc}(\lambda)$ and the black pixel assumption is applied on the updated $\rho_{rc}(\lambda)$ so that a second guess in $\rho_w(\lambda)$ can be achieved for the entire spectral range. The above calculations are repeated until $\rho_w(\lambda_{red})$ changes with less than 2% or if the maximum number of iterations is reached (the default maximum number of iterations is 10). If during the iteration process the retrieved $\rho_w(\lambda)$ reveals to be non-physical (for MODIS Aqua, $\rho_w(\lambda)$ at 443 or 488 nm are negatives or the ratio $\rho_w(443, 488)/\rho_w(547)$ falls outside the range 0.21-30), the iteration is re-initialized assuming that all the reflectances in the red spectral region results only from water (i.e., $\rho_w(\lambda_{red}) = \rho_{rc}(\lambda_{red})$) and the initial Chl_a concentration is set to 10 mg.l^{-1}.

The STD NIR-modelling scheme presents the advantage to be suitable for all ocean colour images presenting at least two NIR bands (e.g., SeaWiFS, MERIS, MODIS). It has a straightforward implementation and does not require a priori constructed look-up tables or neural-network

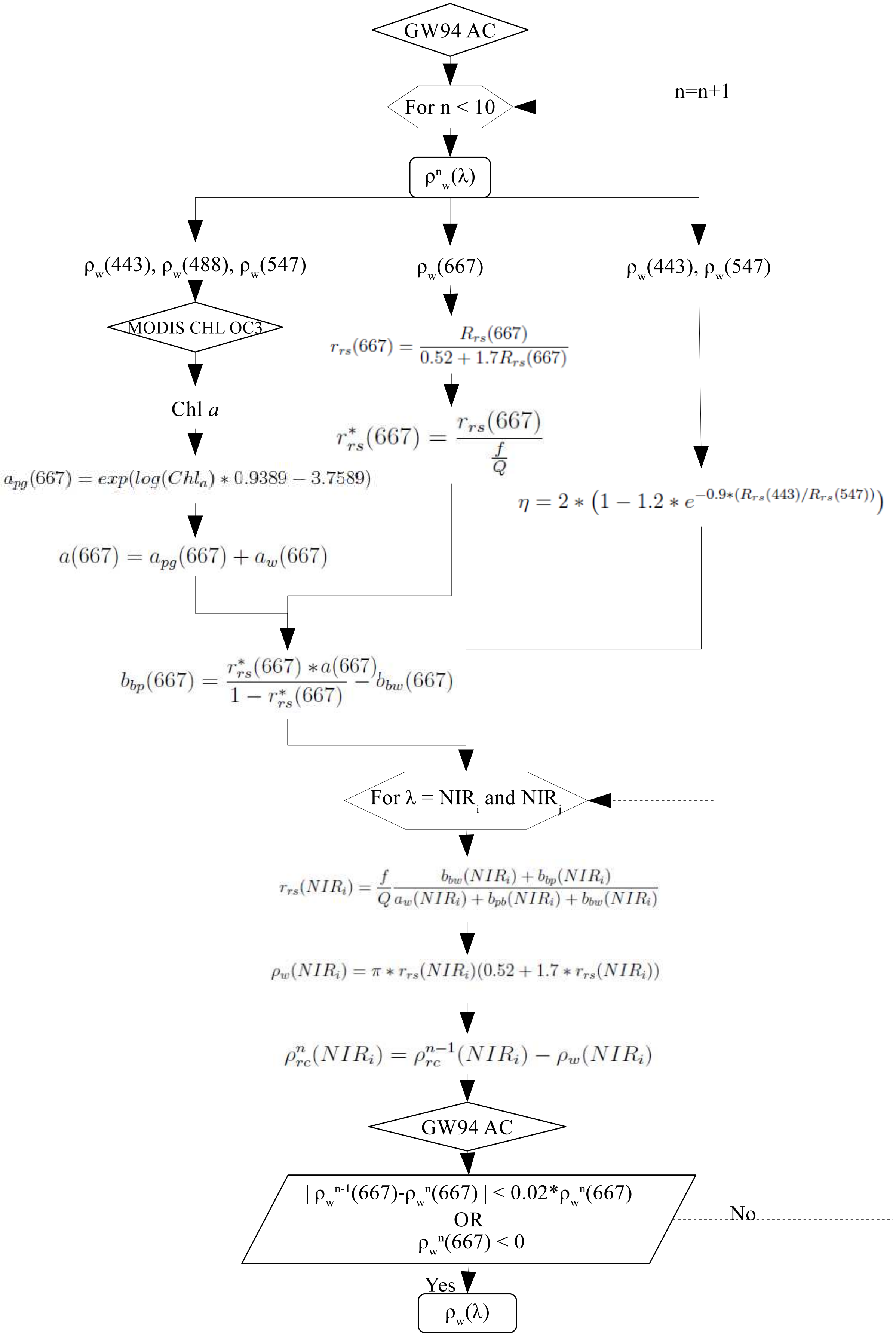

Figure 2.5: *Schematic sketch of the STD AC method as outlined by Bailey et al. (2010) and programmed in SeaDAS version 6.4.*

training. This AC method also accounts for a pixel by pixel aerosol type variability, in contrast, for instance, to the MUMM AC method (Section 2.4.2.2). However, it relies on a bio-optical model which may not be valid for all water types. Indeed, the bio-optical model includes empirically derived relationships (e.g., Eq.(2.22)) based on the global in-situ NASA bio-Optical Marine Algorithm Data set, NOMAD (Werdell and Bailey, 2005). The latter covers mainly oligotrophic to mesotrophic waters. The empirically retrieved relationships may thus no be appropriate for more turbid coastal waters. The large dependence of empirical relationships to the *in situ* data, is also true for the relationship suggested by Lee et al. (2010b) to retrieve the coefficient η_{b_b} (Eq.(2.25)). Moreover, relying solely on Chl_a estimations to retrieve IOPs in the red spectral region and, subsequently, $\rho_w(\lambda_{NIR})$, may be dubious, especially in non-algal particles rich waters. The iterative approach may correct for such imperfections, but only partially.

2.4.2.2 The NIR Similarity spectrum AC method (‘MUMM’)

The NIR Similarity spectrum AC method (referred to hereafter as the MUMM algorithm) is a GW94-based algorithm including assumptions of spatial homogeneity in NIR ratios of $\rho_w(\lambda)$ and $\rho_a(\lambda)$ (Ruddick et al., 2000, 2006). The first assumption, so-called NIR similarity spectrum, arises from the fact that (1) the sea-water NIR spectrum shape is largely determined by pure water absorption, (2) $b_b(\lambda_{NIR})$ can be ignored compared to $a_w(\lambda_{NIR})$, and (3) $b_b(\lambda_{NIR})$ is spectrally independent for a limited spectral range. If these facts are verified, the ratio of any two NIR $\rho_w(\lambda)$ can be considered as constant and equal to:

$$\alpha(\lambda_{NIR1}, \lambda_{NIR2}) = \frac{\rho_w(\lambda_{NIR1})}{\rho_w(\lambda_{NIR2})} = \frac{a_w(\lambda_{NIR2})}{a_w(\lambda_{NIR1})} \tag{2.26}$$

Assuming that the variation of the pure water NIR absorption ratio with salinity is negligible (Pegau et al., 1997) and the impact of temperature relatively small (Ruddick et al., 2006), the constant $\alpha(\lambda_{NIR1}, \lambda_{NIR2})$ can be considered to be independent of region and season. Accordingly, normalizing the reflectance spectra to the reflectance at a single wavelength in the NIR (referred by Ruddick et al. (2000, 2006) as the similarity NIR reflectance spectrum) allows to determine, at any wavelength, the water leaving reflectance shape in the NIR spectral domain.

The second assumption is based on the fact that the atmospheric composition does not vary significantly in space and therefore the ratio of the aerosol reflectance $\rho_a(\lambda) + \rho_{ra}(\lambda)$ can be computed wherever the water signal is negligible and extrapolated to the nearby pixels where non-zero $\rho_w(\lambda_{NIR})$ is observed. In the present research, a clear water sub-scene is defined as any pixel within the image for which $\rho_{rc}(\lambda_{NIR})$ is non-negative and below 0.015.

The MUMM algorithm is thus a three-step process as shown by the schematic flowchart in Fig. 2.5. First the image is processed with the black pixel assumption (i.e. GW94). This allows to estimate $\rho_{rc}(\lambda_{NIR})$ over the area of interest, to select the clear water pixels and to retrieve $\epsilon_m(\lambda_{NIR1}, \lambda_{NIR2}) = \rho_{am}(\lambda_{NIR1})/\rho_{am}(\lambda_{NIR2})$ (with $\rho_{am}(\lambda_{NIR2})$ being the multiple scattering aerosol reflectance, $\rho_a(\lambda_{NIR2}) + \rho_{ra}(\lambda_{NIR2})$, and considered as equal to $\rho_{rc}(\lambda_{NIR2})$ over clear water pixels). Next, fixing $\epsilon_m(\lambda_{NIR1}, \lambda_{NIR2})$ for the entire image and knowing $\alpha(\lambda_{NIR1}, \lambda_{NIR2})$, $\rho_{am}(\lambda)$ can be estimated for the wavelengths λ_{NIR1} and λ_{NIR2} according to the following equations:

$$\rho_{am}(\lambda_{NIR1}) = \epsilon_m(\lambda_{NIR1}, \lambda_{NIR2}) \frac{\alpha(\lambda_{NIR1}, \lambda_{NIR2})\rho_{rc}(\lambda_{NIR2}) - \rho_{rc}(\lambda_{NIR1})}{\alpha(\lambda_{NIR1}, \lambda_{NIR2}) - \epsilon_m(\lambda_{NIR1}, \lambda_{NIR2})} \tag{2.27}$$

$$\rho_{am}(\lambda_{NIR2}) = \frac{\alpha(\lambda_{NIR1}, \lambda_{NIR2})\rho_{rc}(\lambda_{NIR2}) - \rho_{rc}(\lambda_{NIR1})}{\alpha(\lambda_{NIR1}, \lambda_{NIR2}) - \epsilon_m(\lambda_{NIR1}, \lambda_{NIR2})} \tag{2.28}$$

$\rho_{am}(\lambda_{NIR})$ is then removed from $\rho_{rc}(\lambda_{NIR})$ to obtain $\rho_w(\lambda_{NIR})$. The last step consists in estimating $\rho_{as}(\lambda_{NIR})$, and subsequently the aerosol model, given $\rho_a m(\lambda_{NIR})$ (Gordon and Wang, 1994).

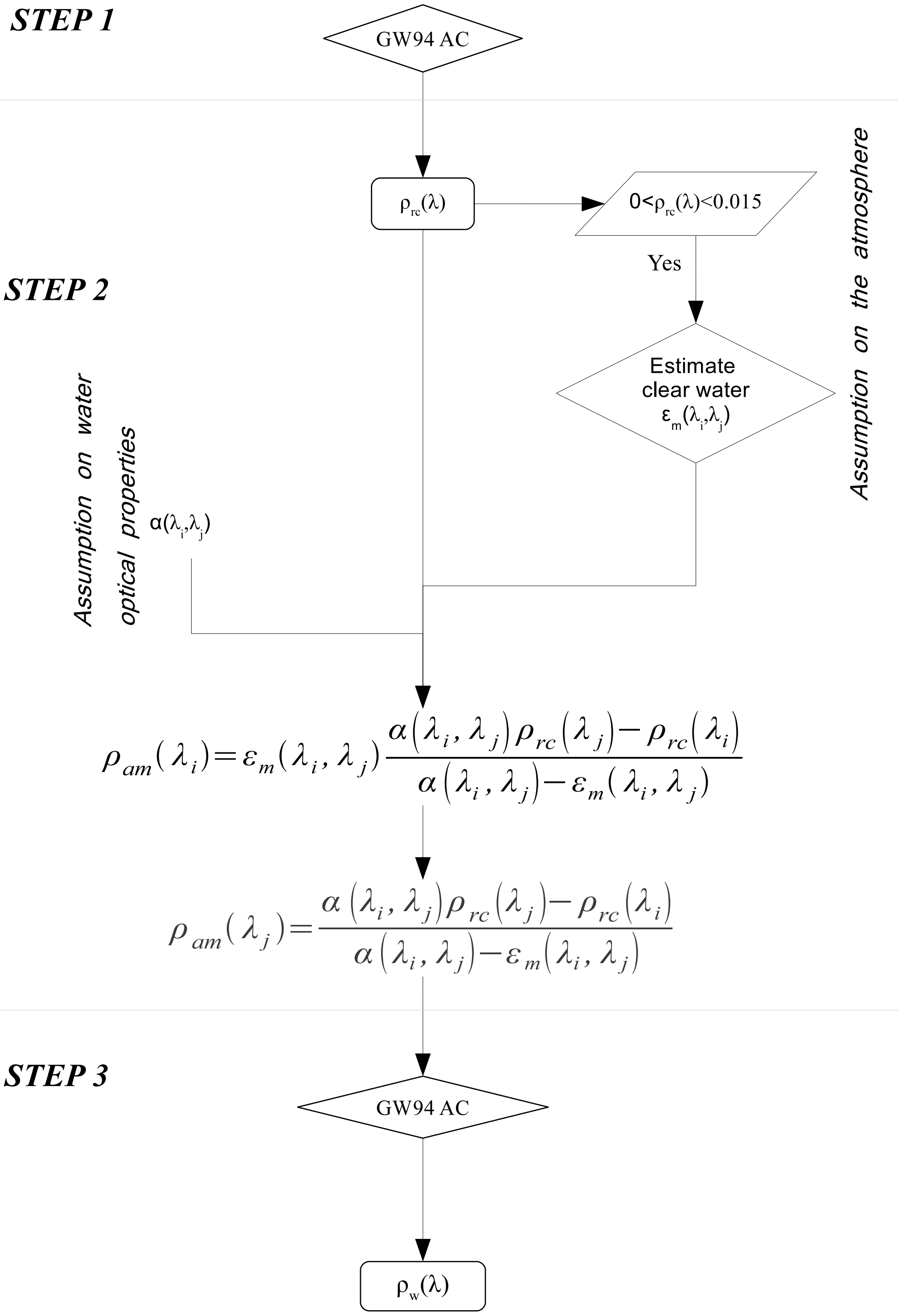

Figure 2.6: *Schematic sketch of the MUMM AC algorithm with i and j being two bands in the NIR spectral domain (Ruddick et al., 2000, 2006).*

Similarly to the STD algorithm, the MUMM AC approach presents the advantage of retrieving $\rho_w(\lambda)$ for any sensor presenting at least two NIR bands. In contrast, instead of relying on an iterative bio-optical model to account for non-zero $\rho_w(\lambda_{NIR})$, it includes a spectral relationship (Eq.(2.26)) with assumptions on the IOPs in the NIR (i.e., $a(\lambda_{NIR}) \approx a_w(\lambda_{NIR})$, $b_b(\lambda_{NIR}) << a_w(\lambda_{NIR})$ and $\delta b_b(\lambda_{NIR})/\delta\lambda = 0$). As shown by Ruddick et al. (2006), these assumptions are valid for water masses presenting $\rho_w(\lambda_{NIR})$ values between 10^{-4} and 10^{-1} (corresponding to SPM concentrations between ~ 0.3 g m^{-3} and 200 g m^{-3} according to the authors). However, outside this range, the constant water reflectance ratio assumption is not verified. Indeed, for very clear waters, $b_b(\lambda)$ is mainly determined by the pure water scattering, which presents more significant spectral dependence compared to $b_{bp}(\lambda)$ (Ruddick et al., 2006). Hence, the assumption $\delta b_b(\lambda_{NIR})/\delta\lambda = 0$ is not valid. However, for such clear waters, $\rho_w(NIR)$ can be assumed as negligible. At the opposite, for extremely turbid waters $b_{bp}(\lambda_{NIR})$ increases significantly such that the assumption $b_b(\lambda_{NIR}) << a_w(\lambda_{NIR})$ is no longer valid (Ruddick et al., 2006) and $R_{rs}(\lambda)$ is not well approximated as proportional to $b_b(\lambda_{NIR})/a(\lambda_{NIR})$ (Sydor et al., 2004). The appropriateness of the MUMM AC method is thus limited by the validity of the constant reflectance ratio assumption.

The MUMM AC approach also presents the advantage of allowing several configurations for the aerosol model. Beside the selection of the candidate models based on the clear water pixels, fixed values, climatologies or local aerosol *in situ* measurements, may also be used and sensitivity tests can be easily performed to evaluate the best configuration. However, when assuming spatial homogeneity in the aerosol contribution, possible spatial variations in atmospheric aerosols may be lost (in particular in coastal areas), leading to inaccuracies in $\epsilon_m(\lambda_{NIR1}, \lambda_{NIR2})$ retrievals and, subsequently, in $\rho_w(\lambda)$ estimations. Moreover, the selection of the candidate models largely depends on how $\epsilon_m(\lambda_{NIR1}, \lambda_{NIR2})$ is retrieved. Indeed, the definition of clear water pixels and their distance to the atmospheric corrected pixel may affect the resulting $\epsilon_m(\lambda_{NIR1}, \lambda_{NIR2})$. Using the approach suggested by Hu et al. (2000), that is, retrieving $\epsilon_m(\lambda_{NIR1}, \lambda_{NIR2})$ using weights defined according to the distance to the atmospheric corrected pixel, may therefore be more accurate. However, such approaches significantly complicate the implementation for operational processing.

2.4.2.3 The GW94-based algorithm using the SWIR bands in very turbid waters (‘NIR-SWIR’)

In the SWIR spectral domain, pure water absorption is relatively large while the contribution of the in-water constituents to scattering is relatively low, such that $\rho_w(\lambda_{SWIR})$ can be safely considered as null even in turbid waters. Accordingly, the SWIR bands can be used for aerosol model selection the same way as in the GW94 AC algorithm. However, actual SWIR bands (e.g., MODIS Aqua and Visible Infrared Imaging Radiometer Suite (VIIRS) bands at 1240, 1640 and 2130 nm) are not meant to be used for ocean colour applications and present a lower signal-to-noise-ratio compared to the NIR bands limiting the advantage gained by using the SWIR bands (Wang, 2007). Therefore, a combined NIR-SWIR approach was suggested (Wang and Shi, 2007; Wang et al., 2009), including a switch between the STD and SWIR-based GW94 AC method such that the SWIR bands are only used in very turbid waters where the STD AC method is expected to fail. Very turbid waters are defined based on a turbidity index computed from $\rho_{rc}(\lambda)$ at 748 and 1240 nm (Shi and Wang, 2007). For any pixel presenting a turbidity index above 1.05, the SWIR AC approach is applied. The refinement of Wang et al. (2009) includes a second turbidity criterion. If, after a first processing with the SWIR aerosol model selection, the estimated $L_{wn}(869)$ is below 0.08 mW cm^{-2} μm^{-1} sr^{-1} and the estimated Chl_a value lower or equal to 1 mg m^{-3}, the AC is reset to the STD AC method. Improvements in the retrievals of $\rho_w(\lambda)$ have been demonstrated in very turbid waters (Wang and Shi, 2007; Dogliotti et al., 2011; Wang et al., 2009). However, the assumption of zero $\rho_w(\lambda)$ in the SWIR may not be universally correct, especially in extremely turbid waters (Shi and Wang, 2009; Werdell et al., 2010; Knaeps et al., 2012). Moreover, in contrast to the STD and MUMM AC methods, the SWIR AC approach can only be applied on a restrictive number of satellites since it requires at least two SWIR spectral bands.

2.4.2.4 Direct inversion approach by neural network ('NN')

The NN algorithm used in this study is based on an inverse modelling of extensive radiative transfer (RT) simulations within a coupled ocean-atmosphere system, similar to an approach previously implemented for MERIS (Schroeder et al., 2007). The direct inversion takes into account the spectral information of both aerosol and water constituents at each wavelength simultaneously. Consequently, the NN method does not attempt to decouple oceanic and atmospheric signals to perform the AC and does not rely solely on the NIR spectral domain to retrieve the aerosol properties such as suggested by the GW94-based AC algorithm. The RT simulations generate a large set of TOA and mean sea-level reflectance data for a variety of oceanic and atmospheric conditions and different sun and observing geometries. The ocean model is characterized by varying concentrations of water constituents typically found in European coastal waters and covering the following concentration ranges: 0.05-50 mg.l^{-1} for Chl_a, 0.05-50 g.l^{-1} for SPM and 0.001-1 m^{-1} for the absorption of CDOM at 443 nm. The total absorption of the sea water is modelled as the sum of the absorption coefficients of pure sea water (taken from Pope and Fry (1997) and Hale and Querry (1973)), of organic particulate matter (estimated as a function of Chl_a according to Bricaud et al. (1998)), of inorganic matter (estimated as a function of SPM according to the parametrization of Babin (2000)), and yellow substance (assumed to be totally absorbing and taken from Babin (2000)). The total scattering coefficient is modelled as the sum of the scattering coefficient from pure sea water (taken from Morel (1974)) and SPM (taken from Babin (2000)). The scattering phase function of pure water is defined according to Morel (1974) while the backscattering probability in Case 2 waters is applied according to the model of Zhang et al. (2002). The maritime and continental aerosol models suggested by Shettle and Fenn (1979) are considered for the simulations. Next, the simulated data are used to adapt the inverse model during a supervised learning procedure. The NN inverse model consists of a multilayer perceptron that approximate through a learning step the relationship between TOA and mean sea-level reflectance. When applied to MODIS data, the algorithm requires as inputs the TOA reflectance at all ocean colour bands as well as information about the sun and observing geometry and surface pressure. In addition, MODIS Level-2 flags are used to mask pixels affected by land, high glint and clouds. The associated NN outputs consist of mean sea-level $R_{rs}(\lambda)$ at eight MODIS bands up to 748 nm as well as the spectral aerosol optical thickness at four AERONET bands (440, 550, 670 and 870 nm). Additional NN flags are used for further quality control of the outputs that check for out-of-scope conditions compared to the simulated data ranges.

While NN-based AC algorithms present the advantage of accounting for ocean and atmosphere simultaneously, it presents the large disadvantage of being highly dependent on the dataset used for the training of the artificial neural network.

- Chapter 3 -

In situ and satellite ocean colour products

This Ph.D. study focus on NASA MODIS Aqua images for $\rho_w(\lambda)$. Sensor specifications, image processing, validation and calibration for this sensor are succinctly described in the present chapter (Sections 3.2.1. and 3.2.2.). A large section of this chapter is also dedicated to the *in situ* data, used as reference for the validation and improvement of the satellite atmospheric correction algorithms. Both in- and above-water *in situ* measurement systems are briefly described together with the *in situ* $\rho_w(\lambda)$ datasets used in the present research. These are the data provided by the Aerosol Robotic Network-Ocean Colour (AERONET-OC) and collected by the Management Unit of the North Sea Mathematical Model (referred to as the MUMM dataset) and the Laboratoire d'Oceanologie et de Geosciences (referred to as the LOG dataset) for $\rho_w(\lambda)$. Some of these *in situ* data were taken during research campaigns I participated in, namely, one in French Guiana during May and June 2012 (hereafter referred to as FG12), and, another, in the southern Atlantic and south-eastern Pacific from mid-February to March 2011 on-board the R/V Melville (hereafter referred to as MV1102).

A one-month stay early 2012 at the MUMM institute in Brussels also allowed me to further develop important skills in the processing of *in situ* measurements. This resulted in the development of a semi-automatic program for the processing of raw *in situ* measurements, from above-water sensor devices, to obtain average $\rho_w(\lambda)$ spectra and associated standard deviations (described in Section 3.2.1.2 together with the MUMM dataset).

Acquiring accurate *in situ* data remains however a difficult task (Rudorff et al., 2013). To illustrate this, two closure exercises showing the agreement and disagreement between $\rho_w(\lambda)$, when collected using different instruments and when modelled based on radiative transfer simulations, are presented (Section 3.2.3). The first closure exercise includes the data taken during the MV1102 sea campaign and is part of a paper I contributed to about the assessment of accurate ocean colour *in situ* radiometry (Rudorff et al., 2013). The second case study includes a closure exercise conducted during the International Ocean Optics Summer School about calibration and validation of ocean colour remote sensing (Darling Marine Centre, Walpole, Maine, 10-31 July 2011). I had the chance to be selected to participate to this summer school and contributed to the resulting on-line available report entitled "Portfolio of Measurement, Processing, and Analysis Techniques for Optical Oceanography Data" (Arellano et al., 2011).

Finally, the last section of this chapter describes the match-up protocols used in the present study to select coincident satellite-*in situ* data pairs.

3.1 MODIS AQUA OCEAN COLOUR PRODUCTS

3.1.1 Satellite characteristics

The MODIS Aqua sensor was designed with 36 spectral bands to support atmospheric, land and ocean observations with a swath of 1500 km. The 9 standard ocean colour bands cover the visible and NIR spectral range with centre wavelengths from 412 to 869 nm and a spatial resolution of approximately 1 km at nadir. Land and atmospheric bands have a higher spatial resolution of 250 and 500 m and present sensor bands ranging from 469 to 2130 nm. Sensor characteristics including wavelength, band width and spatial resolution are given in Table 3.1 for the visible, NIR and SWIR bands. The signal-to-noise ratio (SNR) for a typical top of atmosphere radiance, $L_{typ}(\lambda)$, is also given together with the maximum observable radiance, $L_{max}(\lambda)$ (Franz et al., 2006). The $L_{typ}(\lambda)$ is derived by averaging cloud-free pixels over mesotrophic waters for a range of viewing and solar geometries, while $L_{max}(\lambda)$ is actually the peak radiance preceding saturation. Note that the higher spatial resolution of the atmospheric and land bands includes a shorter integration time and consequently a reduced SNR, which is particularly low for the SWIR MODIS Aqua bands compared to the visible and NIR bands (Table 3.1)). However, these bands saturate at higher signals relative to the ocean colour bands (see $L_{max}(\lambda)$ in Table 3.1). Indeed, the latter have been designed with high sensitivity to cover the range of reflectance typical of open ocean observations with maritime atmospheric conditions (Franz et al., 2006). However, such sensitivity may also be critical, especially in very turbid waters where sensor bands may saturate resulting in inaccurate satellite water signal estimations.

Table 3.1: *MODIS band characteristics adapted from Franz et al. (2006). Wavelengths (nm) in bold indicate the standard ocean colour bands.* $L_{typ}(\lambda)$ *and* $L_{max}(\lambda)$ $(mWcm^{-2}\mu m^{-1}sr^{-1})$ *stand for typical and maximum normalized water-leaving radiance value, respectively, and SNR is the Signal-to-Noise ratio.*

λ	Band width (nm)	Spatial resolution (m)	SNR at $L_{typ}(\lambda)$	$L_{typ}(\lambda)$	$L_{max}(\lambda)$	Gains	
						R2010	R2012
412	15	1000	1773	7.84	26.9	0.9768	0.9731
443	10	1000	2253	6.99	19.0	0.9936	0.9910
469	20	500	556	6.52	59.1	1.0113	1.0132
488	10	1000	2270	5.38	14.0	0.9972	0.9935
531	10	1000	2183	3.87	11.1	0.9946	1.0002
547	10	1000	2200	3.50	8.8	0.9950	0.9994
555	20	500	349	3.28	53.2	0.9999	1.0012
645	50	250	140	1.65	51.2	1.0252	1.0280
667	10	1000	1962	1.47	4.2	0.9961	0.9996
678	10	1000	2175	1.38	4.2	0.9974	0.9998
748	10	1000	1371	0.889	3.5	0.9977	0.9989
859	35	250	103	0.481	24.0	1.0244	1.0254
869	15	1000	1112	0.460	2.5	1.0	1.0
1240	20	500	25	0.089	12.3	1.0	1.0
1640	35	500	19	0.028	4.9	1.0	1.0
2130	20	500	12	0.008	1.7	1.0	1.0

During operational data processing, instrument calibration as well as vicarious calibration are performed. The former includes pre-launch and direct calibration from MODIS solar and lunar diffuser measurements and, when the SeaWiFS instrument was still operational, cross-calibration adjustments based on SeaWiFS measurements (Sun et al., 2007; Xiong et al., 2010; Meister et al., 2012). Vicarious calibration adjusts the top of atmosphere signal for any residual error after instrument calibration and for any systematic bias due to the processing of the images (including atmospheric correction) such that the retrieved remote sensing data fits the *in situ* data (Franz et al., 2006). During operational data processing (see Section 3.1.2), the top of atmosphere radiance is multiplied by the vicarious calibration gain factors at each spectral band.

Since an error of 1% in atmospheric correction or sensor calibration results in approximately 10% difference in $L_w(\lambda)$ and even more in the derived geophysical parameters (Franz et al., 2012), this adjustment is essential to further reduce absolute uncertainty to meet the ocean colour accuracy goals.

For MODIS Aqua, in the visible spectral range, the vicarious calibration gain factors at each wavelength are determined to maximize the agreement between remotely sensed water-leaving reflectance (in combination with the atmospheric correction algorithms) and the hyperspectral Marine Optical Buoy (MOBY) *in situ* data for $\rho_w(\lambda)$. In the NIR spectral range, reliable, simultaneous and co-located measurements of aerosol properties and $\rho_w(\lambda)$ are not widely available (Franz et al., 2007). Therefore, the NASA Ocean colour Biology Processing Group (OBPG) computes NIR vicarious calibration gains by using an assumed aerosol type (Franz et al., 2007). The gain factor at 869 nm is set to unity and the calibration sites are chosen such that the zero NIR $\rho_w(\lambda)$ assumption is verified and the aerosol model corresponds to the most probable maritime aerosol model (maritime aerosol model with 90% humidity). The remaining unknown is thus $L_a(\lambda)$ in the NIR and gain factors can be estimated by comparing observed and modelled $L_a(\lambda_{NIR})$. Gains are averaged over all the clear-water calibration targets to obtain a globally valid correction gain factor for the spectral bands at 748 and 859 nm. The SWIR bands are not vicarious calibrated.

Hence, the gains are not only sensor specific, they also depend on the used AC method. The vicarious calibration gains suggested by NASA OBPG are computed with the STD AC method. However, these can be considered as applicable for the other AC approaches provided that similar aerosol models are used within the other AC methods.

Gains used in the present study are shown in Table 3.1. Since residual instrument calibration errors may vary over time, an update of the vicarious calibration gains may be required to improve the archived products. Therefore, the gains used in Chapters 4 and 6 differ according to the version of the SeaWiFS Data Analysis System (SeaDAS) software (Fu et al., 1998) used for the image processing and the associated OBPG Ocean colour Reprocessing version (`http://oceancolor.gsfc.nasa.gov/WIKI/OCReproc.html`). Gain factors shown in Table 3.1 correspond to the default gains suggested by OBPG for SeaDAS version 6.2 (including the Reprocessing 2010, R2010) and 6.4 (including the Reprocessing 2012, R2012), respectively. Note, however, that the percentage difference does not exceed 0.6% (with a maximum difference at 531 nm). Though, this illustrates one of the difficulties when processing long-term satellite images. Indeed, the MODIS Aqua data archive encountered 5 reprocessing versions since its initial reprocessing in 2004 (i.e., in 2005, 2009, 2010, 2012 and 2013). Although these reprocessing versions often include minor changes, updates may sometimes be important. Accordingly, to ensure consistent AC methods validation and inter-comparison, the entire archive of the satellite images should be reprocessed when a new reprocessing version is released. For comparison and data consistency, images processed with previous vicarious gain factors should thus be reprocessed with new gains. When dealing with large satellite databases, this represents time-consuming efforts.

3.1.2 L1A to L2 MODIS Aqua processing

The entire mission archive of MODIS Aqua images is available on the NASA ocean colour website (`http://oceancolor.gsfc.nasa.gov`) through the on-line OBPG Data Processing System (`http://oceancolor.gsfc.nasa.gov/cgi/browse.pl`). MODIS extracted L1A files, obtained from this archive, are processed from L1A to L1B and subsequently from L1B to L2 using SeaDAS version 6.2 or 6.4 (for the validation exercises outlined in Chapters 4 and 6, respectively). The processing from L1A to L1B requires the generation of the geolocation files. These are created based on the corresponding attitude and ephemeris files which include, among others, coordinate system and spacecraft location information. Next, the 5-minute granule levels contained in the L1A and geolocation file serve as input to produce 1 km, 250 m and 500 m top of atmosphere radiance images in sensor geometry, and instrument calibration is performed to generate the L1B file.

The oceanic optical properties and various derived products (e.g., atmospheric optical thickness, aerosol reflectance, Ångström coefficient) are finally obtained and stored in the L2 file which is generated by applying the atmospheric correction algorithm on the top of atmosphere radiance contained in the L1B file. The Level-2 processing makes use of meteorological and ozone information from ancillary sources.

During the processing of the L2 files, pixel-wise quality tests are also applied to each pixel according to some conditions and retrieved processing parameters with the aim of reducing inaccuracies (at the expense, however, of spatial coverage). This allows to exclude (mask) or notice (flag) some pixel values that may be inaccurate for further data analysis. Pixels are usually masked over land and when cloud/ice conditions are detected. Pixels presenting sun glint and stray light contamination, high satellite and sun zenith angles can also be flagged. AC failure is also noticed (e.g., when the number of iterations before convergence exceeds the maximum allowed iteration number within the iterative process or when non-physical Chl_a concentrations are retrieved in the STD AC method). As noticed previously, a commonly encountered flag in very turbid waters is the high total radiance (HILT) flag resulting from sensor saturation (in terms of digital counts) in the red and NIR bands. When the sensor saturates, sufficient precision is not ensured to correctly characterize aerosols. However, high NIR radiance values may be encountered in coastal areas and may therefore be erroneously masked. Similarly, the standard cloud cover mask is applied on the NIR spectral band around 865 nm ($\rho_{rc}(865) > 0.027$) and may thus be too restrictive in turbid waters. Therefore, several studies suggested to use the MODIS Aqua SWIR bands for cloud flagging (Wang and Shi, 2006; Franz et al., 2006; Dogliotti et al., 2011). Another approach to improve cloud flagging was also suggested by Nordkvist et al. (2009) which is based on the lower spectral variability of clouds compared to sea-water.

3.2 *In situ* WATER-LEAVING REFLECTANCE MEASUREMENTS

3.2.1 Above-water systems

The above-water approach includes measurements obtained by on-board radiometers, used to derive $L_w(\lambda)$ and $E_d(\lambda)$ which, according to Eq.(1.10), allows to derive $\rho_w(\lambda)$. Above-water systems are considered better approaches for turbid coastal waters where the in-water methods are usually more biased due to the high attenuation and stratification of the water column (Mueller et al., 2003). It also retrieves the radiometric quantities in a more similar way as the satellite measurements (Hooker et al., 2007). However, above-water $\rho_w(\lambda)$ are often challenged by rapidly changing sky and intermittent sun shining and shading conditions during measurements explaining the need for clear skies or alternatively homogeneous cloud cover during measurements (Toole et al., 2000; Hooker et al., 2002; Rudorff et al., 2013). Similarly, wind generated wavy facets change the sea surface geometry which may significantly affect the up-welling rays and sky glint contribution. Well defined correction schemes to remove the skylight reflection effects at the ocean surface exist (e.g., Mobley, 1999; Gould et al., 2001; Ruddick et al., 2006; Lee et al., 2010a; Cui et al., 2013). However other sources may have simultaneous effects (e.g., sun and cloud glint and the platform reflection or shadow) making the correction much more difficult (Mobley, 1999; Doyle and Zibordi, 2002; Hooker and Morel, 2003). Hence, an accurate acquisition geometry is essential to avoid self-shading and platform interference and minimize sky and sun glint, platform reflection contamination and bidirectional effects (Mobley, 1999). Nevertheless, under conditions of higher particle concentrations and high solar zenith angles, these effects may not be completely avoided (Morel and Gentili, 1996; Hooker et al., 2002; Morel et al., 2002; Rudorff et al., 2013).

Examples of commonly used above-water instruments for ocean colour are the Analytical Spectral Devices Fieldspec Hand Held (ASD), the Hyperspectral Surface Acquisition Remote Sensing System (HyperSAS), the above-water TriOS RAMSES radiometers or the SeaWiFS Photometer Revision for Incident Surface Measurements (SeaPRISM) (Fig. 3.1). All these radiometers retrieve the sea surface reflection by subtracting the sky radiance measured with a sensor pointing towards the sky from the measured total radiance emerging from the ocean. In the present study, the above-water *in situ* data used for the validation and improvement of the atmospheric correction methods, are mainly provided by the multispectral SeaPRISM and hyperspectral above-water TriOS RAMSES instruments from the AERONET-OC and MUMM datasets, respectively. Both instruments are further described in the next sections together with the specifications of the associated *in situ* measurements. The HyperSAS and ASD instruments were used to measure *in situ* $\rho_w(\lambda)$ data during the Ocean Optics Summer School and the MV1102 campaign, respectively. The closure exercises described in Section 3.2.3, present $\rho_w(\lambda)$ measurements from both instruments.

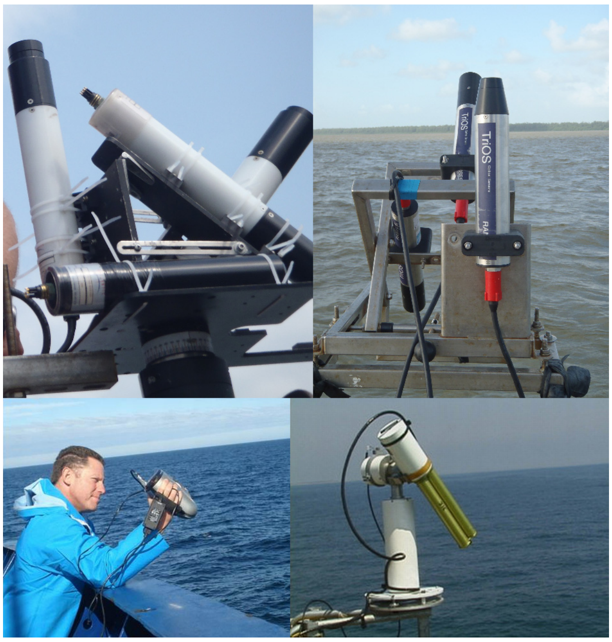

Figure 3.1: *Pictures from the HyperSAS instrument used at the Ocean Optics Summer School 2011 (top left), the above-water TriOS RAMSES used during the FG12 campaign (top right), the ASD instrument used during the MV1102 campaign (bottom left), and the SeaPRISM system placed at the AERONET-OC station MVCO (bottom right)*

3.2.1.1 Aerosol Robotic Network-Ocean Colour (AERONET-OC) data

The AERONET-OC is a network of globally distributed above-water autonomous multispectral radiometers located in coastal regions (less then 25 km from the nearest coast) providing atmospheric observations and $L_{wn}(\lambda)$ data in the 412-1020 nm spectral range (Holben et al., 1998; Zibordi et al., 2009a,b). This network is particularly useful for satellite instrument calibration and product validation with its autonomous $L_{wn}(\lambda)$ measurements at central wavelengths similar to the visible SeaWiFS or MODIS spectral bands (i.e., 412, 443, 488, 531, 547 and 667 nm). Additional measurements are performed at 870, 940 and 1020 nm centre wavelengths to support aerosol and water vapour monitoring and to improve water signal retrievals in turbid waters (Zibordi et al., 2009b). For atmospheric applications, the aerosol optical thickness, $\tau(\lambda)$, is also retrieved and may be used to derive the Ångström exponent. An estimate of overall uncertainty budget in AERONET-OC $L_{wn}(\lambda)$ has shown some typical absolute uncertainties (due to absolute calibrations, environmental variability and uncertainties in the self-shading and tower-shading corrections) ranging from 5% to 10%, with the lowest uncertainties encountered for the blue and green spectral bands and the highest for the red spectral band (Zibordi et al., 2009c, 2012).

The SeaPRISM systems (Fig. 3.1, bottom right picture) are located on fixed platforms such as lighthouses, oil platforms or oceanographic towers. These fixed-platforms ocean colour products are complementary to buoy or shipboard measurements. Indeed, in contrast to the above-water field measurements taken with research vessels, the SeaPRISM systems are deployed with no tilt and their solar illumination can be precisely determined. This stability, the autonomous measurement configuration and the absence of in-water degradation (e.g., bio-fouling on buoy systems), present large advantages allowing to build long-term periodic high quality *in situ* ocean colour measurements and to increase the number of match-up pairs for the validation of ocean colour remote sensing products. The protocol for the deployment structure of the SeaPRISM instruments should also ensure the most favourable measurement conditions avoiding adjacency effects from nearby coastal land, bottom reflectance, structure perturbations, and sea spray. These deployment guidelines and the AERONET-OC data acquisition, calibration, processing, archiving and distribution infrastructures present the benefit to provide open access near-real time and standardized data.

Today the AERONET-OC network is composed of 15 fixed platforms of which 12 present cloud-screened and quality-assured data (Level 2) (Fig. 3.2). More details about instruments, station properties and particularities, and water properties at each station, can be found in, among others, Berthon and Zibordi (2004); Zibordi et al. (2006b); Mélin et al. (2007); Feng et al. (2008); Zibordi et al. (2009b,c).

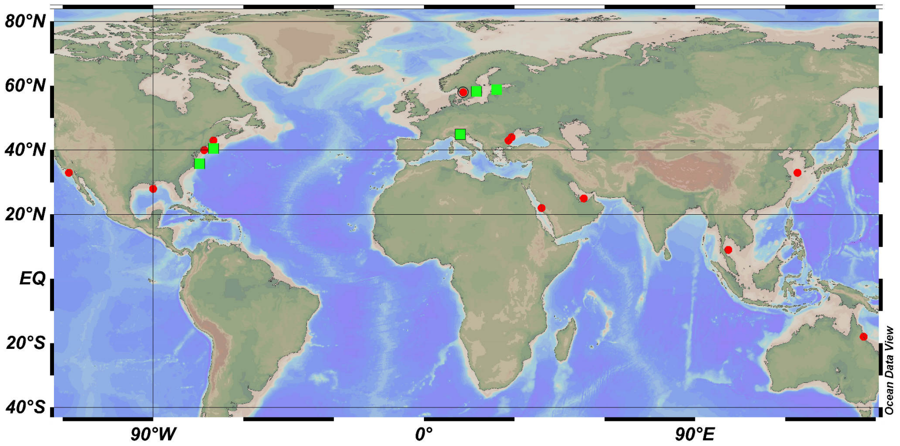

Figure 3.2: *AERONET-OC level-2 stations (red dot). The AAOT, MVCO, COVE, DALEN, and HELSINKI stations are indicated by a green square.*

The AERONET-OC data used in the present research were provided by SeaPRISM systems placed in the Adriatic sea on the Acqua Alta Oceanographic Tower nearby Venice (AAOT), in the Baltic Sea on the Helsinki Lighthouse and Gustav Dalen Tower (HLT and GDLT, respectively) and along the East Coast of the US on the Air-Sea Interaction Tower nearby the Martha's Vineyard Coastal Observatory and on the Chesapeake Lighthouse ocean platform (MVCO and COVE, respectively) (Fig. 3.2). The deployment sites and the number of observations for each site are given in Table 3.2. Table 3.3 shows the minimum, maximum and median values per station and for the entire period of observations. According to this table, each station shows some clear water spectra with relatively large $\rho_w(\lambda)$ values in the blue and near zero values in the NIR spectral domain, as well as some turbid cases with larger $\rho_w(\lambda_{NIR})$ signals ($\rho_w(869)$ $> 10^{-4}$, turbid threshold according to Siegel et al. (2000)).

Table 3.2: *In-situ data location, description and distance from land*

	Lat	Lon	Distance from land (km)	Number of obs.	Period of obs.
AAOT (Adriatic Sea)	45.31° N	12.51° E	15	4348	2002-2007
GDLT (Baltic Proper)	58.59° N	17.467° E	16.5	924	2005-2009
HLT (Gulf of Finland)	59.95° N	24.92° E	22.22	665	2006-2009
MVCO (U.S. Atlantic Coast)	41.32° N	70.57° W	3.7	973	2004-2005
COVE (U.S. Atlantic Coast)	36.90° N	75.71° W	24	450	2006-2009

Table 3.3: *Minimum, maximum and median $\rho_w(\lambda)$ values for the MODIS Aqua bands (centre wavelength in nm) per station and estimated over the period of observations.*

	$\rho_w(\lambda)$	412	443	488	531	547	667	748	869
AAOT	min	0.0046	0.0054	0.0084	0.0138	0.0160	0.0038	0.0000	0.0000
	max	0.0505	0.0557	0.0713	0.0784	0.0773	0.0188	0.0112	0.0017
	median	0.0185	0.0217	0.0292	0.0308	0.0297	0.0063	0.0035	0.0003
GDLT	min	0.0017	0.0033	0.0051	0.0082	0.0094	0.0038	0.0022	0.0001
	max	0.0146	0.0150	0.0239	0.0409	0.0475	0.0143	0.0090	0.0028
	median	0.0049	0.0063	0.0092	0.0139	0.0155	0.0052	0.0031	0.0004
HLT	min	0.0012	0.0025	0.0043	0.0074	0.0084	0.0039	0.0028	0.0000
	max	0.0049	0.0053	0.0084	0.0151	0.0176	0.0060	0.0043	0.0013
	median	0.0033	0.0040	0.0070	0.0116	0.0134	0.0045	0.0032	0.0004
MVCO	min	0.0044	0.0057	0.0096	0.0125	0.0129	0.0038	0.0023	0.0002
	max	0.0155	0.0208	0.0364	0.0432	0.0458	0.0168	0.0108	0.0013
	median	0.0091	0.0113	0.0168	0.0201	0.0200	0.0050	0.0030	0.0005
COVE	min	0.0085	0.0113	0.0172	0.0210	0.0205	0.0041	0.0028	0.0000
	max	0.0258	0.0311	0.0436	0.0509	0.0495	0.0142	0.0104	0.0018
	median	0.0125	0.0157	0.0244	0.0304	0.0307	0.0066	0.0048	0.0006

3.2.1.2 MUMM database: Above-water TriOS RAMSES *in situ* $\rho_w(\lambda)$ data

The MUMM database includes data from TriOS-RAMSES hyperspectral spectro-radiometers (two measuring radiance and one measuring downwelling irradiance) from 63 sea campaigns between 2001 and 2012. Data were collected in coastal waters located in the southern North Sea and English Channel (Ruddick et al., 2006; Nechad et al., 2010), the Celtic Sea, the Ligurian Sea, the Adriatic Sea and in the Atlantic Ocean along the coasts of Portugal and French Guyana (Loisel et al., 2009; Vantrepotte et al., 2011). This dataset is particularly suitable for the validation of remote sensing retrieved $\rho_w(\lambda)$ as it includes measurements over contrasted water types including highly turbid coastal waters. For the present study, *in situ* data processing, averaging and selection were largely based on the processing described in Ruddick et al. (2006). Based on a subset of the MUMM dataset, Ruddick et al. (2006) estimated the relative reflectance uncertainty in the 650-900 nm spectral range between 3% and 5% and between 10% and 20% for turbid and clear water cases, respectively. As mentioned previously, during a one-month stay at the MUMM in Brussels, a set of R programs (`http://www.R-project.org.`) were developed, such that the raw *in situ* measurements are processed semi-automatically for each station to obtain average $\rho_w(\lambda)$ spectra, associated standard deviations and meta-data.

The three TriOS-RAMSES sensors measure simultaneously the downwelling irradiance at the sea surface, $E_d(\lambda)$, the total upwelling radiance from the water and air-sea interface that reaches the water viewing sensor, $L_t(\lambda)$, and the sky radiance that reflects into the direction of the water viewing sensor $L_{sky}(\lambda)$, in the 350-950 nm spectral range with 2.5 nm spectral resolution. The irradiance sensor is equipped with an optical fiber and a cosine collector while radiance sensors present a limited field of view of 7°. The instruments are usually mounted on a steel frame fixed to the bow of the ship, facing forward to minimize ship shadow and reflection (Fig. 3.3).

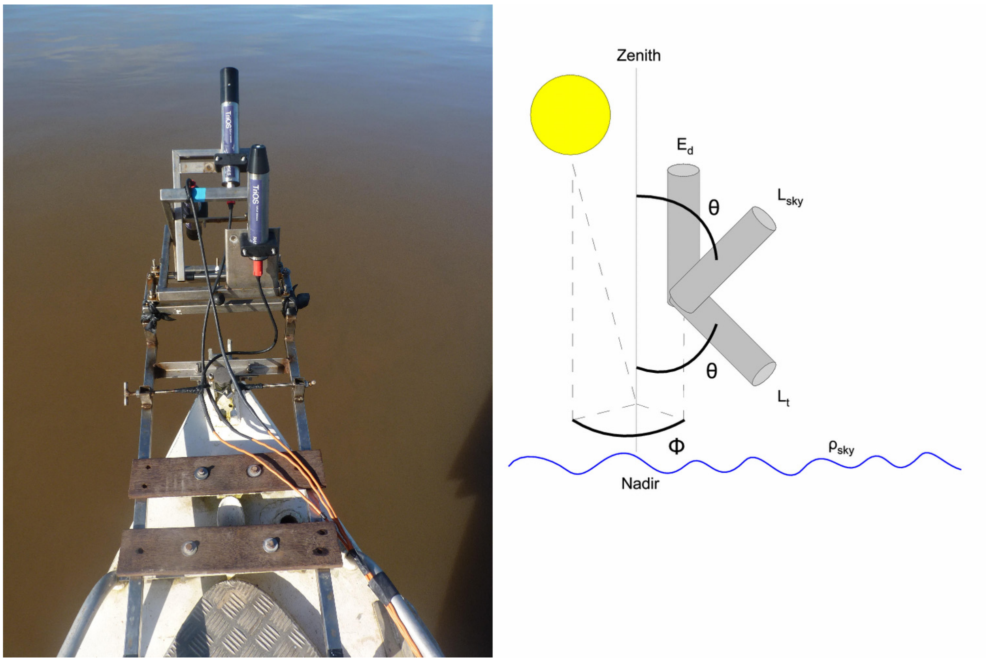

Figure 3.3: *Picture taken during the FG12 sea campaign from the TriOS RAMSES system oriented to minimize sun- and cloud glint and bidirectional effects ($\theta \sim 40°$ and $\psi \sim 135°$ (left) and schematic configuration of TriOS RAMSES instruments for above water $\rho_w(\lambda)$ retrievals (right).*

From $E_d(\lambda)$, $L_t(\lambda)$ and $L_{sky}(\lambda)$, $\rho_w(\lambda)$ can be derived as follows (Mobley, 1999):

$$\rho_w(\lambda) = \pi \frac{L_t(\lambda) - \rho_{sky} \times L_{sky}(\lambda)}{E_d(\lambda)} \tag{3.1}$$

where ρ_{sky} defines the proportion of the total upwelling radiance that is related to the air-water interface reflectance (also called sea surface reflectance factor). The term $\rho_{sky} \times L_{sky}(\lambda)$ can be described as the fraction of $L_t(\lambda)$ that is due to the skylight reflection effects at the sea surface. Subsequently, the difference $L_t(\lambda) - \rho_{sky} \times L_{sky}(\lambda)$ is the water-leaving reflectance just above the sea-surface, $L_w(\lambda)$.

For clear sky conditions ρ_{sky} is approximated as a function of the wind speed, W, while for cloudy conditions the coefficient is considered constant (Mobley, 1999; Ruddick et al., 2006). In the present processing when the wind speed is missing, a default value of 5 m s^{-1} is used. ρ_{sky} is calculated as follows:

$$\rho_{sky} = \begin{cases} 0.0256 + 0.00039W + 0.000034W^2 & \text{when } \frac{L_{sky}(750)}{E_d(750)} < 0.05 \\ 0.0256 & \text{when } \frac{L_{sky}(750)}{E_d(750)} >= 0.05 \end{cases} \tag{3.2}$$

Estimating the appropriate ρ_{sky} value is the most critical part of the above water approach and in particular when the wave facets cause a complex geometrical design between sea-surface and sensor. Equation (3.2) represents in this case an inaccurate simplification (Mobley, 1999; Toole et al., 2000).

To minimize sun glint, bidirectional effect and noise on $\rho_w(\lambda)$ retrievals, the ship is manoeuvred on station such that $L_{sky}(\lambda)$ and $L_t(\lambda)$ are measured at a zenith and relative azimuth angle of 40°and 135°, respectively (Fig. 3.3). Although sun and cloud glint and additional perturbations from platform reflection are minimized with this acquisition geometry, measurements may not be totally corrected for all contaminants. In clear waters, a “white correction” is often applied. This correction assumes a zero baseline in the NIR spectral region. The offset is then simply subtracted from the measured reflectance at each wavelength (Mueller and Austin, 1995; Toole et al., 2000). However, this includes the assumptions of spectrally white contamination and zero $\rho_w(\lambda)$ in the NIR spectral range which are not always valid. Another approach to eliminate residual contamination was suggested by Ruddick et al. (2005, 2006) which is based on the NIR similarity spectrum assumption (i.e., the shape of the NIR $\rho_w(\lambda)$ spectra is almost invariant for moderately to very turbid waters). The offset in the “white correction” is then replaced by a multiplicative correction factor ϵ with $\alpha(\lambda_1, \lambda_2)$ being the constant NIR reflectance ratio (Ruddick et al., 2000, 2005, 2006):

$$\epsilon = \frac{\alpha(\lambda_1, \lambda_2) * \rho_w(\lambda_2) - \rho_w(\lambda_1)}{\alpha(\lambda_1, \lambda_2) - 1} \tag{3.3}$$

This approach allows to account for spectrally dependent residual contamination. However, as demonstrated by Doron et al. (2011) and later in Chapter 4, the assumption of a constant NIR reflectance shape is not always valid. Moreover, the spectral dependency of cloud glint contamination may vary with the cloud properties (thickness, coverage, distribution) (Rudorff et al., 2013). Accordingly, for the present study, residual correction factors are not applied.

At each station, about 60 scans were recorded during 4 to 10 minutes (see, for instance, Fig. 3.4). Shorter recording times were preferred when the tidal stream was significant in order to avoid large deviations of the ship.

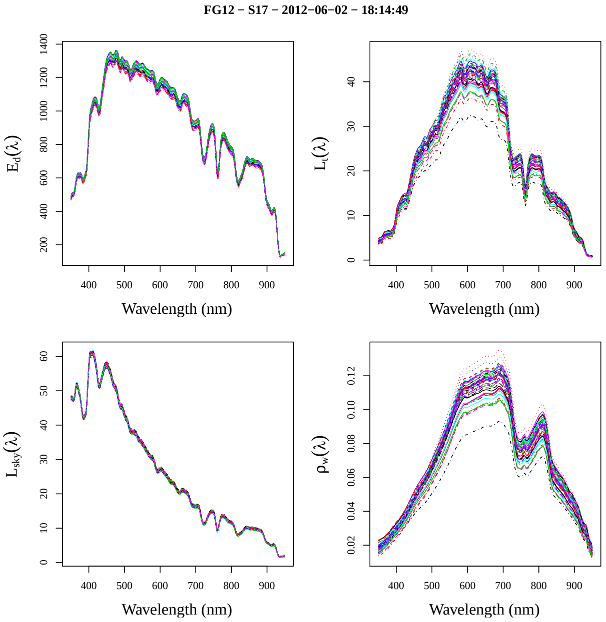

Figure 3.4: *$E_d(\lambda)$ ($mW\ m^{-2}\ nm^{-1}$) (top left), $L_t(\lambda)$ ($mW\ m^{-2}\ nm^{-1}\ sr^{-1}$) (top right), $L_{sky}(\lambda)$ ($mW\ m^{-2}\ nm^{-1}\ sr^{-1}$) (bottom left) and $\rho_w(\lambda)$ (dimensionless) (bottom right) for the 60 scans measured at station S17 during the FG12 field campaign.*

Within each set of 60 scans, scans were rejected when their vertical inclination exceeded 5% and/or when the measured $E_d(550)$, $L_t(550)$ or $L_{sky}(550)$ differed by more than 25% from either neighbouring scans (Fig. 3.5). Scans with sharp intensity changes over the spectral range (i.e. scans showing spectral jumps in $E_d(\lambda)$, $L_t(\lambda)$ or $L_{sky}(\lambda)$ of more than 0.4%, 2% and 0.4%, respectively) were also considered as erroneous and excluded for further data analysis (Fig. 3.5).

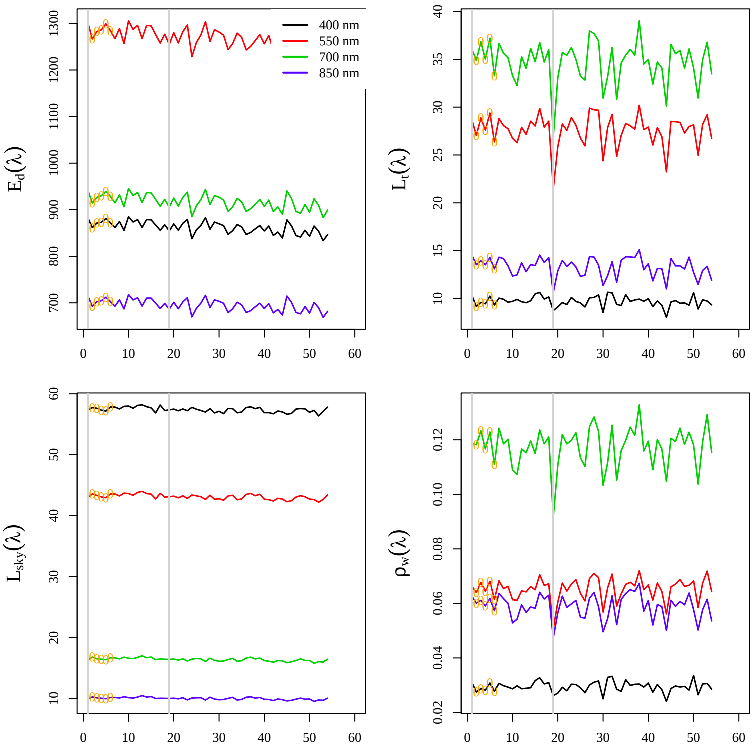

Figure 3.5: *$E_d(\lambda)$ (mW m^{-2} nm^{-1}) (top left), $L_t(\lambda)$ (mW m^{-2} nm^{-1} sr^{-1}) (top right), $L_{sky}(\lambda)$ (mW m^{-2} nm^{-1} sr^{-1}) (bottom left) and $\rho_w(\lambda)$ (dimensionless) (bottom right) at 400, 550 and 700 and 850 nm measured at 60 time-steps at station S17 during the FG12 field campaign. Scans showing spectral jumps relative to the neighbouring scans are eliminated and indicated on the plots by a vertical grey bar.*

Ultimately, as done by Ruddick et al. (2006), the first five scans out of the remaining scans were used to calculate the average and standard deviation of $\rho_w(\lambda)$ at each station (Fig. 3.6).

In order to ensure highly accurate $\rho_w(\lambda)$ retrievals, Ruddick et al. (2006) imposed three additional quality requirements:

1. Measurements taken under clear sky conditions ($L_{sky}(750)/E_d(750) < 0.05$) should only be retained.
2. To ensure low temporal variability, the standard deviation of the five selected $\rho_w(780)$ scans should not overpass 10% of the averaged $\rho_w(780)$.
3. The wind speed should not exceed 10 m s^{-1} during measurement.

With the aim to increase our validation dataset, the appropriateness of retaining only data taken under clear sunny skies was first investigated before it was applied. Indeed, under fully overcast conditions ($L_{sky}(750)/E_d(750) > 0.3$ sr^{-1}), ρ_{sky} remains independent of cloud cover and wavelength and the reflected sky radiance estimations ($\rho_{sky} \times L_{sky}(\lambda)$) are not or

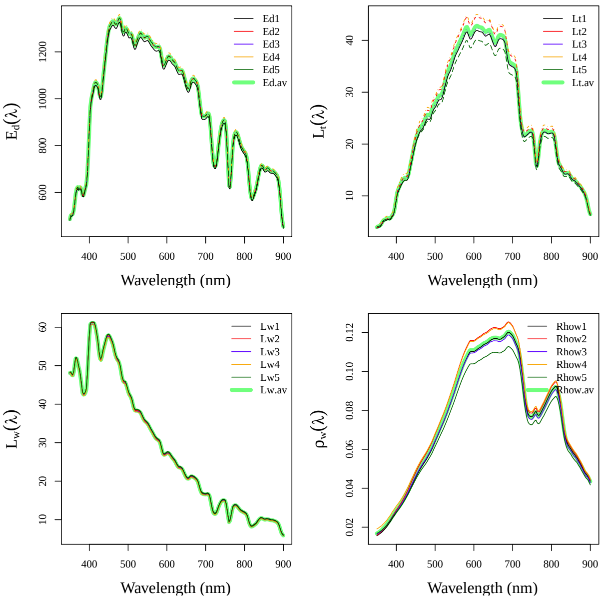

Figure 3.6: *$E_d(\lambda)$ (mW m^{-2} nm^{-1}) (top left), $L_t(\lambda)$ (mW m^{-2} nm^{-1} sr^{-1}) (top right), $L_{sky}(\lambda)$ (mW m^{-2} nm^{-1} sr^{-1}) (bottom left) and $\rho_w(\lambda)$ (dimensionless) (bottom right) of the 5 selected scans used to obtain the final averaged spectra (thick green lines) and associated standard deviations for the station S17 of the FG12 field campaign.*

less affected by sun glint (Mobley, 1999) and sea-state conditions (Toole et al., 2000). This results in significantly lower uncertainty compared to clear sky conditions (Toole et al., 2000). Nonetheless, with fully overcast conditions, even small errors in ρ_{sky} may result in significant $\rho_w(\lambda)$ inaccuracies because of the large contribution of $L_{sky}(\lambda)$ to $L_t(\lambda)$ (Mobley, 1999). Doxaran et al. (2003) also claimed that an accurate correction of the reflection effects under diffuse illumination remains challenging. To investigate if whether or not measurements taken under overcast cloud conditions should be retained, the contribution of $L_{sky}(\lambda)$ to $L_t(\lambda)$ is compared when measured under clear skies ($L_{sky}(750)/E_d(750) < 0.05$ sr^{-1}) and under uniform overcast conditions ($L_{sky}(750)/E_d(750) > 0.3$ sr^{-1}). The relative difference in $\rho_w(\lambda)$ is also investigated after increasing and decreasing the initial ρ_{sky} values by 10%, respectively.

The 63 sea campaigns presented in the MUMM dataset included 860 stations, and consequently, 860 averaged $\rho_w(\lambda)$ spectra. Out of these 860 spectra, 184 spectra passed the selection criteria showing small temporal variability and low wind speeds (below 10 m s^{-1}) during acquisition. Among these 184 remaining spectra, 131 spectra showed clear sky conditions, with $L_{sky}(750)/E_d(750)$ ranging from 0.006 to 0.05 sr^{-1}, 10 spectra showed uniform overcast conditions with $L_{sky}(750)/E_d(750)$ ranging from 0.30 to 0.38 sr^{-1}. The 33 spectra showing non-uniform cloudy conditions ($L_{sky}(750)/E_d(750)$ between 0.05 and 0.3 sr^{-1}) are excluded from data analysis.

As noticed by Mobley (1999), under overcast and thick overcast conditions, a larger contribution of $L_{sky}(\lambda)$ to $L_t(\lambda)$ is observed compared with clear skies (Fig. 3.7(a)). Hence, for such conditions even small errors in ρ_{sky} may induce large errors in $\rho_w(\lambda)$ estimations (Mobley, 1999). Fig. 3.7(b) shows the percent difference on $\rho_w(\lambda)$ after including ± 10% error in the initial ρ_{sky} values. With uniform overcast conditions, 10% error in ρ_{sky} induces less than 10% difference in $\rho_w(\lambda)$ between 400 and 725 nm. However, differences increase in the 740-900 nm range (> 10%). In contrast, for clear sky conditions, 10% error in ρ_{sky} results in less than 10% difference over the entire spectrum.

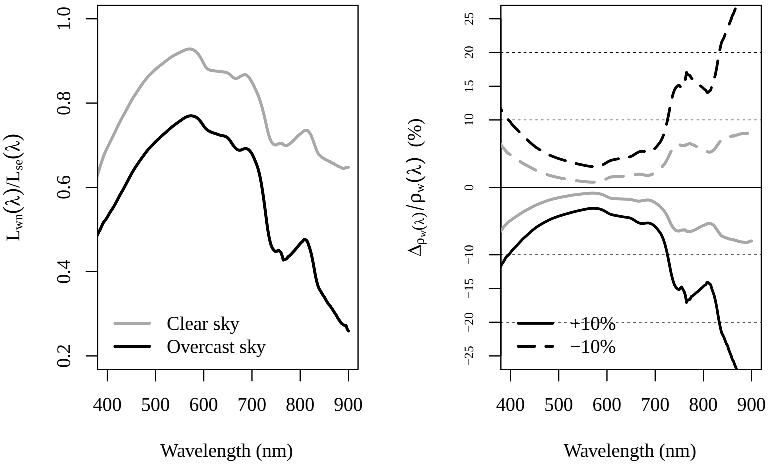

Figure 3.7: *Relative contribution of* $L_w(\lambda)$ *to* $L_t(\lambda)$ *(a) and percent difference (%) on* $\rho_w(\lambda)$ *after including ± 10% error on the initial* ρ_{sky} *for clear sky (grey line) and uniform overcast conditions (black line) (b).*

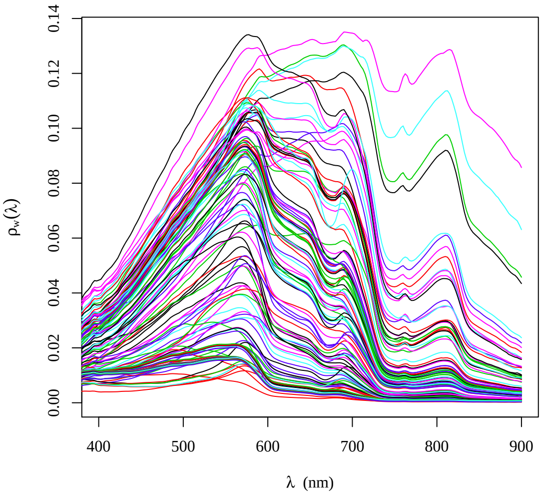

Figure 3.8: *131 selected above-water TriOS RAMSES reflectance spectra from the MUMM database used in the present study for the validation and improvement of AC methods.*

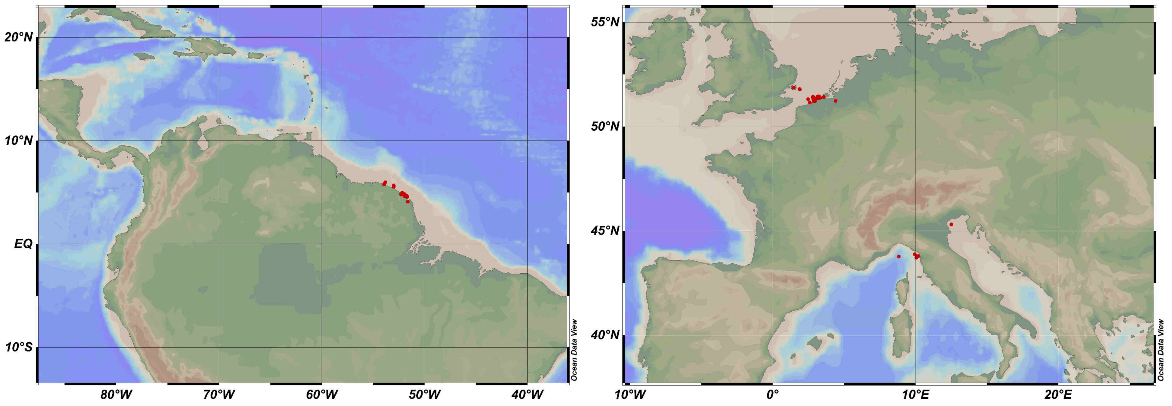

Figure 3.9: *Location of the 131 selected above water TriOS RAMSES spectra from the MUMM database (red dots on the map) along the coast of French Guiana (left) and in the European waters (right) used in the present study for the evaluation and improvement of the AC methods.*

Since the present study requires highly accurate data and to ensure less than 5% uncertainty on $\rho_w(\lambda)$ as recommended by the SeaWiFS protocol (Mueller et al., 1996), retaining only clear sky conditions is justified reducing the number of selected spectra to 131. The 131 selected spectra are shown in Fig. 3.8 and their location in Fig. 3.9. Finally, for comparison with MODIS Aqua retrieved $\rho_w(\lambda)$ data, a linear interpolation is performed in the 350-950 nm spectral range to obtain *in situ* data at the MODIS Aqua central wavelengths.

3.2.2 In-water systems

In situ $\rho_w(\lambda)$ data retrieved from in-water sensors are computed from simultaneous measurements of submersed radiometers recording upwelling radiance, $L_u(\lambda)$, and downwelling irradiance, $E_d(\lambda)$, and possibly a deck sensor that measures above-water downwelling irradiance, $E_s(\lambda)$. Different instrument designs exist, e.g., the sensors attached to moored buoys sampling at stationary depths (e.g., the Hyperspectral Tethered Satlantic Remote Sensing Buoy HTSRB), the profilers winched and attached to deploying cages (e.g., in-water TriOS RAMSES), or the free-falling instruments drifting away from the platform attached solely to the telemetry cable (e.g., the Hyperspectral Optical Profiler, HyperPRO, and High-Resolution Profiling Reflectance Radiometer, PRR). Free falling profilers are usually deployed at the leeward side of the stern to let them drift away from the ship or platform avoiding ship shadow and structure perturbations (Rudorff et al., 2013). Winched profilers such as the in-water TriOS RAMSES system should be deployed at the sun incidence side of the ship to avoid ship shadow.

According to Mueller et al. (2003) and Bailey and Werdell (2006), in-water methods are more standard and extensively used in ocean colour remote sensing for satellite calibration and validation. It is also considered to provide more accurate radiometric measurements compared to the above water methods because contamination of the reflected skylight on the ocean surface is avoided (Rudorff et al., 2013). However, imperfections in in-water $\rho_w(\lambda)$ measurements are also multiple. Measurements need to be corrected for sensor tilt and instrument self-shading including complex extrapolation procedures, along the in-water profile and through the water interface to obtain above-water radiometric measurements, and accounting for variations in the submersed light field (Toole et al., 2000; Mueller et al., 2003; Zibordi and Voss, 2010). Larger biases and uncertainties are encountered when wind speeds are important inducing significant wavy facets and water bubbles resulting in significant illumination variations. To avoid the effect of such perturbation factors, the extrapolation for the retrieval of $\rho_w(\lambda)$ is often done using greater depths where the water column is less affected by the effect of the wind (Rudorff et al., 2013). Nonetheless, this includes the assumption of vertical homogeneity in the water column and thus a constant diffuse attenuation coefficient, $K_d(\lambda)$ (Rudorff et al., 2013). Moreover, in turbid waters, light penetration may be limited, reducing the possible extrapolation depth, especially at larger wavelengths where the water signal is less important (Zibordi et al., 2004a). Therefore, in-water instruments usually provide more accurate $\rho_w(\lambda)$ measurements in clear or moderately turbid waters and at shorter wavelengths, while above-water instruments tend to exhibit better $\rho_w(\lambda)$ estimations in the NIR spectral region and over very turbid waters.

3.2.2.1 LOG database: In-water TriOS-RAMSES *in situ* $\rho_w(\lambda)$ data

The LOG database presents hyperspectral radiometric measurements performed in the visible and NIR spectral range (∼ 350-950 nm) from two in-water radiometers and one deck sensor. The deck sensor measures downward irradiance, $E_d(0+,\lambda)$, and is placed pointing upward on a mast such that any platform shading is avoided (Fig. 3.10). In the profiling cage, one in-water radiometer is pointed upward measuring the in-water irradiance profile, $E_d(z,\lambda)$, the other is pointed downward to measure the nadir upward radiance profile, $L_u(z,\lambda)$ (Fig. 3.10). Similarly to the sensors used for the above water TriOS system, the irradiance sensor is equipped with an optical fibre and a cosine collector while the radiance sensor presents a limited field of view of 7°in the air.

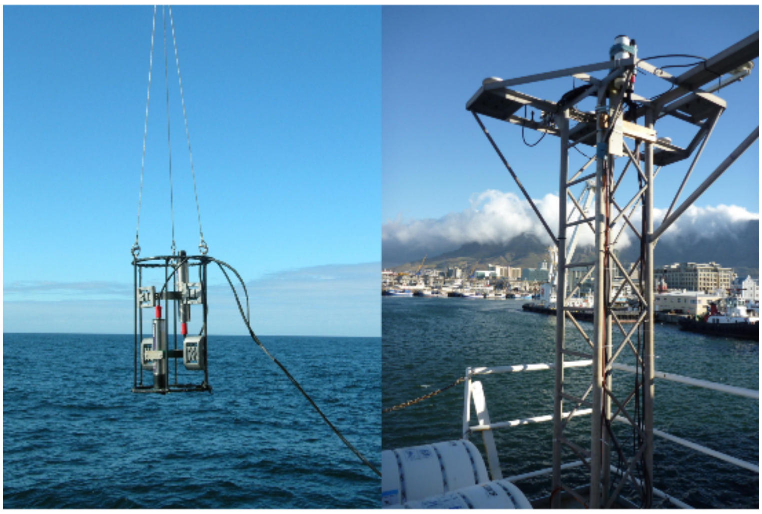

Figure 3.10: *Picture of the in-water TriOS RAMSES system deployed in a cage during the MV1102 measurement campaign (left) and the deck sensor for the normalization of the in-water radiometric measurements to variations in illumination (right).*

First, wavelength dependent correction factors, also called immersion factors, are applied to correct in-water measurements for the reduced solid angle and light transmission due to the water immersion of the sensors (Mueller and Austin, 2003; Ohde and Siegel, 2003). Next, $E_d(z,\lambda)$ and $L_u(z,\lambda)$ are normalised by $E_d(0+,\lambda)$ ($E_{dn}(z,\lambda)$ and $L_{un}(z,\lambda)$, respectively) to minimize illumination variations during acquisition:

$$E_{dn}(z,\lambda) = \frac{E_d(z,\lambda)E_d^{t_0-}(0+,\lambda)}{E_d^{t_z}(0+,\lambda)} \tag{3.4}$$

$$L_{un}(z,\lambda) = \frac{L_u(z,\lambda)E_d^{t_0-}(0+,\lambda)}{E_d^{t_z}(0+,\lambda)} \tag{3.5}$$

where t_{0-} and t_z indicate that $E_d(0+,\lambda)$ is taken at the time when the cage is just below surface and when it is at depth z, respectively. $E_d(z,\lambda)$ and $L_u(z,\lambda)$ are also corrected for self-shading effects as suggested by Gordon and Ding (1992) or Leathers and Downes (2004).

Next, $L_u(z,\lambda)$ and $E_d(z,\lambda)$ are extrapolated just below sea-surface to obtain $L_u(0-,\lambda)$ and $E_d(0-,\lambda)$.

$$E_d(0-,\lambda) = E_{dn}(z,\lambda)e^{z*K_d^{E_d}(\lambda)} \tag{3.6}$$

$$L_u(0-,\lambda) = L_{un}(z,\lambda)e^{z*K_d^{L_u}(\lambda)} \tag{3.7}$$

where $K_d^{L_u}(\lambda)$ and $K_d^{E_d}(\lambda)$ are the downwelling diffuse attenuation coefficients computed as the slope of the self-shading corrected $ln(L_{un}(z,\lambda))$ and $ln(E_{dn}(z,\lambda))$ profiles, respectively (Smith and Baker, 1981; Mueller, 2003).

Knowing $L_u(0-,\lambda)$ and $E_d(0-,\lambda)$, $L_w(0+,\lambda)$ and $E_d(0+,\lambda)$ can be derived to obtain $\rho_w(\lambda)$ using Eq.(1.10), (1.11) and (1.12). The downwelling incident irradiance just above the sea surface can also be obtained with the deck sensor $E_d(0+,\lambda)$ measurements. This approach is preferred and selected to avoid variations in focusing and defocusing sunlight by surface waves and perturbations due to water bubbles. However, perturbations may affect $L_u(z,\lambda)$ and $E_d(z,\lambda)$ in a similar way and are thus cancelled when the radiance-irradiance ratio is computed to estimate $\rho_w(\lambda)$. Moreover, deck sensor $E_d(0+,\lambda)$ values are more affected by variations in illuminations (especially when cloud cover is not homogeneous) and platform tilt (Rudorff et al., 2013).

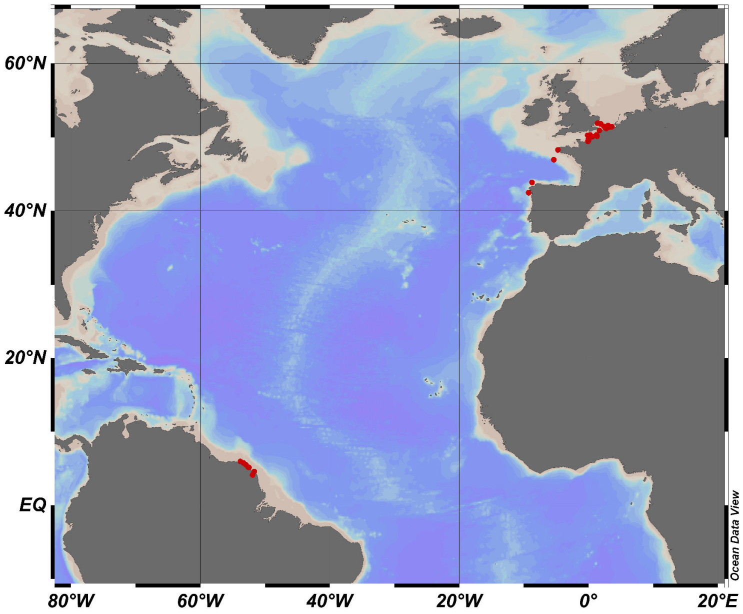

Figure 3.11: *Location of the selected in-water TriOS RAMSES reflectance spectra from the LOG database (red dots) used in the present study for the validation and improvement of AC methods.*

Sampling protocols and data characteristics for the LOG data are further described in, among others, Lubac and Loisel (2007) for the North Sea-English Channel dataset and in Loisel et al. (2009) and Vantrepotte et al. (2011) for French Guiana. The map in Fig. 3.11 shows the location of the LOG data used in the present study for the validation of the AC methods. Figure 3.12 shows the hyperspectral $\rho_w(\lambda)$ spectra of these data per field campaign (i.e., Belgica

2009-2010, Belcolor 2009-2010, French Guiana 2009, Belgica 2010, and Phabop 2004 with 20, 76, 21, and 93 spectra, respectively).

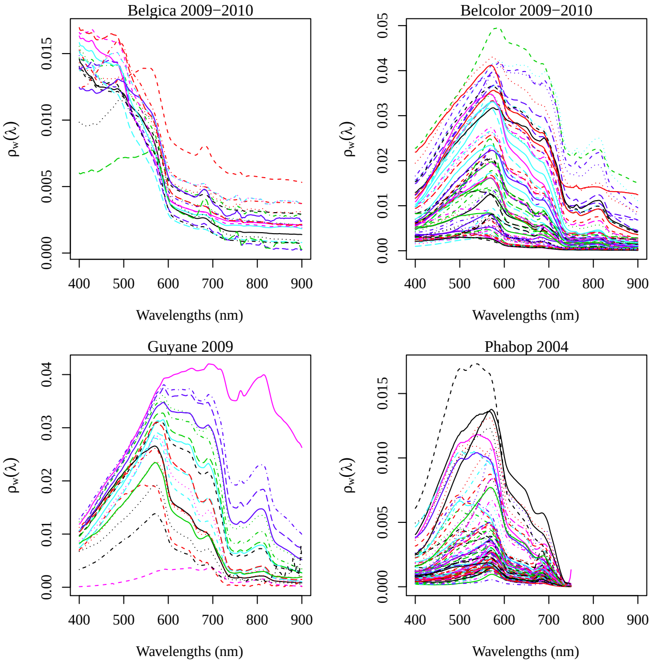

Figure 3.12: *Reflectance spectra from the LOG database used in the present study and per field campaign.*

3.2.3 Closure exercises

3.2.3.1 Inter-comparison of $\rho_w(\lambda)$ data from above and in-water instruments in the southern Atlantic and south-eastern Pacific

This section includes an inter-comparison of $R_{rs}(\lambda)$ data collected during the MV1102 sea campaign and is part of the following paper: N. D. M. Rudorff, R. Frouin, M. Kampel, ***C. Goyens****, X. Meriaux, and B. Schieber (2013). Assessing accurate ocean colour in situ radiometry across the southern Atlantic and south-eastern Pacific. Submitted to Remote Sensing of Environment.*

The MV1102 campaign on-board the R/V Melville (Scripps Institution of Oceanography, SIO) departed from Cape Town (South Africa) on February 22nd 2011 and arrived at Valparaiso (Chile) on March the 13th 2011, end of the austral summer. A total of 20 stations with radiometric and bio-optical measurements were undertaken across the Southern Atlantic (33°-53°S and 15°-70°W) and southeastern Pacific (47-35°S and 74-76°W) (Fig. 3.13).

The sampled regions are characterized by a range of highly diverse and complex systems with coastal regions presenting nutrient enriched waters (South African and South American coastal regions) and highly productive waters (South Chilean coast), frontal zones marked by strong temperature-salinity gradients (South Atlantic Subtropical Convergence Zone), colder less saline and high nutrient low chlorophyll waters (Southern Ocean), and warmer, more saline and oligotrophic waters.

The radiometric stations were undertaken as close as possible to the overpassing times of the MERIS and MODIS satellites. Radiometric measurements were made with an above-water - ASD and with in-water - HyperPRO, PRR and TriOS instruments. Sub-surface bio-optical

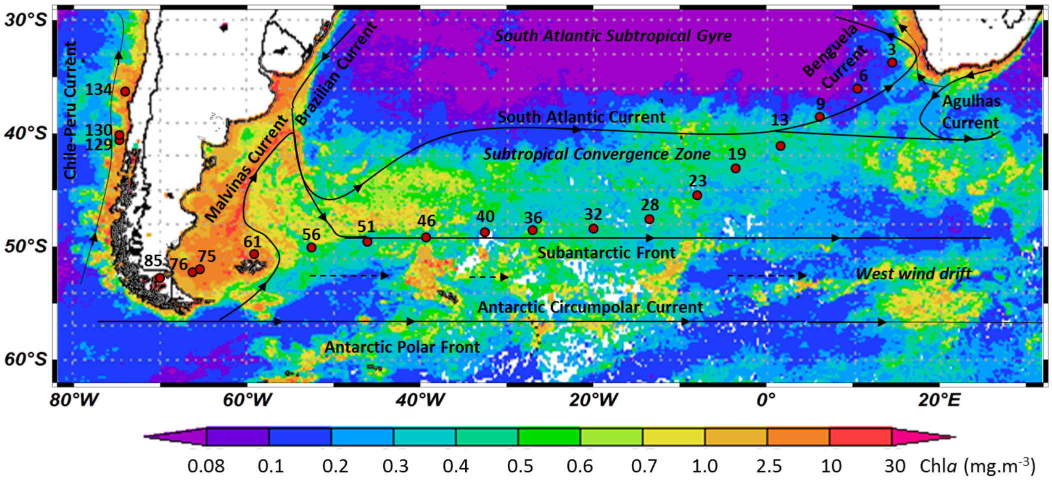

Figure 3.13: *MV1102 radiometric stations shown in a Chl_a map obtained from MODIS Aqua (4 km spatial resolution) averaged in the sampling period (02/18-03/14/2011).*

measurements were also performed for Chl_a and pigment concentrations, and CDOM absorption. A HydroScat (Hobilabs Inc.), ECO-VSF green and red, C-star and BB9 (from Wetlabs) were also deployed to retrieve the backscattering and attenuation coefficients at several wavelengths. Measurements and data processing of the radiometric and bio-optical data are detailed in Rudorff et al. (2013).

First, $R_{rs}(\lambda)$ measurements are analysed and sources of uncertainties are outlined for each instrument. Next, a measurement-measurement comparison exercise is conducted comparing the retrieved $R_{rs}(\lambda)$ values from the different radiometric instruments. Therefore, $R_{rs}(\lambda)$ values from the HyperPRO are taken as a reference to compare the other $R_{rs}(\lambda)$ quantities. The unbiased percent difference (UPD), the modular relative percent difference for absolute differences (RPD*), and the determination coefficient (R^2) of linear regression analysis are used as statistical indices for instrument inter-comparison. The UPD considers that all measurements are biased. The RPD* quantifies the total bias. The R^2 measures the dispersion between the quantities.

According to the resulting $R_{rs}(\lambda)$ measurements, the main sources of uncertainty with the above-water ASD system are associated with cloud glint contamination and illumination variations due to broken clouds. Wind speed is also an important contaminator affecting the sky glint contribution with clear and partially cloudy skies. In this paper we showed that residual contamination from sun and cloud glint and artefacts caused by illumination variation could be reduced but not totally corrected with the residual contamination correction (i.e., subtraction of the 800 nm white offset) and quality control scheme (i.e., excluding scans for which the coefficient of variation in the blue spectral band exceeds 10%).

For the in-water free-falling profilers, HyperPRO and PRR, a significant source of uncertainty is related to the depths interval used for the extrapolation of the radiometric quantities. Surface depths are more desirable but much more subjected to environmental noises with high fluctuations in the light field distribution caused by surface wavy facets and intermittent presence of bubble clouds due to breaking waves. Higher depths, on the other hand, have lower signals resulting in increasing uncertainties, higher $K_d(\lambda)$ variations and Raman scattering effects (Gordon et al., 1993; Berwald et al., 1998; Morel and Gentili, 2004). For the estimation of $R_{rs}(\lambda)$ with the PRR and HyperPRO, no systematic difference is found in the retrieved $R_{rs}(\lambda)$ when the deck or in-water sensors are used to compute $E_d(0+, \lambda)$. Therefore, for both the HyperPRO and PRR instruments, the optimized depth interval is defined based on a best fit for the $K_d(\lambda)$ estimation and the estimated $R_{rs}(\lambda)$ is defined as the average between the $R_{rs}(\lambda)$ computed when the deck and in-water sensor are used for the $E_d(0+,\lambda)$ estimations. In contrast, for the in-water TriOS system, $R_{rs}(\lambda)$ uncertainties are much larger when the deck sensor is used. Indeed, biases in $L_u(\lambda)$ are probably amplified when normalizing with the deck sensor $E_d(0+,\lambda)$. With the in-water sensor $E_d(0+,\lambda)$, $R_{rs}(\lambda)$ values much closer to the other approaches are observed. Therefore, for the TriOS instrument, estimated $R_{rs}(\lambda)$ values are computed with the in-water sensor $E_d(0+,\lambda)$ and the entire profile was used (5-40 m) for the $K_d(\lambda)$ estimation.

Table 3.4 shows the statistics resulting for the measurement-measurement closure exercise between $R_{rs}(\lambda)$ retrieved with the HyperPRO system and retrieved with the PRR, the in-situ TriOS system and the above water ASD. The PRR exhibits a RPD* of approximately 12% with a slight overestimation in $R_{rs}(\lambda)$ compared to the HyperPRO data. Both PRR and HyperPRO are free-falling profilers and have the advantage to drift away from the platform avoiding any type of perturbations from the superstructure. Hence, it is expected that these two approaches are affected by the same type of perturbations and, subsequently, show a close agreement. Most of the uncertainty between these approaches may therefore be associated with intrinsic environmental variability as well as the choice of the extrapolation depth resulting in variations in the $R_{rs}(\lambda)$ estimations.

Table 3.4: *Unbiased percent difference (UPD, %), modular relative percent difference for absolute relative differences (RPD*, %) and determination coefficient of linear regression (R^2, %) between $\rho_w(\lambda)$ measured with HyperPRO and with the PRR, TriOS and ASD, respectively.*

		412	443	510	555	412/555	443/555	510/555
	UPD (%)	0	2	9	6	-6	-4	3
PRR	RPD* (%)	12	13	14	12	7	5	4
N=19	R^2 (%)	91	90	72	72	99	99	99
	UPD (%)	-27	-29	-27	-19	-9	-10	-6
TriOS	RDP* (%)	27	27	25	19	9	10	8
N=12	R^2 (%)	77	80	65	53	96	96	95
	UPD (%)	8	9	9	13	-4	-4	-4
ASD	RDP* (%)	21	19	12	15	13	10	5
N=17	R^2 (%)	86	87	80	94	97	97	97

The TriOS $R_{rs}(\lambda)$ data present the highest differences, with 19-27% RPD* showing generally lower $R_{rs}(\lambda)$ values. This underestimation is possibly due to instrument or platform shading (when the ship is not perfectly oriented according to the sun direction to avoid these effects) and/or greater depths selections for the extrapolation procedure. To verify the impact of greater extrapolation depths, variations in $R_{rs}(\lambda)$ values were investigated relative to the extrapolation depth for both the TriOS and HyperPRO approaches and based on IOP and modeled $R_{rs}(\lambda)$ data (derived from *insitu* bio-optical measurements and based on the model of Morel and Maritorena (2001), more details in Rudorff et al. (2013)). Rudorff et al. (2013) concluded that the overall impact of the bio-optical variability remained small. Similarly, $K_d(\lambda)$ estimations with the HyperPRO appeared to be relatively constant whatever the used extrapolation depth. Nonetheless, the measurements collected with the lower extrapolation depth used with the HyperPRO instrument may be affected by bubble scattering which could possibly result in a slight overestimation in $R_{rs}(\lambda)$, especially for stations under high winds and waves and lower Chl_a concentrations. This is also true for the PRR measurements. Using larger depths, the TriOS instrument may avoid more effectively the bubble effects. Hence, the effect of bubble clouds may contribute to an overestimation in $R_{rs}(\lambda)$ with the HyperPRO instrument while the shading effects of the ship structure may result in lower $R_{rs}(\lambda)$ retrievals with the TriOS instrument.

The ASD sensor shows RPD* values ranging from 15% to 21% and tends to overestimate the water signal relative to the HyperPRO instrument. Overestimations with above-water approaches may result from under-corrections of sky, cloud, and/or sun glint, platform reflection, presence of whitecaps, and in-water bubble clouds. As noticed by Rudorff et al. (2013), these effects are wavelength dependent (e.g., platform reflection may have an impact at specific wavelengths depending on the colour of the structure, bubble clouds causes a peak in $R_{rs}(\lambda)$ in the green bands) explaining the higher RPD* values for blue-green ratios compared to green-green ratios (10% and 13% versus 4%, respectively).

Except for the TriOS system at 555 nm, all instruments also show high co-variations for the spectral bands and band ratios indicating an overall reasonable performance of the different methods. However, in most cases the UPD and RPD* values in Table 3.4 greatly exceed the 5% uncertainty recommended as the maximum retrieval error by the SeaWiFS protocol for accurate in situ $R_{rs}(\lambda)$ (Mueller et al., 1996). In the literature, most inter-comparison studies focused on case 1 waters and applied highly controlled schemes with instrument inter-calibration and similar data processing codes for all instruments (Hooker and Maritorena, 2000; Zibordi et al., 2009c, 2012). Under more diverse conditions and embracing also more eutrophic and turbid coastal waters, Toole et al. (2000) and Garaba and Zielinski (2013) found similar and even greater differences between above and in-water methods. Rudorff et al. (2013) concluded that the uncertainties associated with environmental variabilities for a same system are almost as high as the differences observed between the systems.

This exercise illustrates the need for careful acquisition and data processing schemes for *in situ* radiometry for both above and in-water methods in order to ensure accurate validation data.

3.2.3.2 Radiometric closure between $\rho_w(\lambda)$ data from above and in-water hyperspectral radiometers measured in the Gulf of Maine

This section is largely based on the on-line available report from N. Briggs, H. Chen, A. Dave, F. H. Freitas, ***C. Goyens****, C. Kearney, L. Powers, S. Rivero, and R. Vandermeulen entitled "Hyperspectral radiometers" in Arellano et al. (2011). The latter is an outcome of the three weeks International Ocean Optics Summer School 2011 about calibration and validation of ocean colour remote sensing at the Darling Marine Centre (Walpole, Maine, 10-31 july 2011).*

The field data obtained from the simultaneous deployment of three separate instrument systems, the Satlantic HyperPRO, HyperSAS and HTSRB, provided an excellent opportunity to assess closure between disparate radiometric measurements. Data were collected in the Gulf of Maine (at 43°44.9 North and 69°29.9 West) in the afternoon of July 20th, 2011 ($\sim$ 15:00 local time). The sky conditions on this day were ideal with a bright sun and less than 5% cloud cover. Sea state was very calm with wind speeds below 1 m s^{-1}. For the HyperPRO instrument, two configurations were compared, once when a flotation collar is attached to the instrument such that near surface upwelling irradiance and radiance are measured ("buoy mode"), and once when the instrument is in its initial configuration (i.e., free-falling profiler system). A comprehensive overview of the instrument characteristics and data processing for the three hyperspectral radiometers is given by Briggs et al. (2011).

Figure 3.14 shows that the estimated $R_{rs}(\lambda)$, provided from the different instruments, are in close agreement ($<$ 10% difference) over blue and green wavelength bands. In the red wavelength band, estimates of $R_{rs}(\lambda)$ show significantly greater variations (up to 50%).

Similarly to the previous closure exercise (Section 3.2.3.1, Rudorff et al. (2013)), the differences in $R_{rs}(\lambda)$ reflect the techniques used to transform subsurface and above-water measurements into $L_w(\lambda)$ and $E_d(\lambda)$ values. In the case of subsurface measurements, this entails the extrapolation of $E_d(z, \lambda)$ and $L_u(z, \lambda)$ up to just below the sea surface and the estimation of their transmission through the surface. In the case of above-water measurements, it includes the deconvolution of $L_t(\lambda)$ into $L_w(\lambda)$. Thus, in all cases, $R_{rs}(\lambda)$ estimates are impacted by the state of the sea surface. Small temporal changes in the light field due to cloud effects may also contribute to differences between $R_{rs}(\lambda)$ estimates. Nonetheless, the comparison presented here represents an optimal case, since data were collected within 2 hours near noon on a day with a clear, blue sky and almost flat sea surface.

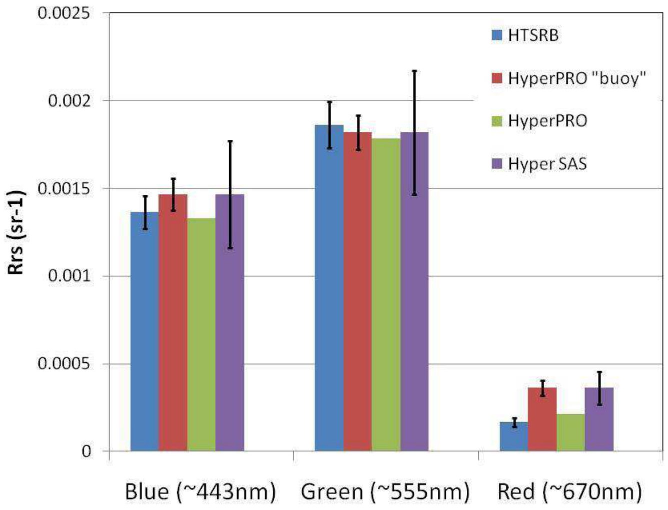

Figure 3.14: *Comparison of $R_{rs}(\lambda)$ estimations from 4 distinct configurations and radiometer systems deployed in the Gulf of Maine in July 2011. Error bars indicate standard deviation for each estimate.*

Next, a measurement-model closure is achieved by investigating whether or not the $R_{rs}(\lambda)$ spectra generated by HydroLight (Mobley, 1989; Mobley and Sundman, 2008) with field-measured IOPs (absorption, backscatter, attenuation and Chl_a concentration) agree with the $R_{rs}(\lambda)$ spectra generated from field data. Before inputing IOP data into HydroLight, extreme care was taken to ensure proper data processing with all corrections for dark signals, blanks, and temperature/salinity differences. The Chl_a concentration was calculated for several depths using the in-situ fluorometer. In the present study, the Chl_a absorption specification model is selected based on Case I water (Mobley and Sundman, 2008). Total absorption and attenuation coefficients and backscattering coefficients are measured using an ac-s and BB9 instrument, respectively. Additionally, the model utilizes a Pope and Fry pure water model (Pope and Fry, 1997). It considers inelastic scattering effects and an infinitely deep water column, and estimates CDOM absorption with a filtered ac-s cast. The wind speed is below 1 m s^{-1} and the sky is as 100% clear. In order to compute the sun position and intensity, measurement location, date and time are supplied to the model. Finally, measured and modelled $R_{rs}(\lambda)$ are compared.

Figure 3.15 shows the measurement-measurement and model-measurement closure for a single cast and the associated uncertainties. The $R_{rs}(\lambda)$ values measured with the three different instruments (with the HyperPRO system in buoy mode) all agree within the uncertainties limits. The modelled $R_{rs}(\lambda)$ spectrum also shows a relatively good fit with field measurements. With the HTSRB system and HydroLight, the characteristic Chl_a peak around 670 nm is clearly observable. Note that for this specific cast, the $R_{rs}(\lambda)$ spectrum for the HTSRB appears to drop below zero at about 700 nm. Negative values for $R_{rs}(\lambda)$ are non-physical. This negative offset most likely results from an old calibration file when processing the data. This illustrates the need to compare the offset of the different radiometers. A good way to do this is to point the radiance and irradiance sensors of each system at a same homogeneous surface and to look at the measurement differences.

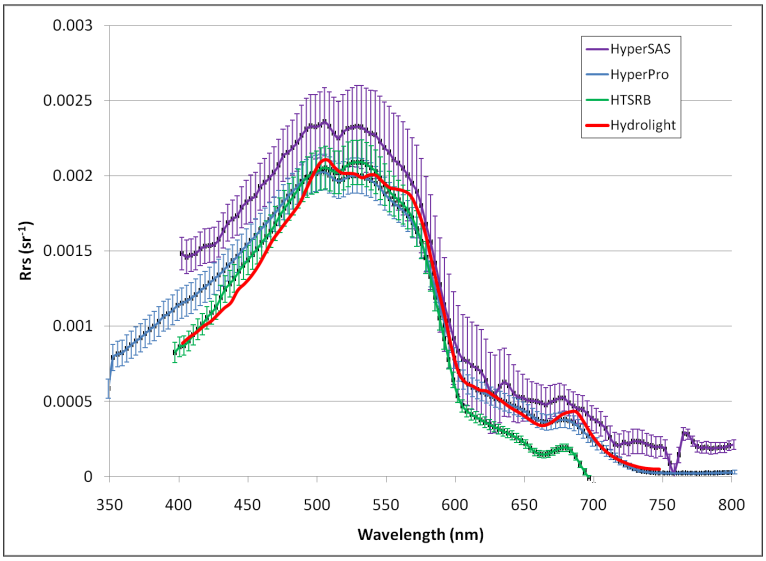

Figure 3.15: *Measurement-model and measurement-measurement closure of* $R_{rs}(\lambda)$ *spectra and their associated uncertainties measured in the Gulf of Maine on July 20th 2011.* $R_{rs}(\lambda)$ *from field measurements using HyperSAS (purple line), HyperPRO (buoy mode) (blue line) and HTSRB (green line) are compared with the modelled (HydroLight)* $R_{rs}(\lambda)$ *(red line).*

3.3 COINCIDENT *in situ* AND SATELLITE $\rho_w(\lambda)$ DATA: MATCH-UPS SELECTION

The datasets described in the previous sections were used to assess the quality of the satellite retrieved $L_{wn}(\lambda)$ values as a function of the four AC approaches (Chapter 2) through a match-up exercise. Match-ups are defined as satellite and field data pairs quasi-coincident in space and time. The selection criteria, used to evaluate the space and time coincidence, greatly influence the number of retained match-ups and their quality. A good match-up configuration should be dependent on the area of interest and the observed water type. Indeed, match-up protocols for water masses highly variable in time and space (e.g., turbid coastal water masses) should be more conservative to ensure contemporaneous satellite-*in situ* observations. In contrast, when the target corresponds to spatially and temporally homogeneous water masses, the selection criteria can be loosed and subsequently ensure a larger number of match-ups. Selection criteria should also be satellite and measurement specific. For instance, the spatial and temporal resolutions of the satellite sensor need to be considered when evaluating the pixel window to determine satellite retrievals, which can range from a single pixel to a full scene.

In the present study, the match-up selection criteria and definition are similar to the approaches described in Bailey and Werdell (2006) and Jamet et al. (2011). For each match-up pair, the median and standard deviation of the MODIS estimated radiometric quantity are calculated over a 3 by 3 pixel window around the station. The median value is preferred to the average value as the former is less sensitive to outliers (although some of these will be excluded with the homogeneity criterion explained hereafter). A 3 by 3 pixels window is used since the MODIS-Aqua images have geolocation accuracy of about 150 m at satellite nadir (Wolfe et al., 2002). A 5 by 5 pixels window, as suggested by the operational OBPG satellite data product validation system (Bailey and Werdell, 2006), is considered here as inappropriately large. Indeed, such a large window is justified for a global validation but over turbid coastal waters it may include diverse water types, especially in regions where high temporal and spatial variability in water masses are observed. Note also that for the MVCO station (see Section 3.2.1.1), the window size was reduced to 2 by 3 pixels to avoid the adjacency effects from nearby land lying only 3 km North of the station (Feng et al., 2008; Jamet et al., 2011).

Prior to data analysis, three exclusion criteria are applied ensuring that the MODIS-Aqua data effectively represent the *in situ* measurements. These are the following:

1. When the time difference between the satellite overpass and the *in situ* measurements exceeds 2 hours, the match-up pair is excluded. If redundant data remain, the match-up with the smallest time difference is retained.
2. Match-up pairs are excluded when in a 3 by 3 pixels window (2 by 3 for the MVCO station) more than 3 pixels are flagged (ensuring a minimum of 6 valid pixels).
3. Spatial homogeneity within the pixel windows is imposed. Match-up pairs presenting MODIS estimated standard deviations in $L_{wn}(547)$ above 20% of the mean value, are excluded.

Additional selection criterion are applied according to the purpose of the study. For the validation of the AC methods for turbid coastal waters (Chapter 4), an additional criterion is used, namely, only the match-up pairs presenting *in situ* $L_{wn}(667)$ above 0.183 mW cm^{-2} μ m^{-1} sr^{-1} are retained. This is done to ensure turbid waters only (Robinson et al., 2003).

Compared to the ± 3 hours temporal coincidence, as suggested by Bailey and Werdell (2006), the time difference of 2 hours between the satellite overpass and *in situ* measurement greatly reduces the number of match-up pairs. However, a small time difference is preferred to ensure that the MODIS estimated $L_{wn}(\lambda)$ actually corresponds to the *in situ* measurements. This is particularly true in coastal regions where variability in water masses is important due to the high tides and rapid currents (e.g., North Sea and English Channel). In the next chapter, the impact of the time interval is briefly investigated by comparing the errors on the satellite retrieved $L_{wn}(\lambda)$ when considering an 1-hour and 3-hour temporal coincidence, respectively.

The homogeneity criterion is applied on $L_{wn}(547)$ (as done by, e.g., Zibordi et al. (2009a); Mélin et al. (2011)) rather than on $\tau(869)$ (as done by Bailey and Wang (2001); Feng et al. (2008); Jamet et al. (2011)), because the former is more restrictive. The spatial variability in $L_{wn}(\lambda)$ is indeed much shorter compared to the spatial variability in atmospheric composition, particularly in turbid waters (Schroeder et al., 2007; Feng et al., 2008). Moreover, Zibordi et al. (2009a) positively tested the appropriateness of the 20% spatial homogeneity criterion at $L_{wn}(547)$. For the intercomparison study described in Chapter 4, the appropriateness of this homogeneity criterion is tested by comparing the selected and excluded match-up pairs when using the homogeneity criterion on $L_{wn}(547)$ and $\tau(869)$.

- Chapter 4 -

Validation and inter-comparison of four turbid water AC methods

In this chapter, four commonly used MODIS Aqua AC methods, developed for turbid coastal waters, are evaluated and compared: (1) the NASA official algorithm (Stumpf et al., 2003; Bailey et al., 2010) (referred to as 'STD'), (2) a GW94-based algorithm assuming spatial homogeneity of the atmosphere in the NIR spectral region over the region of interest and a universal constant NIR water-leaving reflectance ratio (i.e., the NIR similarity assumption) (Ruddick et al., 2000) (referred to as 'MUMM' and as 'SIMIL' by Goyens et al. (2013c)), (3) a NIR-based algorithm using the Short-Wave-Infra-Red (SWIR) bands in very turbid waters (Wang et al., 2009) (referred to as 'NIR-SWIR') and (4) a direct inversion approach using a neural network to invert the top of atmosphere signal in $L_{wn}(\lambda)$ (Schroeder et al., 2007) (referred to as 'NN'). These AC methods have been detailed previously in the second chapter of this manuscript.

Several studies already investigated the performance of these AC approaches. The standard MODIS Aqua products, for instance, have been validated by numerous authors with AERONET-OC data (e.g., Zibordi et al., 2004b, 2006a; Mélin et al., 2007; Feng et al., 2008; Zibordi et al., 2009b; Mélin et al., 2011, 2013). A systematic validation exercise is also performed by the NASA OBPG to measure the quality of the STD AC approach (Franz et al., 2005, 2012). Overall, MODIS Aqua satellite data, processed with the STD AC algorithm, are in good agreement with the *in situ* data. However, large errors and uncertainties are still observed, in particular in the blue and red bands and in complex coastal waters where algal and non-algal particles tend to increase the backscattering in the NIR and the absorption in the blue. This latter results in a reduced water signal in the blue and consequently increases the sensitivity of the retrieved signal to instrumental noise, calibration errors and AC inaccuracies (Franz et al., 2012). Improvements in the satellite retrieved aerosol products with the STD AC algorithms were however observed since the bio-optical model has been revised (Bailey et al., 2010) and the aerosol models updated (Ahmad et al., 2010) (Mélin et al., 2013).

Wang and Shi (2007) tested the performance of the NIR-SWIR AC algorithm for two case studies along the U.S. and China east coast and concluded that this algorithm improved the MODIS-derived ocean colour products in both offshore and near-shore turbid waters, compared to the STD AC algorithm. Similar conclusions were made by Wang et al. (2009) who further evaluated the NIR-SWIR AC algorithm based on a large set of *in situ* data provided by the SeaWiFS Bio-optical Archive and Storage System (SeaBASS) (Werdell and Bailey, 2005). The performance of the NIR-SWIR AC algorithm was also investigated by Werdell et al. (2010). Based on a validation exercise in the turbid waters of the Chesapeake Bay, the authors observed similar performances for the STD and NIR-SWIR AC algorithms. However, the authors found a larger number of negative $L_{wn}(\lambda)$ retrievals with the NIR-SWIR AC algorithm compared to the STD AC algorithm. This suggests, as previously observed by Shi and Wang (2009), that the black pixel assumption is not always valid in the SWIR spectral domain. Similarly, Dogliotti et al. (2011) observed an overestimation of the aerosol reflectance in the most turbid waters of La Plata River estuary when the MODIS Aqua SWIR bands were used for the AC, leading to an underestimation of the water signal. Werdell et al. (2010) also observed that the distribution of the differences between *in situ* and SWIR satellite retrieved $L_{wn}(\lambda)$ was flatter compared to the differences between *in situ* and STD retrieved $L_{wn}(\lambda)$. The authors explained this by the lower signal-to-noise ratio of the SWIR bands resulting in more uncertainty in $L_{wn}(\lambda)$. Consequently, and as suggested by Wang et al. (2009), for future ocean colour satellite sensors the sensor signal-to-noise performance for the SWIR bands should be improved.

The MUMM algorithm was successfully applied to MERIS and MODIS images to retrieve, among others, satellite retrieved Chl_a concentrations (Moses et al., 2009). This AC algorithm was also adjusted to be used for the geostationary SEVIRI meteorological sensor to retrieve SPM concentrations in the North Sea English Channel (Neukermans et al., 2009). However, as demonstrated by Ruddick et al. (2006) and Doron et al. (2011), the assumption of the NIR similarity spectrum is not universally valid.

The NN AC algorithm was initially developed for the AC of MERIS and validated by Schroeder et al. (2007) with *in situ* $\rho_w(\lambda)$ data taken in the North Sea and AERONET data for $\tau(\lambda)$. A good agreement was observed between the *in situ* and satellite data and this approach also resulted in significant improvement in the blue spectral region compared to the default AC algorithm of MERIS (Aiken and Moore, 2000). However, the NN algorithm has never been validated when applied to MODIS Aqua images. This is done in the present chapter.

Most studies regionally validated the turbid water AC algorithms with *in situ* data or compared their performances against the standard AC algorithm. However, with the aim to improve AC methods, it is essential to gain insight in their relative performances and limitations and, subsequently, to conduct a global validation and inter-comparison exercise. Studies of this kind were conducted by Banzon et al. (2009) and Jamet et al. (2011) for SeaWiFS AC approaches. Banzon et al. (2009) compared the performance of the STD AC algorithm with the performance of a multi-spectral matching (Gordon et al., 1997) and a optimization (Kuchinke et al., 2009a) approach-based AC method (SMA and SOA, respectively), with the aim to develop a dust-correction algorithm. The authors concluded that the SMA performed better then the STD AC algorithm, only when absorbing dust was the dominant atmospheric aerosol. Jamet et al. (2011) used AERONET-OC data to evaluate the STD, MUMM and SOA AC algorithm (Kuchinke et al., 2009a). The authors concluded that the performance of the MUMM AC algorithm was highly dependent on the aerosol reflectance ratio retrieved from the neighbouring clear water pixels (i.e., $\epsilon(\lambda_1, \lambda_2)$). According to their results, the STD AC algorithm provided the best retrievals.

The study presented here and published by Goyens et al. (2013c), is a complementary work to the study of Jamet et al. (2011) but focusses on the MODIS Aqua ocean colour products. Based on a similar match-up exercise, the four MODIS Aqua AC algorithms (i.e., STD, MUMM, NIR-SWIR and NN-based AC algorithms) are validated and compared with a global dataset of *in situ* $L_{wn}(\lambda)$ data (from the AERONET-OC network and collected during sea campaigns conducted by the LOG, see Section 3.2.1.1 and 3.2.2.1, respectively). The performance of the algorithms is also investigated as a function of the water type. Therefore, optical water types are allocated to each *in situ* $L_{wn}(\lambda)$ spectrum according to the classification method of Vantrepotte et al. (2012) (Section 1.5).

The following section summarizes the paper of Goyens et al. (2013c) including the most important results. Next, in Sections 4.2.1 and 4.2.2, complementary results are presented. In the former section, the performance of the algorithms is evaluated when considering all the valid match-up pairs. Indeed, the inter-comparison study presented in the paper of Goyens et al. (2013c) only included match-up pairs for which valid ocean colour products were retrieved for the four AC algorithms. In Section 4.2.1, the AC algorithms are compared including all valid match-ups.

As suggested by Vantrepotte et al. (2012), a potential application of class-based approaches is the use of optical water type specific inversion algorithms for the retrieval of biogeochemical parameters (e.g., SPM and Chl_a concentrations). It is thus essential that AC algorithms correctly retrieve the optical water type. Therefore a complementary study is conducted consisting in comparing the derived water optical class, once when based on the MODIS Aqua $L_{wn}(\lambda)$ spectra and, when using the *in situ* $L_{wn}(\lambda)$ values. These results are discussed in Section 4.2.2.

A general conclusion on the inter-comparison exercise is given in Section 4.3 and the paper of Goyens et al. (2013c) is attached in Section 4.4.

4.1 PAPER SUMMARY: "EVALUATION OF FOUR ATMOSPHERIC CORRECTION ALGORITHMS FOR MODIS AQUA IMAGES OVER CONTRASTED COASTAL WATERS"

C. Goyens, C. Jamet and T. Schroeder, published in *Remote Sensing of Environment*, 131, 63-75 (2013)

The STD, MUMM, NIR-SWIR and NN AC methods are evaluated and compared based on coastal AERONET-OC data (Section 3.2.1.1) and data collected during research campaigns conducted by the LOG (Section 3.2.2.1). *In situ* and satellite visible and near infra-red spectral bands $L_{wn}(\lambda)$ are retrieved (i.e., $L_{wn}(\lambda)$ at 412, 443, 488, 531, 547 and 667 nm) as well as the aerosol optical thickness, $\tau(869)$. For the GW94-based AC algorithms (i.e., the STD, MUMM and NIR-SWIR AC algorithms), the Ångström coefficient, $\alpha(531, 869)$, is also compared.

A total of 1973 satellite images coincident in time with the *in situ* data were processed, 838 of which were considered as turbid (Robinson et al., 2003). Next, the selection criteria described in Section 3.3 were applied selecting temporally and spatially coincident *in situ*-satellite match-up pairs. With the NN AC algorithm, match-ups may also be prone to an additional flag when either the top of atmosphere, the geometry or the surface pressure are out of range according to the simulated dataset, used for the neural-network inversion method (referred to as the NN-flag). This latter has an important impact on the number of retrieved match-ups. Indeed, 133 match-up pairs were excluded for further processing because of this selection criterion. The exclusion of these data may favour the NN AC algorithm compared to the other AC methods (explaining the interest of the complementary results comparing the algorithms when including all valid match-up pairs).

The NN AC algorithm showed the lowest coverage with only 14% of match-up pairs followed by the SWIR AC algorithm with 16%. The STD and the MUMM AC algorithms retrieved 18% and 20% match-ups, respectively. The STD AC algorithm was more subjected to atmospheric correction failure (due, for instance, to erroneous Chl_a concentration retrievals within the bio-optical model). The NN AC algorithm presented the disadvantage of being constructed by training and, subsequently, to be limited by the range of the simulated dataset. The NIR-SWIR AC algorithm was more affected by the spatial homogeneity criterion compared to the other algorithms, due to abrupt switches between the STD and SWIR aerosol selection method. For cross comparison, only the match-up pairs presenting valid ocean colour products for the four algorithms were retained, reducing the number of total match-ups to 211.

According to the results, a relatively good agreement exists between estimated MODIS Aqua and observed *in situ* $L_{wn}(\lambda)$ retrievals, in particular in the green spectral domain at 488 and 547 nm with the GW94-based algorithms (RE < 20% and bias ranging from -4 to 1%). However, negative $L_{wn}(\lambda)$ values were retrieved in the blue spectral domain (at 412 and 443 nm) where approximately 60% of the MODIS retrieved $L_{wn}(\lambda)$ were underestimated with the MUMM and STD algorithms, 57% with the NIR-SWIR algorithm and 45% with the NN algorithm.

Overall, the NN AC algorithm performed well when the GW94-based AC algorithms failed, notably, in the blue and red spectral domain at 412 and 667 nm, while higher $L_{wn}(\lambda)$ signals, observed mainly in the green region of the spectrum, tended to be better predicted by the GW94-based algorithms. This fact is explained by the logarithmic cost function used to minimize the error when training the NN algorithm and which tends to lessen the error proportional to the $L_{wn}(\lambda)$ signal.

The performance of the AC algorithms to retrieve the aerosol products is not as good compared to the statistics for $L_{wn}(\lambda)$. For $\alpha(531, 869)$, RE varied between 44% and 52% and biases between 6 and 9%. For $\tau(869)$, RE ranged between 72 and 154% and biases ranged from 47 to 109%. The aerosol product retrievals were the least accurate with the NN algorithm and the most accurate with the NIR-SWIR algorithm. In contrast to the GW94-based AC algorithms, the aerosol products are not used as input with the NN algorithm and the correction method is only based on $L_{wn}(\lambda)$. Accordingly, high aerosol loads did not have any impact on the retrieval errors in $L_{wn}(\lambda)$ with this AC algorithm, while with the GW94-based algorithms high aerosol loads resulted in an underestimation of $L_{wn}(\lambda)$ in the blue spectral domain.

Beside a global evaluation, the AC methods were also evaluated as a function of the water type which is particularly relevant to gain insight in the applicability and limitations of the AC approaches. Therefore, *in situ* data are assigned to different optical water types according to the classification scheme of Vantrepotte et al. (2012). Out of the 211 *in situ* spectra, two spectra remained unclassified, 9 spectra were assigned to the first class (water optical properties mainly determined by detrital and mineral material), 135 to the second class (water masses optically dominated by phytoplankton) and 65 to the fourth class (water masses optically dominated by high concentrations of CDOM and phytoplankton). None of our match-up pairs were assigned to Class 3 (water masses optically influenced by high loads of particulate matter mainly from mineral origin). Indeed, such water masses are often flagged due to sensor saturation in the NIR spectral region or because the high NIR scattering triggers the erroneous allocation of a cloud flag.

The NN AC algorithm showed the best performance for Class 1 waters (RE and bias ranging from 16% to 27%, and from -7% to 5%, respectively), followed by the MUMM AC algorithm (RE and bias ranging from 20% to 43%, and from -42% to -19%, respectively). However, compared to the other AC methods, the latter did not performed as well over the other water classes. Indeed, based on the *in situ* data and the class-specific linear correlation coefficients between $L_{wn}(\lambda_{NIR})$ in the NIR spectral domain, we found that the NIR similarity spectrum assumption, used by the MUMM algorithm to model $L_{wn}(\lambda_{NIR})$, was valid for class 1 waters but less for the others. For the Class 2 water masses, the STD AC algorithm showed the best $L_{wn}(\lambda)$ retrievals (RE and bias ranging from 9% to 24%, and from -8% to -3%, respectively). This may be explained by the fact that the bio-optical model used in the STD AC algorithm was developed based on data provided from oligothrophic to mesotrophic waters (i.e., NOMAD dataset). The STD AC algorithm also showed the most satisfying results for Class 4 waters.

Overall, the study demonstrated that STD AC algorithm showed the best performance except for the water masses optically determined by detrital and mineral material (Class 1). The MUMM AC algorithm was affected by the non-validity of the constant NIR reflectance ratio and/or the absence of clear water pixels in the sub-scene of the image to retrieve $\epsilon(\lambda_1, \lambda_2)$. The NN AC algorithm presented significantly better results where the GW94-based algorithms failed (i.e., in the blue and red part of the spectrum) but appeared to be highly dependent on the training dataset. For this validation exercise the STD and NIR-SWIR AC algorithms did not show significant differences in terms of $L_{wn}(\lambda)$ retrieval performances, but the NIR-SWIR AC algorithm was more affected by the homogeneity selection criterion reducing the number of retrieved match-up pairs relative to the STD AC algorithm.

4.2 Complementary Results

4.2.1 Inter-comparison of MODIS Aqua retrieved $L_{wn}(\lambda)$ when including all valid match-up pairs

As noticed previously, when the AC methods are evaluated based on the 211 common match-ups only, the NN AC algorithm may be favoured because the restrictive NN-flag selection criteria is also applied on the three other AC algorithms. Here, a complementary evaluation exercise is conducted with all the valid match-up pairs for each AC algorithm.

When considering all valid match-ups, the MUMM AC algorithm still presented the largest number of retrieved match-up pairs which is a significant advantage to ensure a broader spatial coverage (Table 4.1). However, the MUMM algorithm also retrieved the largest number of negative $L_{wn}(\lambda)$ values, mainly in the blue spectral domain (8%, 2% and 1% at 412, 443 and 667 nm, respectively, while the other AC methods retrieved less than 4% negative $L_{wn}(\lambda)$ values). Most valid match-up pairs excluded by the NN-flagged selection criteria concern water masses optically dominated by phytoplankton (Class 2) or dominated by CDOM and phytoplankton blooms (Class 4) (Table 4.1).

In contrast to the observations of Werdell et al. (2010), the NIR-SWIR AC algorithm does not show more negative $L_{wn}(\lambda)$ retrievals compared to the STD AC algorithm (Table 4.1) and performances of the two algorithms remain similar. The present *in situ* data may not be turbid enough to significantly differentiate the two algorithms.

Table 4.1: *Total number of retrieved valid match-ups, percentage of negative retrieved $L_{wn}(\lambda)$ at 412, 443 and 667 nm, number of match-up pairs retrieved for each class.*

	Total	$L_{wn}(412) < 0(\%)$	$L_{wn}(443) < 0(\%)$	$L_{wn}(667) < 0(\%)$	Class 1	Class 2	Class 4
MUMM	386	8	2	1	12	232	133
NN	282	-	-	-	10	177	90
STD	364	3	0	1	13	214	127
NIR-SWIR	324	2	0	1	13	205	99

Figure 4.1 shows the statistical performance of the algorithms as a function of wavelength (percentage relative error, RE, root mean square error, RMSE, and percentage bias) when considering only the 211 match-up pairs and when considering all valid match-up pairs. The overall relative performance of the algorithms remains approximately the same. Larger errors are encountered in the blue spectral region with the GW94-based algorithms (RE > 40% at 412 nm), while for the NN AC method larger errors are encountered in the green spectral region (RE of 27% at 488 nm), and all AC approaches systematically underestimate red $\rho_w(\lambda)$ (negative bias ranging from -32% to -15%). Note however that the additional match-up pairs retrieved with the MUMM and STD AC algorithms result in an increase in relative errors in the blue spectral domain (Fig. 4.1). This is mainly due to the larger amount of Class 4 match-ups. These CDOM dominated waters tend indeed to absorb more incoming light in the blue spectral domain and thus often present lower $L_{wn}(\lambda)$ values. These low $L_{wn}(\lambda)$ values increase the sensitivity of the different approaches to AC inaccuracies and, subsequently, result in higher relative errors. When considering only the 211 common valid match-ups, relative errors for Class 4 waters in the blue spectral region are estimated at 45% and 35%, for the MUMM and STD methods, respectively. When considering all valid match-ups, relative errors at 412 nm for Class 4 waters increase up to 60% and 44% for the MUMM and STD methods, respectively. In contrast, the negative bias estimated for the MUMM AC method approaches 0% when considering all valid match-ups (-11% and 2%). Indeed, with the larger number of match-ups, the AC method tend to both over- and underestimate $\rho_w(\lambda)$ such that the overall bias approximates 0%. In contrast, RMSE estimations remain very similar (Fig. 4.1). Hence, apart from these small changes in

RE and bias in the blue spectral region, observations and conclusions made in the paper when considering only the 211 common match-ups, can be considered as exact when considering all valid match-up pairs.

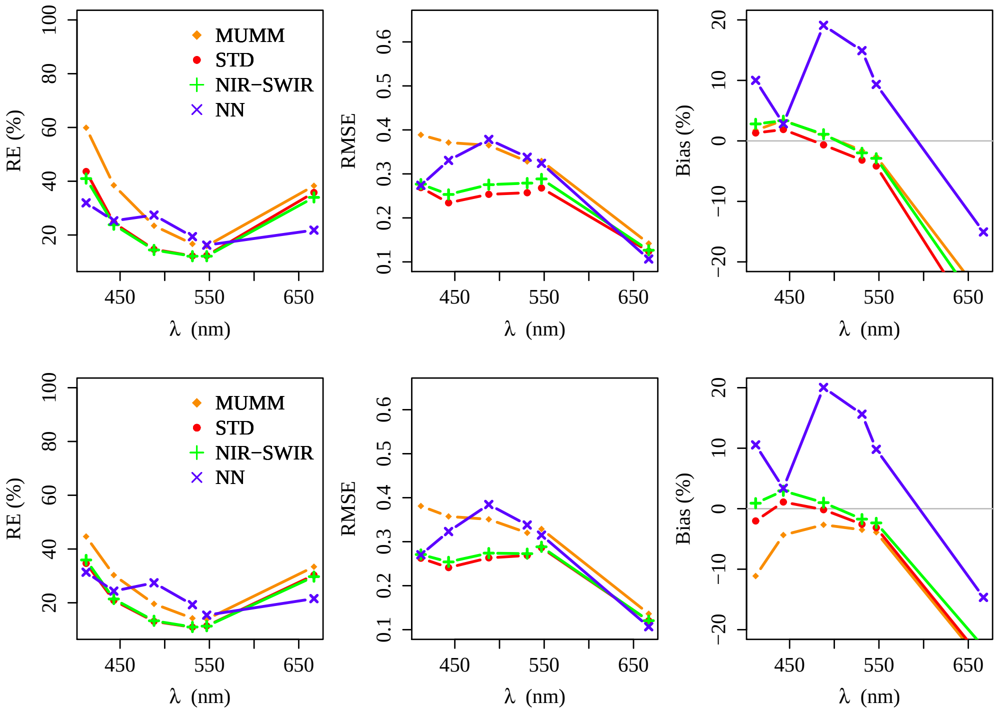

Figure 4.1: *RMSE (*$\mathrm{mW\ cm^{-2}\ \mu m^{-1}\ sr^{-1}}$*), biases (%) and RE (%) per algorithm as a function of wavelength when considering the 211 common match-ups (first row) and when considering all valid match-ups for each algorithm (second row).*

4.2.2 Assessment of optical water class from MODIS Aqua retrieved $L_{wn}(\lambda)$ spectra

A priori knowledge of the optical water type may improve the retrieval of satellite bio-geochemical parameters as it will ease the selection of the appropriate water type specific inversion model (Vantrepotte et al., 2012). It is thus essential to correctly estimate the optical water class from the satellite retrieved $L_{wn}(\lambda)$ spectra which are function of the AC method. In this complementary study, the retrieved optical water classes are compared when estimated based on the satellite and *in situ* $L_{wn}(\lambda)$ spectra.

The MODIS Aqua retrieved $L_{wn}(\lambda)$ spectra normalized by the area below the curve are classified using the same approach as used in the paper of Goyens et al. (2013c) to classify the *in situ* $L_{wn}(\lambda)$ spectra (i.e., the novelty detection method as described in D'Alimonte et al. (2003); Mélin et al. (2011); Vantrepotte et al. (2012)).

Table 4.2 shows the percentage of correctly and erroneously retrieved spectra per algorithm. The percentage given between brackets indicates the percentage when considering only the 211 match-ups. The largest percentage of correctly classified $L_{wn}(\lambda)$ spectra for Class 1 is observed with the MUMM AC approach, with 17% and 22% well classified pixels when considering all and only the 211 common match-up pairs, respectively. With the other AC methods, none of the Class 1 spectra were correctly classified (note however that the number of *in situ* spectra assigned to Class 1 is relatively small, i.e., 9). For Class 2 waters, the four AC methods showed similar percentages (~ 70-80%), while for Class 4 waters, the NN AC approach retrieved the highest percentage of well classified spectra followed by the NIR-SWIR AC approach.

Table 4.2: *Percentage of spectra per class when classified based on MODIS Aqua $L_{wn}(\lambda)$ spectra and when classified based on in situ data. Numbers between brackets indicate the percentage when considering only the 211 common match-up pairs. Numbers in bold indicate the percentage of well classified spectra.*

		In situ		
		Class 1	Class 2	Class 4
NN	Unclass.	0(0)	3(1)	3(3)
	Class 1	**0(0)**	0(0)	0(0)
	Class 2	40(44)	**76(78)**	15(12)
	Class 3	0(0)	0(0)	0(0)
	Class 4	60(56)	21(21)	**82(85)**
MUMM	Unclass.	42(34)	27(18)	54(46)
	Class 1	**17(22)**	0(0)	2(2)
	Class 2	16(11)	**71(80)**	17(15)
	Class 3	0(0)	0(0)	0(0)
	Class 4	25(33)	2(2)	**27(37)**
STD	Unclass.	39(33)	28(14)	44(28)
	Class 1	**0(0)**	0(0)	2(1)
	Class 2	15(11)	**70(83)**	8(14)
	Class 3	0(0)	0(0)	0(0)
	Class 4	46(56)	2(3)	**46(37)**
NIR-SWIR	Unclass.	39(33)	25(14)	34(26)
	Class 1	**0(0)**	0(0)	1(0)
	Class 2	15(11)	**73(83)**	11(16)
	Class 3	0(0)	0(0)	0(0)
	Class 4	46(56)	2(3)	**54(58)**

According to Goyens et al. (2013c), the STD AC algorithm provided overall the best performances. However, the results shown in Table 4.2, indicate that the STD algorithm resulted in a lower percentage of correctly retrieved Class 4 water masses (46% and 37% when considering all and only the 211 common match-up pairs, respectively) compared to the NIR-SWIR and NN AC methods (54-58% and 82-85%, respectively) and did not correctly classify Class 1 spectra. This suggests that the STD algorithm retrieves relatively accurate $L_{wn}(\lambda)$ values at certain wavelengths but does not correctly retrieve the shape of the spectra (reflecting the optical water type (Lubac and Loisel, 2007; Vantrepotte et al., 2012)). Note however that these results are dependent on the set of spectral bands used for the classification. In the present work, the classification of the *in situ* and MODIS Aqua $L_{wn}(\lambda)$ spectra is based the spectral bands at 443, 488, 547 and 667 nm. As shown in Fig. 4.1 and outlined in the paper of Goyens et al. (2013c), the STD AC algorithm greatly underestimates $L_{wn}(\lambda)$ in the red spectral domain. Hence, misclassification with this algorithm may be due to the erroneously retrieved $L_{wn}(667)$ while it could be more successful if the classification scheme used another set of spectral bands. Hence, further research may be needed to evaluate if the classification scheme should be function of the AC method in order to ensure the most appropriate optical water type classification.

4.3 CONCLUSION

Four AC algorithms, all based on distinctive assumptions, have been selected and compared; the GW94-based STD, MUMM and NIR-SWIR AC methods, and the NN algorithm. Satellite retrieved ocean colour products were compared with spatially and temporally coincident *in situ* $L_{wn}(\lambda)$ spectra from contrasted coastal waters from the global AERONET-OC network and collected during sea campaigns conducted by the LOG (Sections 3.2.1.1 and 3.2.2.1, respectively).

The different AC methods were evaluated based on the number of retrieved match-up pairs, on their overall performances to retrieve $L_{wn}(\lambda)$ (when considering all valid match-up pairs and when retaining only the match-up pairs for which valid retrievals were encountered for the four algorithms, reducing the number of 211 'algorithm-equivalent' match-ups) and on their class-specific performances. For the latter, *in situ* and MODIS Aqua retrieved $L_{wn}(\lambda)$ spectra were classified according to the classification scheme of Vantrepotte et al. (2012) (Section 1.5).

Overall, the AC algorithms performed relatively well with RE errors ranging from 11% to 45% and biases from -25% to 16%. The MUMM AC algorithm showed the largest percentage of spatial coverage with approximately 10%, 20% and 30% more valid match-ups pairs compared to the STD, NIR-SWIR and NN AC algorithms, respectively. For water masses optically dominated by detrital and mineral material, this algorithm also provided relatively good $L_{wn}(\lambda)$ retrievals compared to the other GW94-based algorithms. However, in most cases it tended to greatly underestimate $L_{wn}(\lambda)$, in particular in water masses optically dominated by phytoplankton and/or CDOM (bias of -18% and -24% at 412 and 667 nm, respectively), where the NIR similarity spectrum assumption may not be verified. Therefore, the MUMM AC algorithm may be further improved by extending the NIR reflectance function to all water types.

The NN AC approach presented good results compared to the GW94-based methods, and in particular in the blue and red spectral domains (biases of 10%, 3% and -15%, and RE of 30%, 25% and 21% at 412, 443 and 667 mm, respectively). Moreover, when compared to the $L_{wn}(\lambda)$ spectra retrieved with the GW94-based AC methods, more spectra processed with this AC method were well classified (according to the classification scheme of Vantrepotte et al. (2012)). In contrast, in the green spectral region, the NN algorithm tended to greatly overestimate $L_{wn}(\lambda)$, especially for Class 4 waters (biases up to 40% at 488 nm). These larger errors encountered in the green bands were related to the logarithmic cost function, used for the minimization of the errors when training the neural network and resulting in errors proportional to the $L_{wn}(\lambda)$ signal. According to the number of retrieved valid match-ups, the largest drawback of this algorithm appeared to be its sensitivity to the training dataset used for the development of the neural-network inversion method. Therefore, the NN AC algorithm may be further improved by expanding the training dataset with more diverse water types.

For this evaluation study, the NIR-SWIR AC algorithm did not show significant improvements compared to the STD AC algorithm. Indeed, the STD algorithm provided slightly better $L_{wn}(\lambda)$ retrievals. Moreover, with the NIR-SWIR AC algorithm, the number of valid match-ups was slightly lower due to an increase in spatial heterogeneity in $L_{wn}(\lambda)$, probably resulting from the abrupt switch between the NIR and SWIR aerosol model selection approaches.

According to the class-specific evaluation, the NIR-modelling scheme within the STD AC algorithm should be improved to account for more turbid water masses mainly dominated by detrital and mineral material. Indeed, the bio-optical model relies on Chl_a concentration estimations to retrieve red absorption and backscattering coefficients and, subsequently, $L_{wn}(NIR)$. However, relying solely on Chl_a estimations may be inappropriate, in particular in mineral and detrital sediment rich waters. Hence, the NIR-modelling scheme may be revised or updated to account for more diverse water types.

Results from the present study provided a comprehensive description of the limitations and performances of the algorithms, useful to further improve satellite retrieved ocean colour products.

4.4 PAPER: "EVALUATION OF FOUR ATMOSPHERIC CORRECTION ALGORITHMS FOR MODIS AQUA IMAGES OVER CONTRASTED COASTAL WATERS"

C. Goyens, C. Jamet and T. Schroeder, published in *Remote Sensing of Environment* (131), 63-75 (2013).

Remote Sensing of Environment 131 (2013) 63–75

Contents lists available at SciVerse ScienceDirect

Remote Sensing of Environment

journal homepage: www.elsevier.com/locate/rse

Evaluation of four atmospheric correction algorithms for MODIS-Aqua images over contrasted coastal waters

C. Goyens [a], C. Jamet [a,*], T. Schroeder [b]

[a] CNRS, UMR 8187, Univ Lille Nord de France, ULCO, LOG, F-62930 Wimereux, France
[b] CSIRO Land and Water, 41 Boggo Road, Brisbane, QLD 4102, Australia

ARTICLE INFO

Article history:
Received 25 July 2012
Received in revised form 30 October 2012
Accepted 4 December 2012
Available online xxxx

Keywords:
MODIS-Aqua
Ocean color
Atmospheric correction
Turbid water
Validation
Classification

ABSTRACT

The use of satellites to monitor the color of the ocean requires effective removal of the atmospheric signal. This can be performed by extrapolating the aerosol optical properties to the visible from the near-infra-red (NIR) spectral region assuming that seawater is totally absorbent in this latter part of the spectrum, the so-called black pixel assumption. While this assumption is verified for most phytoplankton dominated waters, it is invalid in turbid waters. Consequently, for the past ten years, several algorithms have been developed on alternative assumptions. Studies comparing these algorithms are of great interest for further improvement in water leaving radiance ($L_w(\lambda)$) retrievals from satellite images explaining the focus of the present research. Four published atmospheric correction algorithms for MODIS-Aqua are compared: (1) the standard NIR algorithm of NASA, (2) the NIR similarity spectrum algorithm, (3) the NIR-SWIR algorithm and (4) an Artificial Neural Network algorithm. The MODIS-Aqua estimated normalized $L_w(\lambda)$ are validated with AERONET-Ocean Color data and cruise measurements presenting moderately to highly turbid waters. Based on a match-up exercise, the former three algorithms show the best results in the green region of the spectrum (relative error, RE, between 11 and 20%) and the largest errors in the blue and red region of the spectrum (RE exceeding 30%). In contrast, the Artificial Neural Network algorithm performs better in the red band (RE of 22%). The latter tends to overestimate the normalized $L_w(\lambda)$ at all wavelengths while the NIR similarity spectrum algorithm tends to underestimate it. Retrievals of aerosol products, such as the Ångström coefficient, $\alpha(531,869)$, and the optical thickness, $\tau(869)$, present RE above 44% and 72%, respectively.

The performance of the algorithms is also investigated as a function of water types. For water masses mainly dominated by phytoplankton, the standard NIR algorithm performs better. In contrast, for water masses mainly dominated by detrital and mineral material, the neural network-based algorithm shows the best results. The largest errors are encountered above water masses dominated by high phytoplankton and CDOM concentrations. This work conducted to a number of perspectives for improving the atmospheric correction algorithms.

1. Introduction

With their broad spatial coverage and fine temporal resolutions, satellite remote sensing data represent a crucial tool for monitoring large areas of oceans. The remote sensing of ocean color radiometry, defined as the spectrum of the up-welling light from the sea (Gordon, 1987), allows to investigate the bio-optical properties of the seawater. These are then used as proxies for various geophysical parameters (e.g., concentrations of chlorophyll-a, Chl-a, and suspended particulate matter, SPM). The first satellite dedicated for ocean color research, the Coastal Zone Color Scanner (CZCS), was launched in 1978 and operated till 1986. Eleven years later the Sea-Viewing Wide Field of View Sensor (SeaWiFS) was launched followed by the Moderate Resolution Imaging Spectroradiometer (MODIS-Aqua) and the Medium Resolution Imaging Spectroradiometer (MERIS), both launched in 2002. SeaWiFS and MERIS have been operable until December 2010 and April 2012, respectively.

Since the launch of the CZCS, improvements in radiometric and spectral performances and in the reliability of ocean color products have been impressive. Nevertheless, processing satellite ocean color data remains a challenging task. This includes, among others, the effective removal of the contribution of the atmosphere to the signal measured by the satellite, the so-called atmospheric correction process. In clear open ocean waters, for which the optical properties are mainly driven by phytoplankton and co-varying biological constituents, it is assumed that seawater absorbs all the light in the red and near-infrared (NIR) region of the spectrum, referred as the black-pixel assumption (Gordon & Wang, 1994, thereafter named GW94). This allows to estimate the contribution of the atmosphere and subsequently the light scattered by the water column and measured by the satellite, known as the water-leaving reflectance, $\rho_w(\lambda)$. While the black-pixel assumption is verified in clear ocean waters, it induces significant errors when applied in turbid waters. The latter are indeed optically more complex due to the backscattering

---

[*] Corresponding author. Tel.: +33 3 21 99 64 22.
E-mail address: cedric.jamet@univ-littoral.fr (C. Jamet).

0034-4257/$ – see front matter © 2012 Elsevier Inc. All rights reserved.
http://dx.doi.org/10.1016/j.rse.2012.12.006

and absorption of Colored Dissolved Organic Matter (CDOM) and non-algal particles (Siegel et al., 2000). Moreover these water masses present high spatial and temporal variability. Consequently, global parametrizations are less applicable (e.g., Loisel et al., 2010; Werdell et al., 2007) and significant errors remain in retrieving geophysical parameters and water properties from satellite remote sensing (e.g., Zibordi et al., 2009a, 2009b). Numerous algorithms have been developed with alternative hypotheses taking into account non-negligible NIR ocean contribution to the measured signal. A global validation of these algorithms is required in order to gain insight in their performances and limitations and to aid movement towards improvements. To our knowledge, several studies already compared the performances of new developed algorithms against the standard atmospheric correction algorithms (e.g., Kuchinke et al., 2009; Ruddick et al., 2000; Schroeder et al., 2007; Wang & Shi, 2007; Wang et al., 2009; Werdell et al., 2010). However only few studies (Jamet et al., 2011) have tackled a round-robin evaluation of all available atmospheric correction algorithms. This is the focus of the present research. It is a complementary work to the study of Jamet et al. (2011) who evaluated, based on a similar match-up exercise, three SeaWiFS atmospheric correction algorithms.

MODIS-Aqua images processed with four commonly used atmospheric correction algorithms are compared with coastal in-situ data. The four algorithms are (1) the NASA official algorithm based on an iterative procedure and a bio-optical model (Bailey et al., 2010; Stumpf et al., 2003) (referred later as 'STD'), (2) a GW94-based algorithm assuming spatial homogeneity of the atmosphere and ocean over the region of interest in the NIR (Ruddick et al., 2000) (referred later as 'SIMIL'), (3) a NIR-based algorithm using the Short-Wave-Infra-Red (SWIR) bands in very turbid waters (Wang et al., 2009) (referred later as 'NIR-SWIR') and (4) a direct inversion approach using a neural network (Schroeder et al., 2007) (referred later as 'NN'). Besides a global evaluation of the algorithms, the performances of the algorithms are also investigated as a function of water type. This is particularly relevant to gain insight in their applicability and limitations. Therefore, in-situ data are assigned to different classes of water types (Vantrepotte et al., 2012) and an evaluation is made per water type.

The next section describes the different algorithms used in the present research. Data and methods are outlined in Section 3. This section includes an overview of the in-situ and satellite data used for the evaluation, an explanation of the match-up selection and algorithm evaluation criteria, and a brief description of the classification method of Vantrepotte et al. (2012). In Section 4 the evaluation of the algorithms over the entire validation dataset as well as their sensitivities to different water types are outlined and discussed. These results conducted to the definition of some challenges and perspectives for further improvements.

2. Algorithms

The signal measured by the satellite sensor can be decomposed into several terms (Gordon, 1997):

$$\rho_t(\lambda) = \rho_r(\lambda) + \rho_a(\lambda) + \rho_{ra}(\lambda) + t_v(\lambda)\rho_{wc}(\lambda) + T_v(\lambda)\rho_g(\lambda) + t_v(\lambda)\rho_w(\lambda) \quad (1)$$

where $\rho_t(\lambda)$ represents the reflectance measured by the satellite and $\rho_r(\lambda)$, $\rho_a(\lambda)$ and $\rho_{ra}(\lambda)$ the contribution of the atmosphere, notably, the scattered sunlight by air molecules, aerosols and the coupling between both air and aerosol molecules, respectively. $\rho_{wc}(\lambda)$ is the reflectance related to the whitecaps and $\rho_g(\lambda)$ to the glitter. t_v and T_v are the diffuse and direct atmospheric transmittance from sea to sensor, respectively. Ultimately, $\rho_w(\lambda)$ is the water leaving reflectance. Together, $\rho_r(\lambda)$, $\rho_a(\lambda)$ and $\rho_{ra}(\lambda)$ represent about 90% of $\rho_t(\lambda)$. $\rho_g(\lambda)$ and $\rho_{wc}(\lambda)$ can be calculated for a given sun and sensor zenith angle (Cox & Munk, 1954) and an empirical wind speed formulation (Frouin et al., 1996), respectively. During pre-processing $\rho_t(\lambda)$ is corrected for gas absorption, Rayleigh scattering, white-caps and glitter (Gordon, 1997). This term is referred as the Rayleigh corrected reflectance, $\rho_{rc}(\lambda)$:

$$\rho_{rc} = \rho_t(\lambda) - \rho_r(\lambda) - t_v(\lambda)\rho_{wc}(\lambda) - T_v(\lambda)\rho_g(\lambda). \quad (2)$$

In order to ease the comparison of our results with other studies, we focussed on the normalized water-leaving radiance, $L_{wn}(\lambda)$ which is related to $\rho_w(\lambda)$ as follow:

$$L_{wn}(\lambda) = \frac{\rho_w(\lambda) F_0(\lambda) cos\theta_0}{\pi} \quad (3)$$

with F_0 being the extra-terrestrial solar irradiance at a given wavelength λ and θ_0 the sun zenith angle.

2.1. GW94-based algorithm with iterative procedure ('STD')

The STD algorithm, initially developed by Stumpf et al. (2003) and revised by Bailey et al. (2010), uses an iterative method including a bio-optical model allowing to account for the water contribution in the NIR region of the spectrum. The algorithm uses 80 aerosol models developed with observations from the global AERONET network and the radiative transfer code described in Ahmad et al. (2010). First the algorithm assumes $L_{wn}(\lambda)$ being null in the NIR (i.e. black pixel assumption, GW94) allowing to retrieve $L_{wn}(\lambda)$ in the blue and green region of the spectrum. Estimations of L_{wn} at 443, 488 and 547 nm are then used as inputs into the bio-optical model. The latter allows to achieve a first guess in the concentration of Chl-a (MODIS Chl-a OC3 algorithm, O'Reilly et al. (2000)) which in turn allows to determine the particulate backscattering in the NIR, $b_{bp}(NIR)$. Knowing $b_{bp}(NIR)$, it is possible to determine the contribution of the particles to $L_{wn}(NIR)$. The process is then re-iterated with $L_{wn}(NIR)$ equals zero after the modeled reflectance has been removed from $L_{rc}(NIR)$. The iteration process continues until $L_{wn}(NIR)$ converges. The bio-optical model of the STD algorithm contains assumptions that have been derived empirically from the global in-situ NASA bio-Optical Marine Algorithm Data set, NOMAD (Werdell & Bailey, 2005).

2.2. GW94-based algorithm assuming spatial homogeneity of $\rho_w(NIR)$ and $\rho_a(NIR)$ ratios ('SIMIL')

The SIMIL algorithm includes two alternative assumptions, one on the water optical properties, the NIR similarity spectrum assumption, and one on the atmosphere (Ruddick et al., 2000). The first assumption arises from the fact that the sea-water NIR spectrum shape is largely determined by pure water absorption, and hence invariant, while the magnitude of the signal is approximately proportional to the backscatter coefficient. Consequently, the ratio of any two NIR water leaving reflectances, α, is constant. For MODIS-Aqua images α is defined as:

$$\alpha = \frac{\rho_w(748)/t_v(748)}{\rho_w(869)/t_v(869)} = 1.945. \quad (4)$$

The second assumption is based on the fact that the atmosphere composition does not vary significantly in space and therefore the ratio of the aerosol reflectance $\rho_a(\lambda) + \rho_{ra}(\lambda)$, referred as $\epsilon(\lambda_1,\lambda_2)$, can be considered as spatially homogeneous over the area of interest. In clear waters, where $\rho_w(\lambda)$ in the NIR region of the spectrum is close to zero, $\rho_a(\lambda) + \rho_{ra}(\lambda)$ can be approximated by $\rho_{rc}(\lambda)$. Accordingly, over clear water pixels $\epsilon(748,869)$ is calculated as follows:

$$\epsilon_{(748,869)} = \frac{\rho_{rc}(748)}{\rho_{rc}(869)}. \quad (5)$$

Assuming spatial homogeneity of the atmosphere over the area of interest allows to estimate $\epsilon(748{,}869)$ over a clear water sub-scene and to use it for the atmospheric correction of the entire image. A clear water sub-scene is defined as any pixel within the image for which $L_{rc}(\lambda)$ is non-negative and below 0.015 mW $cm^{-2}\mu m^{-1} sr^{-1}$ at 748 and 869 nm.

The SIMIL algorithm is a three-step process. First the atmospheric correction is done with the initial black pixel assumption (i.e. GW94) in order to retrieve the scatter-plot $\rho_{rc}(748)$ versus $\rho_{rc}(869)$ for the region of interest and subsequently to estimate $\epsilon(748{,}869)$ over the clear water sub-scene. Next, using Eqs. (4) and (5), $\rho_a(\lambda)$ is estimated at each wavelength taking into account the non-zero water leaving reflectance and allowing to determine the appropriate aerosol model for the region of interest. Ultimately, the initial atmospheric correction algorithm of GW94 is run again but forced with the previously selected aerosol model.

2.3. GW94-based algorithm using the SWIR bands in very turbid waters (NIR-SWIR)

The NIR-SWIR approach combines the STD algorithm and the GW94 approach using the SWIR bands depending on the turbidity (Wang & Shi, 2007; Wang et al., 2009). This approach assumes that ocean water absorbs strongly in the SWIR part of the spectrum and that the contribution of the in-water constituents remains null. Accordingly, in highly turbid waters, $\rho_w(SWIR)$ can be safely considered as null and the SWIR bands at 1240 and 2130 nm are used instead of the NIR bands for aerosol model selection. Highly turbid waters are defined based on a turbidity index computed from $\rho_{rc}(\lambda)$ at 748 and 1240 nm (Shi & Wang, 2007). For any pixel presenting a turbidity index above 1.05, the SWIR atmospheric correction approach is applied. The refinement of Wang et al. (2009) includes a second turbidity criterion. If, after a first processing with the SWIR aerosol model selection, the estimated $L_{wn}(869)$ is below 0.08 mW $cm^{-2}\mu m^{-1} sr^{-1}$ and the estimated Chl-a value lower or equal to 1 mg l^{-1}, the atmospheric correction is reset to the STD atmospheric correction method. Improvements in the retrievals of $\rho_w(\lambda)$ have been demonstrated when using the SWIR algorithm in extremely turbid waters (e.g., Dogliotti et al., 2011; Wang & Shi, 2007; Wang et al., 2009).

2.4. Direct inversion approach by neural network (‘NN’)

The MODIS NN algorithm used in this study is based on an inverse modeling of extensive radiative transfer (RT) simulations within a coupled ocean-atmosphere system, similar to an approach previously implemented for MERIS (Schroeder et al., 2007). This method directly inverts $\rho_t(\lambda)$ into remote sensing reflectance, $R_{rs}(\lambda)$, defined as:

$$R_{rs}(\lambda) = \frac{\rho_w(\lambda)\cos\theta_0}{\pi}. \tag{6}$$

The direct inversion takes into account the spectral information at each wavelength simultaneously and not only in the NIR region of the spectrum like the previously described algorithms. Consequently, the NN method does not attempt to decouple oceanic and atmospheric signals to perform the atmospheric correction (see Eq. (1)). Another distinct difference is that the forward model parameterization of the NN includes only 8 aerosol models — compared to 80 for the three other algorithms. The RT simulations consist of reflectance data at top of atmosphere (TOA) and at mean sea level (MSL) and cover a large range of oceanic and atmospheric conditions for a variety of different sun and observing geometries. Specifically, the optically active water constituents cover the following concentration ranges: 0.05–50 mg l^{-1} for Chl-a, 0.05–50 g l^{-1} for SPM and 0.001–1 m^{-1} absorption of CDOM at 443 nm. The simulated data were used to adapt the inverse model during a supervised learning procedure. The NN inverse model consists of a multilayer perceptron that learned the functional relationship between TOA and MSL reflectance. More details about the forward model parameterization can be found in (Schroeder et al., 2007). When applied to MODIS data the algorithm requires the TOA reflectance at all ocean color bands as input with further information about the sun and observing geometry as well as the surface pressure. In addition, MODIS Level-2 flags are used to mask pixels affected by land, high glint and clouds. The associated NN outputs consist of MSL R_{rs} at eight MODIS bands up to 748 nm including spectral aerosol optical thickness at four AERONET bands (440, 550, 670 and 870 nm). Additional NN flags are used for further quality control of the outputs that check for out-of-scope conditions compared to the simulated data ranges.

3. Data and methods

3.1. In-situ measurements

The validation is carried out with the AERONET-Ocean Color network (AERONET-OC) data (Zibordi et al., 2006a, 2009b) and field data from 4 cruises coordinated by the Laboratoire d'Océanographie et Géosciences (LOG). The latter includes a large diversity of water types from moderately turbid waters in the North East Atlantic to very turbid waters in the coastal area of French Guiana and North Sea-English Channel. A detailed description of the sampling protocols and instruments are described in Lubac and Loisel (2007) and Nechad et al. (2010) for the North Sea-English Channel dataset and in Loisel et al. (2009) and Vantrepotte et al. (2011) for French Guiana.

AERONET-OC data provides $L_{wn}(\lambda)$ data in the 412–1020 nm spectral range (Zibordi et al., 2009a, 2009b) and the aerosol optical thickness τ from which we retrieved the Ångström coefficient, $\alpha(531{,}869)$. The AERONET-OC data used in the present research were taken at one site located in the Adriatic Sea (AAOT), two in the Baltic Sea (HLT and GDLT) and two along the East Coast of the USA (MVCO and COVE). The deployment sites and the number of observations for each site are given in Table 1. More details about instruments, station properties and particularities can be found in, among others, Berthon and Zibordi (2004), Zibordi et al. (2006b), Mélin et al. (2007), Feng et al. (2008), Zibordi et al. (2009a, 2009b).

3.2. Satellite data

The MODIS-Aqua instrument has been designed with 9 bands in the visible and NIR from 412 to 869 nm as well as with 3 bands in the SWIR (1240, 1640 and 2130 nm). In the present paper, the data analysis focuses on L_{wn} at 412, 443, 488, 531, 547 and 667 nm. The SWIR bands at 1240 and 2130 nm are used for the SWIR aerosol model selection approach in the NIR-SWIR algorithm.

MODIS-Aqua images were processed from L1A to L1B and subsequently from L1B to L2 for the three GW94-based atmospheric correction algorithms using the SeaWiFS Data Analysis System version 6.1 (SeaDAS 6.1, OBPG http://oceancolor.gsfc.nasa.gov/). In contrast to the other algorithms, the NN algorithm does only provide the $R_{rs}(\lambda)$ as output product. Therefore $R_{rs}(\lambda)$ were converted to $L_{wn}(\lambda)$ as described previously in Section 2.4, with F0 being the full band pass extra-terrestrial solar irradiance. Since the $R_{rs}(\lambda)$ outputs from the NN algorithm are not corrected for bi-directional effects, the AERONET-OC data and $L_{wn}(\lambda)$ retrievals from the STD, SIMIL and SWIR algorithms used in this study were not corrected neither. For the GW94-based algorithms, pixels with excessive cloud cover, large solar (>70°) and sensor (>60°) zenith angles, sun glint contamination or where sensors are saturating, were masked out. For the NN algorithm, pixels flagged as cloud and high glint or contaminated by solar and sensor zenith angles above 75.71° and 52.84°, respectively, were not processed.

Table 1
In-situ data location, description and distance from land.

	Lat	Lon	Distance from land (km)	Number of obs.	Period of obs.
AAOT (Adriatic Sea)	43.31° N	12.51° E	15	4348	2002–2007
GDLT (Baltic Proper)	58.59° N	17.467° E	16.5	924	2005–2009
HLT (Gulf of Finland)	59.95° N	24.92° E	22.22	665	2006–2009
MVCO (U.S. Atlantic Coast)	41.32° N	70.57° W	3.7	973	2004–2005
COVE (U.S. Atlantic Coast)	36.90° N	75.71° W	24	450	2006–2009
Belcolor (2009)	51.17–51.92° N	1.36–3.73° W	–	30	2009/06/18–2009/09/15
Belgica (2009)	42.47–51.39° N	9.46° W–2.81° E	–	14	2009/05/30–2009/06/07
French Guiana (2009)	4.15–5.98° N	53.95–51.29° W	–	30	2009/10/12–2009/10/17

Ultimately, as the spectral channels between the MODIS-Aqua images and the in-situ data differ slightly, a linear interpolation is performed to adjust the in-situ channels to the MODIS-Aqua channels.

3.3. Match-up exercise

The match-up exercise was a similar version of the approach described in Bailey and Werdell (2006) and Jamet et al. (2011). For each match-up pair, the median and standard deviation of the MODIS estimated $L_{wn}(\lambda)$, $R_{rs}(\lambda)$, $\alpha(531{,}869)$ and $\tau(869)$ were calculated over a 3 by 3 pixel window around the station. The median value was preferred to the average value as the former was less sensitive to large outliers and the 3 by 3 pixel window was used since the MODIS-Aqua images have geolocation accuracy of about 150 m at satellite nadir (Wolfe et al., 2002). For the MVCO station, the pixel window size was reduced to 2 by 3 allowing to avoid the adjacency effects from nearby land lying only 3 km North of the station (Feng et al., 2008; Jamet et al., 2011). Prior to data analysis, five exclusion criteria were applied ensuring that the MODIS-Aqua data did effectively represent the in-situ measurements. These were the following:

1. When the time difference between the satellite overpass and the in-situ measurement exceeded 2 hours the match-up pair was excluded. If redundant data remained, the match-up with the smallest time difference was retained.
2. Match-up pairs presenting in-situ $L_{wn}(667)$ below 0.183 mW $\mathrm{cm}^{-2}\mu\mathrm{m}^{-1}\mathrm{sr}^{-1}$ were not retained. This threshold coincides with the turbid flag within SeaDAS and thus ensures that turbid waters only were retained (Robinson et al., 2003).
3. Match-up pairs were excluded when in a 3 by 3 pixel window (2 by 3 for the MVCO station) more than 3 pixels were flagged.
4. Spatial homogeneity within the pixel window was imposed. Match-up pairs presenting a MODIS estimated standard deviation for $L_{wn}(547)$ above 20% of the mean value were excluded.
5. For the NN algorithm, match-up pairs were rejected for further processing when flagged as out of scope compared to the simulated data ranges. This flag is raised if either the TOA radiances, the geometry or the surface pressure become out of range.

A time difference of two hours between the satellite overpass and the in-situ measurement greatly reduced the number of match-up pairs. However, a small time difference was preferred since larger time differences do not ensure that the MODIS estimated $L_{wn}(\lambda)$ actually corresponds to the in-situ measurement. This is particularly true in coastal regions where the spatial and temporal variability in water masses is important due to the high tides and rapid currents (e.g. North Sea and English Channel). Therefore, we also investigated the errors on the retrieved $L_{wn}(\lambda)$ when considering only match-ups with less than 1 hour time difference between in-situ and satellite estimated $L_{wn}(\lambda)$.

The homogeneity criterion was applied on $L_{wn}(547)$ (as done by Zibordi et al. (2009a)) rather than on $\tau(869)$ as the former is more restrictive. The spatial variability in $L_{wn}(\lambda)$ is indeed much shorter compared to the spatial variability in atmospheric composition, particularly in turbid waters (Feng et al., 2008; Schroeder et al., 2007). Moreover, Zibordi et al. (2009a) positively tested the appropriateness of the 20% spatial homogeneity criterion at $L_{wn}(547)$. Nevertheless, in order to verify if these observations were valid with our dataset we also calculated the number of excluded match-up pairs when using the homogeneity criterion on $\tau(869)$.

Besides a visual inspection on scatter-plots, the algorithm performance was compared based on six statistical values: the percent bias, the percent relative error (RE), the root mean square error (RMSE), the spearman correlation (R) and the slope and intercept of the linear regression between in-situ data and MODIS $L_{wn}(\lambda)$ estimates. The bias, RE and RMSE are calculated as follows:

$$\mathrm{BIAS} = \frac{1}{N}\sum\left(100\,\frac{L_{wn}^{est}(\lambda) - L_{wn}^{obs}(\lambda)}{L_{wn}^{obs}(\lambda)}\right), \tag{7}$$

$$\mathrm{RE} = \frac{1}{N}\sum\left(100\,\frac{\left|L_{wn}^{est}(\lambda) - L_{wn}^{obs}(\lambda)\right|}{L_{wn}^{obs}(\lambda)}\right), \tag{8}$$

$$\mathrm{RMSE} = \sqrt{\left(\frac{\sum\left(L_{wn}^{est}(\lambda) - L_{wn}^{obs}(\lambda)\right)^2}{N}\right)}, \tag{9}$$

where L_{wn}^{obs} and L_{wn}^{est} are the in-situ and the MODIS estimated $L_{wn}(\lambda)$, respectively, and N is the number of observations.

Table 2
Excluded and total number of match-up pairs per algorithm. Values in parentheses indicate percent values.

	STD	SIMIL	NN	SWIR
Non-turbid	1135 (58)	1135 (58)	1135 (58)	1135 (58)
<6 pixels	860 (44)	862 (44)	922 (47)	880 (45)
Non-uniform (nLw(547))	155 (8)	121 (6)	100 (5)	337 (17)
Non-uniform (τ(869))	111 (6)	107 (5)	149 (8)	111 (6)
Flagged NN	–	–	370 (19)	–
Total	364 (18)	386 (20)	282 (14)	324 (16)

Table 3
Number of match-up pairs per algorithm after data filtration with the exclusion criteria.

	Belcolor	Belgica	Cove	GDLT	French Guiana	HLT	MVCO	AAOT
STD	2	1	23	54	2	25	54	203
NN	4	0	16	30	1	22	45	164
SIMIL	3	1	23	55	2	27	55	220
SWIR	2	1	21	38	2	21	45	194

3.4. Data classification

In order to understand the behavior of the algorithms as a function of the water type, we used a classification scheme developed by Vantrepotte et al. (2012) including four homogeneous optical classes over contrasted coastal areas. Their classification approach is based on a previous study of Lubac and Loisel (2007) and consists to cluster in-situ $L_{wn}(\lambda)$ spectra normalized by the area below the curve. This normalization allows to classify the spectra based on their shape rather than on their magnitude. The former is indeed related to the nature of the optically significant water constituents rather than on their relative concentrations (Lubac et al., 2008; Mélin et al., 2011; Vantrepotte et al., 2012). In summary, Vantrepotte et al. (2012) defined two optically mixed classes of water masses mainly determined by detrital and mineral material (Class 1) or phytoplankton (Class 2), one class presenting water masses optically influenced by high loads of particulate matter mainly from mineral origin (Class 3), and a last class optically impacted by high concentrations of CDOM and phytoplankton (Class 4). More details about the classification approach and classes properties can be found in Vantrepotte et al. (2012).

The in-situ $L_{wn}(\lambda)$ spectra were assigned to one of the four classes based on the novelty detection method as described in D'Alimonte et al. (2003); Mélin et al. (2011); Vantrepotte et al. (2012).

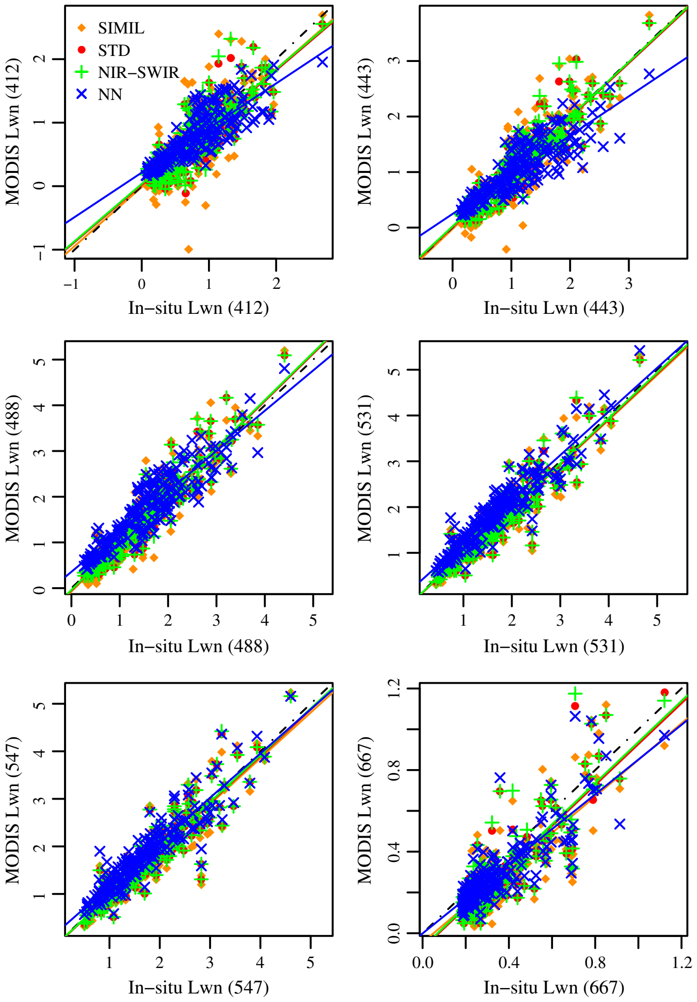

Fig. 1. MODIS-Aqua estimated $L_{wn}(\lambda)$ (mW cm$^{-2}\mu$m^{-1}sr^{-1}) versus in-situ $L_{wn}(\lambda)$ (mW cm$^{-2}\mu$m^{-1}sr^{-1}) at six different wavelengths, 412, 433, 488, 531, 547 and 667 nm. The black dot-dashed line represents the 1:1 line.

4. Results and discussion

4.1. Match-up selection

In total, 1973 match-up pairs, with +/−2 hour time difference between in-situ and satellite $L_{wn}(\lambda)$, have been retained. The match-up dataset was further filtered with the exclusion criteria described in Section 3.3. Table 2 shows the number of match-up pairs per algorithm that did not pass the exclusion criteria out of the 1973 match-ups. Note that there is an overlap between the different exclusion criteria. For instance, for the GW94-based and the NN algorithms about 40 and 48% of the 1135 non-turbid match-ups, respectively, were also excluded because their pixel window showed less than six valid pixels. The bottom line in Table 2 indicates the remaining number of match-up pairs per algorithm. Compared to the other algorithms, the NN algorithm generated more match-ups with less than 6 valid pixels while the NIR-SWIR algorithm was more affected by the spatial homogeneity criterion on $L_{wn}(547)$. A possible explanation for the latter is, as observed by Werdell et al. (2010), the increasing dynamic range in $L_{wn}(\lambda)$ due to the switch between the NIR and SWIR aerosol model selection approach within a single window. For comparison we also checked the number of match-up pairs that should be excluded if the homogeneity criterion was applied on $\tau(869)$. As explained previously, except for the NN algorithm, this homogeneity criterion was less severe (Table 2).

The turbidity criterion appeared to be the most restrictive with more than 50% of the initial number of match-ups excluded from the data analysis. Overall, the SIMIL algorithm showed the largest number of match-up pairs followed by the STD algorithm while the NN algorithm showed the lowest total number of match-ups. However, the latter is filtered by an additional exclusion criteria ('flagged NN' in Table 2). Indeed, out of the 370 flagged NN match-up pairs, 133 match-ups were not excluded by any other exclusion criteria. While the NN algorithm presents the advantage to retrieve $L_{wn}(\lambda)$ at all wavelengths simultaneously and to couple atmospheric and bio-optic model, it presents the disadvantage to be constructed by training and hence to be dependent on the training dataset. If a given water mass is not represented in the training dataset, the algorithm might fail. Moreover, it significantly reduces the number of match-up pairs when $L_t(\lambda)$ is out of the simulated range. Hence, the NN algorithm could be further improved by using a training dataset including more diverse water types. Without excluding the match-ups with inputs out-of-range, the NN algorithm presents the largest amount of match-up pairs (i.e. 415).

Table 3 shows the number of match-ups per station and per algorithm. A significant number of match-up pairs from the North Sea, English Channel and French Guiana were flagged as cloud or presented pixels where the sensor saturated explaining the low number of match-up pairs for these regions. For cross comparison, we imposed that the number of values for each algorithm matched. This means that the data presenting a valid match-up for the 4 algorithms only were retained reducing the number of total match-ups to 211 (2, 1, 14, 21, 18, 32, and 123 match-up pairs for BelColor, French Guiana, COVE, GDLT, HLT, MVCO and AAOT stations, respectively).

4.2. Global $L_{wn}(\lambda)$ validation

Fig. 1 displays the scatter-plots of the MODIS-Aqua estimated $L_{wn}(\lambda)$ versus the measured in-situ $L_{wn}(\lambda)$. Table 4 shows the corresponding statistical performance of each algorithm and per wavelength as well as the number of negative $L_{wn}(\lambda)$ retrievals. When compared to the 1:1 line, Fig. 1 shows good agreements between the MODIS-Aqua estimated $L_{wn}(\lambda)$ and the in-situ measured $L_{wn}(\lambda)$. This is particularly true for the GW94-based algorithms at 443, 488 and 547 nm. At 412 and 667 nm the band of data are more dispersed.

Table 4
Statistical results for the retrieved values of $L_{wn}(\lambda)$ obtained with the SIMIL, STD, NIR-SWIR and NN algorithms and number of negative values for $L_{wn}(\lambda)$: R (dimensionless), Intercept (dimensionless), Slope (dimensionless), RE (%), RMSE (mW cm$^{-2}\mu$m^{-1}sr^{-1}) and Bias (%). For each wavelength, the best statistical performance is rendered in bold.

	R	Intercept	Slope	RE	RMSE	Bias	$L_{wn}<0$
nLw(412)							
SIMIL	0.75	**−0.015**	**0.93**	45	0.381	−11	15
STD	**0.86**	0.021	0.90	35	0.262	−2	2
NIR-SWIR	0.84	0.036	0.90	36	0.271	**1**	1
NN	0.81	0.214	0.70	**31**	**0.270**	11	**0**
nLw(443)							
SIMIL	0.86	−0.025	**1.00**	30	0.357	−4	4
STD	**0.93**	**0.009**	0.98	**21**	**0.241**	**1**	0
NIR-SWIR	0.92	0.023	0.99	21	0.254	3	0
NN	0.86	0.246	0.71	24	0.323	3	0
nLw(488)							
SIMIL	0.92	−0.075	**1.04**	20	0.351	−3	0
STD	**0.95**	−0.052	**1.04**	**13**	**0.263**	**−0.2**	0
NIR-SWIR	0.95	**−0.04**	**1.04**	13	0.274	1	0
NN	0.91	0.357	0.88	27	0.385	20	0
nLw(531)							
SIMIL	0.92	−0.022	0.98	14	0.32	−4	0
STD	**0.95**	−0.024	**0.99**	**11**	**0.269**	−3	0
NIR-SWIR	0.94	**−0.015**	**0.99**	**11**	0.273	**−2**	0
NN	0.94	0.273	0.954	19	0.338	16	0
nLw(547)							
SIMIL	0.91	**−0.003**	0.96	14	0.329	−4	0
STD	**0.93**	−0.02	0.98	**11**	**0.286**	−3	0
NIR-SWIR	**0.93**	−0.011	**0.98**	**11**	0.288	**−2**	0
NN	0.92	0.232	0.93	15	0.315	10	0
nLw(667)							
SIMIL	0.81	−0.046	0.90	33	0.136	−26	0
STD	**0.87**	−0.075	**1.00**	30	0.12	−25	0
NIR-SWIR	0.86	−0.07	**1.00**	30	0.121	−23	0
NN	0.85	**−0.001**	0.85	**22**	**0.107**	**−15**	0

As indicated in Table 4, the SIMIL algorithm retrieved the largest number of negative $L_{wn}(\lambda)$ in the blue (15 and 4 at 412 and 443 nm, respectively) followed by the STD algorithm and the NIR-SWIR algorithm (2 and 1 at 412 nm, respectively). The NN algorithm did not show any negative $L_{wn}(\lambda)$ retrievals as it outputs the reflectance on a logarithmic scale. The SIMIL algorithm tended to underestimate $L_{wn}(\lambda)$ at all wavelengths (negative bias ranging between −3 and −26%). At 412 nm, about 60% of the MODIS retrieved L_{wn} are underestimated with the SIMIL and STD algorithms, 57% with the NIR-SWIR algorithm and 45% with the NN algorithm.

For the STD and NIR-SWIR algorithms, the best results were obtained at 488, 531 and 547 nm with R coefficients above 0.9, biases below −3% and RE around 12%. The SIMIL algorithm showed RE ranging between 14 and 45% (with maxima at 412 and 667 nm) and biases between −26 and −4%. Such as observed by Jamet et al. (2011), who compared three SeaWiFS algorithms and among others

Table 5
Statistical results for the retrieved aerosol products obtained with the SIMIL, STD, NIR-SWIR and NN algorithms: RE (%), RMSE (dimensionless) and Bias (%).

	R	Intercept	Slope	RE	RMSE	Bias
α(531, 869)						
SIMIL	0.319	0.939	0.289	52	0.586	**6**
STD	0.403	0.842	0.374	46	0.553	9
NIR-SWIR	**0.434**	**0.764**	**0.421**	**44**	**0.550**	7
τ(869)						
SIMIL	0.607	0.036	0.680	75	0.042	51
STD	0.606	**0.035**	0.682	74	0.042	49
NIR-SWIR	**0.613**	**0.035**	0.674	**72**	**0.040**	**47**
NN	0.579	0.053	**0.919**	154	0.070	109

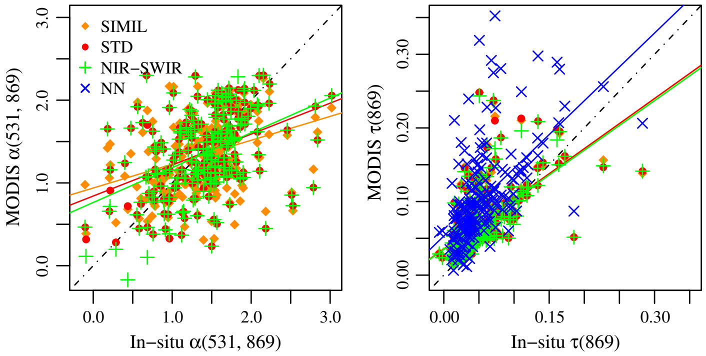

Fig. 2. MODIS-Aqua estimated $\alpha(531,869)$ (left) and $\tau(869)$ (right) versus in-situ aerosol products.

the STD and SIMIL algorithm, our results indicated least accurate $L_{wn}(\lambda)$ retrievals with the SIMIL algorithm compared to the STD algorithm. In contrast, Jamet et al. (2011) observed the largest errors at 670 nm (35 and 43% with the STD and SIMIL algorithms, respectively) while we observed larger errors at 412 nm (35 and 30% at 412 and 667 nm, respectively, for the STD, and 45 and 33% for the SIMIL algorithm).

The performances of the STD and NIR-SWIR algorithms remained very close. For 27% of the match-up pairs the NIR-SWIR algorithm used the NIR approach for the aerosol model selection method and the difference between the STD and NIR-SWIR estimated $L_{wn}(\lambda)$ was below 0.01 mW cm$^{-2}\mu$m^{-1}sr^{-1} for more than 82, 85 and 88% of the match-ups at 412, 547 and 667 nm, respectively. Accordingly, with our in-situ dataset, the NIR-SWIR algorithm did not show significant improvement compared to the STD algorithm. Modifying the turbidity index threshold, as defined by Wang et al. (2009) and/or the cloud albedo threshold or cloud scheme (e.g. using the MODIS 1240 nm band such as Wang et al. (2009)) may result in more pixels processed with the SWIR aerosol

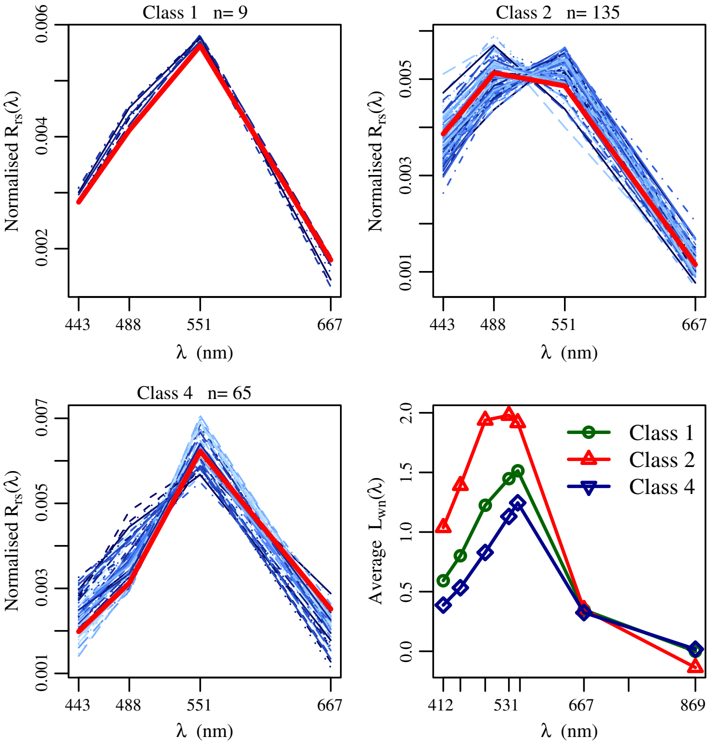

Fig. 3. Top row and bottom left plots: $R_{rs}(\lambda)$ normalized by the area below the curve assigned to each class together with the average normalized spectra given by Vantrepotte et al. (2012) (red plain line). Bottom right plot: average in-situ $L_{wn}(\lambda)$ (mW cm$^{-2}\mu$m^{-1}sr^{-1}) spectra for the three classes. (For interpretation of the references to color in this figure legend, the reader is referred to the web version of this article.).

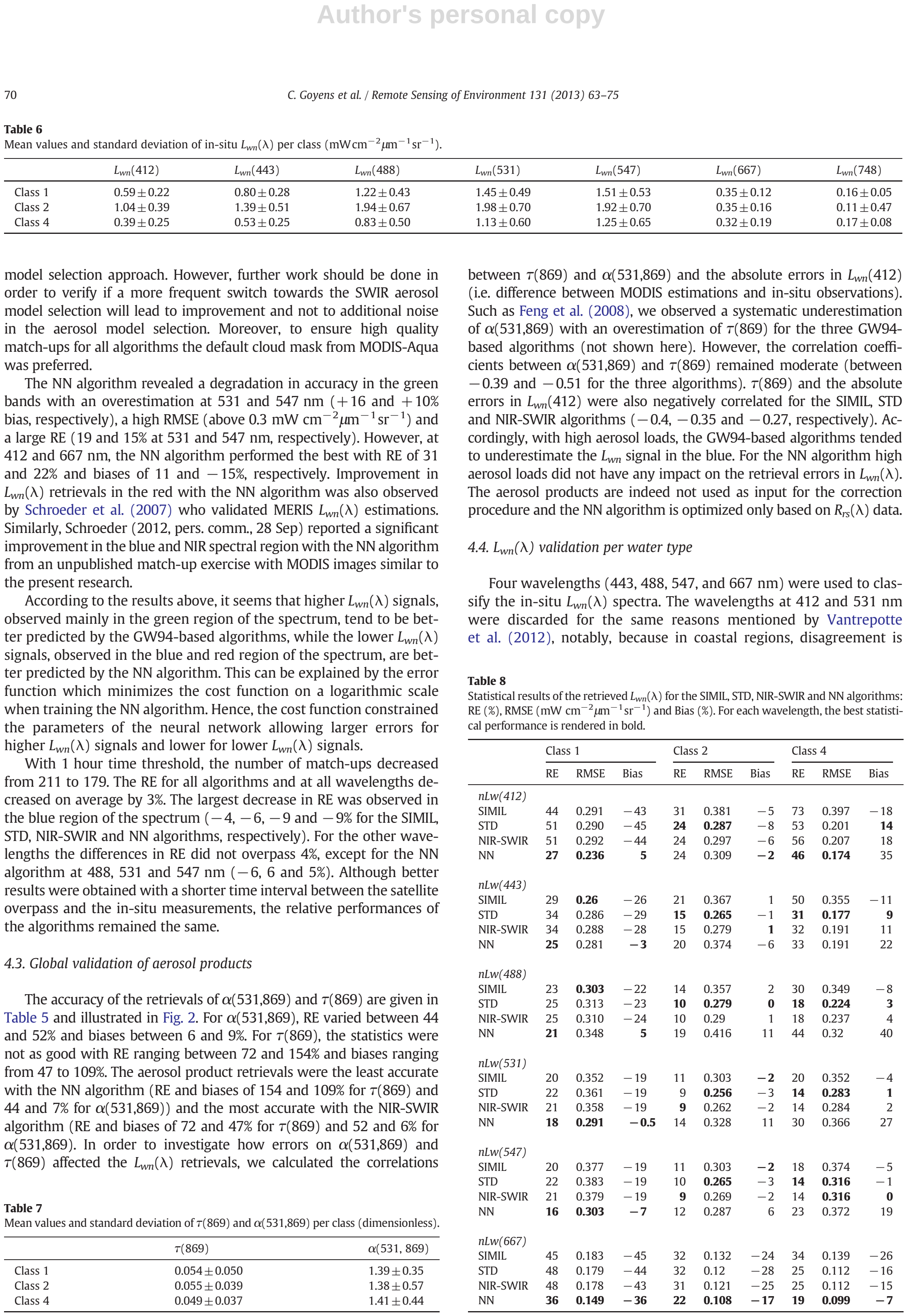

Table 6
Mean values and standard deviation of in-situ $L_{wn}(\lambda)$ per class (mW cm$^{-2}\mu$m^{-1}sr^{-1}).

	$L_{wn}(412)$	$L_{wn}(443)$	$L_{wn}(488)$	$L_{wn}(531)$	$L_{wn}(547)$	$L_{wn}(667)$	$L_{wn}(748)$
Class 1	0.59 ± 0.22	0.80 ± 0.28	1.22 ± 0.43	1.45 ± 0.49	1.51 ± 0.53	0.35 ± 0.12	0.16 ± 0.05
Class 2	1.04 ± 0.39	1.39 ± 0.51	1.94 ± 0.67	1.98 ± 0.70	1.92 ± 0.70	0.35 ± 0.16	0.11 ± 0.47
Class 4	0.39 ± 0.25	0.53 ± 0.25	0.83 ± 0.50	1.13 ± 0.60	1.25 ± 0.65	0.32 ± 0.19	0.17 ± 0.08

model selection approach. However, further work should be done in order to verify if a more frequent switch towards the SWIR aerosol model selection will lead to improvement and not to additional noise in the aerosol model selection. Moreover, to ensure high quality match-ups for all algorithms the default cloud mask from MODIS-Aqua was preferred.

The NN algorithm revealed a degradation in accuracy in the green bands with an overestimation at 531 and 547 nm (+16 and +10% bias, respectively), a high RMSE (above 0.3 mW cm$^{-2}\mu$m^{-1}sr^{-1}) and a large RE (19 and 15% at 531 and 547 nm, respectively). However, at 412 and 667 nm, the NN algorithm performed the best with RE of 31 and 22% and biases of 11 and −15%, respectively. Improvement in $L_{wn}(\lambda)$ retrievals in the red with the NN algorithm was also observed by Schroeder et al. (2007) who validated MERIS $L_{wn}(\lambda)$ estimations. Similarly, Schroeder (2012, pers. comm., 28 Sep) reported a significant improvement in the blue and NIR spectral region with the NN algorithm from an unpublished match-up exercise with MODIS images similar to the present research.

According to the results above, it seems that higher $L_{wn}(\lambda)$ signals, observed mainly in the green region of the spectrum, tend to be better predicted by the GW94-based algorithms, while the lower $L_{wn}(\lambda)$ signals, observed in the blue and red region of the spectrum, are better predicted by the NN algorithm. This can be explained by the error function which minimizes the cost function on a logarithmic scale when training the NN algorithm. Hence, the cost function constrained the parameters of the neural network allowing larger errors for higher $L_{wn}(\lambda)$ signals and lower for lower $L_{wn}(\lambda)$ signals.

With 1 hour time threshold, the number of match-ups decreased from 211 to 179. The RE for all algorithms and at all wavelengths decreased on average by 3%. The largest decrease in RE was observed in the blue region of the spectrum (−4, −6, −9 and −9% for the SIMIL, STD, NIR-SWIR and NN algorithms, respectively). For the other wavelengths the differences in RE did not overpass 4%, except for the NN algorithm at 488, 531 and 547 nm (−6, 6 and 5%). Although better results were obtained with a shorter time interval between the satellite overpass and the in-situ measurements, the relative performances of the algorithms remained the same.

4.3. Global validation of aerosol products

The accuracy of the retrievals of $\alpha(531{,}869)$ and $\tau(869)$ are given in Table 5 and illustrated in Fig. 2. For $\alpha(531{,}869)$, RE varied between 44 and 52% and biases between 6 and 9%. For $\tau(869)$, the statistics were not as good with RE ranging between 72 and 154% and biases ranging from 47 to 109%. The aerosol product retrievals were the least accurate with the NN algorithm (RE and biases of 154 and 109% for $\tau(869)$ and 44 and 7% for $\alpha(531{,}869)$) and the most accurate with the NIR-SWIR algorithm (RE and biases of 72 and 47% for $\tau(869)$ and 52 and 6% for $\alpha(531{,}869)$. In order to investigate how errors on $\alpha(531{,}869)$ and $\tau(869)$ affected the $L_{wn}(\lambda)$ retrievals, we calculated the correlations between $\tau(869)$ and $\alpha(531{,}869)$ and the absolute errors in $L_{wn}(412)$ (i.e. difference between MODIS estimations and in-situ observations). Such as Feng et al. (2008), we observed a systematic underestimation of $\alpha(531{,}869)$ with an overestimation of $\tau(869)$ for the three GW94-based algorithms (not shown here). However, the correlation coefficients between $\alpha(531{,}869)$ and $\tau(869)$ remained moderate (between −0.39 and −0.51 for the three algorithms). $\tau(869)$ and the absolute errors in $L_{wn}(412)$ were also negatively correlated for the SIMIL, STD and NIR-SWIR algorithms (−0.4, −0.35 and −0.27, respectively). Accordingly, with high aerosol loads, the GW94-based algorithms tended to underestimate the L_{wn} signal in the blue. For the NN algorithm high aerosol loads did not have any impact on the retrieval errors in $L_{wn}(\lambda)$. The aerosol products are indeed not used as input for the correction procedure and the NN algorithm is optimized only based on $R_{rs}(\lambda)$ data.

Table 7
Mean values and standard deviation of $\tau(869)$ and $\alpha(531{,}869)$ per class (dimensionless).

	$\tau(869)$	$\alpha(531, 869)$
Class 1	0.054 ± 0.050	1.39 ± 0.35
Class 2	0.055 ± 0.039	1.38 ± 0.57
Class 4	0.049 ± 0.037	1.41 ± 0.44

4.4. $L_{wn}(\lambda)$ validation per water type

Four wavelengths (443, 488, 547, and 667 nm) were used to classify the in-situ $L_{wn}(\lambda)$ spectra. The wavelengths at 412 and 531 nm were discarded for the same reasons mentioned by Vantrepotte et al. (2012), notably, because in coastal regions, disagreement is

Table 8
Statistical results of the retrieved $L_{wn}(\lambda)$ for the SIMIL, STD, NIR-SWIR and NN algorithms: RE (%), RMSE (mW cm$^{-2}\mu$m^{-1}sr^{-1}) and Bias (%). For each wavelength, the best statistical performance is rendered in bold.

	Class 1			Class 2			Class 4		
	RE	RMSE	Bias	RE	RMSE	Bias	RE	RMSE	Bias
nLw(412)									
SIMIL	44	0.291	−43	31	0.381	−5	73	0.397	−18
STD	51	0.290	−45	**24**	**0.287**	−8	53	0.201	**14**
NIR-SWIR	51	0.292	−44	24	0.297	−6	56	0.207	18
NN	**27**	**0.236**	**5**	24	0.309	**−2**	**46**	**0.174**	35
nLw(443)									
SIMIL	29	**0.26**	−26	21	0.367	1	50	0.355	−11
STD	34	0.286	−29	**15**	**0.265**	−1	**31**	**0.177**	**9**
NIR-SWIR	34	0.288	−28	15	0.279	**1**	32	0.191	11
NN	**25**	0.281	**−3**	20	0.374	−6	33	0.191	22
nLw(488)									
SIMIL	23	**0.303**	−22	14	0.357	2	30	0.349	−8
STD	25	0.313	−23	**10**	**0.279**	**0**	**18**	**0.224**	**3**
NIR-SWIR	25	0.310	−24	10	0.29	1	18	0.237	4
NN	**21**	0.348	**5**	19	0.416	11	44	0.32	40
nLw(531)									
SIMIL	20	0.352	−19	11	0.303	**−2**	20	0.352	−4
STD	22	0.361	−19	9	**0.256**	−3	**14**	**0.283**	**1**
NIR-SWIR	21	0.358	−19	**9**	0.262	−2	14	0.284	2
NN	**18**	**0.291**	**−0.5**	14	0.328	11	30	0.366	27
nLw(547)									
SIMIL	20	0.377	−19	11	0.303	**−2**	18	0.374	−5
STD	22	0.383	−19	10	**0.265**	−3	**14**	**0.316**	−1
NIR-SWIR	21	0.379	−19	**9**	0.269	−2	14	**0.316**	**0**
NN	**16**	**0.303**	**−7**	12	0.287	6	23	0.372	19
nLw(667)									
SIMIL	45	0.183	−45	32	0.132	−24	34	0.139	−26
STD	48	0.179	−44	32	0.12	−28	25	0.112	−16
NIR-SWIR	48	0.178	−43	31	0.121	−25	25	0.112	−15
NN	**36**	**0.149**	**−36**	**22**	**0.108**	**−17**	**19**	**0.099**	**−7**

often observed between in-situ and remote sensing $L_{wn}(412)$ and because the inclusion of $L_{wn}(531)$ did not improve the classification due to its low discrimination character. Out of the 211 spectra, two spectra remained unclassified, 9 spectra were assigned to the first class, 135 to the second and 65 to the fourth. None of our match-up pairs were assigned to Class 3.

The three first plots in Fig. 3 show the $R_{rs}(\lambda)$ of the in-situ data normalized by their area for each class. The class averaged normalized $R_{rs}(\lambda)$ calculated by Vantrepotte et al. (2012) are also indicated. The bottom right plot in Fig. 3 shows the average $L_{wn}(\lambda)$ spectra for the three classes obtained with our in-situ data. Table 6 shows the mean and standard deviation of the in-situ $L_{wn}(\lambda)$ for each class.

Class 1 contained six match-ups from the MVCO station, two match-ups from the AAOT station and one from the turbid waters of French Guiana. Class 2 contained almost all in-situ data from the AAOT station (112 out of 123) as well as some in-situ data from COVE and MVCO stations. The AAOT station presents large variabilities in bio-optical quantities as it is located between clear ocean waters and turbid coastal waters with a larger occurrence of open ocean water types (Berthon & Zibordi, 2004; Mélin et al., 2011; Zibordi et al., 2009b). Consequently, it is not surprising that most in-situ data from this station were allocated to Class 2 defined by Vantrepotte et al. (2012) as a mixed class encountered in transition zones between coastal turbid waters and open oceans.

Class 4 corresponds to water masses largely influenced by CDOM concentrations and phytoplankton blooms. All the classified in-situ data from the HLT and GDLT stations were assigned to Class 4. Indeed, as observed in previous studies (e.g., Darecki & Stramski, 2004; Zibordi et al., 2009a, 2009b), these two stations exhibit water masses fed by river discharges rich in humic substances. This results in high CDOM concentrations, an increase in primary production and subsequently in high Chl-a concentrations corresponding to the definition of Class 4. The domination of CDOM absorption can be noticed on the bottom right plot of Fig. 3 and in Table 6 where $L_{wn}(\lambda)$ in the blue is relatively lower (0.39 ± 0.25 mW.cm^{-2}.μm^{-1}.sr^{-1}) compared to the other two classes. The 3 classes presented rather continental aerosol types with average values of $\alpha(531,869)$ around 1.4 (standard deviations $\pm$ 0.5) (Table 7).

Table 8 gives the RMSE, biases and RE per class and per algorithm. For a better comparison, the statistical parameters are also visually represented in Figs. 4 and 5.

The algorithm with the best performance for Class 1 was the NN algorithm with a RE ranging from 16 to 36% and biases from −36 to 5% (Table 8). As shown in Fig. 5, at all wavelengths, the NN algorithms showed lower RE for Class 1 compared to the three other algorithms. For this class, the NIR-SWIR algorithm only switched for one match-up pair towards the SWIR aerosol model selection approach. When comparing only the GW94-based algorithms, the SIMIL algorithm

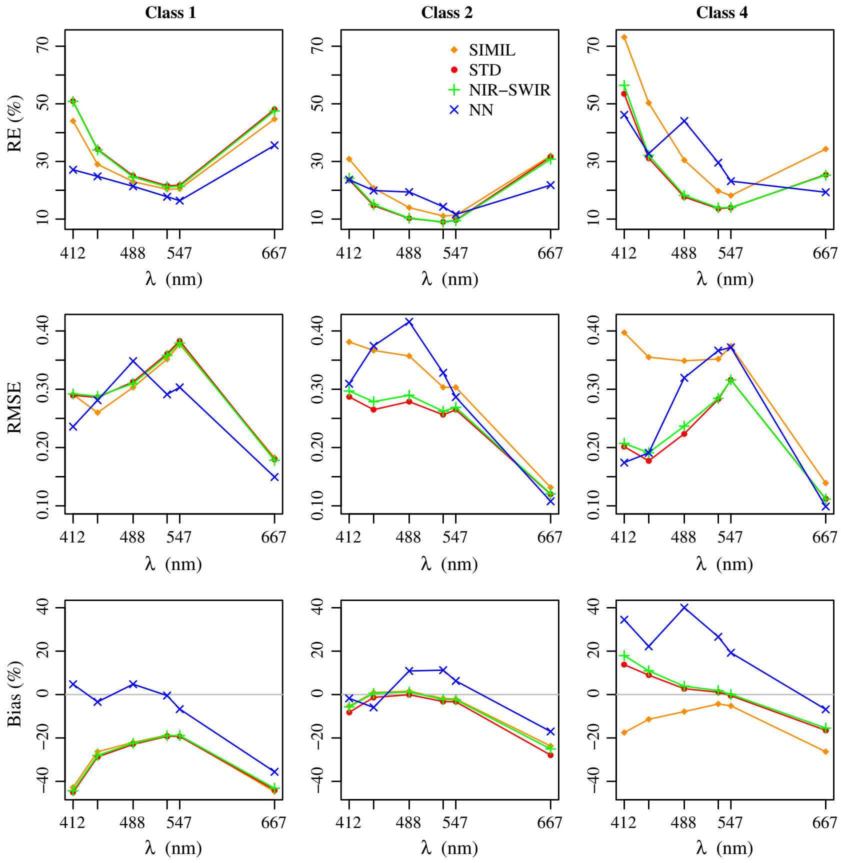

Fig. 4. RMSE (mW cm$^{-2}\mu$m^{-1}sr^{-1}), biases (%) and RE (%) per class (from left to right column: Class 1, 2 and 4) and per algorithm as a function of the wavelength.

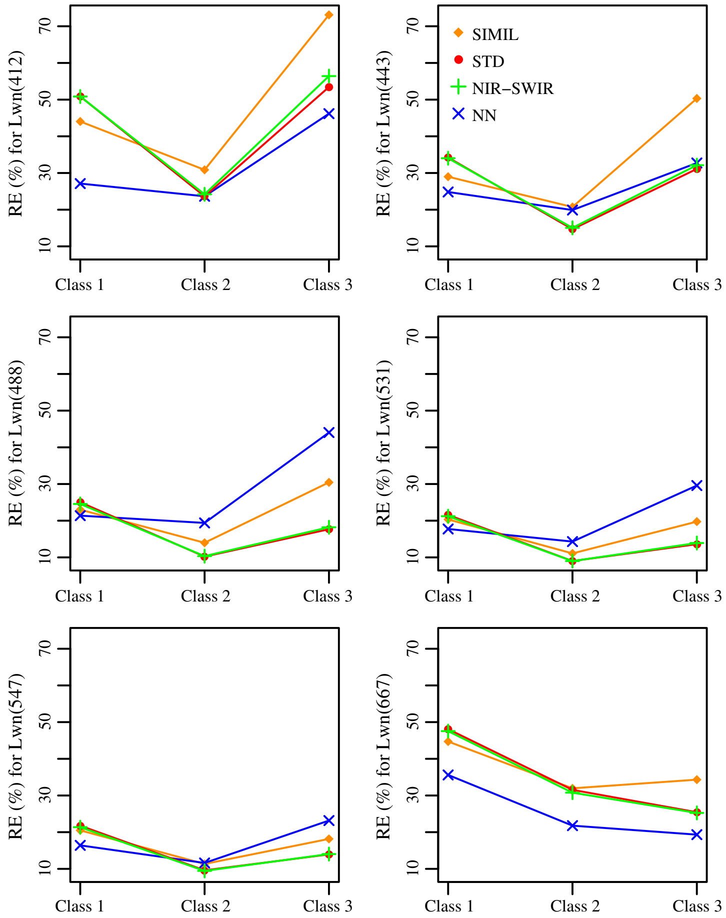

Fig. 5. RE (%) as a function of the water type (Classes 1, 2 and 4) per wavelength.

gave the most satisfying results for this water type. This can be explained by the validity range of the NIR similarity spectrum assumption. Indeed, as observed by several studies (e.g., Doron et al., 2011; Neukermans et al., 2009; Ruddick et al., 2006; Shi & Wang, 2009), the NIR similarity spectrum assumption is only valid for a given range in $L_{wn}(NIR)$. For very clear and extremely turbid waters, Ruddick et al. (2006) mentioned that this assumption should be adjusted. In the present research we found that the linear correlation coefficient between the in-situ $L_{wn}(748)$ and $L_{wn}(869)$ data was about 83% for Class 1, while it was only about 68 and 63% for Class 2 and 4, respectively.

For Class 2, the agreement with the in-situ data was better compared to the other two classes and in particular in the blue and green region of the spectrum for which the biases of the GW94-based algorithms were closer to 0%. The STD algorithm was the most accurate algorithm for this class (RE ranging between 9 and 32% with a maximum at 667 nm and biases ranging between 0 and −28%). Except in the red region of the spectrum, the STD algorithm gave the lowest RE at all wavelengths (Fig. 5). A possible explanation for the good performance of the STD algorithm for Class 2 is the training dataset used to develop the bio-optical model included in the algorithm, notably, the NOMAD dataset. The latter covers indeed mainly mesotrophic to oligotrophic waters (Mélin et al., 2011) which corresponds to the definition of Class 2. Nevertheless, in the red region of the spectrum, both the STD and NIR-SWIR algorithms highly underestimate $L_{wn}(\lambda)$ with RE of 32 and 31% and biases of −25 and −28%, respectively. The statistics of Class 2 are in agreement with the errors observed by Mélin et al. (2011) who validated the MODIS estimated $L_{wn}(\lambda)$ processed with the STD algorithm at the AAOT station. They observed RE varying from 11 to 40% with maxima at 412 and 667 nm. At the same AERONET-OC station, Zibordi et al. (2009b) also observed an underestimation of the MODIS estimated $L_{wn}(667)$ with the STD algorithm. In this region of the spectrum and for the three classes, the NN algorithm performed better than the GW94-based algorithms (Fig. 5).

While the NN algorithm showed a bias close to 0% in the blue region of the spectrum for Classes 1 and 2, it largely overestimated $L_{wn}(412)$ for Class 4 (bias of 34%). The STD and NIR-SWIR algorithms showed a positive bias in the blue too. This is in agreement with previous observations from Zibordi et al. (2009a) who observed biases of 25 and 18% with the STD algorithm at the HLT and GDLT stations, respectively. In contrast to the other algorithms, the SIMIL algorithm underestimated $L_{wn}(\lambda)$ at all wavelengths for Class 4 (biases ranging from −5 to −26%). A possible explanation is the lack of clear water pixels in the MODIS images. Indeed, for more than 90% of the cases in Class 4, the SIMIL algorithm used a climatological $\epsilon(748,869)$ to solve the atmospheric correction.

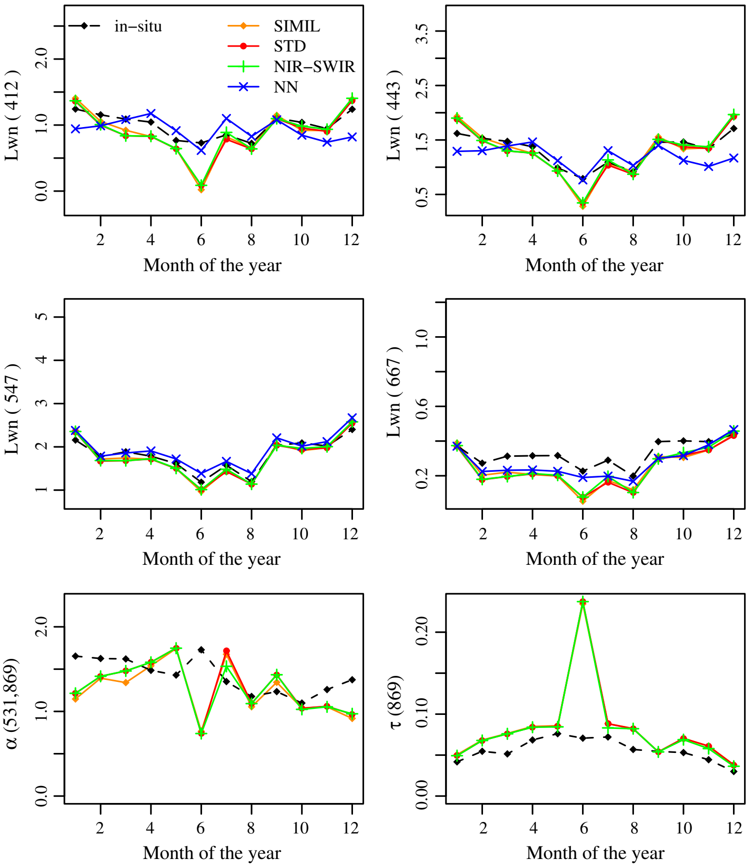

Fig. 6. Annual monthly averages of L_{wn} (mW cm$^{-2}\mu$m^{-1}sr^{-1}) at four different wavelengths (412, 443, 547 and 667 nm) and two atmospheric parameters (α(531,869) and τ(869)) for Class 2.

For Classes 1 and 2 a climatological ϵ(748,869) was used for 77 and 35% of the cases, respectively. The use of a climatological value for ϵ(748,869) might be less accurate and even inappropriate for some situations. As noticed by Jamet et al. (2011), an error in ϵ(748,869) has a significant impact on the retrievals of oceanic products and mainly on L_{wn} estimations at 412, 443 and 667 nm. These bands correspond to the one for which the SIMIL algorithm induced the largest RE, RMSE and negative biases (Table 8).

From Fig. 5 it seems that the errors in $L_{wn}(\lambda)$ at 531 and 547 nm are independent of the water type. Compared to the other wavelengths, at 531 and 547 nm the RE remained quite stable whatever water type was considered (Fig. 5). Accordingly, instead of forcing the algorithms with water type-function relationships to improve atmospheric correction, the algorithms might be constrained by spectral relationships valid for any water type. Therefore, spectral relationships including wavelengths at which the errors in $L_{wn}(\lambda)$ retrievals are independent of the water type (e.g. 531 and 547 nm) should be investigated.

4.5. Algorithm validation over time

Figs. 6 and 7 show the annual monthly averages of $L_{wn}(\lambda)$ at four different wavelengths and the two aerosol parameters for Classes 2 and 4. Time series for Class 1 are not discussed as the number of observations per month is too low and three months only were available. For both classes, the $L_{wn}(\lambda)$ signal is higher and lower in the boreal winter and summer, respectively. This is the consequence of a larger input of sediments in the winter from nearby rivers due to more frequent rainfall events (Berthon & Zibordi, 2004; Mélin et al., 2011). During this period of the year the GW94-based algorithms performed better in the blue region of the spectrum, while in the summer, when the signal is lower, the NN algorithm performed better.

As remarked previously (in Section 4.3.), τ(869) is also mostly overestimated when α(531,869) is underestimated and an overestimation in τ(869) is often associated with an underestimation in $L_{wn}(\lambda)$ in the blue region of the spectrum. For both classes, a disagreement in τ(869) often led to erroneous $L_{wn}(\lambda)$ retrievals (e.g. in June on Fig. 6 and May on Fig. 7). For Class 4, the disparity between the algorithms in terms of $L_{wn}(\lambda)$ retrievals was mostly apparent in the blue and mainly in May and December when τ(869) was largely overestimated and α(531,869) underestimated. During these two months, the STD and NIR-SWIR algorithms performed better in the blue, while in the green and the red the SIMIL algorithm performed better.

5. Conclusion

Several algorithms have been developed in order to bypass the inappropriate application of the black pixel assumption in turbid

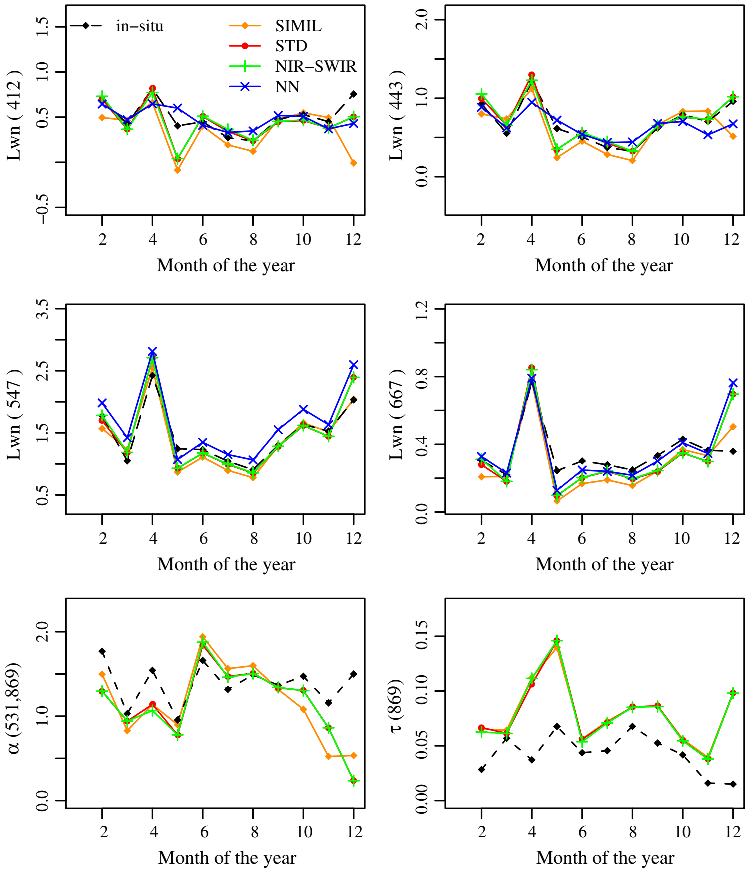

Fig. 7. Same as Fig. 6 for Class 4.

coastal waters. This research reported the accuracy of four MODIS-Aqua atmospheric correction algorithms in contrasted coastal waters using global coastal AERONET-OC data and cruise campaign measurements. The four algorithms were (1) the STD algorithm from NASA, (2) the SIMIL algorithm assuming spatial homogeneity within the area of interest of the reflectance of the atmosphere and the ocean in the NIR region of the spectrum, (3) the NIR-SWIR algorithm which, in highly turbid waters, switches towards the SWIR bands for the aerosol model selection, and, (4) the NN algorithm which applies a direct inversion of $L_t(\lambda)$. The former three algorithms are based on the GW94 atmospheric correction approach. Overall, the atmospheric correction algorithms performed well with RE ranging from 11 to 45% and biases from −25 to +16%. For the GW94-based algorithms, the largest errors were encountered in the blue and red part of the spectrum (at 412 and 667 nm), confirming the challenge of using these bands for retrieving bio-optical parameters. In contrast, the NN algorithm performed slightly better in these bands. The SIMIL algorithm tended to underestimate $L_{wn}(\lambda)$, while the NN algorithm tended to overestimate it.

A closer look to the dataset conducted to an evaluation of the algorithms as a function of the water type. In-situ $L_{wn}(\lambda)$ spectra were classified according to a classification scheme developed by Vantrepotte et al. (2012) which focussed on coastal waters and distinguished the classes based on the water type rather than on the water clarity. For water masses mainly influenced by detrital and mineral material (Class 1), the NN algorithm performed the best at all wavelengths followed by the SIMIL algorithm. For the two other classes, the STD algorithm seemed to perform better followed by the NIR-SWIR algorithm. The NN algorithm could be improved in order to increase the number of match-up pairs and to correct for the large overestimations of $L_{wn}(\lambda)$ in the green part of the spectrum. When considering only the GW94-based algorithms, the SIMIL algorithm performed slightly better for water masses mainly influenced by detrital and mineral material indicating that this algorithm is valuable for a specific range of turbidity only. The largest errors were encountered for water masses dominated by significant concentrations of phytoplankton and CDOM. Overall, the NN algorithm performed better where the GW94-based algorithms failed (mainly in the blue and red region of the spectrum and at all wavelengths for Class 1) and when considering all wavelengths and all water types the STD algorithm performed the best.

Atmospheric correction remains a challenging task and in particular in complex optical coastal waters. The present research provides an overview and validation of the already existing algorithms which is highly valuable for further improvement essential to meet the requirements of the ocean color end-users.

Acknowledgments

The authors would like to thank Dr. Vincent Vantrepotte for providing his classification method and Quinten Vanhellemont for his help with the match-up extraction. Also thanks go to the Ocean Biology Processing Group of NASA for the distribution of the MODIS-Aqua data and the development and support of the SeaDAS Software, as well as to the PIs and maintenance staffs of the AERONET-OC sites used in the present research. The anonymous reviewers are also acknowledged for their comments and suggestions. This work has been supported by the French Spatial Agency (CNES) through the TOSCA program and the "Ministère de l'Enseignement et de la Recherche Française" which provided a PhD scholarship. It has been performed in the frame of the GlobCoast project (www.foresea.fr/globcoast) which is funded by the Agence Nationale de la Recherche (ANR 2011 BS56 018 01). The GlobCoast project is affiliated to the LOICZ and AQUIMER project.

References

Ahmad, Z., Franz, B. A., McClain, C. R., Kwiatkowska, E. J., Werdell, P. J., Shettle, E. P., et al. (2010). New aerosol models for the retrieval of aerosol optical thickness and normalized water-leaving radiances from the SeaWiFS and MODIS sensors over coastal regions and open oceans. *Applied Optics*, *49*, 5545–5560.

Bailey, S. W., Franz, B. A., & Werdell, P. J. (2010). Estimations of near-infrared water-leaving reflectance for satellite ocean color data processing. *Optics Express*, *18*, 7521–7527.

Bailey, S. W., & Werdell, P. J. (2006). A multi-sensor approach for the on-orbit validation of ocean color satellite data products. *Remote Sensing of Environment*, *102*, 12–23.

Berthon, J. -F., & Zibordi, G. (2004). Bio-optical relationships for the northern Adriatic Sea. *International Journal of Remote Sensing*, *25*, 1527–1532.

Cox, C., & Munk, W. (1954). Measurements of the roughness of the sea surface from photographs of the sun's glitter. *Journal of the Optical Society of America*, *44*, 838–850.

D'Alimonte, D., Mélin, F., Zibordi, G., & Berthon, J. -F. (2003). Use of the novelty detection technique to identify the range of applicability of the empirical ocean color algorithms. *IEEE Transactions on Geoscience and Remote Sensing*, *41*, 2833–2843.

Darecki, M., & Stramski, D. (2004). An evaluation of MODIS and SeaWiFS bio-optical algorithms in the Baltic Sea. *Remote Sensing of Environment*, *89*, 326–350.

Dogliotti, A. I., Ruddick, K., Nechad, B., & Lasta, C. (2011). Improving water reflectance retrieval from MODIS imagery in the highly turbid waters of La Plata River. *Proceedings of VI International Conference "Current Problems in Optics of Natural Waters"*. St. Petersburg, Russia: Publishing House "Nauka" of RAS.

Doron, M., Bélanger, S., Doxoran, D., & Babin, M. (2011). Spectral variations in the near-infrared ocean reflectance. *Remote Sensing of Environment*, *115*, 1617–1631.

Feng, H., Vandemark, D., Campbell, J. W., & Holben, B. N. (2008). Evaluation of MODIS ocean color products at a northeast United States coast site near the Martha's Vineyard Coastal Observatory. *International of Remote Sensing*, *29*, 4479–4497.

Frouin, R., Schwindling, M., & Deschamps, P. -Y. (1996). Spectral reflectance of sea foam in the visible and near-infrared: In situ measurements and remote sensing implications. *Journal of Geophysical Research*, *101*, 14361–14371.

Gordon, H. R. (1987). Calibration requirements and methodology for remote sensors viewing the ocean in the visible. *Remote Sensing of Environment*, *22*, 103–126.

Gordon, H. R. (1997). Atmospheric correction of ocean color imagery in the Earth Observing system era. *Journal of Geophysical Research*, *102*, 17081–17106.

Gordon, H. R., & Wang, M. (1994). Retrieval of water-leaving radiance and aerosol optical thickness over the oceans with SeaWiFS: A preminilary algorithm. *Applied Optics*, *33*, 443–452.

Jamet, C., Loisel, H., Kuchinke, C. P., Ruddick, K., Zibordi, G., & Feng, H. (2011). Comparison of three SeaWiFS atmospheric correction algorithms for turbid waters using AERONET-OC measurements. *Remote Sensing of Environment*, *115*, 1955–1965.

Kuchinke, C. P., Gordon, H. R., & Franz, B. A. (2009). *Spectral optimization for constituent retrieval in Case 2 waters I: Implementation and performance*, *Vol. 113*. (pp. 571–587).

Loisel, H., Lubac, B., Dessailly, D., Duforet-Gaurier, L., & Vantrepotte, V. (2010). Effect of inherent optical properties variability on the chlorophyll retrieval from ocean color remote sensing: An in situ approach. *Optics Express*, *18*, 20949–20952.

Loisel, H., Mériaux, X., Poteau, A., Artigas, L., Lubac, B., Gardel, A., et al. (2009). Analyze of inherent optical properties of French Guiana coastal waters for remote sensing applications. *Journal of Coastal Research*, *SI 56*, 1532–1536.

Lubac, B., & Loisel, H. (2007). Variability and classification of remote sensing reflectance spectra in the eastern English Channel and southern North Sea. *Remote Sensing of Environment*, *110*, 45–58.

Lubac, B., Loisel, H., Guiselin, N., Astoreca, R., Artigas, L., & Mériaux, X. (2008). Hyperspectral and multispectral ocean color inversions to detect *Phaeocystis globosa* blooms in coastal waters. *Journal of Geophysiscal Research*, *113*, C06026.

Mélin, F., Vantrepotte, V., Clerici, M., D'Alimonte, D., Zibordi, G., Berthon, J. -F., et al. (2011). Multi-sensor satellite time series of optical properties and chlorophyll-a concentration in the Adriatic Sea. *Progress in Oceanography*, *91*, 229–244.

Mélin, F., Zibordi, G., & Djavidnia, S. (2007). Development and validation of a technique for merging satellite derived aerosol optical depth from SeaWiFS and MODIS. *Remote Sensing of Environment*, *108*, 436–450.

Nechad, B., Ruddick, K., & Park, Y. (2010). Calibration and validation of a generic multisensor algorithm for mapping of total suspended matter in turbid waters. *Remote Sensing of Environment*, *114*, 854–866.

Neukermans, G., Ruddick, K., Bernard, E., Ramon, D., Nechad, B., & Deschamps, P. -Y. (2009). Mapping total suspended matter from geostationary satellites: A feasibility study with SEVIRI in the Southern North Sea. *Optics Express*, *17*, 14029–14052.

O'Reilly, J., Maritorena, S., O'Brien, M., Siegel, D., Toole, D., Menzies, D., et al. (2000). Ocean color chlorophyll a algorithms for seawifs, oc2, and oc4: Version 4. In J. E. O'Reilly (Ed.), *SeaWiFS Postlaunch Calibration and Validation Analyses, Part 3. NASA/Tech. Memo. 2000-206892. Greenbelt, Maryland, NASA Goddard Space Flight Center volume 11*. (pp. 9–23).

Robinson, W. D., Franz, B. A., Patt, F. S., Bailey, S. W., & Werdell, P. J. (2003). Masks and flags updates. In S. B. Hooker, & E. R. Firestone (Eds.), *SeaWiFS Postlaunch Technical Report Series, Chap.6, NASA/TM-2003-206892. Greenbelt, Maryland, NASA Goddard Space Flight Center volume 22*. (pp. 34–40).

Ruddick, K., Cauwer, V. D., Park, Y., & Moore, G. (2006). Seaborne measurements of near infrared water-leaving reflectance: The similarity spectrum for turbid waters. *Limnology and Oceanography*, *51*, 1167–1179.

Ruddick, K., Ovidio, F., & Rijkeboer, M. (2000). Atmospheric correction of SeaWiFS imagery for turbid coastal and inland waters. *Applied Optics*, *39*, 897–912.

Schroeder, T., Behnert, I., Schaale, M., Fischer, J., & Doerffer, R. (2007). Atmospheric correction algorithm for MERIS above case-2 waters. *International Journal of Remote Sensing*, *28*, 1469–1486.

Shi, W., & Wang, M. (2007). Detection of turbid waters and absorbing aerosols for the MODIS ocean color data processing. *Remote Sensing of Environment*, *110*, 149–161.

Shi, W., & Wang, M. (2009). An assessment of the black ocean pixel assumption for MODIS SWIR bands. *Remote Sensing of Environment*, *113*, 1587–1597.

Siegel, D. A., Wang, M., Maritorena, S., & Robinson, W. (2000). Atmospheric correction of satellite ocean color imagery: The black pixel assumption. *Applied Optics*, *39*, 3582–3591.

Stumpf, R. P., Arone, R. A., Gould, R. W., & Ransibrahmanakul, V. (2003). A partially coupled ocean-atmosphere model for retrieval of water-leaving radiance from SeaWiFS in coastal waters. In S. B. Hooker, & E. R. Firestone (Eds.), *SeaWiFS Postlaunch Technical Report Series, Chap.9, NASA/TM-2003-206892. Greenbelt, Maryland, NASA Goddard Space Flight Center volume 22*. (pp. 51–59).

Vantrepotte, V., Loisel, H., Dessailly, D., & Mériaux, X. (2012). Optical classification of contrasted coastal waters. *Remote Sensing of Environment*, *123*.

Vantrepotte, V., Loisel, H., Mériaux, X., Jamet, C., Dessailly, D., Neukermans, G., et al. (2011). Seasonal and inter-annual (19982010) variability of the suspended particulate matter as retrieved from satellite ocean color sensors over the French Guiana coastal waters. *Journal of Coastal Research*, *SI64*, 1750–1754.

Wang, M., & Shi, W. (2007). The NIR-SWIR combined atmospheric correction approach for MODIS ocean color data processing. *Optics Express*, *15*, 15722–15733.

Wang, M., Son, S., & Shi, W. (2009). Evaluation of MODIS SWIR and NIR-SWIR atmospheric correction algorithms using SeaBASS data. *Remote Sensing of Environment*, *113*, 635–644.

Werdell, P. J., & Bailey, S. W. (2005). An improved bio-optical data set for ocean color algorithm development and satellite data product validation. *Remote Sensing of Environment*, *98*, 122–140.

Werdell, P. J., Franz, B. A., & Bailey, S. W. (2010). Evaluation of shortwave infrared atmospheric correction for ocean color remote sensing of Chesapeake bay. *Remote Sensing of Environment*, *114*, 2238–2247.

Werdell, P. J., Franz, B. A., Bailey, S. W., Harding., L. W., Jr., & Feldman, G. C. (2007). Approach for the long-term spatial and temporal evaluation of ocean color satellite data products in a coastal environment. *Proceeding of SPIE, Vol. 6680*. (pp. 12).

Wolfe, R. E., Nishihama, M., Fleig, A., Kuyper, J. A., Roy, D. P., Storey, J. C., et al. (2002). Achieving sub-pixel geolocation accuracy in support of MODIS land pixel. *Remote Sensing of Environment*, *83*, 31–49.

Zibordi, G., Berthon, J. -F., Mélin, F., D'Alimonte, D., & Kaitala, S. (2009). Validation of satellite ocean color primary producs at optically complex coastal sites: Northern Adriatic Sea, Northern Baltic Proper and Gulf of Finland. *Remote Sensing of Environment*, *113*, 2574–2591.

Zibordi, G., Holben, B., Hooker, S. B., Mélin, F., Berthon, J. -F., Slutsker, I., et al. (2006). A network for standardized ocean color validation measurements. *EOS Transactions*, *87*, 293–297.

Zibordi, G., Holben, B., Slutsker, I., Giles, D., D'Alimonte, D., Mélin, F., et al. (2009). Aeronet-oc: A network for the validation of ocean color primary products. *Journal of the Atmospheric and Oceanic Technology*, *26*, 1634–1651.

Zibordi, G., Stroembeck, N., Mélin, F., & Berthon, J. -F. (2006). Tower-based radiometric observations at a coastal site in the Baltic Proper. *Estuarine, Coastal and Shelf Science*, *69*, 649–654.

- Chapter 5 -

Spectral relationships to improve NIR-modelling schemes for atmospheric correction

As demonstrated by the validation and comparison exercises presented in the previous chapter of this work, the turbid water AC methods, and subsequently associated assumptions and correction approaches, present some limitations. Improvements in satellite $\rho_w(\lambda)$ retrievals are thus still needed.

The present chapter focuses on improving two AC methods, the GW94-based STD and MUMM AC method. According to the results of the previous chapter, the former showed overall the best performances for the retrieval of $\rho_w(\lambda)$. However, the NIR-modelling scheme of this algorithm relies on a Chl_a-based bio-optical model (Stumpf et al., 2003; Bailey et al., 2010), which may be inappropriate, in particular in water types optically dominated by non-algal particles. The latter AC method presented a wider spatial coverage in $\rho_w(\lambda)$ estimations and, compared to the other GW94-based algorithms, resulted in more satisfying $\rho_w(\lambda)$ retrievals for water masses optically dominated by detrital and mineral material. However, for other water types, this algorithm greatly underestimated $\rho_w(\lambda)$, which is possibly due to an inappropriate application of the constant NIR reflectance ratio to retrieve $\rho_w(\lambda_{NIR})$.

A possible approach to improve these algorithms consists of forcing the algorithm with universally valid spectral relationships of the form $\rho_w(\lambda_j) = f(\rho_w(\lambda_i))$. These relationships reflect the spectral dependence of the marine signal itself, including the spectral dependence of the total absorption and backscattering simultaneously. Hence, it does not require retrieval of IOPs and can be easily implemented in existing NIR-modelling schemes to improve $\rho_w(\lambda)$ retrievals where current AC methods fail.

For the CZCS AC method, empirical spectral relationships have already been proposed to model $\rho_w(670)$ where the black pixel assumption is invalid (e.g., Smith and Wilson, 1980; Austin and Petzold, 1980; Sturm, 1981, 1983; Viollier and Sturm, 1984; Bricaud and Morel, 1987). Later, a red spectral relationship was also suggested by Nicolas et al. (2005) for the AC of the POLarization and Directionality of the Earth's Reflectances-2 (POLDER-2) sensor. Similarly, several studies investigated the marine reflectance in the NIR region of the spectrum to correct the second generation ocean colour satellite images for atmospheric contribution (e.g., Ruddick et al., 2000, 2006; Doron et al., 2011; Wang et al., 2012; Ahn et al., 2012). A commonly used NIR spectral relationship is the constant NIR reflectance ratio used in the MUMM NIR-modelling scheme. More recently, a polynomial NIR spectral relationship was suggested by Wang et al. (2012) for the AC method of the Korean Geostationary Ocean Colour Imager (GOCI).

The main objective of this chapter consists in evaluating the potential of spectral relationships to improve actual NIR-modelling schemes for the AC. Therefore, a literature review of the spectral relationships used in the context of ocean colour is conducted and the encountered spectral relationships are validated. This work led to a first paper summarized in the next section (Section 5.1) and attached in Section 5.5 (Goyens et al., 2013a).

Next, the negative and/or positive impact of spectral relationships constraints within the STD and MUMM NIR-modelling schemes, is investigated based on a sensitivity study. This sensitivity study resulted in a second paper (Goyens et al., 2013b) summarized in Section 5.2 and attached in Section 5.6.

In addition to the papers, four complementary studies have been conducted (Section 5.3). First, additional red-NIR and blue-green spectral relationships are developed with the MUMM *in situ* dataset (Section 5.3.1). These relationships are used to further constrain, and eventually improve, the STD NIR-modelling scheme.

Second, a complementary study is conducted attempting to confirm the empirically retrieved spectral relationships with a theoretical basis in order to gain insight in the spectral dependence of the water signal itself and to investigate if the form of the relationship satisfies all water types. This is outlined in Section 5.3.2.

Third, following the conclusions of the two papers linked to this chapter (Goyens et al., 2013a,b) and the complementary results, two additional modified NIR-modelling schemes are suggested to extent the GW94 AC algorithm to turbid and highly productive waters (Section 5.3.3) and validated.

A last section (Section 5.3.4) briefly discusses the solution for $\rho_w(\lambda)$ at 748 nm for the modified MUMM AC NIR-modelling scheme. Indeed, Goyens et al. (2013a) suggested to replace the assumption of the constant NIR water reflectance ratio in the initial MUMM AC approach by the polynomial function used by Wang et al. (2012) for the AC of GOCI. Replacing the constant NIR reflectance ratio of $\rho_w(\lambda)$ by a polynomial function, involves two solutions for $\rho_w(\lambda)$ (i.e., a positive and negative square root). Section 5.3.4 demonstrates why the positive square root is clearly non-physical and, consequently, the negative square root is preferred for $\rho_w(748)$.

General conclusions are outlined in Section 5.4 together with perspectives to implement improved AC approaches for the processing of MODIS Aqua satellite images.

5.1 PAPER SUMMARY: "SPECTRAL RELATIONSHIPS FOR ATMOSPHERIC CORRECTION. I. VALIDATION OF RED AND NEAR INFRA-RED SPECTRAL RELATIONSHIPS"

C. Goyens, C. Jamet, and K. Ruddick, published in *Optics Express*, 21(18), 21162-21175 (2013).

The paper presents an extensive overview of red and NIR spectral relationships found in the literature. Sixteen published spectral relationships, estimating $\rho_w(\lambda)$ in the red or NIR spectral region, were retained. Since most of these spectral relationships have been developed with restrictive datasets, a validation is required to select globally valid spectral relationships. We selected therefore 105 *in situ* $\rho_w(\lambda)$ spectra from the MUMM dataset (Section 3.2.1.2), including contrasted coastal waters with $\rho_w(\lambda_{NIR})$ values ranging from near zero to 10^{-1}. For the validation, a distinction is also made between moderately, very and extremely turbid waters. Moderately turbid waters include data presenting $\rho_w(869)$ values between 10^{-4} and 3.10^{-3}. Very turbid waters include all data with $\rho_w(869)$ values superior to 3.10^{-3} and, among the very turbid waters, extremely turbid waters are defined as the spectra presenting $\rho_w(869)$ values superior to 10^{-2}. The threshold of 10^{-4} is approximately the upper limit for which the black pixel assumption can be successfully applied (Siegel et al., 2000) and the limit of 3.10^{-3} corresponds to the threshold value used by Wang et al. (2009) to switch for the SWIR aerosol model selection in the combined NIR-SWIR AC algorithm.

Most red spectral relationships have been proposed for the AC of CZCS images to estimate $\rho_w(670)$ from $\rho_w(\lambda)$ in the blue and green region of the spectrum (Smith and Wilson, 1980;

Austin and Petzold, 1980; Sturm, 1981, 1983; Viollier and Sturm, 1984; Bricaud and Morel, 1987; Viollier and Sturm, 1984; Sturm et al., 1999). More recently, Lee et al. (2009) also suggested, to correct $\rho_w(667)$ values within the Quasi-Analytical Algorithm (QAA), bounding red equations to evaluate the limits of $\rho_w(667)$ according to $\rho_w(555)$ and a red spectral relationship between $\rho_w(667)$ and the ratio $\rho_w(490)/\rho_w(555)$.

Similarly to the red spectral relationships, several studies investigated the spectral dependence of the marine reflectance in the NIR region of the spectrum to model $\rho_w(\lambda_{NIR})$ for the AC of second generation ocean colour satellites (e.g., Ruddick et al., 2000, 2006; Wang et al., 2012). Ruddick et al. (2000, 2006) suggested a universal constant NIR reflectance ratio for the NIR-modelling scheme of the GW94-based MUMM AC algorithm. Similarly, Wang et al. (2012) proposed for the NIR-modelling scheme of the AC algorithm of GOCI, a polynomial spectral relationship allowing to retrieve $\rho_w(869)$ from $\rho_w(748)$.

Results from the validation exercise showed that overall the red spectral relationships are not valid for all turbidity ranges encountered in the *in situ* dataset. This suggests that either the red spectral functions need to be updated or that water type-specific spectral relationships should be used. In contrast, bounding equations, as suggested by Lee et al. (2009), allow more variability and are thus more appropriate to force red or NIR-modelling schemes for the AC when a priori information on the water type or turbidity level is not available or when the AC method is expected to perform globally. In contrast, the polynomial NIR spectral relationship, initially developed with MODIS Aqua remote sensing reflectances over the Western Pacific (Wang et al., 2012), presented satisfying results for moderately to extremely turbid waters. Goyens et al. (2013a) concluded that both the red bounding equations and NIR polynomial spectral relationship may be used to constrain actual NIR-modelling schemes (e.g., the MUMM and STD NIR-modelling schemes) to improve AC algorithms. This is investigated in the companion paper by Goyens et al. (2013b).

5.2 Paper summary: “Spectral relationships for atmospheric correction. II. Improving the NASA Standard and MUMM near infra-red modeling schemes”

C. Goyens, C. Jamet, and K. Ruddick, published in *Optics Express*, 21(18), 21176-21187 (2013).

The main objective of this paper was to investigate if spectral relationships may improve $\rho_w(\lambda)$ retrievals by forcing the NIR-modelling schemes in the AC algorithms. Therefore, the previously validated bounding red equations (Lee et al., 2009) and the NIR polynomial spectral relationship (Wang et al., 2012) were used to force the STD and MUMM NIR-modelling schemes, and a sensitivity study was conducted.

For the sensitivity study, simulated $\rho_{rc}(\lambda)$ data were computed by combining the 105 *in situ* $\rho_w(\lambda)$ spectra with a simplified power law model for the multiple-scattering aerosol reflectance, $\rho_{am}(\lambda_0)$, and by including an Ångström coefficient as a function of the aerosol model. Therefore, two coastal models were selected with 50% and 90% relative humidity (hereafter referred to as C50 and C90) (Shettle and Fenn, 1979; Gordon and Wang, 1994).

Similarly to the first paper, a distinction is made between moderately ($\rho_w(869)$ values between 10^{-4} and 3.10^{-3}), very ($\rho_w(869) > 3.10^{-3}$) and extremely ($\rho_w(869) > 10^{-2}$) turbid waters.

For the STD NIR-modelling scheme, the bounding red equations of Lee et al. (2009) are used to correct $\rho_w(667)$ when these are out of limit according to $\rho_w(555)$, and, instead of extrapolating the backscattering coefficient from 667 nm to 869 nm to obtain $\rho_w(869)$, $\rho_w(869)$ is estimated from $\rho_w(748)$ with the NIR polynomial relationship of Wang et al. (2012) (referred to as the

STD$_{\text{Con}}$ AC method). For the MUMM AC algorithm, the constant NIR $\rho_w(\lambda)$ ratio is replaced by the NIR polynomial relationship in order to extent the algorithm to extremely turbid waters (referred to as the MUMM$_{\text{Poly}}$ AC method).

A comparison of the median bias between *in situ* and retrieved $\rho_w(\lambda)$, obtained with the initial and the constrained STD NIR-modelling scheme for AC, suggested that the STD$_{\text{Con}}$ approach performed better for all turbidity ranges and, particularly, in the blue spectral domain (percentage bias decreased by approximately 50% relative to the initial STD NIR-modelling scheme). However, with this new constrained approach, more reflectance spectra were flagged due to non-physical Chl_a concentration estimations.

Replacing the constant NIR reflectance ratio by the NIR polynomial spectral relationship within the NIR-modelling scheme of the MUMM AC algorithm resulted in lower $\rho_w(\lambda)$ retrieval errors and in particular in extremely turbid waters (percentage bias decreased by approximately 50% to 75%). However, including the polynomial NIR relationship significantly increased the sensitivity of the AC approach to errors on the retrieved aerosol model. Hence, the added value of the polynomial NIR spectral relationship constraint will be significantly reduced when the aerosol model is not correctly retrieved in the sub-scene of the image.

Hence, the STD$_{\text{Con}}$ NIR-modelling scheme should be further improved such that $\rho_w(\lambda)$ retrievals are less affected by erroneous estimations of Chl_a concentrations, and, the MUMM$_{\text{Poly}}$ AC approach should be improved to reduce its sensitivity to erroneous selection of aerosol models.

5.3 COMPLEMENTARY RESULTS

5.3.1 Additional red-NIR and blue-green spectral relationships

Previous sections suggested to force the STD NIR-modelling schemes with bounding equations relating $\rho_w(667)$ to $\rho_w(555)$ and a NIR spectral relationship retrieving $\rho_w(869)$ from $\rho_w(748)$ (i.e., STD$_{\text{Con}}$ approach). However, to account for the spectral information at all wavelengths, additional red-NIR and blue-green spectral relationships may also be used. Moreover, a red-NIR spectral relationship may avoid the approximation of the total absorption by the pure water absorption in the NIR spectral region, and, the extrapolation of the backscattering coefficient from the red to the NIR spectral domain within the STD bio-optical model. Similarly, blue-green spectral relationships may correct for negative blue $\rho_w(\lambda)$ values before it is used to estimate the Chl_a concentration in the STD bio-optical model. Therefore, additional red-NIR and blue-green spectral relationships are developed here and validated with the *in situ* MUMM $\rho_w(\lambda)$ measurements.

By minimizing the lowest sum of squared absolute error with 80% of the 105 *in situ* MUMM reflectance spectra, an hyperbolic relation is found between $\rho_w(\lambda)$ at 667 nm and 748 nm (Fig. 5.1(a)). The model parameters and statistical performances (i.e., percentage relative error, RE, percentage bias, R^2 and percentage of data presenting less then 10% difference with modelled data), estimated with the 20% remaining spectra, are reported in Table 5.1. As shown by the negative bias (-10%), the model tends to slightly underestimate $\rho_w(748)$. For only 33% of the data, modelled and *in situ* $\rho_w(748)$ differed by less than 10%. However, a R^2 of 0.97 indicates a very good fit.

Similarly, a simple linear blue-green spectral relationship is found between $\rho_w(443)$ and $\rho_w(547)$ (Fig. 5.2(b)). Percentage RE and bias are relatively low and the R^2 of 0.95 indicates a relatively good fit (Table 5.1). About 62% of the modelled data lies within ±10% of the *in situ* data.

According to the statistics in Table 5.1, the red-NIR hyperbolic spectral relationship should be further investigated to improve $\rho_w(748)$ retrievals from $\rho_w(667)$ (e.g., reduce the negative bias). In contrast, the simple linear blue-green spectral relationship appeared to be globally

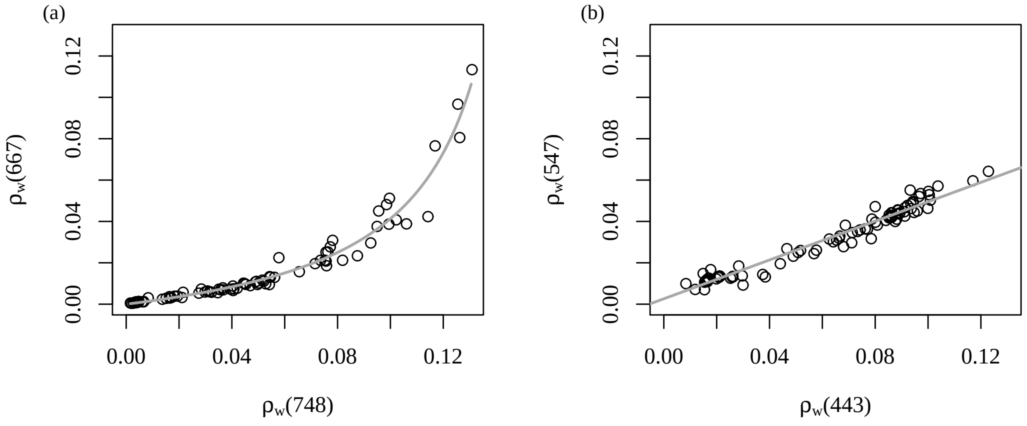

Figure 5.1: *Red-NIR hyperbolic (a) and blue-green simple linear spectral relationships (b) (thick light-grey lines) together with the 105 MUMM in situ* $\rho_w(\lambda)$ *data.*

Table 5.1: *Empirical spectral relationships and statistical performances (RE stands for the percentage relative error) estimated with 20% of the in situ MUMM data.*

Spectral Relationship	Parameters	RE (%)	Bias (%)	R^2	% data with $<$ 10% difference
$\rho_w(748) = \frac{\rho_w(667)}{a+b\rho_w(667)}$	a= 6.32 b = -39	17	-9	0.97	43
$\rho_w(443) = a + b\rho_w(547)$	a=0.0025 b = 0.47	12	3	0.96	52

valid. Hence, the latter could be applied to correct negative $\rho_w(443)$ estimations in the STD NIR-modelling scheme (Section 2.4.2.1).

5.3.2 Theoretical explanation of the red-NIR and NIR-NIR spectral relationships

Empirical spectral relationships largely depend on the used *in situ* data and are subsequently often not universal (Goyens et al., 2013a). However, although the empirically retrieved function parameters (such as suggested in Table 5.1 and by Wang et al. (2012)) may not be valid for diverse water types, the type of relationships may be. Therefore, the present study attempts to confirm the empirically retrieved spectral relationships with a theoretical basis and to understand the meaning of the empirical parameters. Two empirical spectral relationships, potentially useful to force the NIR-modelling schemes of the STD and MUMM AC approaches, are considered; (1) the red-NIR hyperbolic spectral relationship described in the previous section (Eq.(5.1)), and (2) the polynomial NIR spectral relationship suggested by Wang et al. (2012) (Eq.(5.2)).

$$\rho_w(748) = \frac{\rho_w(667)}{6.32 - 39\rho_w(667)} \tag{5.1}$$

$$\rho_w(869) = 0.495\rho_w(748) + 2.185\rho_w(748)^2 \tag{5.2}$$

a. Short reminder of some IOPs, AOPs and other radiometric quantities

To theoretically approximate the red-NIR and NIR polynomial spectral relationships, we start from Eq.(1.20) which relates $\rho_w(\lambda)$ to the IOPs. As suggested in the first chapter of this manuscript, for sub-satellite pixels, $\Re$ can be estimated as ≈ 0.529 (Morel and Gentili, 1996; Doxaran et al., 2002, 2003) and, except for very low Chl_a concentrations, the spectral dependence of the f/Q ratio is considered as relatively small (Loisel and Morel, 2001; Morel et al., 2002; Doxaran et al., 2003; Ruddick et al., 2006) (Section 1.3). Subsequently, in the red and NIR spectral range, the term $\pi f \Re / Q$ (hereafter referred to as ψ) can be considered as wavelength independent such that both $\rho_w(748)/\rho_w(667)$ and $\rho_w(748)/\rho_w(869)$ ratios can be written as a function of the IOPs only:

$$\frac{\rho_w(748)}{\rho_w(667)} = \frac{b_b(748)}{a(748)+b_b(748)} \frac{a(667)+b_b(667)}{b_b(667)} = \frac{b_b(748)a(667)+b_b(748)b_b(667)}{a(748)b_b(667)+b_b(748)b_b(667)} \tag{5.3}$$

$$\frac{\rho_w(748)}{\rho_w(869)} = \frac{b_b(748)}{a(748)+b_b(748)} \frac{a(869)+b_b(869)}{b_b(869)} = \frac{b_b(748)a(869)+b_b(869)b_b(748)}{a(748)b_b(869)+b_b(869)b_b(748)} \tag{5.4}$$

Ruddick et al. (2000, 2006) suggested to approximate the NIR reflectance ratio by the pure water absorption ratio. However, this approximation can not be claimed as universal (Ruddick et al., 2006; Shi and Wang, 2009; Doron et al., 2011; Goyens et al., 2013a).

$b_b(\lambda)$ can be decomposed in particulate and pure water backscattering coefficients as follows:

$$b_b(\lambda) = b_{bp}(\lambda_0)\gamma + b_{bw}(\lambda) \tag{5.5}$$

where $b_{bp}(\lambda_0)$ is the particulate backscattering coefficient at the reference wavelength λ_0 (which is 667 nm in the MODIS Aqua STD AC method) and γ is the backscattering spectral dependency which can take several forms but is often approximated by a power function (e.g., Reynolds et al., 2001; Stramska et al., 2003; Loisel et al., 2006):

$$\gamma = \left[\frac{\lambda_0}{\lambda}\right]^{\eta_{b_b}} \tag{5.6}$$

η_{b_b} depends on the nature of the in-water constituents with values ranging from 0 to 4 (e.g., Loisel et al., 2006). In pure sea water, η_{b_b} reaches values up to 4 and, according to Eq.(5.6), γ values of approximately 1.8 (with λ and λ_0, equal to 490 and 555 nm, respectively). In very turbid waters, η_{b_b} decreases until 0 and γ reaches its minimum value, 1. Lee et al. (2010b) suggested to approximate η_{b_b} as a function of a blue-green remote sensing reflectance ratio:

$$\eta_{b_b} = 2 * \left(1 - 1.2 * e^{-0.9*(R_{rs}(\lambda_B)/R_{rs}(\lambda_G))}\right) \tag{5.7}$$

where $R_{rs}(\lambda_B)$ and $R_{rs}(\lambda_G)$ are the blue and green remote sensing reflectance, respectively (for MODIS Aqua, $\lambda_B = 443$ nm and $\lambda_G = 547$ nm).

Since red and NIR pure water backscattering remain very small (4.10^{-4} m^{-1}, 3.10^{-4} m^{-1} and 1.10^{-4} m^{-1} at 667, 748 and 869 nm, respectively), Eq.(5.5) is often approximated by:

$$b_b(\lambda) = b_b(\lambda_0)\gamma. \tag{5.8}$$

b. Theoretical approximation of red-NIR hyperbolic spectral relationship

According to the above mentioned Eqs.(5.5) and (5.8), Eq.(5.9) can be rewritten as follows:

$$\frac{\rho_w(748)}{\rho_w(667)} = \frac{b_b(748)a(667)}{a(748)b_b(667)+b_b(748)b_b(667)} + \frac{b_b(748)b_b(667)}{a(748)b_b(667)+b_b(748)b_b(667)} \tag{5.9}$$

and, according to Eq.(5.8), simplified as follows:

$$\frac{\rho_w(748)}{\rho_w(667)} = \frac{a(667)}{\frac{a(748)}{\gamma} + b_b(667)} + \frac{b_b(748)}{a(748) + b_b(748)} \tag{5.10}$$

If the second term of the equation, $b_b(748)/(a(748) + b_b(748))$, is written as a function of $\rho_w(748)$ (Eq.(1.20)), Eq.(5.10) becomes:

$$\frac{\rho_w(748)}{\rho_w(667)} = \frac{a(667)}{\frac{a(748)}{\gamma} + b_b(667)} + \frac{\rho_w(748)}{\psi} \tag{5.11}$$

Next, Eq.(5.11) is rewritten in the form $\rho_w(748) = f(\rho_w(667))$ according to the following steps:

$$\rho_w(748) = \left[\frac{a(667)}{\frac{a(748)}{\gamma} + b_b(667)} \right] \rho_w(667) + \frac{\rho_w(667)\rho_w(748)}{\psi} \tag{5.12}$$

$$\rho_w(748) \left[1 - \frac{\rho_w(667)}{\psi} \right] = \left[\frac{a(667)}{\frac{a(748)}{\gamma} + b_b(667)} \right] \rho_w(667) \tag{5.13}$$

$$\rho_w(748) = \frac{\left[\frac{a(667)}{\frac{a(748)}{\gamma} + b_b(667)} \right] \rho_w(667)\psi}{\psi - \rho_w(667)} \tag{5.14}$$

Defining A equal to $a(667)/\left[\frac{a(748)}{\gamma} + b_b(667)\right]$ allows to simplify Eq.(5.14) and to retrieve an hyperbolic function with the same form as the empirical relation (Eq.(5.1)):

$$\rho_w(748) = \frac{\rho_w(667)}{\frac{1}{A} - \frac{1}{A\psi}\rho_w(667)} \tag{5.15}$$

According to Eq.(5.1), the parameter $1/A$ is ≈ 6.32 and the second parameter $1/(A\psi) \approx 39$. A is thus ≈ 0.16 and subsequently also ψ. This involves (assuming $\Re \approx 0.529$) that the ratio f/Q equals 0.096 which is slightly below the average values suggested by Gordon et al. (1988) and by Loisel and Morel (2001) for turbid waters (i.e., 0.11 and 0.13, respectively) but still in the typical range of f/Q values (i.e., 0.08-0.12 according to Morel and Gentili (1996); Morel et al. (2002)). So the empirically retrieved parameters in Eq.(5.1) appear to be meaningful.

For very clear waters, the total absorption $a(667)$ and $a(748)$ can be approximated by $a_w(667)$ and $a_w(748)$, respectively, and $b_b(667)$ by $b_{bw}(667)$ in Eq.(5.14). The ratio f/Q can be approximated by 0.09 for a nearly normal sun and viewing direction and for a Chl_a concentration inferior to 0.03 mg m^{-3} (Morel et al., 2002). Based on our theoretical approximation the hyperbolic curve relating $\rho_w(667)$ to $\rho_w(748)$ can thus be computed for very clear waters. As shown in Fig. 5.2(a), this new clear water red-NIR spectral relationship does not fit well the empirical curve retrieved with our *in situ* coastal waters data (Eq.(5.1)). The term A in Eq.(5.15) is indeed highly sensitive to variations in total absorption and backscattering and thus in variations in in-water constituents. The parameters of the hyperbolic curve are thus function of the water type and, consequently, a single red-NIR hyperbolic model can not be taken as globally valid. Semi-empirical (e.g., Eq.(5.14)) or class-specific spectral relationships should thus be preferred to force NIR-modelling schemes for AC.

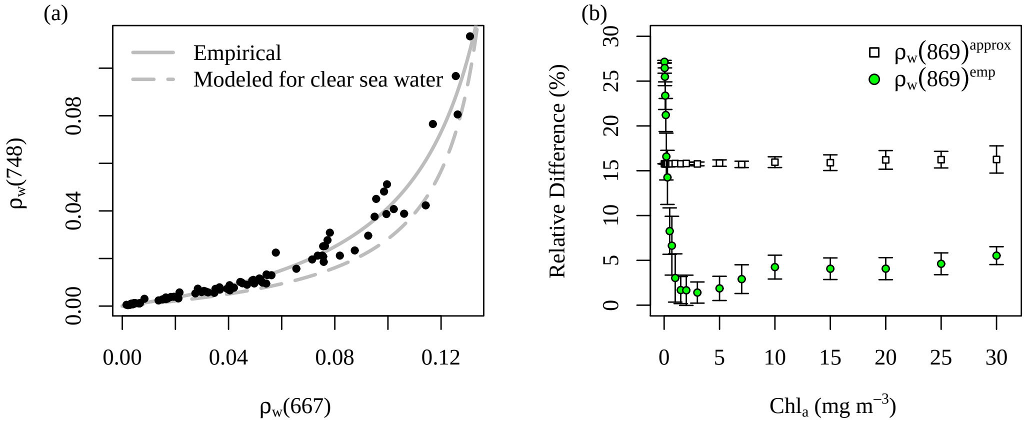

Figure 5.2: *Empirical hyperbolic curve fitted through the in situ MUMMM $\rho_w(667)$ and $\rho_w(748)$ data and theoretical hyperbolic curve according to Eq.(5.14) when considering very clear sea water ($a(667) \approx a_w(667)$, $a(748) \approx a_w(748)$ and, $b_b(667) \approx b_{bw}(667)$) (a), and percentage relative difference between $\rho_w(869)^{sim}$ and $\rho_w(869)^{approx}$ (squares, calculated according to Eq.(5.23)) and between $\rho_w(869)^{sim}$ and $\rho_w(869)^{emp}$ (green circles, estimated with the polynomial function suggested by Wang et al. (2012)) for different levels of Chl_a concentrations (b). The coloured squares correspond to the median relative difference and above and below horizontal bars to the standard deviations.*

c. Theoretical approximation of the NIR polynomial spectral relationship

Similarly to the red-NIR reflectance ratio, $\rho_w(869)$ can be written as a function of $\rho_w(748)$:

$$\rho_w(869) = \rho_w(748) \frac{a(748)b_b(869) + b_b(748)b_b(869)}{a(869)b_b(748) + b_b(869)b_b(748)} \tag{5.16}$$

As noticed previously, in the NIR spectral region, $b_b(\lambda)$ is dominated by $b_{bp}(\lambda)$ such that Eq.(5.16) can be written as:

$$\rho_w(869) = \rho_w(748) \frac{a(748)\frac{b_b(748)}{\gamma} + b_b(748)\frac{b_b(748)}{\gamma}}{a(869)b_b(748) + b_b(748)\frac{b_b(748)}{\gamma}} \tag{5.17}$$

If we multiply numerator and denominator by $\gamma/b_b(748)$, we obtain the following equation (with $\gamma = b_b(869)/b_b(748)$):

$$\rho_w(869) = \rho_w(748) \frac{a(748) + b_b(748)}{\gamma a(869) + b_b(748)} \tag{5.18}$$

Expanding Eq.(5.18) as a sum of two ratios, results in:

$$\rho_w(869) = \rho_w(748) \frac{a(748)}{\gamma a(869) + b_b(748)} + \rho_w(748) \frac{b_b(748)}{\gamma a(869) + b_b(748)} \tag{5.19}$$

In the NIR spectral range, water reflectance is nearly insensitive to phytoplankton as well as to suspended particles and CDOM absorption such that the total absorption can be approximated by $a_w(\lambda)$ (Babin and Stramski, 2002). The sensitivity of the water absorption ratio

$a_w(869)/a_w(748)$ (hereafter referred to as the constant α) to salinity and temperature can also be assumed as negligible (Ruddick et al., 2006). Accordingly, $a(\lambda)$ can be replaced by $a_w(\lambda)$ in Eq.(5.19) and $\alpha = a_w(869)/a_w(748)$ can be considered as universal. Eq.(5.19) becomes then:

$$\rho_w(869) = \rho_w(748)\frac{a_w(748)}{\gamma a_w(869) + b_b(748)} + \rho_w(748)\frac{b_b(748)}{\gamma\alpha a_w(748) + b_b(748)} \tag{5.20}$$

Ruddick et al. (2006) suggested empirical and theoretical α parameters derived from *in situ* measurements and based on the pure water absorption spectrum of Kou et al. (1993) equal to 1.945 and 1.639, respectively. As noticed previously, γ varies between 1.8 and 1 for clear to extremely turbid waters. Hence, if $\gamma\alpha a_w(748)$ greatly exceeds $b_b(748)$, the following assumptions can be made:

$$\frac{\rho_w(748)a_w(748)}{\gamma a_w(869) + b_b(748)} \approx \frac{a_w(748)}{\gamma a_w(869)}\rho_w(748) \tag{5.21}$$

$$\frac{\rho_w(748)b_b(748)}{\gamma\alpha a_w(748) + b_b(748)} \approx \frac{1}{\gamma\alpha\psi}\rho_w(748)^2 \tag{5.22}$$

If these two assumptions are verified, the polynomial function relating $\rho_w(748)$ to $\rho_w(869)$ can be retrieved and Eq.(5.20) becomes:

$$\rho_w(869) = \frac{1}{\gamma\alpha}\rho_w(748) + \frac{1}{\gamma\alpha\psi}\rho_w(748)^2 \tag{5.23}$$

However, the simplifying assumptions in Eqs.(5.21) and (5.22), may not be verified for all water types and for all turbidity ranges. To investigate the impact of these assumptions on the retrieved $\rho_w(869)$, a sensitivity study is conducted using a synthesized dataset built for the IOCCG Report 5 (IOCCG, 2006). This dataset contains 500 spectra in the 400-800 nm range for different illumination geometries constructed with HydroLight radiative transfer simulations. It is particularly useful for the present study since it provides data for $\rho_w(748)$, $b_b(748)$, $a(748)$ and Chl_a concentrations and covers a wide range of water types encountered in the field including a variety of algal and non-algal particle concentrations and CDOM (`http://www.ioccg.org/groups/OCAG_data.html`). For this sensitivity study, $a(869)$ is approximated by the pure water coefficient, $a_w(869)$ (Pope and Fry, 1997).

The simulated $\rho_w(869)$, hereafter referred to as $\rho_w(869)^{sim}$, are computed with Eq.(5.20), avoiding the simplifying assumptions in Eqs.(5.21) and (5.22). The approximated $\rho_w(869)$, hereafter referred to as $\rho_w(869)^{approx}$, are computed with Eq.(5.23) and the empirically derived $\rho_w(869)^{emp}$ are calculated with the empirical polynomial function suggested by Wang et al. (2012) (Table 5.1). To calculate $\rho_w(869)^{sim}$ and $\rho_w(869)^{approx}$, γ is estimated according to Eqs.(5.6) and (5.7). To estimate ψ, $\Re$ is considered as constant (≈ 0.529) and the ratio f/Q is retrieved from the look-up tables suggested by Morel et al. (2002) (assuming a near-nadir viewing angle, with satellite and sun in the same vertical plane) according to the solar zenith angle and Chl_a concentration associated with the corresponding spectra. The percentage relative difference (or percentage bias) between $\rho_w(869)^{sim}$ and $\rho_w(869)^{approx}$, and between $\rho_w(869)^{sim}$ and $\rho_w(869)^{emp}$, respectively, are calculated for each spectra:

$$\text{Relative difference} = 100 * \frac{|\rho_w(869)^{approx,emp} - \rho_w(869)^{sim}|}{\rho_w(869)^{sim}} \tag{5.24}$$

Results are shown in Fig. 5.2(b) for a solar zenith angle of 30° for the different levels of Chl_a concentrations encountered in the simulated dataset. Considering a solar zenith angle of 0° and 60° leads to very similar results (not shown here).

According to Fig. 5.2(b), the approximations in Eqs.(5.21) and (5.22) (i.e., $\rho_w(869)^{approx}$) leads to an average percentage difference of 16% (±0.5%) and the deviance from the average difference increases slightly with an increase in Chl_a concentrations. The empirical spectral relationship as suggested by Wang et al. (2012) leads to significantly better results when the Chl_a concentration exceeds 0.7 mg m^{-3}, with an average percentage difference of 3% (±1.8%). However, for Chl_a concentrations lower or equal to 0.7 mg m^{-3}, which corresponds to $\rho_w(869)^{simil}$ values below 3.10^{-4}, the empirical function results in percentage differences up to 27%. Hence, assumptions made in Eqs.(5.21) and (5.22) to retrieve the polynomial model relating $\rho_w(748)$ to $\rho_w(869)$ does not result in accurate $\rho_w(869)$ retrievals, and in particular for large concentrations of Chl_a. In contrast, the empirical NIR spectral relationship accurately retrieves $\rho_w(869)$ from $\rho_w(748)$ for Chl_a concentrations above 0.7 mg m^{-3}.

d. Conclusion

We can thus conclude that the empirically red-NIR marine spectral relationship relating $\rho_w(667)$ to $\rho_w(748)$ (Eq.(5.1)) is not universally valid. However, the hyperbolic form of the relationship seems to be appropriate for all water types when including function parameters variable according to $a(\lambda)$ at 667 nm and 748 nm and $b_b(667)$. The empirical polynomial function relating $\rho_w(748)$ and $\rho_w(869)$ (Eq.(5.2)), suggested by Wang et al. (2012) and previously validated with turbid coastal *in situ* $\rho_w(\lambda)$ data (Goyens et al., 2013a), shows good agreement with the simulated dataset for Chl_a concentrations ranging from 0.7 mg m^{-3} to 30 mg m^{-3}. For Chl_a concentrations below 0.7 mg m^{-3}, the application of the NIR spectral relationship results in significant errors. Nonetheless, within the STD AC approach when the Chl_a concentration is estimated below or equal to 0.7 mg m^{-3}, $\rho_w(\lambda_{NIR})$ is automatically reset to 0.

Results of the present study suggest that the STD NIR-modelling scheme may be improved by replacing, within the bio-optical model, the interpolation of $b_b(\lambda)$ from the red to the NIR spectral domain (see Section 2.4.2.1) by the red-NIR theoretical spectral relationship and the empirical NIR polynomial function.

5.3.3 Two additional adapted NIR-modelling schemes to improve MODIS Aqua $\rho_w(\lambda)$ retrievals

5.3.3.1 An STD NIR-modelling scheme forced with theoretical and empirical spectral relationships

Goyens et al. (2013a) suggested to constrain the STD NIR-modelling scheme with bounding red equations (Lee et al., 2009) and an empirical NIR polynomial relationship (Wang et al., 2012), referred to as the STD$_{\mathrm{Con}}$ NIR-modelling scheme. Here, with the aim to further improve $\rho_w(\lambda)$ retrievals, both the theoretical red-NIR and empirical blue-green spectral relationships, discussed in previous sections, are used as additional constraints. This new modified STD AC approach is referred to as the STD$_{\mathrm{Contheor}}$ AC method.

As shown in Fig. 5.2, the NIR empirical spectral relationship leads to large inaccuracies in $\rho_w(869)$ retrievals when Chl_a concentrations are below or equal to 0.7 mg m^{-3}. However, as mentioned in Section 5.3.2, this Chl_a concentration corresponds to the threshold for which $\rho_w(\lambda_{NIR})$ is reset to 0 in the STD NIR-modelling scheme. Note that this readjustment is maintained in the iterative method of the new STD$_{\mathrm{Contheor}}$ AC approach.

A schematic overview of the modified STD AC method is given in Fig. 5.3. The blue-green constraint allows to correct for negative $\rho_w(443)$ estimations, used to retrieve the backscattering spectral slope within the bio-optical model (Section 2.4.2.1). This constraint is applied when the estimated $\rho_w(443)$ is negative and provided that $\rho_w(547)$ is positive. The theoretical red-NIR spectral relationship (Eq.(5.14)) replaces the direct interpolation of $b_b(667)$ to $b_b(748)$ to retrieve $\rho_w(748)$.

These new constraints present some significant advantages as illustrated by the following sensitivity study, based on the previously mentioned synthesized dataset of the IOCCG Report

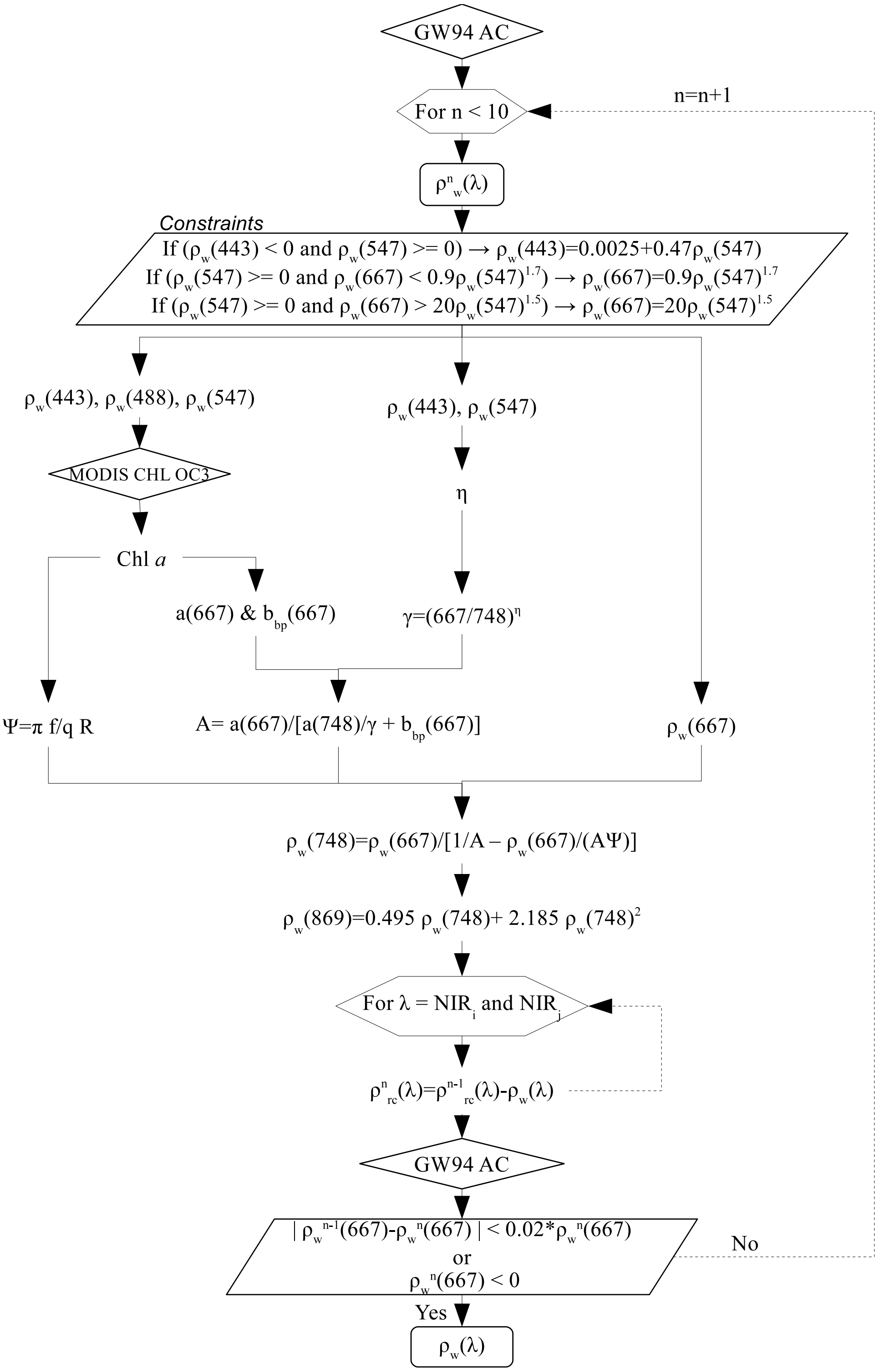

Figure 5.3: *Schematic flowchart of the constrained* $\mathrm{STD}_{\mathrm{Contheor}}$ *AC method.*

5 (IOCCG, 2006). The sensitivity study set up is the following:

1. First, it is considered that both the STD and $\text{STD}_{\text{Contheor}}$ AC approaches perfectly retrieve $\rho_w(\lambda)$. Therefore, for each algorithm, the IOCCG synthesized $\rho_w(\lambda)$ at 443, 547 and 667 nm (IOCCG, 2006) are used as input in the AC algorithm to retrieve $\rho_w(748)$ and $\rho_w(869)$ (hereafter referred to as $\rho_w(\lambda)^P$, i.e., the perfectly retrieved $\rho_w(\lambda)$).

2. Next, the Rayleigh corrected reflectance, $\rho_{rc}(\lambda)$, serving as input for the AC algorithms are simulated for each spectra:

$$\rho_{rc}^{TOA} = \rho_{am}^{TOA}(\lambda) + t(\lambda)\rho_w^P(\lambda). \tag{5.25}$$

   with $t(\lambda)$ being the atmospheric diffuse transmittance and $\rho_{am}(\lambda)$, the multiple-scattering aerosol reflectance. For the latter, a simplified power law model is used:

$$\rho_{am}(\lambda) = \rho_{am}(\lambda_0)\left(\frac{\lambda}{\lambda_0}\right)^{-\eta} \tag{5.26}$$

   with η being the Ångström exponent. For the present study, a coastal model is considered with 50% relative humidity (C50, $\eta = 0.75$). $t(\lambda)$ and $\rho_{am}(\lambda_0)$ (λ_0 is 869 nm) are set equal to 1 and 0.015, respectively.

3. For each algorithm, the sensitivity study is conducted by adding errors within the bio-optical model of ± 10%, ± 20% and ± 50% on Chl_a concentrations, γ and $b_{bp}(\lambda_{red})$.

4. To investigate the sensitivity of the initial STD and modified $\text{STD}_{\text{Contheor}}$ NIR-modelling schemes, the relative difference between the retrieved $\rho_w(\lambda)$ and $\rho_w(\lambda)^P$ at 748 and 869 nm are compared.

Results of the sensitivity study show thus the impact of imperfections on the retrieved Chl_a concentrations, γ and $b_{bp}(\lambda)$, considering that all other parameters are perfectly retrieved. These are shown in Figs. 5.4 and 5.5 for $\rho_w(748)$ and $\rho_w(869)$, respectively.

According to Figs. 5.4 and 5.5, an error on the estimated $b_{bp}(\lambda_{red})$ induces a smaller percentage difference when using the $\text{STD}_{\text{Contheor}}$ NIR-modelling scheme ($\sim$ 1%) compared to the initial STD NIR-modelling scheme (ranging from 9% to 55%). Moreover, the percentage relative difference resulting from errors on the estimated $b_{bp}(\lambda_{red})$ remains almost constant whatever the error when using the $\text{STD}_{\text{Contheor}}$ approach. In contrast, a small error in the spectral dependence of the backscattering coefficient, γ, induces a greater difference on the $\text{STD}_{\text{Contheor}}$ retrieved $\rho_w(\lambda)$ compared to STD retrieved $\rho_w(\lambda)$. For a same error on γ, the $\text{STD}_{\text{Contheor}}$ NIR-modelling scheme induces systematically a percentage relative difference 1% to 2% superior to the percentage relative difference encountered with the initial NIR-modelling scheme. Nevertheless, these percentage differences between the two NIR-modelling schemes are significantly inferior compared to the differences induced with a similar error on $b_{bp}(\lambda_{red})$.

Errors on the estimated Chl_a concentration result in similar percentage differences for $\rho_w(\lambda)$ with both NIR-modelling schemes. Note however that this statement is based on the median relative difference and that some outliers are observed on both Figs. 5.4 and 5.5.

Overall, we can conclude that the $\text{STD}_{\text{Contheor}}$ approach is less sensitive to errors on $b_{bp}(\lambda_{red})$ compared to the initial STD algorithm. Knowing that the bio-optical model, used in both the STD and $\text{STD}_{\text{Contheor}}$ NIR-modelling schemes, largely relies on $b_{bp}(\lambda_{red})$ to estimate $\rho_w(\lambda)$ at 748 and 869 nm, reducing the sensitivity to errors on $b_{bp}(\lambda_{red})$ represents a large advantage.

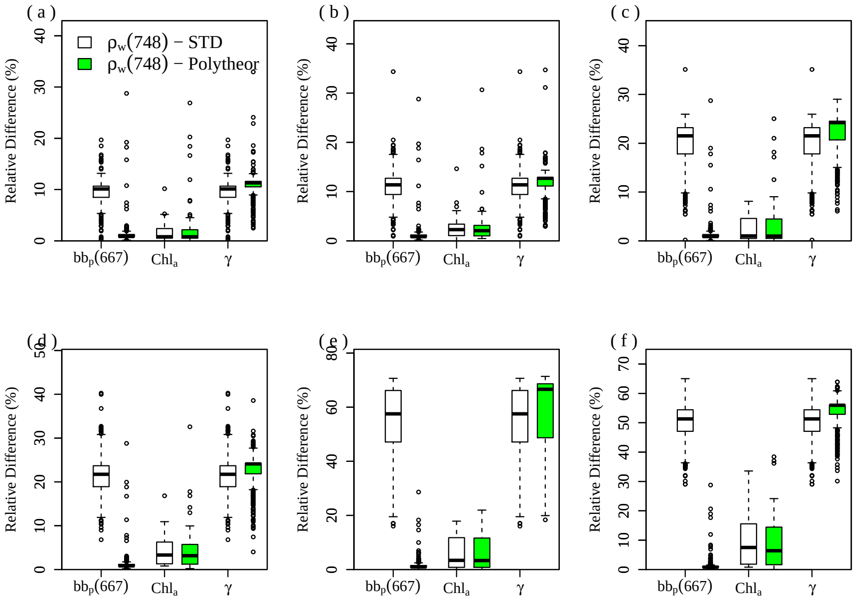

Figure 5.4: *Percentage relative difference between $\rho_w^P(748)$ (estimated as if the STD and the* STD$_{\text{Contheor}}$ *NIR-modelling schemes perfectly retrieved $\rho_w(\lambda)$) and $\rho_w(748)$ retrieved when errors are added to $b_{bp}(\lambda_{red})$, Chl_a and γ within both NIR-modelling schemes (a: +10%, b: -10%, c: +20%, d: -20%, e: +50%, f: -50%). Box plots indicate median with first and third quartiles, upper and lower whiskers and outliers (± 1.5IQR).*

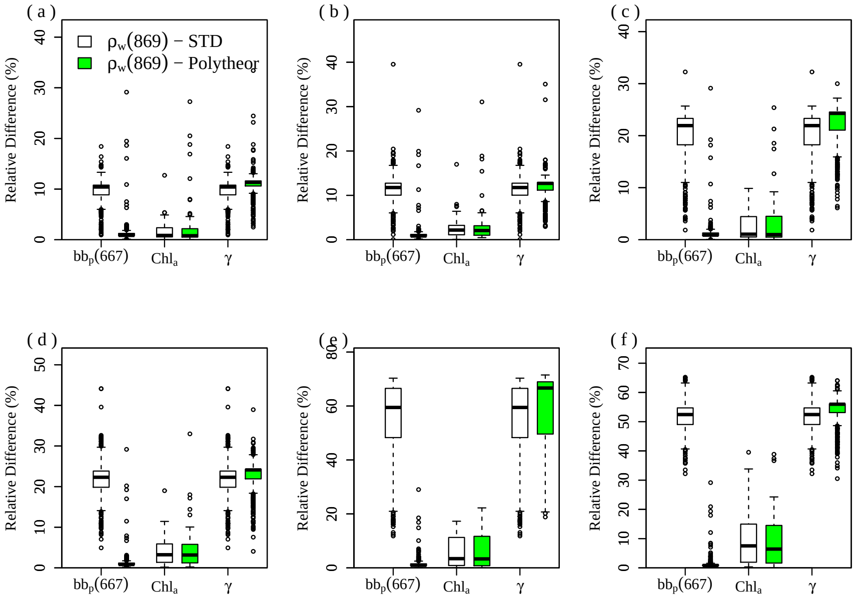

Figure 5.5: *Same as Fig. 5.4 but for $\rho_w(\lambda)$ at 869 nm.*

5.3.3.2 A combined $\mathrm{MUMM_{Poly}}$ and $\mathrm{STD_{Contheor}}$ NIR-modelling scheme for AC

The $\mathrm{MUMM_{Poly}}$ and $\mathrm{STD_{Contheor}}$ NIR-modelling schemes have been evaluated and compared in the previous sections and by Goyens et al. (2013b). Results indicated that when the $\mathrm{STD_{Con}}$ algorithm failed to retrieve $\rho_w(\lambda)$ (e.g., non-physical negative values), the $\mathrm{MUMM_{Poly}}$ approach often succeeded. Similarly, it was also observed in Chapter 4 and by Goyens et al. (2013c), that, overall, the initial STD AC algorithm tended to better retrieve $\rho_w(\lambda)$ compared to the NN, MUMM and NIR-SWIR AC algorithms, but that the MUMM approach ensured a larger spatial coverage. Accordingly, in order to reduce the number of excluded match-up pairs due to AC failure or erroneously retrieved Chl_a concentrations (i.e., an important limitation of the STD AC approach), a second modified NIR-modelling scheme is suggested consisting in combining the $\mathrm{MUMM_{Poly}}$ and $\mathrm{STD_{Contheor}}$ approaches (referred hereafter to as the COMB AC approach). A schematic overview of the combined $\mathrm{MUMM_{Poly}}$ and $\mathrm{STD_{Contheor}}$ AC method is given in Fig. 5.6.

In the COMB AC approach, the $\mathrm{MUMM_{Poly}}$ NIR-modelling scheme (including the hypothesis of spatial homogeneity in NIR aerosol reflectance ratio) is used when the estimated $\rho_w(\lambda_{NIR})$ is superior to $\rho_{rc}(NIR)$ (resulting in negative $\rho_{am}(\lambda)$) or when a Chl_a failure flag is assigned to a spectra (resulting from negative $\rho_w(\lambda)$ estimations in the blue and green spectral region and subsequently in non-physical Chl_a concentrations and $\rho_w(\lambda)$ estimations). In the initial STD AC approach, when such conditions occur, the iteration is re-initialized assuming $\rho_w(\lambda)$ equals $\rho_{rc}(\lambda)$ ($\rho_{am}(\lambda) = 0$) and the Chl_a concentration is set to 10 mg m^{-3} (Bailey et al., 2010). With the COMB AC approach, if at a given iteration such conditions occur, the algorithm switches towards the $\mathrm{MUMM_{Poly}}$ NIR-modelling scheme. Next, the estimated $\rho_w(\lambda_{NIR})$ is removed from $\rho_{rc}(\lambda_{NIR})$ and the GW94 AC algorithm is applied. If $\rho_w(\lambda_{red})$ does not converge after this switch and the maximum number of iterations is not exceeded, the COMB NIR-modelling scheme iterates again with the $\mathrm{STD_{Contheor}}$ approach. Accordingly, with the COMB NIR-modelling scheme, a retrieved $\rho_w(\lambda)$ spectra is considered as non-valid only when either the maximum number of iterations is attained or when non-physical Chl_a concentrations are retrieved or atmospheric correction failure flags are assigned more than twice to the same spectrum.

A sensitivity study comparable to the study conducted by Goyens et al. (2013b) has been performed to evaluate and compare the performances of the $\mathrm{MUMM_{Poly}}$, $\mathrm{STD_{Contheor}}$ and the COMB NIR-modelling schemes for AC. Results are shown in Fig. 5.7. For both the $\mathrm{MUMM_{Poly}}$ and COMB NIR-modelling schemes two cases are included, one considering that the aerosol properties are well retrieved from nearby clear water pixels and one considering that the aerosol model is not correctly estimated (i.e., the C90 aerosol model is selected in the sensitivity study while the C50 aerosol model is used to construct the simulated $\rho_{rc}(\lambda)$). The performances of the different approaches are evaluated in terms of percentage bias between retrieved and *in situ* $\rho_w(\lambda)$ at 412, 547, 667, 748 and 869 nm. The sensitivity study is conducted for the 105 *in situ* data from the MUMM dataset and for moderately (Fig. 5.7(a-e), 49 spectra out of 105) and very (Fig. 5.7(f-j), 56 spectra out of 105) turbid waters. Among the very turbid waters, we also distinguish the extremely turbid waters (Fig. 5.7(k-o), 24 spectra out of 105).

For moderately turbid waters, all approaches retrieve the same number of valid $\rho_w(\lambda)$ (i.e., 49). For this turbidity level, the COMB algorithm does not turn to the $\mathrm{MUMM_{Poly}}$ NIR-modelling scheme (no flags are encountered for Chl_a concentration and/or atmospheric correction failure). Hence, the $\mathrm{STD_{Contheor}}$ and the COMB AC show the same performance with median bias between *in situ* and modelled $\rho_w(\lambda)$ ranging from -54% to -2% (with the smallest and largest percentages encountered at 547 and 869 nm, respectively, Fig. 5.7(a-e)). The $\mathrm{MUMM_{Poly}}$ NIR-modelling scheme also tends to underestimate the signal with median biases ranging from -41% to -2%. In contrast, if the C90 aerosol model is selected, instead of the correct C50 aerosol model, $\rho_w(\lambda)$ is greatly overestimated with median biases ranging from 17% to 139%. Hence, for this turbidity level, the $\mathrm{STD_{Contheor}}$ should be preferred when information

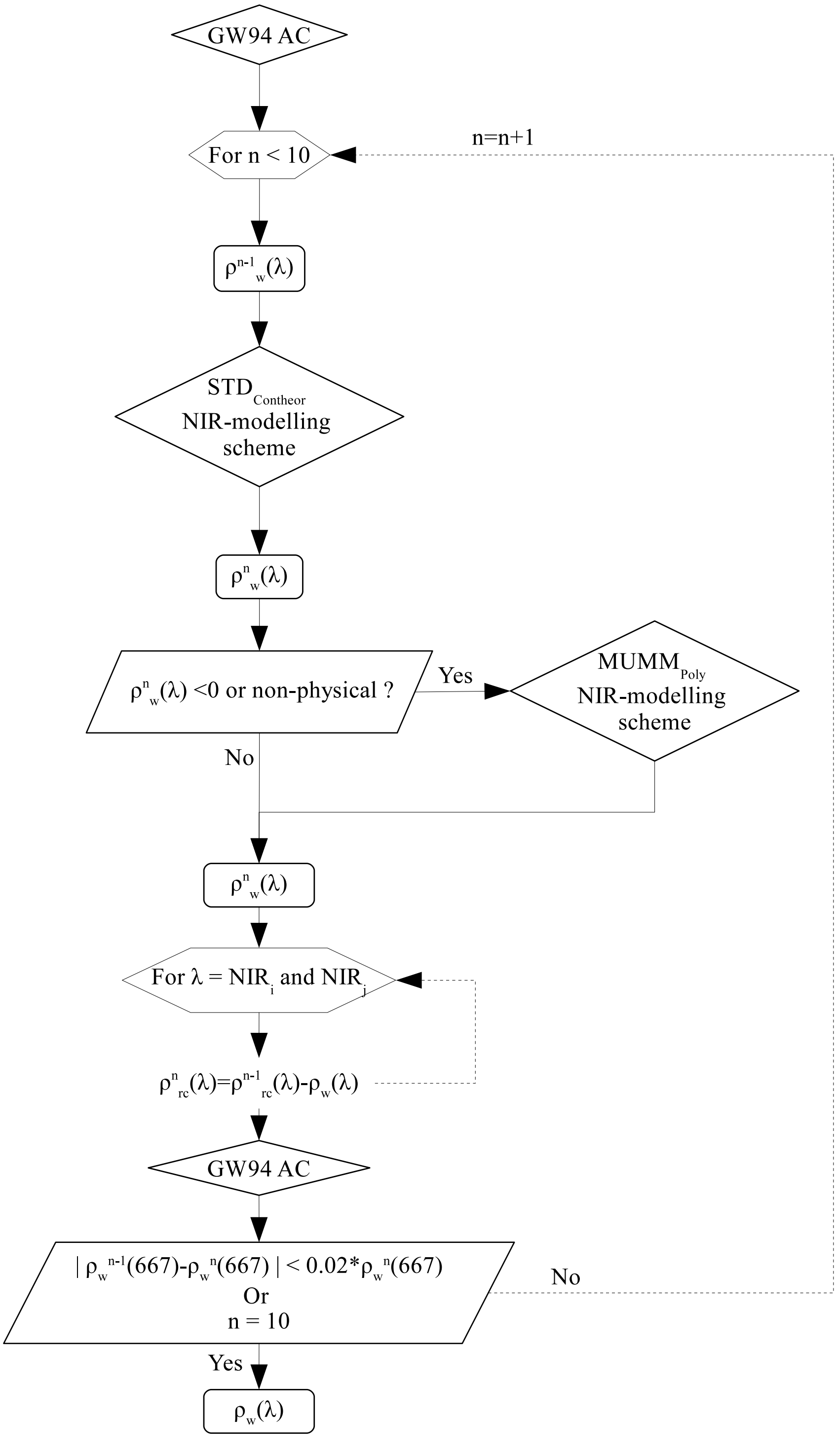

Figure 5.6: *Schematic flowchart of the combined* $\mathrm{MUMM_{Poly}}$ *and* $\mathrm{STD_{Contheor}}$ *AC method.*

about atmospheric aerosols is missing.

For very turbid waters, the number of retrieved $\rho_w(\lambda)$ differs. The COMB AC approach shows performances similar to the $\mathrm{STD}_{\mathrm{Contheor}}$ algorithm (percentage bias ranging from 2% to 12%) but retrieved 7% more valid $\rho_w(\lambda)$ spectra (49 versus 46 spectra). Compared to the $\mathrm{MUMM}_{\mathrm{Poly}}$ AC approach, it retrieves about 12% less valid $\rho_w(\lambda)$ spectra (56 versus 49 spectra). Hence, the COMB AC approach still retrieves less spectra compared to the $\mathrm{MUMM}_{\mathrm{Poly}}$ approach.

Percentage median bias for very turbid waters are the smallest at all wavelengths when using the $\mathrm{MUMM}_{\mathrm{Poly}}$ NIR-modelling scheme, provided that the aerosol model is correctly retrieved (median bias ranging from 0 to 5%, Fig. 5.7(f-j)). For this turbidity level, the $\mathrm{MUMM}_{\mathrm{Poly}}$ NIR-modelling scheme is also less sensitive to erroneously retrieved aerosol models (the median bias does not exceed 25% with the $\mathrm{MUMM}_{\mathrm{Poly}}$ NIR-modelling scheme). However, if spatial homogeneity in aerosol reflectance is not verified, the $\mathrm{STD}_{\mathrm{Contheor}}$ AC method should be preferred (percentage median biases vary between 2% and 12%, Fig. 5.7(f-j)).

For the extremely turbid waters the COMB AC approach retrieves about 20% more valid $\rho_w(\lambda)$ spectra relative to the $\mathrm{STD}_{\mathrm{Contheor}}$ algorithm but 30% less than the $\mathrm{MUMM}_{\mathrm{Poly}}$ approach (17, 14 and 24 spectra for the COMB, $\mathrm{STD}_{\mathrm{Contheor}}$ and $\mathrm{MUMM}_{\mathrm{Poly}}$ approaches, respectively). For this turbidity level, the $\mathrm{MUMM}_{\mathrm{Poly}}$ approach also provided significantly better results compared to the $\mathrm{STD}_{\mathrm{Contheor}}$ approach (median biases vary between 1% and 4%, and between -28% and -4%, with the $\mathrm{MUMM}_{\mathrm{Poly}}$ and $\mathrm{STD}_{\mathrm{Contheor}}$ AC method, respectively, Fig. 5.7(k-o)). However, when the C90 aerosol model is selected (instead of the correct C50 aerosol model), $\rho_w(\lambda)$ is overestimated (median bias ranging from 5% to 25%).

Hence, for moderately and very turbid waters the $\mathrm{STD}_{\mathrm{Contheor}}$ AC method performs better, while for extremely turbid waters the $\mathrm{MUMM}_{\mathrm{Poly}}$ AC approach should be preferred. The COMB AC approach appears to be a good compromise since it results in a greater spatial coverage, compared to the $\mathrm{STD}_{\mathrm{Contheor}}$ AC approach, and its sensitivity to erroneously retrieved clear water-aerosol properties is reduced compared to the $\mathrm{MUMM}_{\mathrm{Poly}}$ NIR-modelling scheme.

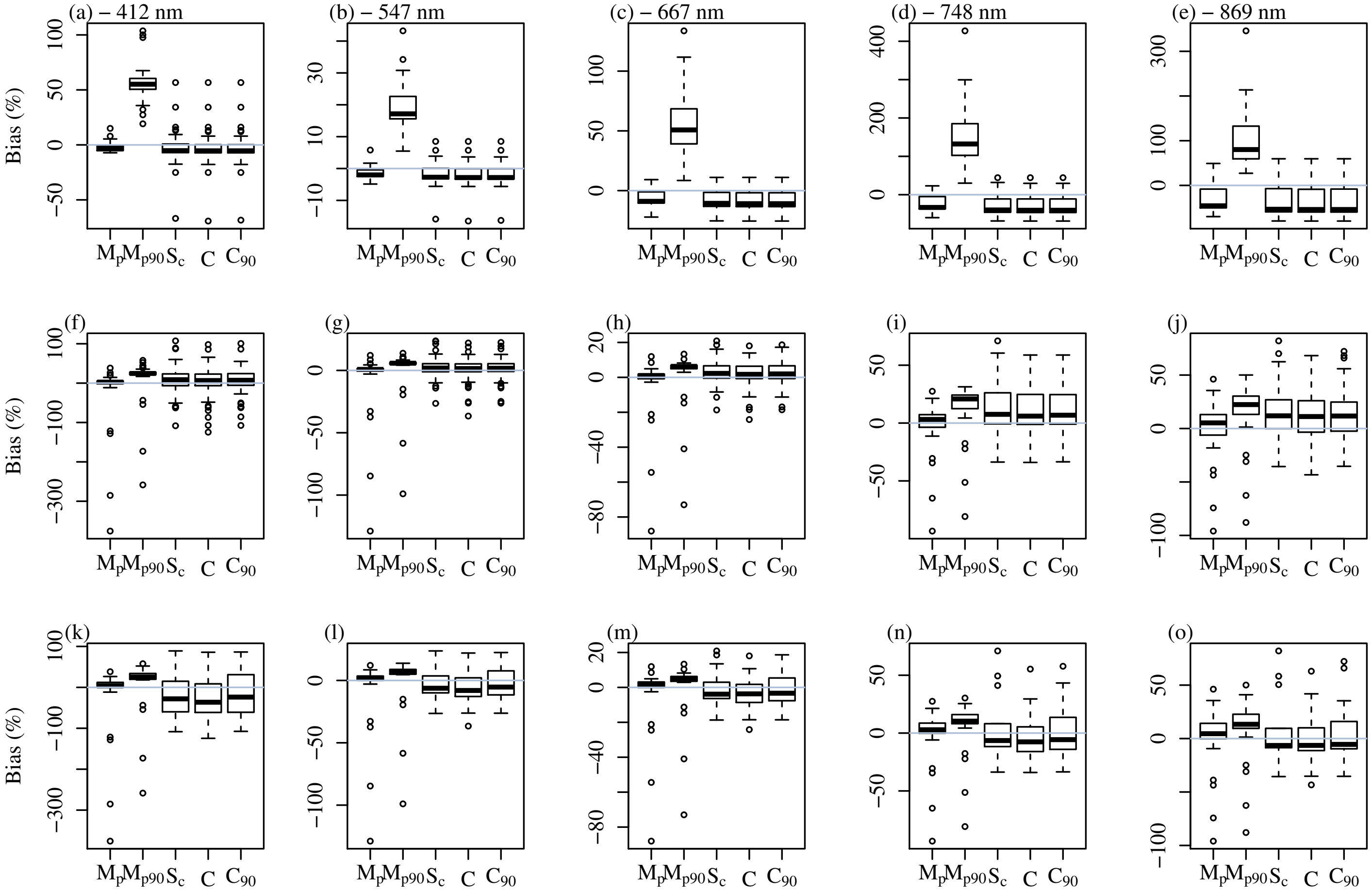

Figure 5.7: *Percentage bias between retrieved and in situ* $\rho_w(\lambda)$ *spectra at 412, 547, 667, 748 and 869 nm.* $\mathrm{M_p}$ *stands for* $\mathrm{MUMM_{Poly}}$ *when assuming correct clear water pixel aerosol properties,* $\mathrm{M_{p90}}$ *for* $\mathrm{MUMM_{Poly}}$ *when considering the incorrect C90 aerosol model,* $\mathrm{S_c}$ *for the* $\mathrm{STD_{Contheor}}$*, and C and* $\mathrm{C_{90}}$ *for the COMB AC approach when considering the correct C50 and incorrect C90 aerosol model, respectively. Results are shown for moderately (first row) and very (second row) turbid waters, and when considering only extremely turbid waters (third row). Box plots indicate median with first and third quartiles, upper and lower whiskers and outliers (small circles, ± 1.5IQR).*

5.3.3.3 Evaluation of the different modified NIR-modelling schemes for AC and comparison with the initial approaches.

In this section a sensitivity study is conducted similar to the sensitivity study conducted by Goyens et al. (2013b)(based on the 105 MUMM *in situ* $\rho_w(\lambda)$ spectra and including a simplified power law model for the multiple scattering aerosol reflectance) to compare and evaluate the performances of all the modified NIR-modeling schemes suggested in the previous sections. For each modified NIR-modelling scheme (i.e., $\mathrm{MUMM_{Poly}}$, $\mathrm{STD_{Contheor}}$, and COMB approach) and the initial MUMM and STD AC approaches, the median bias between *in situ* and estimated $\rho_w(\lambda)$ are compared, for moderately (Fig. 5.8(a)) and very (Fig. 5.8(b)) turbid waters, and when considering only the most extremely turbid waters (Fig. 5.8(c)). Table 5.2 shows the number of retrieved $\rho_w(\lambda)$ for each turbidity level. For the initial MUMM, $\mathrm{MUMM_{Poly}}$ and COMB AC approaches, the performance is also investigated when an erroneous aerosol model is selected from the nearby clear water pixels (the C90 aerosol model is assumed while the C50 aerosol model is used to simulate $\rho_{rc}(\lambda)$, referred to as $\mathrm{MUMM_{C90}}$, $\mathrm{MUMM_{Poly-C90}}$ and $\mathrm{COMB_{C90}}$).

Table 5.2: *Number of retrieved valid $\rho_w(\lambda)$ spectra per AC approach and per turbidity level.*

NIR-modelling scheme	Moderately (out of 49 spectra)	Very (out of 56 spectra)	Extremely (out of 24 spectra)
STD	49	46	14
MUMM	49	56	24
$\mathrm{MUMM_{C90}}$	49	56	24
$\mathrm{MUMM_{Poly}}$	49	56	24
$\mathrm{MUMM_{Poly-C90}}$	49	56	24
$\mathrm{STD_{Contheor}}$	49	46	14
COMB	49	49	17
$\mathrm{COMB_{C90}}$	49	48	16

For the moderately turbid waters, the STD-based NIR-modelling schemes (i.e., the initial STD, $\mathrm{STD_{Contheor}}$ and COMB approaches) result in similar median biases ranging from 0 to -50%. The MUMM and $\mathrm{MUMM_{Poly}}$ AC approaches seem to be highly sensitive to the aerosol properties selected from the nearby clear water pixels resulting in large $\rho_w(\lambda)$ errors when these are erroneously retrieved (median bias exceeding 130%). In contrast, when the aerosol properties are correctly retrieved, these NIR-modelling schemes perform slightly better than the STD-based NIR-modelling schemes.

As mentioned previously, for very turbid waters, the MUMM and $\mathrm{MUMM_{Poly}}$ algorithms retrieve the largest number of valid $\rho_w(\lambda)$ spectra followed by the COMB AC approach (Table 5.2). When the aerosol properties are correctly retrieved from the nearby clear water pixels, the $\mathrm{MUMM_{Poly}}$ AC approach tends to slightly overestimate $\rho_w(\lambda)$ with positive median biases ranging from 0 to 5%, while the initial MUMM algorithm underestimates $\rho_w(\lambda)$ with negative biases up to -5%. The STD approach significantly underestimates $\rho_w(\lambda)$ in the blue spectral region and overestimate $\rho_w(\lambda)$ in the NIR (median biases varying from -13% in the blue to 21% in the NIR spectral domain). The COMB and constrained $\mathrm{STD_{Contheor}}$ algorithms result in very similar $\rho_w(\lambda)$ retrievals (median bias varying between 1% and 11% with both NIR-modelling schemes) suggesting that the switch towards the $\mathrm{MUMM_{Poly}}$ NIR-modelling scheme rarely occurs or that even with this reset, the spectra are considered as non valid (i.e., flagged more than twice or the maximum iteration number is exceeded).

For extremely turbid waters, the $\mathrm{MUMM_{Poly}}$ NIR-modelling scheme returns the best results, provided that the aerosol properties are correctly retrieved from the nearby clear water pixels (median bias ranging from 1% to 4%), while the STD NIR-modelling scheme results in the largest retrieval errors (median bias ranging from -60% to 16%). The COMB and $\mathrm{STD_{Contheor}}$ approaches perform relatively well with a median bias varying between -30 and -3%.

Hence, according to Fig. 5.8 and Table 5.2, the $\mathrm{MUMM_{Poly}}$ NIR-modelling scheme shows significant improvements compared to the initial MUMM approach, particularly in very and

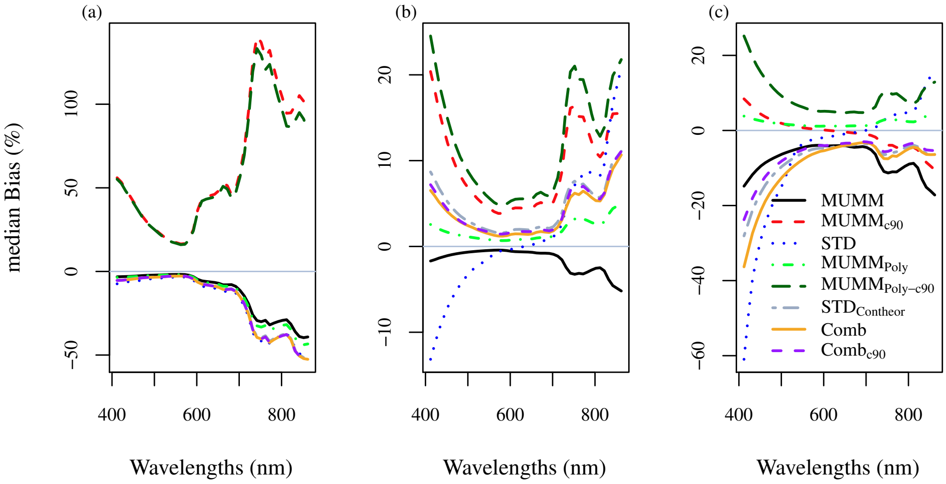

Figure 5.8: *Median relative difference as a function of wavelength between in situ and retrieved* $\rho_w(\lambda)$ *for (a) moderately and (b) very turbid waters and (c) when considering only extremely turbid waters (*$\rho_w(869) > 10^{-2}$*) with the initial MUMM and STD, the* $\mathrm{MUMM_{Poly}}$ *(assuming correct clear water pixel aerosol properties), the* $\mathrm{MUMM_{Poly-c90}}$ *(assuming the incorrect C90 aerosol model), the* $\mathrm{STD_{Contheor}}$*, the COMB (assuming the correct aerosol properties) and* $\mathrm{COMB_{c90}}$ *(assuming the incorrect C90 aerosol model) NIR-modelling schemes for AC.*

extremely turbid waters. However, it is still affected by its sensitivity to the retrieved aerosol properties from nearby clear water pixels and in particular over moderately turbid waters. The $\mathrm{STD_{Contheor}}$ NIR-modelling scheme returns better results relative to the initial STD algorithm. However, it is affected by Chl_a concentration and AC failure flags reducing the number of retrieved valid spectra. Consequently, the COMB AC approach presents a good alternative to retrieve more valid $\rho_w(\lambda)$ spectra by using the $\mathrm{MUMM_{Poly}}$ NIR-modelling scheme when the Chl_a concentration is not a valid proxy to estimate $\rho_w(\lambda_{NIR})$ or if the first guess in $\rho_w(\lambda)$ exceeds $\rho_{rc}(\lambda)$. Note however, that the switch between the $\mathrm{MUMM_{Poly}}$ and $\mathrm{STD_{Contheor}}$ schemes may result in non-physical spatially heterogeneous $\rho_w(\lambda)$ patterns.

5.3.4 The appropriate solution for $\rho_w(748)$ within the $\mathrm{MUMM_{Poly}}$ NIR-modelling scheme

Goyens et al. (2013b) demonstrated how the MUMM algorithm could be extended to extremely turbid waters by replacing the constant NIR reflectance ratio (Ruddick et al., 2000, 2006) by a NIR polynomial function (Wang et al., 2012) (Eq.(5.2)). This included, however, some modifications in the initial MUMM NIR-modelling scheme.

Goyens et al. (2013b) found the following quadratic function:

$$b\epsilon t^*_{869}\rho_w(748)^2 + (a\epsilon t^*_{869} - t^*_{748})\rho_w(748) + [\rho_{rc}(748) - \epsilon\rho_{rc}(869)] = 0 \qquad (5.27)$$

with a and b being the function parameters of the polynomial relationship (Eq.(5.2), Wang et al. (2012)). Accordingly, if the Rayleigh corrected reflectance, $\rho_{rc}(\lambda)$, the transmittance coefficients, t^*_λ, and the aerosol reflectance ratio ϵ are known, the water signal at 748 nm and, subsequently, at 869 nm can be derived.

Similarly to the MUMM AC algorithm (detailed in Section 2.4.2.2), ϵ is retrieved from the nearby clear water pixels, t^*_λ is calculated given the viewing and incident geometry and selected aerosol model, and $\rho_{rc}(\lambda)$ is estimated from the sensor measured signal after subtraction of sun glint, Rayleigh and white caps reflectance (Gordon and Wang, 1994). Hence, as mentioned by Goyens et al. (2013b), Eq.(5.27) is a quadratic polynomial function with an unknown quantity, $\rho_w(748)$, and for which two solutions exist:

$$\rho_w(748) = \frac{[t^*_{748} - a\epsilon t^*_{869}] \pm \sqrt{[a\epsilon t^*_{869} - t^*_{748}]^2 - 4b\epsilon t^*_{869}[\rho_{rc}(748) - \epsilon\rho_{rc}(869)]}}{2b\epsilon t^*_{869}} \tag{5.28}$$

However, in reality, only one unique solution exists for $\rho_w(748)$. Indeed, as mentioned by Goyens et al. (2013b), the positive root in Eq.(5.28) is non-physical. This can be demonstrated as follows. Taking the positive square root involves that the second term in the nominator is positive. Accordingly, the following inequality can be stated:

$$\rho_w(748) \geqslant \frac{[t^*_{748} - a\epsilon t^*_{869}]}{2b\epsilon t^*_{869}} \tag{5.29}$$

Since the two transmittance coefficients t^*_{748} and t^*_{869} are usually very close (t^*_{748} and t^*_{869} differ from each other by about 1% for the same geometry and aerosol model (Shettle and Fenn, 1979; Gordon and Wang, 1994)), we can approximate Eq.(5.29) by the following equation:

$$\rho_w(748) \geqslant \frac{[1 - a\epsilon]}{2b\epsilon} \tag{5.30}$$

with the function parameters a and b being equal to 0.495 and 2.185 as given in Eq.(5.2) and suggested by Wang et al. (2012). The minimum $\rho_w(748)$ value in Eq.(5.30) can thus be estimated as a function of ϵ, ranging approximately from 0.9 to 1.5 when considering oceanic, maritime, coastal and tropospheric aerosol models with relative humidities varying between 50 and 99% (Fig. 2.3, Section 2.4.1). Fig. 5.9(a) shows the minimum value for $\rho_w(748)$ according to Eq.(5.30) and as a function of ϵ. According to this figure, with the positive square root, the minimum $\rho_w(748)$ estimations, and subsequent estimated $\rho_w(869)$ (when solving the NIR polynomial function), represent extremely turbid waters ($> 10^{-2}$), and this whatever the selected aerosol model. Hence, taking the positive square root may thus lead to erroneous $\rho_w(\lambda)$ retrievals since it will often result in $\rho_w(\lambda_{NIR})$ estimations greatly exceeding the $\rho_w(\lambda_{NIR})$ values encountered in the oceans.

The non-valid positive solution for $\rho_w(748)$ can also be demonstrated with the simulated dataset computed for the sensitivity studies outlined in the previous sections (IOCCG, 2006). As done for the sensitivity studies conducted by Goyens et al. (2013b) and outlined in Section 5.2.3, $\rho_{rc}(\lambda)$ is simulated assuming a fixed aerosol model, and associated Ångström coefficient, and a simplified power law model for the multiple-scattering aerosol reflectance, $\rho_{am}(\lambda)$. Next, the transmittance coefficients t^*_{748} and t^*_{869} are set equal to 1 and ϵ is estimated from the simulated NIR $\rho_{am}(\lambda)$ ratio. $\rho_w(748)$ can then be estimated according to Eq.(5.28) and $\rho_w(869)$ with the NIR polynomial relationship. Fig. 5.9(b) shows the resulting $\rho_w(\lambda_{NIR})$ with the positive and negative square roots, and when considering a coastal aerosol model with 50% relative humidity. This plot clearly indicates the systematic and significant overestimation of $\rho_w(\lambda_{NIR})$ when considering the positive square root. In contrast, when taking the negative root, most spectra fall on the 1:1 line (data points located away from the 1:1 line correspond to the *in situ* data measured in the coastal regions of French Guiana and for which the NIR polynomial function suggested by Wang et al. (2012) appeared to be invalid, see Goyens et al. (2013a)). Hence, the unique solution for $\rho_w(748)$ for the NIR-modelling scheme of the MUMM AC approach should be:

$$\rho_w(748) = \frac{[t^*_{748} - a\epsilon t^*_{869}] - \sqrt{[a\epsilon t^*_{869} - t^*_{748}]^2 - 4b\epsilon t^*_{869}[\rho_{rc}(748) - \epsilon\rho_{rc}(869)]}}{2b\epsilon t^*_{869}} \tag{5.31}$$

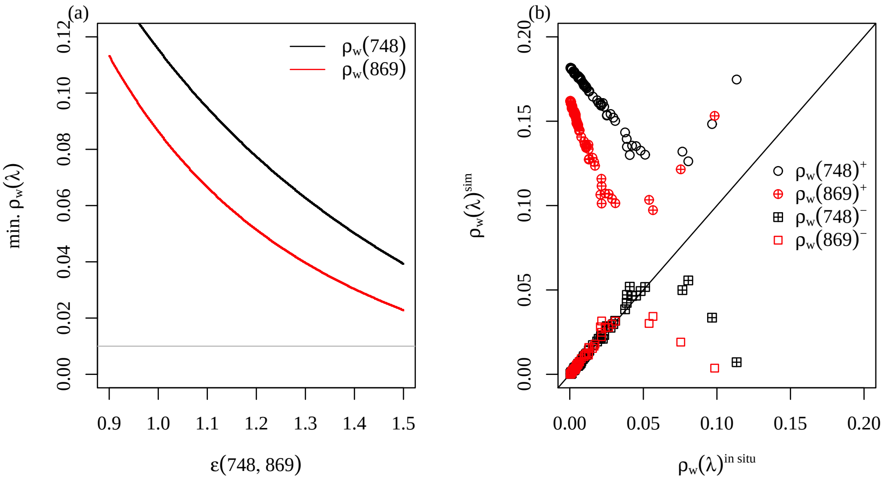

Figure 5.9: *Minimum estimated $\rho_w(\lambda)$ at 748 nm (black line) and 869 nm (red line) as a function of ϵ. Grey line corresponds to the extremely turbid water threshold ($\rho_\lambda > 10^{-2}$) (a), and simulated versus in situ $\rho_w(\lambda)$ at 748 and 869 nm when considering the positive and negative root for the solution of $\rho_w(748)$ (referred to as $\rho_w(\lambda)^+$ and $\rho_w(\lambda)^-$, respectively) (b).*

5.4 CONCLUSION

The present chapter focused on spectral relationships and their potential to improve NIR-modelling schemes for satellite $\rho_w(\lambda)$ retrievals. Numerous spectral relationships were found in the literature and most have been developed with the aim to improve red and NIR-modelling schemes to retrieve $\rho_w(\lambda)$ in optically complex waters. A validation of these spectral relationships resulted in a published paper entitled: "Spectral relationships for atmospheric correction. I. Validation of red and near infra-red spectral relationships" (Goyens et al., 2013a).

From this validation study, we found that the bounding red equations suggested by Lee et al. (2009), to correct satellite retrieved $\rho_w(667)$ estimations for the Quasi-Analytical Algorithm (QAA), and the NIR polynomial function used to estimate $\rho_w(869)$ from $\rho_w(748)$ (Wang et al., 2012) were valid for moderately to extremely turbid waters. The potential of these red and NIR spectral relationships to improve satellite retrieved $\rho_w(\lambda)$, was investigated in a second paper entitled "Spectral relationships for atmospheric correction algorithms. II. Improving the NASA Standard and MUMM atmospheric correction algorithms" (Goyens et al., 2013b). Results from the sensitivity studies conducted in this paper, showed that the STD NIR-modelling scheme forced with the red and NIR spectral relationships performed better for all turbidity ranges and, in particular in the blue spectral domain, compared to the initial STD scheme. Results also demonstrated that replacing the constant NIR reflectance ratio by the NIR polynomial spectral relationship within the MUMM NIR-modelling scheme, reduced the $\rho_w(\lambda)$ retrieval errors and, in particular, in extremely turbid waters. The constrained STD ($\text{STD}_{\text{Contheor}}$) and polynomial-based MUMM ($\text{MUMM}_{\text{Poly}}$) NIR-modelling schemes presented thus better results relative to the initial approaches. However, for both schemes, the added value of the spectral relationships was slightly reduced due to a decrease in valid retrieved $\rho_w(\lambda)$ spectra with the $\text{STD}_{\text{Contheor}}$ NIR-modelling scheme and an increase in sensitivity to erroneously retrieved aerosol properties with the $\text{MUMM}_{\text{Poly}}$, compared to the initial approaches.

Next, to further investigate the potential of spectral relationships to improve NIR-modelling schemes for AC, additional spectral relationships were suggested, a red-NIR spectral relationship, relating $\rho_w(667)$ and $\rho_w(748)$ with an hyperbolic function, and a blue-green linear spectral relationship relating $\rho_w(443)$ and $\rho_w(547)$. In order to have a better insight in the validity of the spectral relationships, I also attempted to find a theoretical basis for the empirically retrieved spectral relationships. This was done based on radiative transfer simulated data (IOCCG, 2006) and resulted in the following conclusions. The empirically red-NIR spectral relationship parameters appeared to be only valid for turbid waters, but the hyperbolic form of the relationship appeared to be valid for all water types. In contrast, the empirical polynomial function relating $\rho_w(748)$ and $\rho_w(869)$ (Wang et al., 2012) fitted well with the simulated dataset while no theoretical basis of this empirical function was found adequate for all water types. Hence, the STD NIR-modelling scheme may be improved by replacing, within the bio-optical model, the interpolation of $b_b(\lambda)$ from the red to the NIR spectral domain by the theoretical red-NIR hyperbolic and empirical NIR polynomial spectral relationships, and, by adding the red bounding and blue-green spectral constraints. This new modified scheme was referred to as $\mathrm{STD_{Contheor}}$ NIR-modelling scheme.

Following the conclusion made by Goyens et al. (2013b), a second modified NIR-modelling scheme was also suggested combining the $\mathrm{STD_{Contheor}}$ and $\mathrm{MUMM_{Poly}}$ schemes, referred to as the COMB AC method. This combined algorithm presented a good alternative to retrieve more valid $\rho_w(\lambda)$ spectra by using the $\mathrm{MUMM_{Poly}}$ NIR-modelling scheme when Chl_a concentrations were erroneously retrieved with the $\mathrm{STD_{Contheor}}$ method or if the first guess in $\rho_w(\lambda)$ exceeds $\rho_{rc}(\lambda)$.

Overall, sensitivity studies conducted in this chapter showed that the modified NIR-modelling schemes (i.e., $\mathrm{STD_{Contheor}}$, $\mathrm{MUMM_{Poly}}$ and COMB NIR-modelling schemes) presented promising results with improved $\rho_w(\lambda)$ retrievals and/or broader spatial coverages compared to the initial schemes (i.e., STD and MUM). Nonetheless, these improved NIR-modelling schemes should be evaluated with actual satellite data. Indeed, compared to the sensitivity studies, a validation based on satellite data includes, among others, a more complex set of aerosol models which may reduce the added value of the modified NIR-modelling schemes. Moreover, aerosol reflectance is computed according to the nearest two discrete aerosol models. Hence, improvement with the modified NIR-modelling schemes may still not be accurate enough to retrieve the correct $\rho_{am}(\lambda_{NIR})$ and, subsequently, the appropriate set of aerosol models. Hence, the modified NIR-modelling scheme may return the same set of aerosol models as the initial approach. Using simulated datasets also avoids cloud masks or other flags such as red and NIR sensor band saturation and stray light contamination. Improvements resulting from the constrained AC algorithms may be excluded by these flags since noticeable amelioration mainly concern extremely turbid waters. Note also that satellite-*in situ* match-up exercises requires spatial homogeneity within the pixel window. This is not taken into account with the sensitivity study. Though, it may significantly reduce the number of valid match-up pairs especially with the COMB NIR-modelling scheme. Therefore, a comprehensive evaluation of the modified NIR-modelling schemes based on MODIS Aqua data, is outlined in the next chapter.

5.5 PAPER: "SPECTRAL RELATIONSHIPS FOR ATMOSPHERIC CORRECTION. I. VALIDATION OF RED AND NEAR INFRA-RED SPECTRAL RELATIONSHIPS"

C. Goyens, C. Jamet, and K. Ruddick, published in *Optics Express*, 21(18), 21162-21175 (2013).

Spectral relationships for atmospheric correction. I. Validation of red and near infra-red marine reflectance relationships

C. Goyens,[1] **C. Jamet,**[1*] **and K. G. Ruddick**[2]

[1] *CNRS, UMR 8187, Université Lille Nord de France, ULCO, LOG, F-62930 Wimereux, France*

[2] *Management Unit of the North Sea Mathematical Models (MUMM), Royal Belgian Institute for Natural Sciences (RBINS), 100 Gulledelle, B-1200 Brussels, Belgium*

[*] *cedric.jamet@univ-littoral.fr*

Abstract: The present study provides an extensive overview of red and near infra-red (NIR) spectral relationships found in the literature and used to constrain red or NIR-modeling schemes in current atmospheric correction (AC) algorithms with the aim to improve water-leaving reflectance retrievals, $\rho_w(\lambda)$, in turbid waters. However, most of these spectral relationships have been developed with restricted datasets and, subsequently, may not be globally valid, explaining the need of an accurate validation exercise. Spectral relationships are validated here with turbid *in situ* data for $\rho_w(\lambda)$. Functions estimating $\rho_w(\lambda)$ in the red were only valid for moderately turbid waters ($\rho_w(\lambda_{NIR}) < 3.10^{-3}$). In contrast, bounding equations used to limit $\rho_w(667)$ retrievals according to the water signal at 555 nm, appeared to be valid for all turbidity ranges presented in the *in situ* dataset. In the NIR region of the spectrum, the constant NIR reflectance ratio suggested by Ruddick et al. (2006) (Limnol. Oceanogr. **51**, 1167-1179), was valid for moderately to very turbid waters ($\rho_w(\lambda_{NIR}) < 10^{-2}$) while the polynomial function, initially developed by Wang et al. (2012) (Opt. Express **20**, 741-753) with remote sensing reflectances over the Western Pacific, was also valid for extremely turbid waters ($\rho_w(\lambda_{NIR}) > 10^{-2}$). The results of this study suggest to use the red bounding equations and the polynomial NIR function to constrain red or NIR-modeling schemes in AC processes with the aim to improve $\rho_w(\lambda)$ retrievals where current AC algorithms fail.

OCIS codes: (010.0010) Atmospheric and oceanic optics; (010.1285) Atmospheric correction; (010.4450) Oceanic optics; (010.1690) Color.

References and links

1. H. R. Gordon and M. Wang, "Retrieval of water-leaving radiance and aerosol optical thickness over the oceans with SeaWiFS: A preminilary algorithm," Appl. Opt. **33**, 443–452 (1994).
2. H. R. Gordon, "Removal of atmospheric effects from satellite imagery of the oceans," Appl. Opt. **17**, 1631–1636 (1978).
3. D. A. Siegel, M. Wang, S. Maritorena, and, W. Robinson, "Atmospheric correction of satellite ocean color imagery: The black pixel assumption," Appl. Opt. **39**(21), 3582–3591 (2000).

#193503 - $15.00 USD Received 8 Jul 2013; revised 12 Aug 2013; accepted 13 Aug 2013; published 3 Sep 2013

4. R. P. Stumpf, R. A. Arnone, J. R. W. Gould, P. M. Martinolich, and, V. Ransibrahmanakul, “A partially coupled ocean-atmosphere model for retrieval of water-leaving radiance from SeaWiFS in coastal waters,” in *SeaWiFS Postlaunch Technical Report Series, Volume 22, NASA Tech. Memo. 2003-206892*, S. B. Hooker and E. R. Firestone, eds., (NASA Goddard Space Flight Center, Greenbelt, Maryland), pp. 51–59 (2003).
5. S. W. Bailey, B. A. Franz, and, P. J. Werdell, “ Estimations of near-infrared water-leaving reflectance for satellite ocean color data processing,” Opt. Express **18**(7), 7521–7527 (2010).
6. C. Jamet, S. Thiria, C. Moulin, and, M. Crepon “ Use of neuro-variational inversion for retrieving oceanic and atmospheric constituents from ocean color imagery, ” J. Atmos. Ocean. Tech. **22**(4), 460–464 (2005).
7. T. Schroeder, I. Behnert, M. Schaale, J. Fischer, and, R. Doerffer, “ Atmospheric correction algorithm for MERIS above case-2 waters, ” Int. J. Remote Sens. **28**(7), 1469–1486 (2007).
8. J. Brajard, R. Santer, M. Crepon, and, S. Thiria, “ Atmospheric correction of MERIS data for case 2 waters using neuro-variational inversion, ” Remote Sens. Environ. **126**, 51–61 (2012).
9. M. Wang, S. Son, and, W. Shi, “ Evaluation of MODIS SWIR and NIR-SWIR atmospheric correction algorithms using SeaBASS data, ” Remote Sens. Environ. **113**, 635–644 (2009).
10. R. C. Smith and W. H. Wilson, “Ship and satellite bio-optical research in the Calofornia Bight,” in *Oceanography from Space*, J. F. R. Gower, eds., (Plenum Publishing Corporation, New York), pp. 281–294 (1980).
11. R. W. Austin and T. Petzold, “The determination of the diffuse attenuation coefficient of sea water using the Coastal Zone Color Scanner,” in *Oceanography from Space*, J. F. R. Gower, eds., (Plenum Publishing Corporation, New York), pp. 239–256 (1980).
12. B. Sturm, “The atmospheric correction of remotely sensed data and the quantitative determination of suspended matter in marine water surface layers,” in *Remote Sensing in Meteorology, Oceanography and Hydrology*, A. P. Cracknel, eds., (Chister, UK: Ellis Horwood), pp. 163–197 (1981).
13. B. Sturm, “Selected topics of coastal zone color scanner (CZCS) data evaluation,” in *Remote Sensing Applications in Marine Science and Technology*, A. P. Cracknel, eds., (Dordrecht, The Netherlands: D. Reidel), pp. 137–168 (1983).
14. M. Viollier and B. Sturm, “CZCS data analysis in turbid coastal water,” J. Geophys. Res. **89**, 4977–4985 (1984).
15. A. Bricaud and A. Morel, “Atmospheric corrections and interpretation of marine radiances in CZCS imagery: Use of a reflectance model,” Oceanol. Acta **33-50 N.SP**, (1987).
16. B. Sturm, V. Barale, D. Larkin, J. H. Andersen, and, M. Turner, “OCEAN code: the complete set of algorithms and models for the level 2 processing of European CZCS historical data, ” Int. J. Remote Sens. **20**(7), 1219–1248 (1999).
17. J. M. Nicolas, P. Y. Deschamps, H. Loisel, and, C. Moulin, ”POLDER-2: Ocean Color Atmospheric correction Algorithms, “Version 1.1. Algorithm Theoretical Basis Document, LOA, pp.17 (2005).
18. K. G. Ruddick, F. Ovidio, and, M. Rijkeboer, “Atmospheric correction of SeaWiFS imagery for turbid coastal and inland waters,” Appl. Opt. **39**, 897–912 (2000).
19. K. G. Ruddick, V. De Cauwer, Y. Park, and, G. Moore, “Seaborne measurements of near infrared water-leaving reflectance: The similarity spectrum for turbid waters,” Limnol. Oceanogr. **51**, 1167–1179 (2006).
20. M. Wang, W. Shi, and, L. Jiang, “Atmospheric correction using near-infrared bands for satellite ocean color data processing in the turbid western pacific region,” Opt. Express **20**, 741–753 (2012).
21. Z. Lee, B. Lubac, J. Werdell, and, R. Arnone, “An update of the Quasi-Analytical Algorithm (QAA v5), ” available at: `http://www.ioccg.org/groups/Software_OCA/QAA_v5.pdf` (2009).
22. C. Goyens, C. Jamet, and, K. Ruddick, “Spectral relationships for atmospheric correction. II. Improving NASA’s standard and MUMM near infra-red modeling schemes, ” accepted for publication in Opt. Express (2013).
23. M. Doron, S. Bélanger, D. Doxaran, and, M. Babin, “Spectral variations in the near-infrared ocean reflectance,” Remote Sens. Environ. **115**, 1617–1631 (2011).
24. A. Morel and L. Prieur, “Analysis of variations in ocean color, ” Limnol. Oceanogr. **22**, 709–722 (1977).
25. B. Sturm, G. Maracci, P. Schlittenhardt, C. Ferrari, and, L. Alberotanza, “Chlorophyll-a and total suspended matter concentration in the North Adriatic Sea determined from Nimbus-7 CZCS,” paper presented at the Statutory Meeting, Int. Counc. for Explor. of the Sea, Woods Hole, Mass:, Oct. 6-12, (1981).
26. A. Morel and B. Gentili, “Diffuse reflectance of oceanic waters. III. Implication of bidirectionality for the remote-sensing problem, ” Appl. Opt. **35**, 4850–4862 (1996).
27. C. D. Mobley, “Estimation of the remote-sensing reflectance from above-surface measurements,” Appl. Opt. **38**, 7442–7455 (1999).
28. L. Kou, D. Labrie, and, P. Chylek, “Refractive indices of water and ice in the 0.65 mm to 2.5 mm spectral range,” Appl. Opt. **32**, 3531–3540 (1993).
29. W. Shi and M. Wang, “An assessment of the black ocean pixel assumption for MODIS SWIR bands,” Remote Sens. Environ. **113**, 1587–1597 (2009).
30. M. Wang, S. Son, and, L. W. Harding Jr., “Retrieval of diffuse attenuation coefficient in the Chesapeake Bay and turbid ocean regions for satellite ocean color applications,” J. Geophys. Res. **114**, c10011 (2009).
31. M. Wang, J. Ahn, L. Jiang, W. Shi, S. Son, Y. Park, and, J. Ruy, “Ocean color products from the Korean Geostationary Ocean Color Imager (GOCI),” Opt. Express **21**(3), 3835–3849 (2013).
32. B. Nechad, K. Ruddick, and, Y. Park, “Calibration and validation of a generic multisensor algorithm for mapping

of total suspended matter in turbid waters," Remote Sens. Environ. **114**, 854–866 (2010).

33. H. Loisel, X. Mériaux, A. Poteau, L. F. Artigas, B. Lubac, A. Gardel, J. Caillaud, and, S. Lesourd, "Analyze of the inherent optical properties of French Guiana coastal waters for remote sensing applications," J. Coastal Res. **56**, 1532–1536 (2009).
34. V. Vantrepotte, H. Loisel, X. Mériaux, C. Jamet, D. Dessailly, G. Neukermans, D. Desailly, C. Jamet, E. Gensac, and, A. Gardel, "Seasonal and inter-annual (1998-2010) variability of the suspended particulate matter as retrieved from satellite ocean color sensors over the French Guiana coastal waters," J. Coastal Res. **64**, 1750–1754 (2011).
35. D. Doxaran, J. M. Froidefond, and, P. Castaing, "Remote-Sensing reflectance of turbid sediment-dominated waters," Appl. Opt. **42**(15), 2623–2634 (2003).
36. D. Doxaran, N. Cherukuru, and, S. J. Lavender, "Apparent and inherent optical properties of turbid estuarine waters: measurements, empirical quantification relationships and modeling," Appl. Opt. **45**(10), 2310–2324 (2006).
37. H. R. Gordon, O. B. Brown, R. H. Evans, J. W. Brown, R. C. Smith, K. S. Baker, and, D. K. Clark "A semianalytic radiance model of ocean color," J. Geophys. Res. **93**, 10909–10924 (1988).
38. A. Bricaud, A. Morel, M. Babin, K. Allali, and, H. Claustre, "Variations of light absorption by suspended particles with the chlorophyll a concentration in oceanic (case 1) waters: Analysis and implications for bio-optical models," J. Geophys. Res. **103**, 31033–31044 (1998).
39. K. L. Carder, F. R. Chen, Z. P. Lee, S. K. Hawes, and, D. Kamykowski, "Semianalytic Moderate-Resolution Imaging Spectrometer algorithms for chlorophyll a and absorption with bio-optical domains based on nitrate-depletion temperatures," J. Geophys. Res. **104**, 5403–5422 (1999).
40. Jr. R. W. Gould, R. A. Arone, and, P. M. Martinolich "Spectral dependence of the scattering coefficient in case 1 and case 2 waters," Appl. Opt. **38**(12), 2377–2383 (1999).

---

1. Introduction

The marine reflectance measured just above the water surface, $\rho_w(\lambda)$ (also referred to as $\rho_w^{0+}(\lambda)$ or normalized water-leaving reflectance [1]), retrieved from ocean color satellite images, allows to estimate biogeochemical parameters with a high revisit frequency and over large areas of oceans. The accuracy of these parameters depends however on the processing of the sensor-measured radiance, $L(\lambda)$, at the top of the atmosphere (TOA) used to obtain $\rho_w(\lambda)$. This processing includes, among others, the removal of the atmospheric contribution, the so-called atmospheric correction (AC) [1]. The top of atmosphere reflectance, $\rho^{TOA}(\lambda)$, is derived from the sensor-measured radiance and corrected for gas absorption, Rayleigh scattering, white-caps reflection and sun glint, to obtain the Rayleigh corrected reflectance, $\rho_{rc}^{TOA}(\lambda)$ [1]:

$$\rho_{rc}^{TOA}(\lambda) = \rho_a^{TOA}(\lambda) + \rho_{ra}^{TOA}(\lambda) + t_{\theta_v}(\lambda) t_{\theta_0}(\lambda) \rho_w(\lambda) \tag{1}$$

where $\rho_a^{TOA}(\lambda)$ and $\rho_{ra}^{TOA}(\lambda)$ represent the scattered sunlight by the aerosols and the coupling between both air and aerosol molecules, respectively. $t_{\theta_v}(\lambda)$ is the diffuse transmittance of the atmosphere along the viewing direction and $t_{\theta_0}(\lambda)$ is the diffuse transmittance of the atmosphere along incident direction. According to Eq. (1), if the optical properties and the concentrations of the aerosols are known, the quantities $\rho_a^{TOA}(\lambda)$, $\rho_{ra}^{TOA}(\lambda)$, $t_{\theta_0}(\lambda)$ and $t_{\theta_v}(\lambda)$ can be estimated and hence $\rho_w(\lambda)$ can be calculated.

At the time of the Coastal Zone Color Scanner (CZCS) satellite, the initial AC procedure assumed zero $\rho_w(\lambda)$ at 670 nm allowing to retrieve the atmospheric contributions from the total signal [2] (hereafter referred to as the black pixel assumption). With the addition of near infrared (NIR) bands for the next generation of ocean color satellite sensors (e.g., SeaWiFS, MODIS and MERIS), the 700-900 nm spectral range was used to estimate the aerosol contributions in the AC processes. Gordon and Wang [1] suggested to apply the black pixel assumption to the NIR spectral bands allowing to estimate $\rho_a^{TOA}(\lambda_{NIR})$ and $\rho_{ra}^{TOA}(\lambda_{NIR})$ and to select the appropriate aerosol optical models (hereafter referred to as the GW94 AC procedure). However in highly productive and turbid waters, due to absorption and backscattering of significant loads of algal and non-algal water constituents, the assumption of zero $\rho_w(\lambda)$ is not valid neither in the red nor in the NIR region of the spectrum [3, 4]. Assuming zero red or NIR $\rho_w(\lambda)$ in such water masses leads to an overcorrection of the atmospheric effects and subsequently to an underestimation of $\rho_w(\lambda)$ [3].

To avoid the inappropriate application of the black pixel assumption, numerous red or NIR-modeling schemes have been developed to account for non-zero red or NIR $\rho_w(\lambda)$ within the AC processes. The standard NASA AC procedure for the processing of SeaWiFS and MODIS Aqua images, for instance, is a GW94-based AC procedure which includes a NIR-modeling iterative scheme with a bio-optical model to retrieve $\rho_w(\lambda_{NIR})$ where the black pixel assumption is not valid [4, 5]. Other AC approaches have also been suggested, e.g., coupled ocean-atmosphere optimization methods, such as the the direct inversion approaches using artificial neural networks [6–8]. For MODIS Aqua, the black pixel assumption was successfully applied in the Short-Wave-Infra-Red (SWIR) spectral domain where even turbid seawater appears to be totally absorbent [9].

Another approach to extent the GW94 AC procedure to turbid waters, consists of forcing the AC process with spectral relationships estimating red or NIR $\rho_w(\lambda)$ by means of $\rho_w(\lambda)$ at shorter wavelengths (i.e., $\rho_w(\lambda_j) = f(\rho_w(\lambda_i))$). These relationships reflect thus the spectral dependence of the marine signal itself, including the spectral dependence of the total absorption and backscattering simultaneously. Hence, it does not require retrieval of inherent optical properties. Moreover, it can be easily implemented in current red or NIR-modeling schemes to improve $\rho_w(\lambda)$ retrievals where current AC algorithms fail.

For the CZCS AC, empirical spectral relationships have been proposed to estimate $\rho_w(670)$ from $\rho_w(\lambda)$ in the blue and green region of the spectrum (hereafter referred to as red spectral relationships) [10–16]. An empirical spectral relationship was also used by Nicolas et al. [17] within the AC procedure of the POLarization and Directionality of the Earth's Reflectances-2 (POLDER-2) sensor. Similarly, several studies investigated the spectral dependence of the marine reflectance in the NIR region of the spectrum to model $\rho_w(\lambda_{NIR})$ for the AC of second generation ocean color satellite images (hereafter referred to as the NIR spectral relationships) [18–20]. Lee et al. [21] also suggested to correct remote sensing $\rho_w(667)$ estimations (due, for instance, to imperfect AC) for the Quasi-Analytical Algorithm by means of spectral relationships between $\rho_w(667)$ and $\rho_w(555)$.

Most of these spectral relationships have been developed with restricted datasets and have not been confirmed theoretically nor validated with independent *in situ* datasets. An overview and validation of these different red and NIR marine spectral relationships are thus essential to verify if these relationships are globally valid and if they can be used to improve AC for past, present and future ocean color sensors. In a companion paper, Goyens et al. [22] investigate how these spectral relationships can be implemented in current NIR-modeling schemes [5, 18, 19] to improve AC processes in turbid coastal waters.

In the present study, the AC literature is reviewed from the launch of the CZCS satellite till today giving a non-exhaustive list of various red and NIR spectral relationships used to estimate the water signal in the red (Section 2) and the NIR spectral region (Section 3) from $\rho_w(\lambda)$ at shorter wavelengths. Most spectral relationships encountered in the literature were initially developed for the CZCS sensor to retrieve $\rho_w(\lambda_{red})$. However, since the CZCS spectral bands are relatively close to the second generation satellite sensor spectral bands (e.g., SeaWiFS, MODIS Aqua or MERIS), these CZCS-oriented spectral relationships may eventually lead to red spectral relationships also valuable to constrain actual NIR-modeling schemes (e.g., the iterative scheme suggested by Stumpf et al. [4] and Bailey et al. [5] modeling $\rho_w(\lambda_{NIR})$ according to $\rho_w(\lambda_{red})$).

With the arrival of SWIR ocean color bands, a similar exercise could be performed to evaluate spectral relationships allowing to estimate $\rho_w(\lambda)$ in the NIR from $\rho_w(\lambda)$ in the SWIR spectral domain, and inversely. However, the present study is limited by the spectral range of the *in situ* reflectance measurements, notably, from 400 to 900 nm, and is thus valuable for sensors with visible and NIR spectral bands (e.g., SeaWiFS, MODIS and MERIS sensors, the SEVIRI instrument on MSG, the Geostationary Ocean Color Imager (GOCI) and possibly the future GOCI-2 carried by COMS) as well as for studies covering decadal time scales including data from past and current sensors.

After reviewing the red and NIR spectral relationships, *in situ* reflectance spectra are described and their selection is outlined ensuring highly accurate reflectance spectra (Section 4). Next, red and NIR spectral relationships are validated (Section 5). A similar exercise has been done by Doron et al. [23] with *in situ*, remote sensing and simulated data. However the authors only focussed on the constant NIR reflectance ratio suggested by Ruddick et al. [18, 19]. Here a comprehensive overview and validation of 16 spectral relationships encountered in the literature are proposed.

2. Red spectral relationships

Initially the CZCS AC algorithm used the spectral band at 670 nm to estimate the aerosol contribution [2]. However, at 670 nm, both atmospheric and marine turbidity affect the TOA signal making it difficult to estimate either the aerosol content or the water reflectance with this single band [15]. Therefore, red-modeling schemes have been developed based on, e.g., spectral relationships to estimate the water signal at 670 nm from $\rho_w(\lambda)$ at shorter wavelengths. Smith and Wilson [10] and Austin and Petzold [11] related $\rho_w(670)$ with the reflectance ratio $\rho_w(443)/\rho_w(550)$ and the amplitude of reflectance at either 443 or 520 nm (Table 1). According to Austin and Petzold [11] using the reflectance at 520 nm was more appropriate to account for variations in non-algal particles while the ratio $\rho_w(443)/\rho_w(550)$ accounts for the pigment concentrations.

In the open ocean, the optical properties are essentially dominated by phytoplankton (often referred to as Case 1 waters) while in optically complex waters, the optical properties are dominated by other constituents such as dissolved organic matter and suspended sediments (often referred to as Case 2 waters) [24]. Hence, Sturm [13] proposed an iterative approach to solve the AC suggesting three equations according to the water type. The three equations are of the same type (Table 1). $\rho_w(670)$ is estimated from the water reflectance at 550 nm and an average blue-green ratio function β related to the total suspended matter (TSM) [14, 25]. The empirically defined constant terms of the equations were based on previous works and differed for clear waters [11], turbid near coastal waters [12] and *in situ* measurements taken in the northern Adriatic Sea (AAOT data) [12].

Viollier and Sturm [14] observed simple linear relations between $\rho_w(670)$ and $\rho_w(550)$ as a function of the water type. In the turbid coastal waters of the eastern English Channel, $\rho_w(670)$ represented 40% of $\rho_w(550)$ while, over a coccolithophorid bloom, it represented only 15%. In order to satisfy both water types, Viollier and Sturm [14] proposed a non-linear relationship similar to Smith and Wilson [10] and Austin and Petzold [11], but including the $\rho_w(520)/\rho_w(550)$ ratio instead of the blue-green ratio $\rho_w(443)/\rho_w(550)$ (Table 1).

Similarly to Sturm [13], Bricaud and Morel [15] demonstrated that AC could be improved by discriminating between Case 1 and Case 2 waters in the red-modeling scheme. They suggested several functions according to the water type, relating the Chlorophyll-a (Chl_a) absorption bands ratio $\rho_w(443)/\rho_w(670)$ and the blue-green ratio $\rho_w(443)/\rho_w(550)$ (Table 1). When the water type could not be defined as turbid or clear, Bricaud and Morel [15] used an intermediate relationship similar to the model of Smith and Wilson [10] (Table 1).

The OCEAN code, developed to process the level-2 European CZCS historical data [16], used both the relations of Viollier and Sturm [14] and Bricaud and Morel [15] within the red-modeling scheme to correct CZCS images for atmospheric contribution in turbid waters.

#193503 - $15.00 USD Received 8 Jul 2013; revised 12 Aug 2013; accepted 13 Aug 2013; published 3 Sep 2013

According to a first guess for $\rho_w(443)$ (based on the Black Pixel Assumption), the algorithm iterates with either the reflectance function of Viollier and Sturm [14] ($\rho_w(443) < 3.10^{-5}$) or the function of Bricaud and Morel [15] ($\rho_w(443) > 3.10^{-5}$) to account for non-zero $\rho_w(670)$.

Inspired by the CZCS red-modeling scheme proposed by Viollier and Sturm [14], Nicolas et al. [17] proposed an operational AC algorithm for POLDER-2 including a linear relationship between the marine signal at 565 and 670 nm (Table 1). The authors estimated $\rho_a(670)$ as the difference between the observed and modeled $\rho_w(\lambda)$. According to Nicolas et al. [17], this approach was satisfactory for most cases except for waters with high yellow substance absorption.

The Quasi Analytical Algorithm (QAA v.5) [21], used to derive the inherent optical properties from satellite $\rho_w(\lambda)$ estimations, includes three spectral relationships to correct erroneous satellite retrieved $\rho_w(667)$. $\rho_w(667)$ values are constrained within an upper and lower range defined by two spectral functions relating $\rho_w(\lambda)$ at 667 and 555 nm (Table 1). When the retrieved $\rho_w(667)$ is missing or out of limit, $\rho_w(667)$ is estimated from $\rho_w(555)$ and the ratio $\rho_w(490)/\rho_w(555)$ (Table 1).

As observed in Table 1, some spectral relationships are written in terms of sub-surface radiance, $L_{ss}(\lambda)$ or remote sensing reflectance, $R_{rs}(\lambda)$. For data analysis all functions are expressed here in terms of $\rho_w(\lambda)$. $L_{ss}(\lambda)$ and $R_{rs}(\lambda)$ are converted into $\rho_w(\lambda)$ following Morel and Gentili, [26] and considering the approximation for the ratio $(1-r_F)/n_w$ (with r_F being the Fresnel reflectance and n_w the water refractive index) suggested by, e.g., Bricaud and Morel [15], Morel and Gentili [26], and Mobley [27].

3. NIR spectral relationships

Constant reflectance ratios in the NIR region of the spectrum were suggested by Ruddick et al. [18]. With assumptions on the backscattering and absorption in the NIR, the authors approximated $\rho_w(\lambda_1)/\rho_w(\lambda_2)$ by the water absorption ratio $a_w(\lambda_2)/a_w(\lambda_1)$ (with λ_1 and λ_2 being two wavelengths in the NIR). Ruddick et al. [19] further investigated these assumptions with radiative transfer simulations as well as above-water *in situ* measurements. The authors concluded that the NIR reflectance spectral shape is almost invariant for moderate turbidity and observed, as a function of λ_1 and λ_2, a constant reflectance ratio $\alpha(\lambda_1,\lambda_2)$ (Table 1). Accordingly, normalizing the reflectance spectra to the reflectance at a single wavelength in the NIR (referred by the authors to as the similarity NIR reflectance spectrum) allows to determine, at any wavelength, the water leaving reflectance shape in the NIR. This assumption is used to extent the GW94 AC process to turbid waters (hereafter referred to as the MUMM NIR-modeling scheme) [18, 19].

Ruddick et al. [19] also suggested theoretical values for $\alpha(\lambda_1,\lambda_2)$ based on the pure water absorption spectrum of Kou et al. [28] for the MUMM NIR-modeling scheme of MODIS, MERIS and SeaWiFS. However, the similarity NIR reflectance spectrum assumption appeared to be only valid for a certain range of turbidity. Indeed, variations in $\alpha(\lambda_1,\lambda_2)$ were observed when the NIR reflectance values were outside the 10^{-4} - 10^{-1} range [19]. A similar conclusion was made by Shi and Wang [29] who observed a quasi linear relationship between $\rho_w(645)$ and $\rho_w(859)$ for $\rho_w(859)$ values below 0.03. For waters with $\rho_w(859)$ above this threshold, $\rho_w(\lambda)$ at 645 nm saturated and remained almost constant ($\sim$ 0.012). Doron et al. [23] also observed some deviations from the constant reflectance ratio with both *in situ* and satellite derived data. According to that study, for $\rho_w(865)$ between 10^{-4} and 10^{-2}, $\alpha(765,865)$ varied little between 1.73 and 1.84 as suggested by Ruddick et al. [19], but decreased with an increase in turbidity.

Wang et al. [20] proposed an NIR-modeling scheme for the AC of the Korean Ocean Satellite GOCI including a polynomial relationship between the water signal at 748 and 869 nm (Table 1, hereafter referred to as the GOCI NIR-modeling scheme). Initially, $\rho_w(\lambda)$ is retrieved with the GW94 AC algorithm allowing to calculate the water diffuse attenuation coefficient at 490

Table 1. Review of the spectral relationships and their applications

Source	Relation	Constant	Empirical/Theoretical	Application
Smith and Wilson (1980)	$L_{ss}(670) = aL_{ss}(443) \times \left[\frac{L_{ss}(443)}{L_{ss}(550)}\right]^b$	a=0.083 and b=-1.66	Empirical	CZCS AC
Austin and Petzold (1980)	$L_{ss}(670) = aL_{ss}(520) \times \left[\frac{L_{ss}(443)}{L_{ss}(550)}\right]^b$	a=0.0746, b=-0.919	Empirical	CZCS AC
Austin and Petzold (1980) in Sturm (1983)	$L_{ss}(670) = L_{ss}(550) \times 10^{-(a+b(\log(\beta))+c(\log(\beta))^2}$ with $\beta = d\frac{L_{ss}(443)}{L_{ss}(550)} + e\frac{L_{ss}(520)}{L_{ss}(550)} - f$	a=1.048, b=0.764, c=0.07 d=0.642, e=0.891, f=0.533	Empirical	CZCS AC clear water
Sturm (1981) in Sturm (1983)	$L_{ss}(670) = L_{ss}(550) \times 10^{-(a+b(\log(\beta))+c(\log(\beta))^2}$ β see Austin and Petzold (1980)	a=1.177, b=1.168, c= 0.292	Empirical (SPM >4-5 mg l^{-1})	CZCS AC turbid water
Sturm (1981) in Sturm (1983)	$L_{ss}(670) = L_{ss}(550) \times 10^{-(a+b(\log(\beta)))}$ β see Austin and Petzold (1980)	a=0.881, b=0.816	Empirical	*in situ* data in northern Adriatic Sea
Viollier and Sturm (1984)	$L_{ss}(670) = aL_{ss}(550)$	a=0.15	Empirical	$L_{ss}(\lambda)$ over Coccolithophorid bloom
	$L_{ss}(670) = aL_{ss}(550)$	a=0.40	Empirical	*in situ* data from coastal English Channel
	$L_{ss}(670) = aL_{ss}(550) \times \left[\frac{L_{ss}(520)}{L_{ss}(550)}\right]^b$	a=0.23 and b=-2	Empirical	CZCS AC
Bricaud and Morel (1987)	$\frac{L_{ss}(443)}{L_{ss}(670)} = a\left[\frac{L_{ss}(443)}{L_{ss}(550)}\right]^b$	a=5.89 and b=1.47	Empirical	Case 1 waters
	$\frac{L_{ss}(443)}{L_{ss}(670)} = a\left[\frac{L_{ss}(443)}{L_{ss}(550)}\right]^b$	a=14.55 and b=2.48	Empirical	Case 2 waters
	$\frac{L_{ss}(443)}{L_{ss}(670)} = a\left[\frac{L_{ss}(443)}{L_{ss}(550)}\right]^b$	a=6.73 and b=1.55	Empirical	Case 1 and 2 waters
Ruddick *et al.* (2000)	$\alpha = \frac{\rho_w(765)}{\rho_w(865)} = \frac{a_w(865)}{a_w(765)}$	α=1.72	Theoretical & empirical	SeaWiFs AC
Nicolas *et al.* (2005)	$\rho_w(670) = a\rho_w(565) + b$	a=0.20 and b=-0.0005	Empirical	Polder-2 AC
Ruddick *et al.* (2006)	$\alpha = \frac{\rho_w(\lambda_1)}{\rho_w(\lambda_2)}$	$\alpha = f(\lambda_1, \lambda_2)$	Theoretical & empirical	MODIS and SeaWiFS AC
Lee *et al.* (2009)	$R_{rs}(667) = aR_{rs}(555)^b$	Upper limit: a=20 and b=1.5 Lower limit: a=0.9 and b=1.7	Empirical	Upper and Lower bounds for $R_{rs}(667)$ in QAA v.5
Lee *et al.* (2009)	$R_{rs}(667) = aR_{rs}(555)^b + c\left[\frac{R_{rs}(490)}{R_{rs}(555)}\right]^d$	a=1.27, b=1.47, c=0.00018 and d=-3.19	Empirical	QAA v.5 for missing/erroneous $R_{rs}(667)$
Wang *et al.* (2012)	$L_{wn}(869) = aL_{wn}(748) + bL_{wn}(748)^2$	a=0.368 and b=0.040	Empirical	GOCI AC

#193503 - $15.00 USD Received 8 Jul 2013; revised 12 Aug 2013; accepted 13 Aug 2013; published 3 Sep 2013
(C) 2013 OSA 9 September 2013 | Vol. 21, No. 18 | DOI:10.1364/OE.21.021162 | OPTICS EXPRESS 21168

nm, $K_d(490)$ [30]. Next, polynomial relations are used to estimate $\rho_w(748)$ from $K_d(490)$ and $\rho_w(869)$ from $\rho_w(748)$. These empirical relations were developed based on long term MODIS Aqua images over the turbid western Pacific region and processed with the NIR-SWIR GW94-based AC algorithm [9]. Although the GOCI NIR-modeling scheme provided satisfying results in the western Pacific region [20, 31], the polynomial relationship between $\rho_w(748)$ and $\rho_w(869)$ has not yet been validated with *in situ* data and applied to other coastal regions.

4. *In situ* data

Above-water reflectance measurements were made using TriOS-RAMSES hyperspectral radiometers during 63 sea campaigns undertaken between 2001 and 2012 (860 stations). Data were collected in coastal waters located in the southern North Sea and English Channel [32], the Celtic Sea, the Ligurian Sea, the Adriatic Sea and in the Atlantic Ocean along the coasts of Portugal and French Guyana [33, 34]. This dataset is particularly suitable for the validation of the spectral relationships as it includes measurements over contrasted and optically complex coastal waters. *In situ* data processing, averaging and selection are described in Ruddick et al. [19].

Out of the 860 stations, 105 *in situ* reflectance spectra satisfy the selection criteria and were not used by Ruddick et al. [19] for the calibration of the NIR similarity spectrum. Table 2 provides an overview of the minimum, maximum, average and standard deviation for $\rho_w(\lambda)$ of the selected spectra for the ocean color MODIS Aqua visible and NIR bands. The largest standard deviations in marine reflectance are encountered in the green and red region (Table 2). Around 869 nm the marine signal ranges from near zero to approximately 0.1, confirming the non-valid zero water-leaving reflectance assumption in the NIR. All spectra present $\rho_w(\lambda_{NIR})$ values above 10^{-4}, which is approximately the limit of validity for the black pixel assumption [3]. Out of the 105 spectra, 53% presents moderate turbidity with $\rho_w(869)$ ranging from 10^{-4} to 3.10^{-3} and 47% of the data presents very turbid waters with $\rho_w(869)$ exceeding 3.10^{-3}. This latter value corresponds to the threshold used by Wang et al. [9] to switch for the SWIR algorithm in the combined NIR-SWIR GW94-based AC algorithm.

Table 2. Statistics of the 105 $\rho_w(\lambda)$ (dimensionless) spectra for the ocean color bands of MODIS Aqua in the 412-869 nm range.

λ (nm)	min	max	mean	median	standard deviation
412	0.0069	0.0488	0.0230	0.0219	0.0114
443	0.0070	0.0642	0.0292	0.0301	0.0159
488	0.0080	0.0919	0.0414	0.0461	0.0234
531	0.0093	0.1144	0.0523	0.0594	0.0302
547	0.0084	0.1229	0.0568	0.0654	0.0334
667	0.0016	0.1309	0.0382	0.0316	0.0361
678	0.0018	0.1315	0.0376	0.0301	0.0359
748	0.0004	0.1134	0.0131	0.0061	0.0200
869	0.0002	0.0985	0.0079	0.0032	0.0148

Figure 1 shows the spectra in the 400-900 nm range and the red-NIR reflectance spectra normalized at 780 nm ($\rho_{wn780}(\lambda)$) as suggested by Ruddick et al. [18, 19]. Most spectra exhibit an increasing signal from the blue to the green region of the spectrum followed by a large peak between 550 and 600 nm [Fig. 1(a)]. A second peak is observed around 800 nm. Out of the 105 spectra, three spectra, taken in the Ligurian Sea, show a shape similar to clear ocean waters (peak in the blue followed by a decreasing signal with an increase in wavelength). In contrast, seven spectra present a lower peak around 550 and 600 nm and a higher peak around 690 nm followed by a relatively large signal at 800 nm and beyond.

According to Doxaran et al. [35], water masses with a reflectance spectrum showing a larger

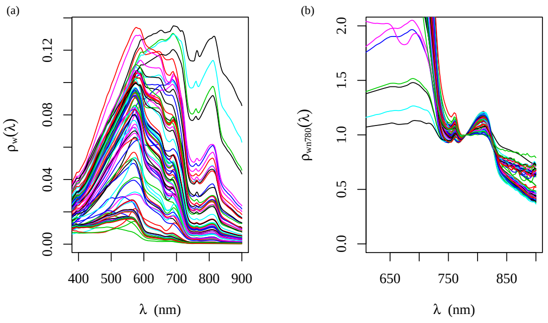

Fig. 1. Selected $\rho_w(\lambda)$ spectra between 400 and 900 nm and reflectance spectra normalized at 780 nm, $\rho_{wn780}(\lambda)$, in the 600-900 nm range.

peak at 550-600 nm are characterised by lower SPM values ($<$ 100 mg l^{-1}), while water masses with a large reflectance peak around 700 and 800 nm present larger concentrations of SPM ($>$ 100 mg l^{-1}). Indeed, these seven spectra are from the coastal waters of French Guiana known as being influenced by important river-discharge resulting in extremely turbid waters [33, 34]. These *in situ* measurements also exhibit distinctive $\rho_{wn780}(\lambda)$ spectra [Fig. 1(b)]. As observed by Ruddick et al. [19], most spectra present similar spectral shapes between 710 and 900 nm with a peak at 805-812 nm [Fig. 1 (b)]. The extremely turbid spectra from French Guiana instead show relatively lower $\rho_{wn780}(\lambda)$ values around 710 nm and often higher values at 850 nm and beyond.

5. Validation experiment

Spectral relationships are validated by comparing modeled and measured $\rho_w(\lambda)$ values qualitatively and quantitatively. The average percent relative error (RE), percent bias, root mean square error (RMSE), and R-squared coefficient (R^2) are calculated for each spectral relationship.

The percentage of data for which the RE does not exceed 10% of the observed value is also calculated as well as the validity ranges of each function in the visible. Validity ranges are determined by fitting a non-linear regression line through the observed and modeled $\rho_w(\lambda)$. The reflectance range for which the spectral relationship is satisfactory is defined by a difference between the regression and 1:1 line less than 10%.

5.1. Validation of spectral relationships in the visible

The statistical parameters comparing modeled and observed $\rho_w(670)$ are given in Table 3. Most functions tend to underestimate $\rho_w(670)$ (negative bias ranging from -3 to -63%). Two functions indicate a positive bias, notably, the function of Sturm [12] developed with AAOT data and the function of Viollier and Sturm developed with data from the English Channel (18 and 31%, respectively). However these spectral relationships overestimate $\rho_w(670)$ values below 0.05 but largely underestimate $\rho_w(670)$ values above this threshold. The relations from Smith and Wilson [10], Austin and Petzold [11], Bricaud and Morel [15] for the Case 2 waters, Nicolas et al. [17], and Viollier and Sturm [14] for the Coccolithophorid blooms show the lowest statistical performances. Statistics in Table 2 indicate that linear functions including a larger multiplication factor between the water signal in the red and the green spectral region result in better $\rho_w(670)$ retrievals (Table 1). Indeed the relation of Viollier and Sturm [14] developed with *in situ* data from the English Channel (multiplication factor of 0.4) provides more satisfying results (see Table 2; lower bias, larger percentage of data with less than 10% RE and larger validity range) compared to the relations of Viollier and Sturm [14] over a coccolithophorid bloom (multiplication factor of 0.15) and Nicolas et al. [17] (multiplication factor of 0.2) (Table 1).

Table 3. Statistical performance of spectral relationships in the red (av. RE: average Relative Error, av. Bias: average Bias and RMSE: Root Mean Square Error)

	av. RE (%)	av. Bias (%)	RMSE	R^2 (%)	Percentage within 10%	Validity range
Smith and Wilson (1980)	60	-60	0.04	77	1	0-0.012
Austin and Petzold (1980)	63	-63	0.04	74	1	0-0.011
Austin and Petzold (1980) in Sturm et al. (1983)	34	-29	0.03	79	**27**	0-0.024
Sturm (1981) in Sturm et al. (1983), CZCS AC	**33**	-26	0.03	78	22	0-0.027
Sturm (1981) in Sturm et al. (1983), AAOT data	42	**18**	0.02	78	19	**0-0.043**
Viollier and Sturm (1984), Coccolithophorid bloom	51	-51	0.04	77	6	0-0.013
Viollier and Sturm (1984), English Channel	65	31	0.03	77	13	**0-0.036**
Viollier and Sturm (1984), CZCS AC	44	**-3**	0.03	**82**	8	**0-0.029**
Bricaud and Morel (1987), Case 1	41	-26	0.04	77	4	0-0.022
Bricaud and Morel (1987), Case 2	44	-44	0.04	74	7	0-0.019
Bricaud and Morel (1987), Case 1 and 2	39	-32	0.04	77	22	0-0.020
Nicolas *et al.* (2005)	48	-47	0.04	79	3	0-0.016
Lee *et al.* (2009) in QAA v.5	43	-43	0.04	**81**	4	0-0.020

As mentioned in Section 2, the algorithm described in the OCEAN code for the CZCS AC over turbid coastal waters [16] used the function of Viollier and Sturm [14] to model $\rho_w(670)$ when the retrieved $\rho_w(443)$ was below 3.10^{-5} and the Case 1 and 2 spectral relationships of Bricaud and Morel [15] otherwise. Although none of our *in situ* $\rho_w(443)$ values are below 3.10^{-5}, the reflectance function of Viollier and Sturm [14] yields better $\rho_w(670)$ retrievals (Table 3).

Similarly to the other spectral relationships, the relation suggested by Lee et al. [21] to estimate $\rho_w(667)$ when it is missing or erroneously retrieved (i.e, outside the bounding equations, Table 1), tends to underestimate larger $\rho_w(667)$ values. According to the R^2 this spectral relationship shows a relatively good fit with our *in situ* data (Table 3). However, the average bias and RE remain large (43% and -43%, respectively) and the percentage of values within 10% of the 1:1 line remains small (4%). In contrast, the bounding equations used by the authors to evaluate $\rho_w(667)$ according to $\rho_w(555)$ correspond to the limit of our *in situ* data [Fig. 2(a)].

Functions showing the best fit with the observed data are shown in Figs. 2(b)-2(d). These are the relations proposed by Austin and Petzold [11] and the two spectral relationships of Sturm [12] in [13]. The three relationships are of the same type (Table 1). They include the average blue green ratio β and the magnitude reflectance at 550 nm which can be related to the total absorption and the backscattering coefficient, respectively [14]. The maximum validity range in Table 3 and the plots in Figs. 2(b)-2(d) indicate that these functions largely underestimate $\rho_w(670)$ when the marine signal is greater than 0.03, which corresponds to very turbid waters ($\rho_w(869) \geq 3.10^{-3}$).

5.2. *Validation of NIR spectral relationships*

To evaluate the validity of the constant NIR reflectance ratios used in the MUMM NIR-modeling scheme [19], $\rho_w(\lambda_1)$ versus $\rho_w(\lambda_2)$ for the NIR bands of the SeaWiFS, MERIS and MODIS sensors are plotted in Figs. 3(a)-3(c). Ruddick et al. [19] suggested empirical and theoretical $\alpha(\lambda_1, \lambda_2)$ parameters derived from *in situ* measurements and from $a_w(\lambda)$ [28] (considering wavelength independent backscattering), respectively. With λ_1 taken in the red region of the

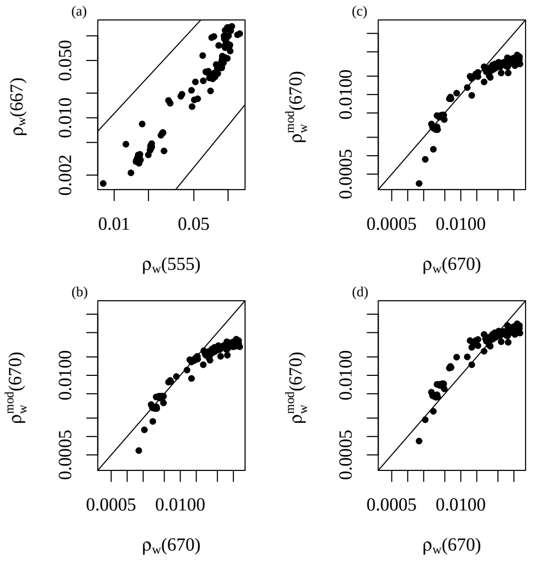

Fig. 2. (a) *In situ* $\rho_w(667)$ versus $\rho_w(555)$ including the upper and lower bounds to constrain $\rho_w(667)$ as suggested by Lee et al. (2009), and observed versus modeled $\rho_w(670)$ according to the spectral relationships suggested by (b) Austin and Petzold (1980) in Sturm (1983), (c) Sturm (1981, used for the CZCS AC over turbid waters) in Sturm (1983) and (d) Sturm (1981, developed with AAOT data) in Sturm (1983).

spectrum (600-700 nm range), constant reflectance ratios are valid for moderately/very turbid water with $\rho_w(\lambda_{NIR})$ below 10^{-2}. With λ_1 taken in the NIR region of the spectrum (700-800 nm range) the constant ratios are also valid for extremely turbid waters ($\rho_w(\lambda_{NIR}) > 10^{-2}$) [Figs. 3(a)-3(c)]. Accordingly, $\alpha(\lambda_1, \lambda_2)$ has a wider validity range when λ_1 is taken at longer wavelengths ($>$ 750 nm). However, the constant $\alpha(\lambda_1, \lambda_2)$ values are not valid for $\rho_w(\lambda_{NIR})$ above 3.10^{-2}. $\rho_w(\lambda_{NIR})$ is systematically underestimated for these water masses [Figs. 3(a)-3(c)]. This suggests that one or more assumptions made by Ruddick et al. [18, 19] are not verified with the present dataset and result in variations of the reflectance ratio $\alpha(\lambda_1, \lambda_2)$ with turbidity. Indeed, Ruddick et al. [18, 19] assumed a negligible backscattering coefficient, $b_b(\lambda)$, compared to the absorption $a(\lambda)$ in the NIR region of the spectrum. However, in extremely turbid waters, $b_b(\lambda)$ may largely exceed $a(\lambda)$ resulting in an asymptote for $b_b(\lambda)/(b_b(\lambda) + a(\lambda))$ and subsequently in $\rho_w(\lambda)$. Since pure water absorption decreases with wavelength, the asymptote in $b_b(\lambda)/(b_b(\lambda) + a_w(\lambda))$ is reached earlier at shorter wavelengths, explaining the flattening of the ratios with turbidity as shown in Figs. 3(a)-3(c). This is in agreement with the observations of Doxaran et al. [36], who showed a flattening of the reflectance ratios $\rho_w(850)/\rho_w(550)$ and $\rho_w(850)/\rho_w(650)$ with increasing TSM concentrations, and with the conclusions of Shi and Wang [29], who observed a maxima in $\rho_w(675)$ for $\rho_w(859)$ values greater than 0.03.

Our results also confirm the observations of Doron et al. [23] who observed deviations from the constant ratios of $\rho_w(\lambda)$ in the NIR with variations in turbidity and mineral particle types.

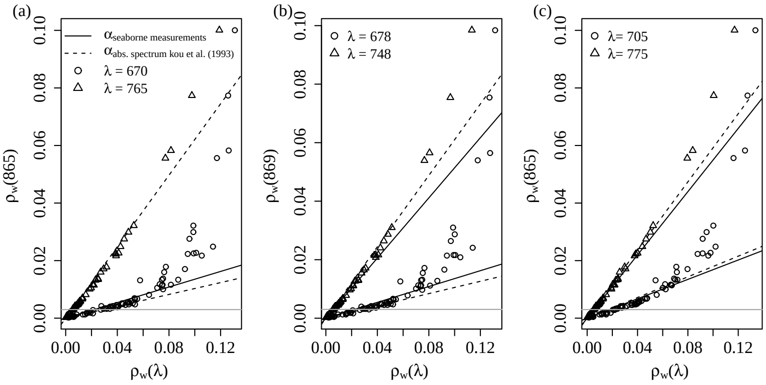

Fig. 3. Reflectance ratio in the red and the NIR for (a) SeaWiFS: $\rho_w(865)$ versus $\rho_w(670)$ and $\rho_w(765)$, (b) MODIS: $\rho_w(869)$ versus $\rho_w(678)$ and $\rho_w(748)$, and (c) MERIS: $\rho_w(865)$ versus $\rho_w(705)$ and $\rho_w(775)$. The constant $\alpha(\lambda_1,\lambda_2)$ suggested by Ruddick et al. (2006) based on *in situ* measurements and on $a_w(\lambda)$ (Kou et al., 1993) are represented for each reflectance ratio by a plain and dashed line, respectively. Horizontal grey lines indicate the limit between moderately turbid and very turbid waters (3.0^{-3})

.

Figures 4(a-b) show the NIR reflectance ratio for the SeaWiFS bands for moderately turbid and very turbid waters, respectively. Ruddick et al. [19] reported for this band ratio a constant $\alpha(765,865)$ of 1.61 based on the pure water absorption model of Kou et al. [28]. Similarly to Doron et al. [23], we observe a larger NIR reflectance ratio in moderately turbid waters ($\alpha(765,865) \sim 1.84$) and a ratio closer to 1.61 for $\rho_w(865)$ values up to 10^{-2} [Fig. 4(b)]. For extremely turbid waters ($\rho_w(865) > 10^{-2}$), $\alpha(765,865)$ is below 1.5 as noticed by Doron et al. [23].

Since the parameter $\alpha(\lambda_1,\lambda_2)$ appeared to vary with turbidity, the polynomial relationship suggested by Wang et al. [20], between $\rho_w(\lambda)$ at 748 and 869 nm (Table 1), may be more appropriate. Their function, developed with satellite data over the western Pacific region, is validated with our *in situ* data for moderately turbid and very turbid waters [Figs. 4(c) and 4(d)]. A RE of 10%, a small bias (-7%) and a R^2 of 99% are calculated between estimated and modeled $\rho_w(869)$. About 65% of the estimated $\rho_w(869)$ ranges within $\pm$ 10% of the corresponding observations. For moderately turbid waters, the constant NIR reflectance ratio of Ruddick et al. [19] and the polynomial function of Wang et al. [20] are close [Fig. 4(c)]. For very turbid waters, the function performs better than the constant NIR reflectance ratio [Fig. 4(d)]. However, the polynomial function could be further refined in order to enclose the most turbid data points where it underestimates $\rho_w(\lambda_{NIR})$ (see triangles in Fig. 4(d)).

6. Conclusion

The present study aimed to review spectral relationships in order to select appropriate functions which could be used as constraints to improve red or NIR-modeling schemes in current AC processes. Spectral relationships found in the literature were developed with restricted or regional datasets explaining the need of an accurate validation.

Sixteen published spectral relationships, estimating $\rho_w(\lambda)$ in the visible or NIR spectral region, were validated using 105 highly accurate *in situ* above-water reflectance measurements

#193503 - $15.00 USD Received 8 Jul 2013; revised 12 Aug 2013; accepted 13 Aug 2013; published 3 Sep 2013

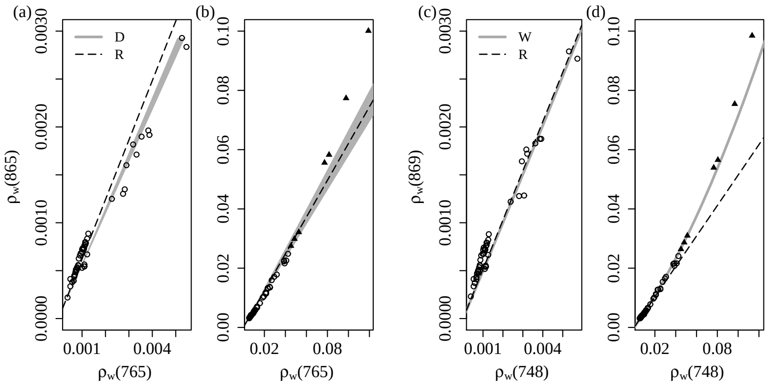

Fig. 4. $\rho_w(765)$ versus $\rho_w(865)$ according to Ruddick et al. (2006) (R, dashed line) and Doron et al. (2011) (D, grey bands) for (a) moderately turbid and (b) very turbid waters and $\rho_w(748)$ versus $\rho_w(869)$ for (c) moderately turbid and (d) very turbid waters with the polynomial function proposed by Wang et al. (2012) (W, plain grey line) and the constant ratio proposed by Ruddick et al. (2006) (R, dashed line). Spectra from extremely turbid coastal waters of French Guiana described in Section 4 are indicated by a triangle.

taken in diverse coastal water types. Functions used to model $\rho_w(\lambda)$ at 670 nm for CZCS AC processes [10–12, 15], systematically underestimated the water signal for very turbid waters. Similarly, the function suggested by Lee et al. [21] to estimate $\rho_w(667)$ from the water signal in the green and the blue-green reflectance ratio, tends to underestimate higher $\rho_w(667)$ values. In contrast, the bounding equations used in the latest version of the QAA, to evaluate maximum and minimum $\rho_w(667)$ estimations according to the water signal in the green, appear to be valid for the entire range of turbidity encountered in the *in situ* dataset.

In the NIR spectral region, the constant reflectance ratio $\alpha(\lambda_1,\lambda_2)$, suggested by Ruddick et al. [18, 19] to extend the GW94 AC algorithm to turbid waters, was valid for moderately to very turbid waters with $\rho_w(865-869)$ values below 10^{-2}, while the polynomial function of Wang et al. [20] was also valid for extremely turbid water masses. However, the latter slightly underestimated $\rho_w(869)$ for water masses with $\rho_w(\lambda_{NIR})$ exceeding 0.05.

From this study we can conclude that the red spectral relationships are not appropriate for the entire range of coastal turbidity encountered in our *in situ* dataset suggesting that either the red spectral functions need to be updated or that the functions should differ according to the optical water type and/or the turbidity range. In contrast, bounding equations, as suggested by Lee et al. [21], allow some variability and may thus be more appropriate to force red or NIR-modeling schemes within AC processes when a priori informations on the water type or turbidity levels are not available or when the AC procedure is expected to perform globally. The polynomial NIR function, initially developed with remote sensing reflectances over the Western Pacific [20], presented a satisfying fit with our *in situ* data.

The actual standard NASA CZCS AC procedure assumes a fixed aerosol type and includes an iteration scheme to estimate $\rho_w(670)$ from inherent optical properties at 555 nm and Chl_a concentration estimations [4, 37–40]. Hence, in turbid waters where $\rho_w(670)$ is not solely determined by algal particles, CZCS $\rho_w(\lambda)$ retrievals may be improved by forcing the iteration scheme with the red bounding equations suggested by Lee et al. [21]. However, to further improve red-modeling schemes, more work into developing globally valid red spectral relationships is required.

For the second generation ocean color satellite images, bounding red and NIR polynomial spectral relationships may be used to improve NIR-modeling schemes in current AC algorithms (e.g., the iteration scheme in the standard NASA AC algorithm for MODIS Aqua [5] and the MUMM NIR-modeling scheme [18, 19]). How these spectral relationships may lead to improved $\rho_w(\lambda)$ retrievals, is investigated in the companion paper of this study by Goyens et al. [22].

Acknowledgments

Most of the *in situ* measurements used here were collected in the framework of the BELCOLOUR-1 and BELCOLOUR-2 projects funded by the Belgian Science Policy Office STEREO programme. Griet Neukermans and Barbara Van Mol are acknowledged for data acquisition. This work has been supported by the French Spatial Agency (CNES) through the TOSCA program and the ”Ministère de l’Enseignement et de la Recherche Française” which provided a PhD scholarship.

5.6 PAPER: “SPECTRAL RELATIONSHIPS FOR ATMOSPHERIC CORRECTION. II. IMPROVING THE NASA STANDARD AND MUMM NEAR INFRA-RED MODELING SCHEMES”

C. Goyens, C. Jamet, and K. Ruddick, published in *Optics Express*, 21(18), 21176-21187 (2013).

Spectral relationships for atmospheric correction. II. Improving NASA's standard and MUMM near infra-red modeling schemes.

C. Goyens,[1] **C. Jamet,**[1*] **and K. G. Ruddick**[2]

[1] *CNRS, UMR 8187, Université Lille Nord de France, ULCO, LOG, F-62930 Wimereux, France*
[2] *Management Unit of the North Sea Mathematical Models (MUMM), Royal Belgian Institute for Natural Sciences (RBINS), 100 Gulledelle, B-1200 Brussels, Belgium*
[*] *cedric.jamet@univ-littoral.fr*

Abstract: Spectral relationships, reflecting the spectral dependence of water-leaving reflectance, $\rho_w(\lambda)$, can be easily implemented in current AC algorithms with the aim to improve $\rho_w(\lambda)$ retrievals where the algorithms fail. The present study evaluates the potential of spectral relationships to improve the MUMM (Ruddick et al., 2006, Limnol. Oceanogr. **51**, 1167-1179) and standard NASA (Bailey et al., 2010, Opt. Express **18**, 7521-7527) near infra-red (NIR) modeling schemes included in the AC algorithm to account for non-zero $\rho_w(\lambda_{NIR})$, based on *in situ* coastal $\rho_w(\lambda)$ and simulated Rayleigh corrected reflectance data. Two modified NIR-modeling schemes are investigated: (1) the standard NASA NIR-modeling scheme is forced with bounding relationships in the red spectral domain and with a NIR polynomial relationship and, (2) the constant NIR $\rho_w(\lambda)$ ratio used in the MUMM NIR-modeling scheme is replaced by a NIR polynomial spectral relationship. Results suggest that the standard NASA NIR-modeling scheme performs better for all turbidity ranges and in particular in the blue spectral domain (percentage bias decreased by approximately 50%) when it is forced with the red and NIR spectral relationships. However, with these new constrains, more reflectance spectra are flagged due to non-physical Chlorophyll-a concentration estimations. The new polynomial-based MUMM NIR-modeling scheme yielded lower $\rho_w(\lambda)$ retrieval errors and particularly in extremely turbid waters. However, including the polynomial NIR relationship significantly increased the sensitivity of the algorithm to errors on the selected aerosol model from nearby clear water pixels.

OCIS codes: (010.0010) Atmospheric and oceanic optics; (010.1285) Atmospheric correction; (010.4450) Oceanic optics; (010.1690) Color.

References and links

1. H. R. Gordon and M. Wang, "Retrieval of water-leaving radiance and aerosol optical thickness over the oceans with SeaWiFS: A preminilary algorithm," Appl. Opt. **33**, 443-452 (1994).
2. D. A. Siegel, M. Wang, S. Maritorena, and W. Robinson, "Atmospheric correction of satellite ocean color imagery: The black pixel assumption," Appl. Opt. **39**, 3582-3591 (2000).

#193504 - $15.00 USD Received 8 Jul 2013; revised 12 Aug 2013; accepted 13 Aug 2013; published 3 Sep 2013
(C) 2013 OSA 9 September 2013 | Vol. 21, No. 18 | DOI:10.1364/OE.21.021176 | OPTICS EXPRESS 21176

3. R. P. Stumpf, R. A. Arnone, J. R. W. Gould, P. M. Martinolich, and, V. Ransibrahmanakul, "A partially coupled ocean-atmosphere model for retrieval of water-leaving radiance from SeaWiFS in coastal waters," in *SeaWiFS Postlaunch Technical Report Series, Volume 22, NASA Tech. Memo. 2003-206892*, S. B. Hooker and E. R. Firestone, eds., (NASA Goddard Space Flight Center, Greenbelt, Maryland), pp. 51-59 (2003).
4. K. G. Ruddick, V. De Cauwer, Y. Park and G. Moore, "Seaborne measurements of near infrared water-leaving reflectance: The similarity spectrum for turbid waters," Limnol. Oceanogr. **51**, 1167-1179 (2006).
5. S. W. Bailey, B. A. Franz, and P. J. Werdell, " Estimations of near-infrared water-leaving reflectance for satellite ocean color data processing," Opt. Express **18**, 7521-7527 (2010).
6. K. G. Ruddick, F. Ovidio, and M. Rijkeboer, "Atmospheric correction of SeaWiFS imagery for turbid coastal and inland waters," Appl. Opt. **39**, 897-912 (2000).
7. C. Jamet, H. Loisel, C. P. Kuchinke, K. Ruddick, G. Zibordi, and H. Feng, "Comparison of three SeaWiFS atmospheric correction algorithms for turbid waters using AERONET-OC measurements," Remote Sens. Environ. **115**(8), 1955-1965 (2011).
8. C. Goyens, C. Jamet, and T. Schroeder, " Evaluation of four atmospheric correction algorithms for MODIS-Aqua images over contrasted coastal waters," Remote Sens. Environ. **131**, 63-75 (2013).
9. T. Schroeder, I. Behnert, M. Schaale, J. Fischer, and R. Doerffer, " Atmospheric correction algorithm for MERIS above case-2 waters, " Int. J. Remote Sens. **28**(7), 1469-1486 (2007).
10. M. Wang, S. Son, and W. Shi, " Evaluation of MODIS SWIR and NIR-SWIR atmospheric correction algorithms using SeaBASS data, " Remote Sens. Environ. **113**, 635-644 (2009).
11. M. Doron, S. Bélanger, D. Doxaran, and M. Babin, "Spectral variations in the near-infrared ocean reflectance," Remote Sens. Environ. **115**, 1617-1631 (2011).
12. C. Goyens, C. Jamet, and K. Ruddick, " Spectral relationships for atmospheric correction. I. Review and evaluation of red and near infra-red spectral relationships, " accepted for publication in Opt. Express (2013).
13. R. C. Smith and W. H. Wilson, "Ship and satellite bio-optical research in the Calofornia Bight," in *Oceanography from Space*, J. F. R. Gower, eds., (Plenum Publishing Corporation, New York), pp. 281-294 (1980).
14. R. W. Austin and T. Petzold, "The determination of the diffuse attenuation coefficient of sea water using the Coastal Zone Color Scanner," in *Oceanography from Space*, J. F. R. Gower, eds., (Plenum Publishing Corporation, New York), pp. 239-256 (1980).
15. A. Bricaud and A. Morel,"Atmospheric corrections and interpretation of marine radiances in CZCS imagery: Use of a reflectance model," Oceanol. Acta **33-50 N.SP**, (1987).
16. B. Sturm, V. Barale, D. Larkin, J. H. Andersen, and M. Turner, " OCEAN code: the complete set of algorithms and models for the level 2 processing of European CZCS historical data, " Int. J. Remote Sens. **20**(7), 1219-1248 (1999).
17. J. Ahn, Y. Park, J. Ryu, B. Lee, and I. S. Oh, "Development of Atmospheric Correction Algorithm for Geostationary Ocean Color Imager (GOCI)," Ocean Sci. J. **47**(3), 247-259 (2012).
18. M. Wang, W. Shi and L. Jiang, " Atmospheric correction using near-infrared bands for satellite ocean color data processing in the turbid western pacific region," Opt. Express **20**, 741-753 (2012).
19. Z. Lee, B. Lubac, J. Werdell, and, R. Arnone, "An update of the Quasi-Analytical Algorithm (QAA v5), " available at: `http://www.ioccg.org/groups/Software_OCA/QAA_v5.pdf` (2009).
20. E. P. Shettle and R. W. Fenn, "Models of the aerosols of the lower atmosphere and the effects of humidity variations on their optical properties, " Rep. AFGL-TR-79-0214, U.S. Air Force Geophysics Laboratory, Hanscom Air Force Base, Mass. (1979).
21. J. E. O'Reilly, S. Maritorena, D. Siegel, M. C. O'Brien, D. Toole, B. G. Mitchell, M. Kahru, F. P. Chavez, P. Strutton, G. E. Cota, S. B. Hooker, C. R. McClain, K. L. Carder, F. Muller-Krager, L. Harding, A. Magnuson, D. Phinney, G. F. Moore, J. Aiken, K. R. Arrigo, R. Letelier, and M. Culver, " Ocean color chlorophyll a algorithms for SeaWiFS, OC2, and OC4: Version 4, " in *SeaWiFS Postlaunch Technical Report Series, Volume 11, NASA Tech. Memo. 2000-206892*, S. B. Hooker and E. R. Firestone, eds., (NASA Goddard Space Flight Center, Greenbelt, Maryland), pp. 9-23 (2000).
22. P. J. Werdell and S. W. Bailey, " An improved bio-optical data set for ocean color algorithm development and satellite data product validation," Remote Sens. Environ. **98**, 122-140 (2005).
23. Z. P. Lee, K. L. Carder, C. D. Mobley, R. G. Steward, and J. S. Patch, " Hyperspectral remote sensing for shallow waters: 1. A semianalytical model, " Appl. Opt. **37**(27) 6329-6338 (1998).
24. Z. Lee, K. L. Carder, and R. A. Arnone, " Deriving inherent optical properties from water color: a multiband quasi-analytical algorithm for optically deep waters, " Appl. Opt. **41**(27), 5755-5772 (2002).
25. A. Morel and L. Prieur, "Analysis of variations in ocean color, " Limnol. Oceanogr. **22**, 709-722 (1977).

1. Introduction

The marine reflectance $\rho_w(\lambda)$ estimated from ocean color satellite images is directly related to the inherent optical properties of the water (e.g., sea water absorption $a(\lambda)$ and backscattering $b_b(\lambda)$) allowing the derivation of biogeochemical parameters over the oceans. The accuracy of

#193504 - $15.00 USD Received 8 Jul 2013; revised 12 Aug 2013; accepted 13 Aug 2013; published 3 Sep 2013

these satellite derived parameters depends however on the processing of the sensor-measured radiance at the top of the atmosphere (TOA) used to obtain $\rho_w(\lambda)$. This processing includes, among others, the removal of the atmospheric contribution, the so-called atmospheric correction (AC) [1].

Initially, it was assumed that sea water absorbs all the incident light in the NIR spectral region (referred to as the black pixel assumption) allowing to estimate the atmospheric contributions and to select the appropriate aerosol model from the total signal. Next, the aerosol properties are extrapolated from the NIR to the visible spectral domain to obtain $\rho_w(\lambda)$ [1] (referred to as the GW94 AC algorithm). However in highly productive or turbid waters the assumption of zero NIR $\rho_w(\lambda)$ is not valid [2,3]. Assuming zero $\rho_w(\lambda_{NIR})$ generally leads to an overestimation of the aerosol contributions and subsequently to an underestimation of $\rho_w(\lambda)$ in highly productive or turbid waters [2]. Numerous algorithms have been developed with alternative hypotheses or including NIR-modeling schemes to account for the NIR ocean contribution to the measured signal [2–6]. However, global evaluations of these algorithms concluded that improvement is still required, especially in optically complex waters [7,8].

In a previous study, Goyens et al. [8] concluded, based on a validation of MODIS-Aqua images processed with four commonly used AC algorithms [4,5,9,10], that the standard NASA GW94-based AC algorithm, which includes a NIR-modeling scheme to retrieve $\rho_w(\lambda_{NIR})$ [3,5] (hereafter referred to as the STD algorithm), provided overall the best performances. However, in water masses optically dominated by detrital and mineral material, the GW94-based AC algorithm assuming a NIR similarity spectrum to account for non-zero $\rho_w(\lambda_{NIR})$, [4,6] (hereafter referred to as the MUMM algorithm) performed slightly better. The NIR-modeling scheme used in the STD algorithm is based on an iterative procedure including a bio-optical model with a Chlorophyll-a (Chl_a) based relationship to estimate $a(667)$ and assumptions on $b_b(\lambda)$ to extrapolate $\rho_w(\lambda)$ from the red to the NIR spectral domain [5]. In the MUMM algorithm, the GW94 AC algorithm is extended to turbid waters by considering spatial homogeneity in the aerosol properties over the area of interest and approximating the NIR $\rho_w(\lambda)$ ratio by a universal constant [4,6]. However, these assumptions show some limitations leading to imperfections in the AC. For instance, in waters optically dominated by non-algal particles, the Chl_a based relationship used in the bio-optical model of the STD algorithm may not be appropriate resulting in imperfections in the retrieved backscattering coefficients and subsequently in $\rho_w(\lambda_{NIR})$. Similarly, the constant NIR reflectance ratio used in the MUMM algorithm relies on the assumption that the NIR reflectance spectral shape is merely determined by the pure water absorption [4,6]. However, this assumption is not verified for all turbidity ranges and is valid for a limited spectral range [4,11,12].

An alternative to improve the STD algorithm is to constrain the iterative NIR-modeling scheme with spectral relationships. Similarly, a NIR spectral relationship may be used to correct the MUMM algorithm when the constant NIR reflectance ratio is not valid. Similar approaches have already been applied in several studies [12–18]. However, as observed by Goyens et al. [12], most spectral relationships appeared to be only valid for a certain range of turbidity. Nonetheless, the authors concluded that the bounding red spectral relationships, suggested by Lee et al. [19] to correct $\rho_w(667)$ according to $\rho_w(555)$ in the Quasi-Analytical Algorithm, and that the NIR polynomial relationship, suggested by Wang et al. [18] to extent the GW94 AC algorithm to the turbid western Pacific region for the processing of the GOCI ocean color images, were globally valid and potentially useful to improve satellite $\rho_w(\lambda)$ retrievals.

The objective of this study is to evaluate if the STD and MUMM algorithms can be improved by forcing the NIR-modeling schemes in both algorithms with these spectral relationships. Two modified NIR-modeling schemes are evaluated: (1) a modified MUMM NIR modeling scheme where the NIR constant $\rho_w(\lambda)$ ratio is replaced by the polynomial NIR spectral relationship, and (2) a modified STD NIR-modeling scheme constrained with the bounding red spectral relationships suggested by Lee et al. [19] and the NIR polynomial relationship [18] to evaluate $\rho_w(869)$ from $\rho_w(748)$. Hence two original algorithms are taken into account (i.e., MUMM and STD algorithms) and different modifications are applied to each algorithm.

The evaluation is based on a sensitivity test including *in situ* $\rho_w(\lambda)$ spectra from European and Southern Atlantic coastal waters. Data and methods are outlined in section 2. To evaluate the degree of improvement, initial algorithms are compared with modified algorithms, briefly discussed in sections 2.2 and 2.3, respectively. The performances of the initial algorithms are evaluated for moderately and very turbid waters (section 3.1) and compared to the modified algorithms evaluated and discussed in section 3.2.

2. Data and methods

2.1. Sensitivity study set-up

The top of atmosphere (TOA) reflectance, $\rho^{TOA}(\lambda)$, is derived from the sensor-measured radiance and corrected for gas absorption, Rayleigh scattering, white-caps reflection and sun glint, to obtain the Rayleigh corrected reflectance, $\rho_{rc}^{TOA}(\lambda)$, written as [1]:

$$\rho_{rc}^{TOA} = \rho_a^{TOA}(\lambda) + \rho_{ra}^{TOA}(\lambda) + t_{\theta_v}(\lambda) t_{\theta_0}(\lambda) \rho_w(\lambda). \tag{1}$$

where $\rho_a^{TOA}(\lambda)$ and $\rho_{ra}^{TOA}(\lambda)$ represent the scattered sunlight by the aerosols and the coupling between both air and aerosol molecules, respectively. $t_{\theta_v}(\lambda)$ is the diffuse transmittance of the atmosphere along the viewing direction and $t_{\theta_0}(\lambda)$ is the diffuse transmittance of the atmosphere along the incident direction. According to Eq. (1), if the optical properties and the concentrations of the aerosols are known, the quantities $\rho_a^{TOA}(\lambda)$, $\rho_{ra}^{TOA}(\lambda)$, $t_{\theta_0}(\lambda)$ and $t_{\theta_v}(\lambda)$ can be estimated and subsequently the above water $\rho_w(\lambda)$. For notational simplicity, the TOA notation is dropped hereafter.

For the present research a simulated dataset of $\rho_{rc}(\lambda)$ is build by combining the 105 *in situ* $\rho_w(\lambda)$ spectra (from above water TRIOS Ramses hyper-spectral radiometers, further detailed in the companion paper of this study [12]) with a simplified power law model for the multiple-scattering aerosol reflectance, $\rho_{am}(\lambda_0)$ (the sum of $\rho_a(\lambda_0)$ and $\rho_{ra}(\lambda_0)$ in Eq. (1)):

$$\rho_{am}(\lambda) = \rho_{am}(\lambda_0) \left(\frac{\lambda}{\lambda_0}\right)^{-\eta} \tag{2}$$

with η being the Ångström coefficient for the aerosol reflectance. For these tests we set the atmospheric diffuse transmittances, $t_{\theta_v}(\lambda)$ and $t_{\theta_0}(\lambda)$, to 1 and simulate $\rho_{rc}(\lambda)$ simply as the sum of $\rho_{am}(\lambda)$ and the *in situ* $\rho_w(\lambda)$. As shown by the flowchart in Fig. 1, $\rho_{rc}(\lambda)$ is then inverted using either the STD or the MUMM algorithm to estimate $\rho_w(\lambda)$ which for a perfect model would be equal to the *in situ* $\rho_w(\lambda)$.

For the sensitivity study two coastal models are selected, considered as the dominating aerosol types in coastal regions and derived from the work of Shettle and Fenn [20] and introduced by Gordon and Wang [1] with 50 and 90% relative humidity (hereafter referred to as C50 and C90). The corresponding Ångström coefficients η are set equal to 0.75 and 0.43, respectively, and $\rho_{am}(\lambda_0)$ at 869 nm to 0.015.

The initial and modified algorithms are evaluated and compared based on the median percentage bias between the estimated and *in situ* $\rho_w(\lambda)$ ($\rho_w^{est}(\lambda)$ and $\rho_w^{in\ situ}(\lambda)$, respectively):

$$\text{Bias} = 100\, \frac{\rho_w^{est}(\lambda) - \rho_w^{in\ situ}(\lambda)}{\rho_w^{in\ situ}(\lambda)} \tag{3}$$

A distinction is also made between moderately and very turbid waters defined as the spectra presenting $\rho_w(869)$ values between 10^{-4} and 3.10^{-3} and superior to 3.10^{-3}, respectively. All spectra presented $\rho_w(\lambda_{NIR})$ values above 10^{-4}, which is approximately the upper limit for which the GW94 AC algorithm can be successfully applied [2]. Out of the 105 spectra, 53% present moderate turbidity with $\rho_w(869)$ ranging from 10^{-4} to 3.10^{-3} and 47% of the data present very turbid waters with $\rho_w(869)$ exceeding 3.10^{-3}. This latter value corresponds to the threshold used by Wang et al. [10] to switch for the SWIR algorithm in the combined NIR-SWIR GW94-based AC process. Among the very turbid waters, extremely turbid waters are also investigated. These are water masses presenting $\rho_w(869)$ values superior to 10^{-2} and represent about 23% of the total *in situ* dataset.

2.2. *Initial STD and MUMM algorithms*

2.2.1. The STD algorithm

The NIR-modeling scheme within the STD algorithm, initially developed by Stumpf et al. [3] and later revised by Bailey et al. [5], uses an iterative method including a bio-optical model to account for the water contribution in the NIR region of the spectrum. The STD algorithm can be resumed as follows: First the algorithm uses the GW94 AC algorithm, assuming the black pixel assumption, to obtain a first guess in $\rho_w(\lambda)$. Blue and green $\rho_w(\lambda)$ estimations are then used to estimate Chl_a concentrations (MODIS Chl-a OC3 algorithm [21], assumption 1 in Fig. 1), which in turn serves to retrieve particulate and CDOM absorption in the red [22] (assumption 2 in Fig. 1), $a_{pg}(667)$. Knowing $a_{pg}(\lambda_{red})$ and below water $\rho_w^-(\lambda_{red})$ (by converting the estimated above water $\rho_w(667)$ to below water radiance reflectance [23]) it is possible to determine the red particulate backscattering coefficient, $b_{bp}(\lambda_{red})$. Next, $b_{bp}(\lambda_{NIR})$ is approximated by a power-law function of wavelength [24] (assumption 3 in Fig. 1). As, in the NIR region of the spectrum, absorption by CDOM, phytoplankton-related pigments, and other suspended particulate matter is assumed to be negligible, $a(\lambda_{NIR})$ can be approximated by the pure water absorption $a_w(\lambda_{NIR})$. Accordingly, knowing $a(\lambda_{NIR})$ and $b_{bp}(\lambda_{NIR})$, below water $\rho_w^-(\lambda_{NIR})$ can be estimated [25] and converted in above water $\rho_w(\lambda_{NIR})$. $\rho_w(\lambda_{NIR})$ is removed from $\rho_{rc}(\lambda_{NIR})$ and the newly estimated $\rho_{rc}(\lambda)$ is then inverted again with the GW94 AC algorithm to obtain $\rho_w(\lambda)$.

The process is re-iterated until $\rho_w(\lambda_{red})$ converges or if the maximum number of iterations is exceeded. In this study, when the estimated Chl_a is non-physical (e.g., because the retrieved $\rho_w(\lambda)$ are negative) or if the estimated $\rho_{am}(\lambda_0)$ is negative, an AC failure flag is assigned to the spectrum and $\rho_{am}(\lambda_0)$ is set to 0 and Chl_a to 10 mg l^{-1} for the next iteration. If the AC failure flag is assigned twice to a same spectrum, it is excluded for further data analysis.

2.2.2. The MUMM algorithm

The MUMM algorithm includes two alternative assumptions, one on the atmosphere (assumption 1 in Fig. 1) and one on the water optical properties, the NIR similarity spectrum assumption (assumption 2 in Fig. 1) [4,6]. The first assumption is based on the fact that the atmosphere composition does not vary significantly in space and time and therefore the Ångström coefficient for the aerosol reflectance, η, can be considered as spatially homogeneous over the area of interest. In clear waters, where $\rho_w(\lambda)$ in the NIR region of the spectrum is close to zero, $\rho_a(\lambda)+\rho_{ra}(\lambda)$ can be approximated by $\rho_{rc}(\lambda)$ and, subsequently, η can be retrieved. The clear water retrieved η is then used for the AC of the entire image.

The second assumption arises from the fact that the sea-water spectrum shape in the NIR spectral domain is largely determined by pure water absorption, and hence invariant. The magnitude of the signal is approximately proportional to the backscatter coefficient. Consequently, the ratio of any two NIR water leaving reflectances, $\alpha(\lambda_i,\lambda_j)$, is constant. For MODIS-Aqua

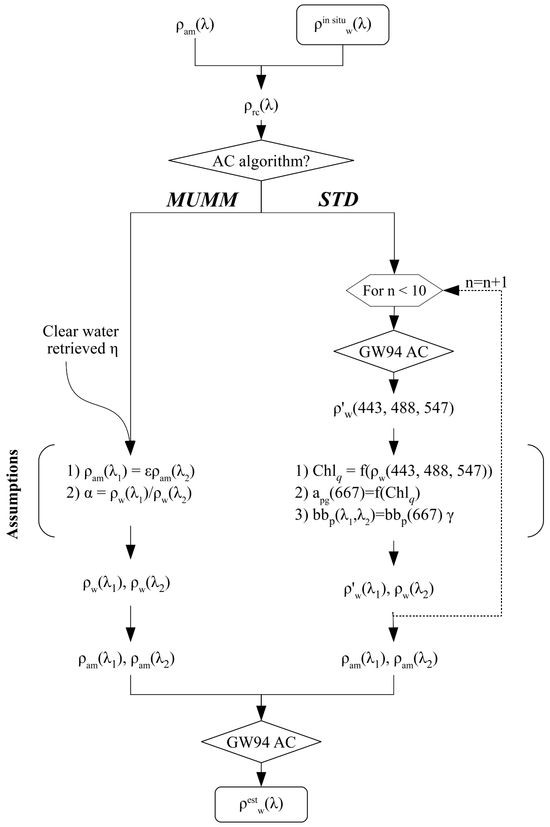

Fig. 1. Schematic flowchart of the sensitivity study set-up for the STD and MUMM algorithms. $\rho_w^{in\ situ}(\lambda)$ and $\rho_w^{est}(\lambda)$ are the *in situ* and estimated $\rho_w(\lambda)$, respectively, and λ_1 and λ_2 designate the two wavelengths in the NIR spectral region. Dashed lines indicate the iterative processes for the STD algorithm.

#193504 - $15.00 USD Received 8 Jul 2013; revised 12 Aug 2013; accepted 13 Aug 2013; published 3 Sep 2013

images $\alpha(748, 869)$ is defined as:

$$\alpha = \frac{\rho_w(748)}{\rho_w(869)} = 1.945 \tag{4}$$

Next, knowing η and $\alpha(\lambda_i, \lambda_j)$, $\rho_{am}(\lambda)$ is estimated for two NIR bands allowing to retrieve the appropriate aerosol model.

$$\rho_{am}(\lambda_i) = \varepsilon(\lambda_i, \lambda_j)\frac{\alpha(\lambda_i, \lambda_j)\rho_{rc}(\lambda_j) - \rho_{rc}(\lambda_i)}{\alpha(\lambda_i, \lambda_j) - \varepsilon(\lambda_i, \lambda_j)} \tag{5}$$

$$\rho_{am}(\lambda_j) = \frac{\alpha(\lambda_i, \lambda_j)\rho_{rc}(\lambda_j) - \rho_{rc}(\lambda_i)}{\alpha(\lambda_i, \lambda_j) - \varepsilon(\lambda_i, \lambda_j)} \tag{6}$$

The initial GW94 AC algorithm is then run again but forced with the previously selected aerosol model.

As shown in Fig. 1, the MUMM algorithm requires thus an a priori defined η. For the sensitivity study, a correct retrieved η is initially assumed. Next, to assess the sensitivity of the algorithm to errors on the selected aerosol model, we consider an η value corresponding to the C90 aerosol model while the C50 aerosol model was used to simulate $\rho_{rc}(\lambda)$ (error on η of $\sim -40\%$) and vice versa (error on η of $\sim 70\%$).

2.3. *Modified STD and MUMM algorithms*

2.3.1. Polynomial-based MUMM algorithm

The MUMM algorithm is modified here to take into account also extremely turbid waters. Indeed, the validation exercise conducted by Goyens et al. [12] showed that the validity range of the constant NIR reflectance ratio [4, 6] was limited to moderately and very turbid waters with $\rho_w(\lambda_{NIR}) < 10^{-2}$, while the polynomial function of Wang et al. [18] was also valid for extremely turbid waters. Subsequently, in order to improve $\rho_w(\lambda)$ retrievals in extremely turbid waters, the NIR constant reflectance ratio in the MUMM algorithm (assumption 2 in Fig. 1) is replaced by the polynomial function of Wang et al. [18] (therefore referred to as the polynomial-based MUMM algorithm). This includes some modifications in the initial algorithm. Using Eq. (1) and the polynomial function from Wang et al. [18], the following relationships and unknown quantities are obtained:

$$\rho_{rc}(748) = \rho_{am}(748) + t^*_{748}\rho_w(748) \tag{7}$$

$$\rho_{rc}(869) = \rho_{am}(869) + t^*_{869}\left[a\rho_w(748) + b\rho_w(748)^2\right] \tag{8}$$

where a and b are the constant values of the polynomial function [18] and t^*_λ the viewing and incident atmospheric transmittance corrected for the two-way ozone and oxygen absorption using the terminology of Ruddick et al. [4].

Provided that the aerosol model is correctly retrieved, the atmospheric correction parameter $\varepsilon(748, 869)$ (written hereafter as ε for notational simplicity) is equal to the aerosol reflectance ratio at 748 and 869 nm and thus, according to Eq. (2), related to η as follow:

$$\varepsilon = \frac{\rho_{am}(748)}{\rho_{am}(869)} = \left(\frac{\lambda}{\lambda_0}\right)^{-\eta} \tag{9}$$

Eq. (8) can then be rewritten as:

$$\rho_{rc}(869) = \frac{1}{\varepsilon}\rho_{am}(748) + at^*_{869}\rho_w(748) + bt^*_{869}\rho_w(748)^2. \tag{10}$$

Accordingly, the system Eq.(7)-ε Eq.(10) gives:

$$b\varepsilon t^*_{869}\rho_w(748)^2 + [a\varepsilon t^*_{869} - t^*_{748}]\,\rho_w(748) + [\rho_{rc}(748) - \varepsilon\rho_{rc}(869)] = 0. \tag{11}$$

$\rho_{rc}(\lambda)$ at 748 and 869 nm are known for each spectra and t^*_λ is derived from the viewing and incident geometry and selected aerosol model. Hence, the remaining unknown quantity is $\rho_w(748)$. Eq. (11) is a quadratic function with two solutions, one of which is clearly non-physical. Accordingly, the unique solution for $\rho_w(748)$ is:

$$\rho_w(748) = \frac{[t^*_{748} - a\varepsilon t^*_{869}] - \sqrt{[a\varepsilon t^*_{869} - t^*_{748}]^2 - 4b\varepsilon t^*_{869}[\rho_{rc}(748) - \varepsilon\rho_{rc}(869)]}}{2b\varepsilon t^*_{869}} \tag{12}$$

Next, knowing $\rho_w(748)$, $\rho_w(869)$ can be retrieved by evaluating the polynomial function of Wang et al. [18] and, by means of Eqs. (1) and (2), $\rho_w(\lambda)$ can be retrieved for the entire spectrum.

2.3.2. Constrained STD algorithm

To improve $\rho_w(\lambda)$ retrievals, red and NIR spectral relationships are used to constrain the NIR-modeling scheme within the STD algorithm (therefore referred to as the constrained-STD algorithm). The red spectral relationships are already used as bounding relationships in the last updated version of the Quasi Analytical Algorithm (QAA v5) to correct imperfections in the retrieved $\rho_w(667)$ [19]. Similarly to the polynomial relationship suggested by Wang et al. [18], these red spectral relationships have been validated previously by Goyens et al. [12] with the *in situ* data mentioned in section 2.1. To force the STD algorithm, the spectral relationships are implemented within the iterative process as follows: If within the iterative process, the previously retrieved $\rho_w(555)$ is non-negative and $\rho_w(667)$ is out of limit according the bounding red spectral relationships, $\rho_w(667)$ is corrected and set equal to the closest limit. Next, the NIR spectral polynomial relationship [18] is used to retrieve $\rho_w(869)$ from the estimated $\rho_w(748)$, avoiding imperfections due to the extrapolation of $b_{bp}(\lambda)$ from 667 to 869 nm.

3. Results and discussion

3.1. *Performances of initial STD and MUMM algorithms in turbid waters*

To delineate the areas of improvements, the performances of the initial AC algorithms are first evaluated. Statistics (median, first and third quartile) of the percentage bias between *in situ* and estimated $\rho_w(\lambda)$ for the STD and MUMM algorithms are shown in Fig. 2, for moderately and very turbid waters and when considering only extremely turbid waters. Relative performances of the algorithms are similar when the C50 or C90 aerosol model is considered and the percentage bias calculated with the C50 aerosol model and the C90 aerosol model remain close. Therefore, results are shown here with the C50 aerosol model only.

For moderately turbid waters, the two algorithms retrieves the same number of reflectance spectra. In contrast, due to AC failure (observed for 9 spectra) and because $\rho_w(667)$ did not converged after 10 iterations (for 1 spectrum), for very turbid waters the STD algorithm retrieves 46 reflectance spectra out of the 56. The excluded spectra present all $\rho_w(869)$ values superior to 10^{-2} (defined previously as extremely turbid).

The STD algorithm tends to underestimate $\rho_w(\lambda)$ at all wavelengths for moderately turbid waters (median bias ranging from -51% to -3%) [Figs. 2(a)-2(e)]. For the very turbid waters the algorithm provides relatively good results in the green but underestimates $\rho_w(\lambda)$ in the blue and largely overestimates $\rho_w(\lambda)$ at 869 nm (median bias of -13% and 22%, respectively) [Figs.

2(a)-2(e)]. When considering only the most turbid waters ($\rho_w(869) > 10^{-2}$, 14 extremely turbid spectra), the underestimation of $\rho_w(\lambda)$ in the blue spectral domain is even more pronounced with a median bias ranging from -60% at 412 nm to 18% at 869 nm. This suggests that the STD NIR-modeling scheme is appropriate for very turbid waters, however negative $\rho_w(\lambda)$ values in the blue are still retrieved and the performance of the algorithm decreases with an increase in turbidity. For moderately turbid waters, the assumptions made in the STD algorithm results in relatively low errors at 412 nm but in large retrieval errors in the red and NIR spectral domain.

For moderately turbid waters and over the 412-667 nm spectral range, the median percentage bias varies from -2% to -8% for the MUMM algorithm. However, at 748 and 869 nm, the median percentage bias reaches values up to -30 and -41%, respectively [Figs. 2(f)-2(j)]. For very turbid waters, the median bias ranges from -0.5% to -5% [Figs. 2(f)-2(j)]. When considering only the most turbid waters ($\rho_w(869) > 10^{-2}$, 24 extremely turbid spectra) the median bias further decreases ranging from -18% to -4%. This may be explained by the underestimation of the water signal in extremely turbid waters when a constant NIR reflectance ratio is considered. Indeed, as observed with the validation exercise of Doron et al. [11] and Goyens et al. [12], the constant NIR reflectance ratio used in the MUMM algorithm tends to underestimate $\rho_w(\lambda)$ in the NIR spectral domain when $\rho_w(\lambda_{NIR})$ increases. Note however that these results are obtained when η is correctly estimated over the clear water pixels and thus considering that the assumption of spatial homogeneity in aerosol properties is verified.

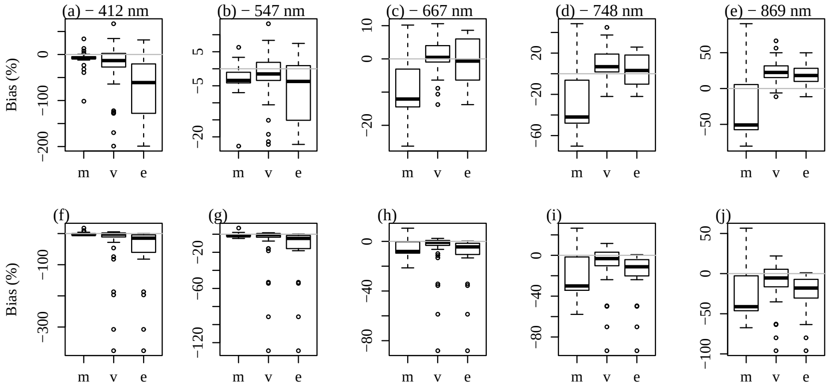

Fig. 2. Box plots of percentage bias for the STD (a-e) and MUMM (f-j) algorithms for moderately (m, $\rho_w(869) > 10^{-4}$ and $\rho_w(869) < 3.10^{-3}$) and very (v, $\rho_w(869) > 3.10^{-3}$)) turbid waters and when considering only the extremely turbid waters (e, $\rho_w(869) > 10^{-2}$). Box plots indicate median with first and third quartiles, upper and lower whiskers and outliers (small circles, $\pm 1.5IQR$). The horizontal grey lines indicate a bias of 0% (occurring when $\rho_w(\lambda)$ are perfectly retrieved).

3.2. *Performances of the algorithms with the proposed modifications*

In Figs. 3(a)-3(c) the performances of the initial and modified algorithms are compared. To evaluate the impact of imperfections in the retrieved η, Figs. 3(a)-3(c) also show the performances of the MUMM and polynomial-based MUMM algorithms when η is estimated for a

C90 aerosol model while the C50 aerosol model was used to simulate $\rho_{rc}(\lambda)$ (error on η of $\sim -40\%$). Table 1 shows the number of retrieved data and the median, mean and standard deviation of the percentage bias per wavelength when considering all retrieved reflectance spectra. Since the initial STD algorithm retrieves more spectra compared to the constrained algorithm, statistics are also given for the initial STD algorithm when only the spectra retrieved with the constrained STD algorithm are considered.

Table 1. Number of retrieved reflectance spectra and median (average, standard deviation) percentage bias per wavelength (412, 488, 547, 667, 748, and 869 nm). For comparison, statistics for the original STD algorithm are also given when considering only the spectra retrieved with the constrained STD algorithm.

	Numb. spectra	412	488	547	667	748	869
STD	95	-8 (-16, 40)	-4 (-5, 12)	-2 (-2, 6)	-2 (-4, 8)	-1 (-10, 28)	10 (-4, 40)
	90	-8 (-11, 29)	-4 (-4, 11)	-2 (-2, 5)	-2 (-5, 8)	-4 (-11, 28)	9 (-6, 40)
STD_{Con}	90	-4 (-2, 23)	-2 (-2, 10)	-1 (-1, 5)	-2 (-4, 8)	-6 (-13, 28)	-6 (-17, 34)
MUMM	105	-2 (-14, 54)	-1 (-7, 27)	-1 (-5, 17)	-2 (-5, 12)	-8 (-13, 21)	-13 (-17, 28)
$\text{MUMM}_{\text{Poly}}$	105	-1 (-8, 49)	0 (-4, 25)	0 (-3, 16)	-1 (-4, 12)	-2 (-11, 23)	-4 (-14, 30)

Overall the constrained STD algorithm shows improvements compared to the initial algorithm (lower median, mean and standard deviation). For moderately turbid waters, initial and constrained STD algorithms show similar results. Improvement with the constrained STD algorithm are more pronounced for very turbid waters and in particular in the blue and NIR region of the spectrum [Figs. 3(b) and 3(c)]. However, as shown in Table 1, the number of retrieved spectra is lower when the algorithm is constrained. Indeed, 15 spectra (all presenting extremely turbid water masses, $\rho_w(869) > 10^{-2}$) are excluded because the estimated Chl_a concentration was non-physical at least twice during the iterative process, while, with the initial STD algorithm, 9 spectra are excluded because the algorithm failed to retrieve Chl_a concentrations more than twice and 1 spectrum is excluded because the retrieved $\rho_w(667)$ did not converge within 10 iterations. For 13 spectra, out of the 15 spectra, $\rho_w(667)$ was corrected during the iterative process because it exceeded the maximum limit according to the red bounding spectral relationships suggested by Lee et al. [19]. When excluding this constrain (i.e., only retaining the NIR spectral relationship [18] in the NIR-modeling scheme), the number of excluded spectra decreases from 15 to 8. However, the performance of the algorithm decreases too, and in particular in the blue region of the spectrum over very turbid waters (not shown here). When considering only equivalent spectra, the STD algorithm constrained with both red and NIR spectral relationships slightly improves $\rho_w(\lambda)$ for all water types compared to the initial STD algorithm (Table 1). Hence, overall both the red and NIR spectral constrains improved the retrieved $\rho_w(\lambda)$ for all turbidity ranges. However, more work should be done to increase the number of retrieved spectra and thus reducing the sensitivity of the algorithm to non-physical Chl_a concentration estimations.

As expected from the validation exercise conducted by Goyens et al. [12], replacing the constant MUMM algorithm with the NIR polynomial relationship reduces the bias (Table 1) and mainly when considering only extremely turbid waters [Fig. 3(c)]. However, when including the NIR polynomial relationship, the algorithm seems to be more sensitive to errors on the estimated η. Hence, the added value of the polynomial NIR spectral relationship will be significantly reduced, when η is not correctly retrieved [Figs. 3(b)-3(c)]. Errors on the estimated η may be due to missing clear water pixels within the area of interest or if the assumption of spatial homogeneity in aerosol properties is not verified. This confirms the conclusion of Jamet et al. [7], notably that the sensitivity of the algorithm to the selected aerosol model remains an issue for the MUMM algorithm. Hence, compared to the MUMM algorithm, the STD algorithm presents a large advantage as it does not require an initial guess for η and does not

#193504 - $15.00 USD Received 8 Jul 2013; revised 12 Aug 2013; accepted 13 Aug 2013; published 3 Sep 2013

imposes spatial homogeneity in aerosol properties since it retrieves the aerosol properties on a pixel-by-pixel basis. However, as mentioned earlier, the STD algorithm is affected by erroneous Chl_a estimations. Moreover, relying only on a Chl_a based relationship to estimate $\rho_w(\lambda_{NIR})$ in optically complex waters may be dubious.

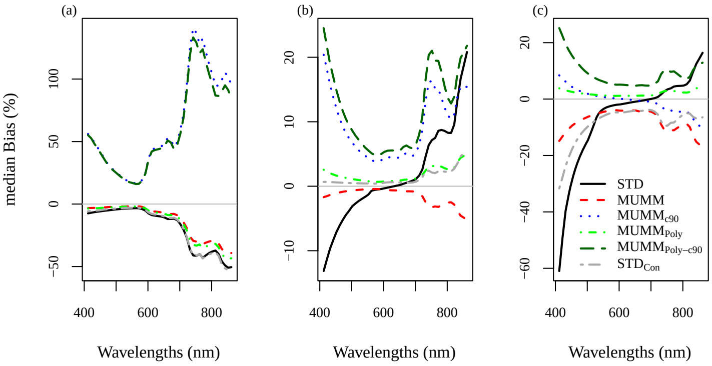

Fig. 3. Median percentage bias as a function of wavelength for (a) moderately and (b) very turbid waters and (c) when considering only the most turbid waters ($\rho_w(869) > 10^{-2}$) with STD: initial STD Algorithm, MUMM: initial MUMM algorithm assuming the correct aerosol model, MUMM$_{c90}$: MUMM algorithm assuming the incorrect C90 aerosol model, MUMM$_{Poly}$: polynomial-based MUMM algorithm, MUMM$_{Poly-c90}$: polynomial-based MUMM algorithm assuming the incorrect C90 aerosol model, and STD$_{Con}$: constrained STD algorithm.

4. Conclusion

More work needs to be done to further reduce inaccuracies in $\rho_w(\lambda)$ retrieved from ocean color images and particularly in turbid and optically complex waters [8]. Therefore, the present study aims to evaluate if $\rho_w(\lambda)$ retrievals can be improved by forcing the NIR-modeling scheme within the standard NASA and MUMM GW94-based AC algorithms (referred to as the STD and MUMM algorithms) with spectral relationships validated previously in a companion paper from Goyens et al. [12]. According to the authors, the red bounding relationships used in the QAA [19] as well as the NIR spectral relationship suggested to extent the GW94 AC algorithm for the AC of GOCI images [18], were valid for moderately turbid and very turbid waters. These relationships are used here to constrain the initial MUMM and STD algorithms. Two modified algorithms are evaluated: (1) a modified MUMM algorithm where the NIR constant $\rho_w(\lambda)$ ratio is replaced by the polynomial NIR spectral relationship, and (2) a modified STD algorithm where the iterative NIR-modeling scheme is constrained with the bounding red spectral relationships suggested by Lee et al. [19] and the NIR polynomial relationship [18] to evaluate $\rho_w(869)$ from $\rho_w(748)$. The degree of improvement resulting from the spectral relationship constrains are investigated by comparing *in situ* $\rho_w(\lambda)$ with $\rho_w(\lambda)$ retrieved with the initial and modified STD and MUMM algorithms.

When the STD algorithm is forced with the bounding red and the NIR polynomial spectral relationships, the algorithm performs better for all turbidity ranges and over the entire spectrum. However, the number of retrieved $\rho_w(\lambda)$ spectra is slightly reduced because more spectra are flagged due to non-physical Chl_a concentration estimations in the NIR-modeling scheme.

When the constant NIR reflectance ratio used in the initial MUMM algorithm to account for non-zero $\rho_w(\lambda_{NIR})$, is replaced by the NIR polynomial relationship [18], errors in estimated $\rho_w(\lambda)$ are reduced, particularly in extremely turbid waters. However, compared to the initial algorithm, the polynomial-based MUMM algorithm is more sensitive to erroneously estimated η from nearby clear water pixels.

Compared to the MUMM algorithm, the STD algorithm presents a large advantage as it does not require an initial guess for η neither imposes spatial homogeneity in aerosol properties. Accordingly, the MUMM algorithm should be further improved to reduce the sensitivity of the algorithm to the selected aerosol model. Meanwhile, the STD algorithm should be modified such that $\rho_w(\lambda)$ retrievals are less affected by erroneous estimations of Chl_a concentrations. Accordingly, further improvements in $\rho_w(\lambda)$ retrievals may be achieved by, for instance, combining both polynomial-based MUMM and constrained STD algorithms. This may be investigated in a future research.

The present study investigates the feasibility to constrain NIR-modeling schemes with spectral relationships in the aim to improve AC processes and subsequently satellite estimated $\rho_w(\lambda)$. This study should be confirmed by an *in situ*-satellite data match-up exercise to verify and quantify the effective improvement in satellite $\rho_w(\lambda)$ retrievals resulting from the suggested modifications.

Acknowledgments

Most of the *in situ* measurements used here were collected in the framework of the BELCOLOUR-1 and BELCOLOUR-2 projects funded by the Belgian Science Policy Office STEREO programme. Griet Neukermans and Barbara Van Mol are acknowledged for data acquisition. This work has been supported by the French Spatial Agency (CNES) through the TOSCA program and the "Ministère de l'Enseignement et de la Recherche Française" which provided a PhD scholarship.

#193504 - $15.00 USD Received 8 Jul 2013; revised 12 Aug 2013; accepted 13 Aug 2013; published 3 Sep 2013

- Chapter 6 -

Spectral relationship-forced STD and MUMM NIR-modelling schemes to improve AC in turbid waters

Chapter 5 suggested several modifications based on valid theoretical and empirically retrieved spectral relationships to improve NIR-modelling schemes for the AC. In the present chapter, these newly suggested NIR-modelling schemes are compared and validated with satellite and *in situ* data. The modified NIR-modelling schemes are:

- the $\text{MUMM}_{\text{Poly}}$ scheme which replaces the constant NIR reflectance ratio of the initial MUMM NIR modelling scheme by the NIR polynomial spectral relationship suggested by Wang et al. (2012),
- the $\text{STD}_{\text{Contheor}}$ scheme which is the STD NIR modelling scheme constrained by (1) an empirical blue-green and bounding red spectral relationships to correct for erroneous $\rho_w(\lambda)$ retrievals in the visible spectral domain before it is used as input for the STD bio-optical model, (2) a theoretical red-NIR hyperbolic spectral relationship to reduce the sensitivity of the initial STD NIR-modelling scheme to errors on $b_{bp}(\lambda_{red})$, and, (3) an empirical NIR polynomial spectral relationship to avoid the simple extrapolation of $b_{bp}(\lambda)$ from the red to the NIR spectral domain, and,
- the COMB NIR-modelling scheme which consists in using the $\text{MUMM}_{\text{Poly}}$ NIR-modelling scheme when the $\text{STD}_{\text{Contheor}}$ approach fails to retrieve valid Chl_a concentrations.

The performances of the modified NIR-modelling schemes are compared with the initial MUMM and STD approach. The initial SeaDAS 6.4 Level-2 processing program was therefore adapted to include the modified NIR-modelling schemes.

First a validation of the NIR-modelling schemes is conducted with the same *in situ* AERONET-OC and LOG $\rho_w(\lambda)$ measurements used in the inter-comparison study discussed in Chapter 4 and published by Goyens et al. (2013c) (Section 6.1). This validation exercise includes an overall inter-comparison of the ocean colour products and an evaluation of the number of valid and negative retrieved $\rho_w(\lambda)$ values. Similarly to Goyens et al. (2013c), a class-specific validation is also performed to investigate the behavior and limitations of the modified NIR-modelling schemes as a function of the optical water type according to the classification scheme developed by Vantrepotte et al. (2012) (Sections 1.5 and 4.2). For this global validation, and as done by Goyens et al. (2013c), the default flags and parameters suggested by the NASA OBPG are used. This allows to reproduce the processing conducted by common ocean colour users. Note however that the processing is performed here with the updated SeaDAS version 6.4, while Goyens et al. (2013c) processed the images with the version 6.2 of SeaDAS. Hence, small differences may be observed, mainly due to slight changes in the gain factors (Chapter 3, Table 3.1). However, these changes should only slightly affect the AC performances and differences should be small.

The AERONET-OC dataset present mainly $\rho_w(\lambda)$ spectra over moderate turbidity ranges. As observed in Chapter 5, the spectral relationship-forced NIR-modelling schemes, essentially improved $\rho_w(\lambda)$ retrievals in very or extremely turbid waters. Therefore, a second match-up exercise is conducted with the turbid water *in situ* data collected by the LOG (Section 6.2). Beside a comparison between *in situ* and MODIS retrieved $\rho_w(\lambda)$ data, a visual inspection of the MODIS Aqua images is also performed to evaluate the differences in spatial $\rho_w(\lambda)$ patterns resulting from the distinctive NIR-modelling schemes.

6.1 GLOBAL VALIDATION OF THREE MODIFIED STD AND MUMM NIR-MODELLING SCHEMES

6.1.1 Data and Methods

Validation is carried out with the AERONET-OC data and field data from four cruises coordinated by the LOG. Both datasets are detailed in Chapter 3 and discussed in Chapter 4 and by Goyens et al. (2013c).

A total of 1456 satellite images is processed with the five different NIR-modelling schemes for the extension of the GW94 AC algorithm to turbid waters, namely, the initial STD and MUMM approaches and the newly suggested $\text{MUMM}_{\text{Poly}}$, $\text{STD}_{\text{Contheor}}$ and COMB NIR-modelling schemes.

In the previous chapter, the water signal in the NIR spectral region was used to differentiate moderately from very and extremely turbid waters. According to these turbidity classes and based on the *in situ* $\rho_w(869)$ data, among the 1456 match-up pairs, most spectra present moderately turbid waters (1143) and only a few data present non-turbid (291, $\rho_w(869) < 10^{-4}$), very turbid (22, $\rho_w(869) > 3.10^{-3}$) and extremely turbid waters (4, $\rho_w(869) > 10^{-2}$).

Based on the classification scheme of Vantrepotte et al. (2012), out of the 1456 *in situ* data, about 2% are allocated to optically mixed water masses dominated by detrital and mineral material (referred to as Class 1), 54% to optically mixed waters dominated by phytoplankton (referred to as Class 2), only one spectra to water masses strongly impacted by mineral material (referred to as Class 3), and, 38% to CDOM and phytoplankton dominated waters (referred to as Class 4). 6% of the *in situ* spectra remained unclassified.

Match-up selection and validation set-up are similar to those outlined in the paper of Goyens et al. (2013c) and described in Section 3.4. Note, however, that in the validation exercise of Goyens et al. (2013c), an additional selection criteria was used such that only the turbid waters were considered. Indeed, any spectra showing $\rho_w(667)$ values below 6.10^{-3} ($\sim L_{wn}(\lambda) <$ 0.183 mW cm^{-2} μm^{-1} sr^{-1}, according to the definition of Robinson et al. (2003)) were excluded for further data analysis. For the present study, this exclusion criterion is not applied to ensure a greater set of match-up pairs. Moreover, ocean colour end-users often expect globally valid AC methods. Hence, the NIR-modelling scheme should provide satisfactory $\rho_w(\lambda_{NIR})$ estimations for all optical water classes and turbidity ranges.

The study of Goyens et al. (2013c) also imposed that the match-up pairs for each algorithm match. Here the performance of the algorithms is compared when including all the match-up pairs for which each AC approach retrieved valid $\rho_w(\lambda)$ spectra (including the non-turbid water masses), and when including only the 211 common match-up pairs selected by Goyens et al. (2013c) (thus excluding the non-turbid water masses).

The algorithm performances are compared qualitatively based on scatter-plots and quantitatively based on statistical parameters computed between satellite and *in situ* $\rho_w(\lambda)$ estimations, i.e., the percent bias, the percent relative error (RE), the root mean square error (RMSE), the spearman correlation (R) and the slope and intercept of the linear regression. Bias, RE and RMSE are calculated as follows:

$$BIAS = \frac{1}{N}\Sigma\left(100\frac{\rho_w^{est}(\lambda) - \rho_w^{obs}(\lambda)}{\rho_w^{obs}(\lambda)}\right), \tag{6.1}$$

$$RE = \frac{1}{N}\Sigma\left(100\frac{|\rho_w^{est}(\lambda) - \rho_w^{obs}(\lambda)|}{\rho_w^{obs}(\lambda)}\right), \tag{6.2}$$

$$RMSE = \sqrt{\left(\frac{\Sigma(\rho_w^{est}(\lambda) - \rho_w^{obs}(\lambda))^2}{N}\right)}, \tag{6.3}$$

where ρ_w^{obs} and ρ_w^{est} are the in-situ and the MODIS estimated $\rho_w(\lambda)$, respectively, and N the number of observations.

6.1.2 Results and discussion

6.1.2.1 Match-up selection

Table 6.1 shows the number of excluded spectra because more than 3 pixels within the 3 by 3 pixels window are flagged, and/or, because the homogeneity criterion is not verified. Out of the 1456 processed images, for the 5 NIR-modelling schemes, 592 pixels windows present less then 6 valid pixels.

Table 6.1: *Excluded and total number of match-up pairs per AC approach. Values in parentheses indicate the amount of excluded match-ups because of non-homogeneity only.*

Selection Criteria	$STD_{Contheor}$	COMB	$MUMM_{Poly}$	MUMM	STD
$< 6pixels$	592	592	592	592	592
Non-uniform ($\rho_w(547)$)	101(93)	104 (92)	92(81)	92(81)	114(103)
Total valid match-ups	771	772	783	783	761

When the homogeneity criterion is applied, the largest number of excluded match-up pairs is observed with the initial STD AC approach (114 excluded spectra) while the lowest number is encountered with the MUMM and $\text{MUMM}_{\text{poly}}$ approaches (92 excluded spectra). The COMB approach was expected to be affected by a more important number of excluded spectra because of non-homogeneous pixels windows. Indeed, as mentioned by Goyens et al. (2013c) for the NIR-SWIR AC method, the switching between the $\text{STD}_{\text{Contheor}}$ and $\text{MUMM}_{\text{poly}}$ NIR-modelling scheme may induce an abrupt change in $\rho_w(\lambda)$ within the pixels window. However, this is not noticeable here since the number of excluded non-homogeneous satellite-*in situ* data pairs is not significantly higher with the COMB AC method compared to the other methods (Table 6.1).

When non-homogeneous and flagged pixels windows are excluded, 772 and 771 spectra are retained with the COMB and $\text{STD}_{\text{Contheor}}$ approaches, respectively. The MUMM and $\text{MUMM}_{\text{poly}}$ approaches retrieve the largest number of spectra (783) while the initial STD approach retrieves the lowest amount of spectra (761, Table 6.1).

Hence, as observed with the sensitivity study in the previous chapter, the largest spatial coverage is ensured with the MUMM and $\text{MUMM}_{\text{poly}}$ algorithms followed by the COMB and the $\text{STD}_{\text{Contheor}}$ approaches. Because the MUMM and $\text{MUMM}_{\text{poly}}$ algorithms consider spatial homogeneity in aerosol properties, these algorithms may indeed be less affected by the homogeneity criterion compared to the other algorithms retrieving aerosol properties on a pixel basis.

When the number of excluded $\rho_w(\lambda)$ spectra are compared as a function of the turbidity level and for the different algorithms, no specific trend is observed. Indeed, the newly suggested AC methods do not seem to retrieve more valid $\rho_w(\lambda)$ values at higher turbidity levels compared to the initial AC methods. For all the AC methods, about 80% of the remaining *in situ* spectra present moderate turbidity, less than 1% present very turbid waters and the remaining 20% present low turbidity. Hence, the four extremely turbid water match-ups are excluded for further data analysis with all AC methods and this because less then 6 valid pixels are encountered within the pixels windows. The sensitivity studies conducted in the previous chapter concluded that improvements, with the modified NIR-modelling schemes, are more pronounced for very and extremely turbid waters. Hence, with the present *in situ* dataset, improvements are expected to be relatively small. However, a class-specific validation may be useful to delineate limitations and added values of the modified NIR-modelling schemes.

Table 6.2 shows the number of valid retrieved $\rho_w(\lambda)$ spectra per optical water class and per NIR-modelling scheme. According to these results, the MUMM-based AC algorithms tend to retrieve more valid spectra than the STD-based algorithm mainly over phytoplankton optically dominated waters (Class 2). For Class 4 waters (optically dominated by phytoplankton and CDOM), the COMB and $\text{STD}_{\text{Contheor}}$ NIR-modelling schemes retrieve more valid $\rho_w(\lambda)$ spectra compared to the initial STD scheme and the same amount of spectra as the MUMM-based NIR-modelling schemes. This is a valuable observation showing that these modified NIR-modelling schemes retrieve the same number of Class 2 spectra as the initial STD scheme but are more adequate to retrieve $\rho_w(\lambda)$ spectra in water masses not optically dominated by algal-particles. For Class 1 waters, all approaches retrieve the same number of valid spectra (Table 6.2).

Table 6.2: *Number of valid match-up pairs per class and per NIR-modelling scheme for AC.*

	Unclassified	Class 1	Class 2	Class 4
$\text{STD}_{\text{Contheor}}$	45	20	357	349
COMB	46	20	357	349
$\text{MUMM}_{\text{Poly}}$	45	20	369	349
MUMM	45	20	369	349
STD	46	20	357	338

6.1.2.2 Global $\rho_w(\lambda)$ validation

Table 6.3 gives the overall performance and the performance of the AC methods when including only the 211 common match-up pairs validated by Goyens et al. (2013c).

No large differences are observed between the AC methods in terms of statistical performances. When considering all match-up pairs, RE and bias range from 18 to 166% and from -1.3 to -91.4%, respectively. When considering only the 211 similar match-ups pairs, RE and bias range from 17 to 48% and from -8.8 to -25.9%, respectively. The largest bias and RE are encountered at 412 nm where the signal is usually lower. The lowest bias are encountered at 547 nm where the signal is more significant (as observed by Goyens et al. (2013c)). Although the results remain very similar, when considering all wavelengths, the $\text{STD}_{\text{Contheor}}$ AC method shows the best statistics followed by the STD approach (Table 6.3).

Figure 6.1 shows the MODIS-Aqua versus in-situ $\rho_w(\lambda)$ data for the five AC methods. For a better visibility, only the 211 common valid match-up pairs are considered in this figure.

According to Fig. 6.1, data points seem to be more dispersed around the 1:1 line when using the MUMM-based NIR-modelling schemes and the COMB approach. Hence, though the resulting statistics are relatively good with the MUMM-based approaches (especially the bias in the green and red spectral region, Table 6.3), large over- and underestimations in $\rho_w(\lambda)$ are encountered with these NIR-modelling schemes. A possible explanation for this may be the erroneously retrieved aerosol properties from climatological data or nearby clear water pixels.

As expected, no large differences are observed between the MUMM and $\text{MUMM}_{\text{Poly}}$ AC methods. Indeed, according to the study of Goyens et al. (2013a), for moderately turbid waters, the constant NIR reflectance ratio and polynomial function result in very similar $\rho_w(\lambda_{NIR})$ retrievals.

Biases are negative at all wavelengths and with all algorithms. Hence, either the NIR-modelling schemes still tend to underestimate $\rho_w(\lambda_{NIR})$, or the approach to estimate aerosol

Table 6.3: *Statistical results for* $\rho_w(\lambda)$ *retrieved with the* $STD_{Contheor}$*, COMB,* $MUMM_{poly}$*, MUMM and STD AC approaches and percentage of negative retrieved values. Statistics between brackets correspond to the values obtained when only the 211 common match-up pairs are retained. The best statistics per spectral band are indicated in bold.*

	R^2	Intercept	Slope	RE (%)	RMSE	Bias (%)	$\rho_w(\lambda) < 0$ (%)
$\rho_w(412)$							
STD$_{\text{Contheor}}$	**0.84** (**0.85**)	-0.0004 (**-0.0007**)	0.83 (0.88)	126 (**33**)	**0.0047** (**0.0053**)	-51.1 (**-16.3**)	15 (2)
COMB	0.80 (0.76)	-0.0011 (-0.0011)	**0.86** (**0.89**)	166 (38)	0.0056 (0.0070)	-91.4 (-19.9)	17 (4)
MUMM$_{\text{poly}}$	0.74 (0.75)	-0.0002 (-0.0011)	**0.86**(0.87)	164 (48)	0.0063 (0.0073)	-60.2 (-25.9)	19 (8)
MUMM	0.74 (0.75)	-0.0003 (-0.0009)	**0.86** (0.87)	164 (48)	0.0063 (0.0071)	-60.3 (-24.1)	19 (7)
STD	0.83 (**0.85**)	**0.0000** (-0.0010)	0.80 (0.88)	**123** (34)	0.0048 (0.0056)	**-39.0** (-19.5)	13 (2)
$\rho_w(443)$							
STD$_{\text{Contheor}}$	**0.93** (**0.92**)	**-0.0001** (**-0.0007**)	0.92 (0.96)	**37** (**21**)	**0.0034** (**0.0044**)	-6.4 (**-8.8**)	3 (0)
COMB	0.91 (0.88)	-0.0006 (-0.0011)	**0.94** (**0.97**)	48 (24)	0.0041 (0.0055)	-17.6 (-11.4)	9 (2)
MUMM$_{\text{poly}}$	0.86 (0.87)	0.0002 (-0.0010)	0.93 (0.95)	58 (32)	0.0050 (0.0059)	-5.1 (-14.7)	9 (3)
MUMM	0.86 (0.87)	0.0002 (-0.0009)	0.93 (0.94)	58 (32)	0.0050 (0.0059)	-5.1 (-14.0)	9 (3)
STD	**0.93** (**0.92**)	0.0003 (-0.0010)	0.90 (0.96)	38 (22)	0.0035 (0.0046)	**-1.3** (-11.2)	2 (0)
$\rho_w(488)$							
STD$_{\text{Contheor}}$	**0.97** (**0.95**)	-0.0006 (**-0.0015**)	0.92 (0.95)	**21** (**16**)	**0.0033** (**0.0051**)	-13.7 (**-12.4**)	0 (0)
COMB	0.96 (0.94)	-0.0010 (-0.0018)	**0.93** (**0.96**)	25 (18)	0.0038 (0.0055)	-17.9 (-13.6)	3 (1)
MUMM$_{\text{poly}}$	0.94 (0.93)	**-0.0002** (**-0.0015**)	0.92 (0.94)	31 (22)	0.0043 (0.0058)	-11.9 (-14.9)	3 (0)
MUMM	0.94 (0.92)	**-0.0002** (-0.0016)	0.92 (0.94)	31 (22)	0.0043 (0.0060)	-11.9 (-15.0)	3 (0)
STD	**0.97** (0.94)	-0.0003 (-0.0018)	0.91 (0.95)	22 (17)	0.0035 (0.0054)	**-11.2** (-13.9)	0 (0)
$\rho_w(531)$							
STD$_{\text{Contheor}}$	0.96 (0.92)	-0.0002 (-0.0014)	0.86 (**0.91**)	**18** (**17**)	**0.0042** (0.0065)	-13.8 (**-15.0**)	0 (0)
COMB	0.96 (**0.93**)	-0.0003 (-0.0015)	**0.87** (**0.91**)	19 (18)	0.0043 (**0.0064**)	-15.1 (-15.5)	0 (0)
MUMM$_{\text{poly}}$	0.94 (0.92)	0.0005 (**-0.0010**)	0.85 (0.89)	22 (19)	0.0046 (0.0067)	-11.4 (-15.9)	0 (0)
MUMM	0.94 (0.91)	0.0005 (-0.0012)	0.85 (0.89)	22 (20)	0.0046 (0.0070)	**-11.3** (-16.4)	0 (0)
STD	0.96 (0.92)	**0.0001** (-0.0017)	0.85 (**0.91**)	19 (18)	0.0043 (0.0068)	-12.6 (-16.3)	0 (0)
$\rho_w(547)$							
STD$_{\text{Contheor}}$	**0.96** (0.91)	-0.0002 (-0.0013)	**0.85** (0.88)	**19** (**19**)	**0.0045** (0.0070)	-16.1 (**-16.8**)	0 (0)
COMB	0.95 (**0.92**)	-0.0003 (-0.0013)	**0.85** (**0.89**)	20 (**19**)	**0.0045** (**0.0068**)	-16.9 (-17.1)	0 (0)
MUMM$_{\text{poly}}$	0.94 (0.91)	0.0005 (**-0.0006**)	0.82 (0.86)	21 (20)	0.0048 (0.0071)	**-13.4** (-17.4)	0 (0)
MUMM	0.94 (0.90)	0.0005 (-0.0008)	0.82 (0.86)	21 (20)	0.0048 (0.0074)	**-13.4** (-17.9)	0 (0)
STD	0.95 (0.90)	**0.0001** (-0.0016)	0.84 (**0.89**)	20 (20)	0.0046 (0.0073)	-15.1 (-18.0)	0 (0)
$\rho_w(667)$							
STD$_{\text{Contheor}}$	**0.90** (**0.87**)	-0.0011 (-0.0018)	**0.85** (**0.96**)	**48** (**36**)	**0.0023** (**0.0028**)	-46.7 (**-33.6**)	5 (0)
COMB	0.89 (0.86)	-0.0011 (-0.0014)	0.83 (0.89)	50 (37)	0.0024 (0.0029)	-49.3 (-34.2)	6 (0)
MUMM$_{\text{poly}}$	0.81 (0.82)	**-0.0005** (-0.0012)	0.75 (0.83)	**48** (39)	0.0024 (0.0031)	-38.3 (-35.3)	4 (0)
MUMM	0.81 (0.82)	**-0.0005** (**-0.0011**)	0.75 (0.82)	**48** (39)	0.0024 (0.0031)	**-38.0**(-34.8)	4 (0)
STD	0.87 (**0.87**)	-0.0010 (-0.0017)	0.83 (0.93)	49 (37)	**0.0023** (0.0029)	-44.6 (-34.6)	5 (0)

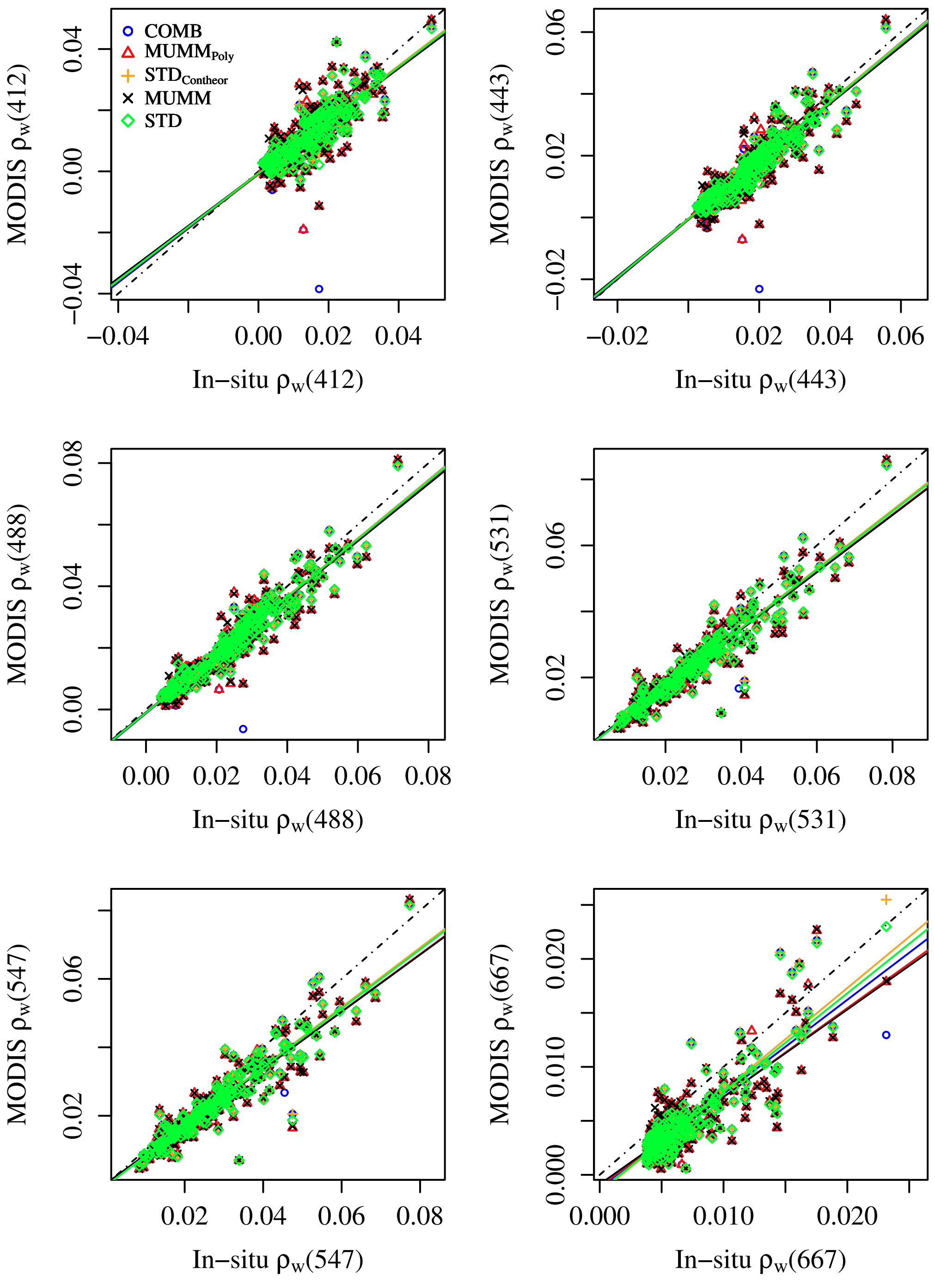

Figure 6.1: *MODIS-Aqua estimated versus in situ* $\rho_w(\lambda)$ *at six different wavelengths (412, 433, 488, 531, 547 and 667 nm) for the 211 common valid match-up pairs. The black dot-dashed line represents the 1:1 line.*

reflectance is inappropriate (i.e., the aerosol model selection method based on modelled $\rho_w(\lambda_{NIR})$ as suggested by Gordon and Wang (1994)).

The MUMM-based NIR-modelling schemes retrieve the largest number of negative $\rho_w(\lambda)$

retrievals in the blue (i.e., at 412, 443 and 488 nm) but the lowest in the red. Hence, the MUMM-based AC approaches tend to retrieve more valid (according to the selection criteria in Section 6.2.1.2) match-up points but, present more negative $\rho_w(\lambda)$ retrievals (Table 6.3). This greater number of negative $\rho_w(\lambda)$ values with the MUMM-based AC approaches may be explained by the underestimation of $\rho_w(\lambda)$ at 869 nm in moderately turbid waters with both the NIR reflectance ratio and polynomial function, as shown previously by Doron et al. (2011) and Goyens et al. (2013a) (see Section 5.2 and Fig. 4 in Goyens et al. (2013a)). At the opposite, the STD AC method retrieves less valid match-up pairs but also less negative $\rho_w(\lambda)$ retrievals. When looking into the negative values, we observe that the expected improvement in terms of spatial coverage provided with the modified STD NIR-modelling schemes is slightly reduced. Indeed, both the COMB and $\text{STD}_{\text{Contheor}}$ NIR-modelling schemes retrieved more valid match-up pairs compared to the initial STD approach, but most of these added valid match-up pairs show negative $\rho_w(\lambda)$ values (9 out of 10, and 8 out of 11, at 412 and 443 nm, respectively). Hence, the COMB and $\text{STD}_{\text{Contheor}}$ NIR-modelling schemes ensure a greater spatial coverage but generate more negative $\rho_w(\lambda)$ retrievals and, subsequently, higher negative biases (Table 6.3). However, the $\text{STD}_{\text{Contheor}}$ NIR-modelling scheme still improves the AC compared to the initial STD NIR-modelling scheme, as it retrieves overall better $\rho_w(\lambda)$ values when comparing the AC approaches based on the 211 common match-ups.

6.1.2.3 Global validation of aerosol products

The statistical performance of the algorithms to retrieve $\alpha(531, 869)$ and $\tau(869)$ is given in Table 6.4 and illustrated in Fig. 6.2 (for a better visualisation only the 211 valid common match-up pairs are shown). For both aerosol products, the RE remains high (> 60% and 40% when considering all match-ups and when considering only the common match-up pairs, respectively) and R^2 and slope remain small (<0.39 and 0.69 for $\alpha(531, 869)$ and $\tau(869)$, respectively). All algorithms tend to overestimate $\tau(869)$ (Table 6.3) which is expected since they tend to underestimate $\rho_w(\lambda)$ (e.g., negative bias in Table 6.3). According to the percentage bias for $\alpha(531, 869)$, most algorithms retrieve lower $\alpha(531, 869)$ values and thus rather oceanic aerosol models or/and higher relative humidities. Only the STD AC method tends to overestimate $\alpha(531, 869)$.

Table 6.4: *Statistical results for $\alpha(531, 869)$ and $\tau(869)$ retrieved with the $STD_{Contheor}$, COMB, $MUMM_{Poly}$, MUMM and STD AC methods. Statistics between brackets correspond to the values obtained when only the 211 common match-up pairs are retained. The best statistics per aerosol product are indicated in bold.*

	R^2	Intercept	Slope	RE (%)	RMSE	Bias (%)
$\alpha(531)$						
$\text{STD}_{\text{Contheor}}$	**0.39** (**0.37**)	**0.972** (**0.781**)	**0.37** (**0.37**)	85 (**45**)	**0.554** (**0.593**)	-7.5 (**1.8**)
COMB	0.38 (0.32)	1.010 (0.860)	0.35 (0.32)	90 (48)	0.566 (0.616)	-7.7 (5.8)
$\text{MUMM}_{\text{poly}}$	0.33 (0.26)	1.026 (0.961)	0.30 (0.25)	79 (53)	0.562 (0.626)	-5.1 (4.3)
MUMM	0.33 (0.27)	1.031 (0.935)	0.30 (0.27)	80 (51)	0.562 (0.633)	**-4.6** (**1.8**)
STD	**0.39** (0.32)	0.997 (0.864)	0.36 (0.33)	**65** (48)	0.562 (0.623)	16.2 (4.4)
$\tau(869)$						
$\text{STD}_{\text{Contheor}}$	0.55 (0.52)	0.042 (0.038)	**0.58** (0.60)	64 (77)	0.046 (0.045)	56.7 (48.5)
COMB	0.55 (**0.60**)	0.042 (**0.033**)	0.57 (**0.69**)	65 (75)	0.046 (0.042)	57.3 (46.4)
$\text{MUMM}_{\text{poly}}$	0.55 (**0.60**)	0.042 (0.034)	0.57 (0.68)	65 (75)	0.046 (**0.041**)	57.5 (47.0)
MUMM	0.55 (0.53)	**0.041** (0.037)	0.57 (0.60)	64 (75)	0.046 (0.044)	57.0 (45.0)
STD	**0.56** (0.53)	**0.041** (0.036)	0.57 (0.61)	**63** (**74**)	**0.045** (0.044)	**55.5** (**43.5**)

In order to evaluate the impact of erroneously retrieved aerosol properties on the retrieved $\rho_w(\lambda)$, simple rank correlation coefficients are calculated for the estimated RE and bias between $\rho_w(\lambda)$ and $\alpha(531, 869)$, and $\rho_w(\lambda)$ and $\tau(869)$, respectively. As shown in Figs. 6.3(a) and 6.3(b), the calculated correlations between the bias observed for the aerosol properties and the water

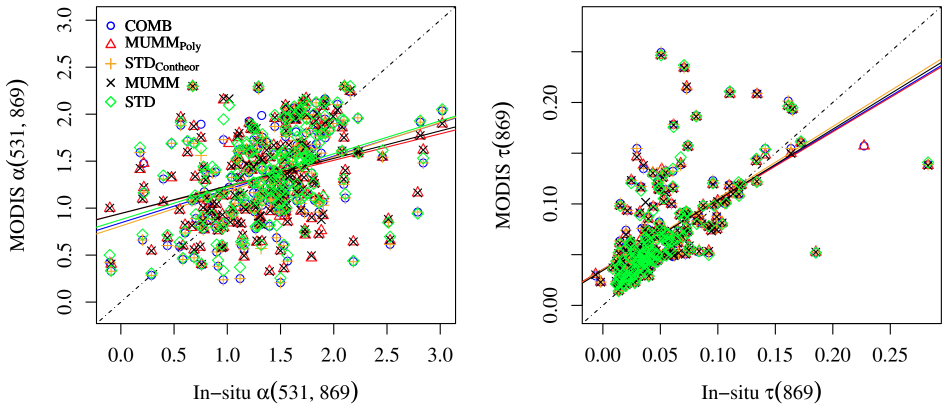

Figure 6.2: *MODIS-Aqua estimated versus in situ* $\alpha(531, 869)$ *and* $\tau(869)$. *The black dot-dashed line indicates the 1:1 line.*

signal, are not significant with maximum coefficients around 0.2. Results are similar when considering the observed RE. Hence, there is no significant trend between the errors in aerosol properties and $\rho_w(\lambda)$ retrievals. Similarly, to investigate if a good separation exists between the aerosol properties and the water signal, correlation coefficients are calculated between $\rho_{am}(\lambda_{NIR})$ and $\rho_w(\lambda)$ at different wavelengths and for each NIR-modelling scheme. Resulting coefficients, shown in Figs. 6.3(c) and 6.3(d), indicate a relatively good separation between aerosol and water reflectances for all NIR-modelling schemes.

6.1.2.4 $\rho_w(\lambda)$ validation per water type

Figures 6.4 and 6.5 show the class-specific average RE, RMSE and bias as a function of wavelength for each NIR-modelling scheme when considering all valid match-ups and when considering the 211 common match-ups, respectively. For comparison, the statistics are also given when including all data (Fig. 6.5(a)). Hence, these statistics also include the unclassified spectra.

As expected from Table 6.3, Fig. 6.4(a) indicates that while the RMSE is usually better with the STD$_{\text{Contheor}}$ algorithm, the bias is usually lower with the STD approach. This is also true when looking at the class-specific statistics and is possibly due to the more important fraction of negative $\rho_w(\lambda)$ values retrieved with the STD$_{\text{Contheor}}$ NIR-modelling scheme (Table 6.5), pulling the bias down towards lower negative values. Note that according to Table 6.5, the STD AC method also retrieves more negative values for the Class 1 waters compared to the other methods (1 out of 9 $\rho_w(\lambda)$ spectra showed negative values with the STD NIR modelling scheme while the other methods did not retrieve any negative values for Class 1 waters). This confirms the observations made by Goyens et al. (2013c), namely that the bio-optical model within the initial STD NIR-modelling scheme is invalid for mineral and detrital sediment-rich waters. However, this percentage remains very low.

For all classes, the RE in $\rho_w(\lambda)$ for the STD$_{\text{Contheor}}$ and STD approaches remain very similar (Figs. 6.4(b-d), RE ranging from 13% to 130% and bias from -45% to 10%, for both approaches). For the Class 1 spectra, statistics resulting from the COMB AC approach are similar to the statistics of the other STD-AC approaches. For the Class 4 waters the COMB AC approach results in higher errors (RE and bias attain values up to 181% and -87%, respectively). For Class 2, the COMB AC approach switched more often to the MUMM$_{\text{Poly}}$ NIR-modelling scheme explaining the closer match in statistical performances between the COMB and MUMM-based AC approaches. However, the COMB AC approach still retrieves larger negative biases

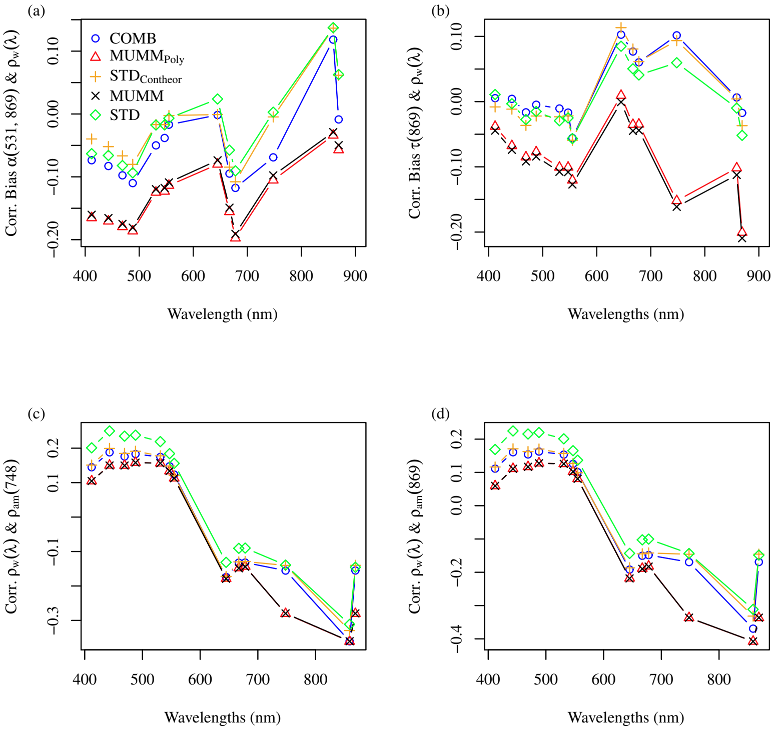

Figure 6.3: *Correlation coefficients as a function of wavelength between (a) the estimated bias for $\alpha(531, 869)$ and for $\rho_w(\lambda)$, (b) the estimated bias for $\tau(869)$ and for $\rho_w(\lambda)$, (c) $\rho_w(\lambda)$ and $\rho_{am}(748)$ and (d) $\rho_w(\lambda)$ and $\rho_{am}(869)$.*

Table 6.5: *Overall and per class percentage of negative $\rho_w(\lambda)$ values retrieved with the* STD$_{\text{Contheor}}$*, COMB,* MUMM$_{\text{poly}}$*, MUMM and STD AC methods. Numbers between brackets indicate the percentages obtained when considering only the 211 valid match-up pairs.*

% of $\rho_w(\lambda) < 0$	All	Class 1	Class 2	Class 4
STD$_{\text{Contheor}}$	15 (2)	0 (0)	2 (1)	27 (6)
COMB	16 (4)	0 (0)	2 (1)	30 (12)
MUMM$_{\text{poly}}$	19 (7)	0 (0)	3 (2)	34 (20)
MUMM	19 (8)	0 (0)	3 (2)	34 (19)
STD	13 (2)	5 (11)	2 (1)	22 (5)

varying between -55% and -8% while the MUMM-based approaches show biases ranging from -38% to 0%.

When considering the 211 common match-up pairs retrieved with each AC method, the STD$_{\text{Contheor}}$ approach gives for all classes better statistics relative to the other methods (Fig. 6.5). Indeed, this modified NIR-modelling scheme results systematically in 1 to 3% lower RE and biases compared to the initial STD AC approach.

As noticed previously, the MUMM and MUMM$_{\text{Poly}}$ NIR-modelling schemes provide very similar performances (RE and bias do not differ by more than 1%). However, for Class 4 waters, defined as optically dominated by algal particles and high concentrations of CDOM, the MUMM$_{\text{Poly}}$ NIR-modelling scheme exhibits higher negative biases and higher RMSE, especially in the blue spectral region (Fig. 6.5(c), bias varying between -40% and -19%, and -35% and -19% for the MUMM$_{\text{Poly}}$ and MUMM NIR-modelling schemes, respectively). Hence, while Goyens et al. (2013a) showed similar performances for the constant NIR reflectance ratio and

(a) All

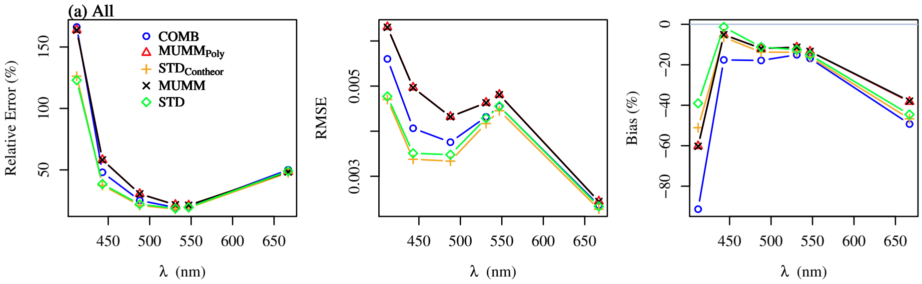

(b) Class 1

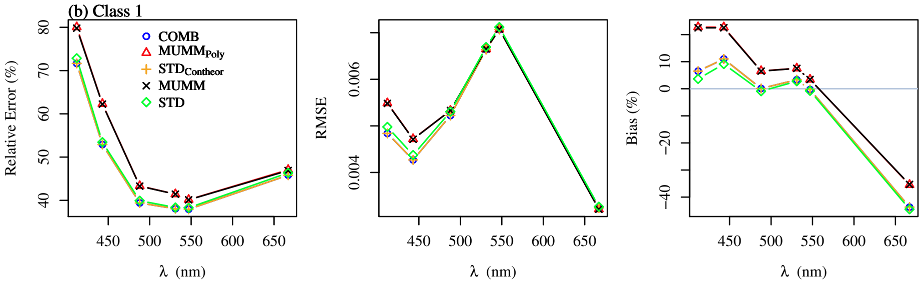

(c) Class 2

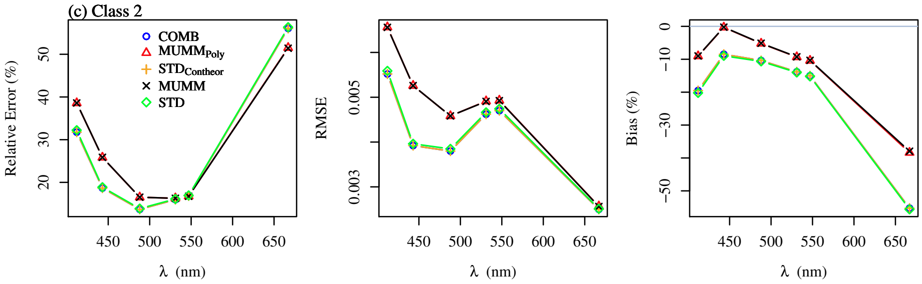

(d) Class 4

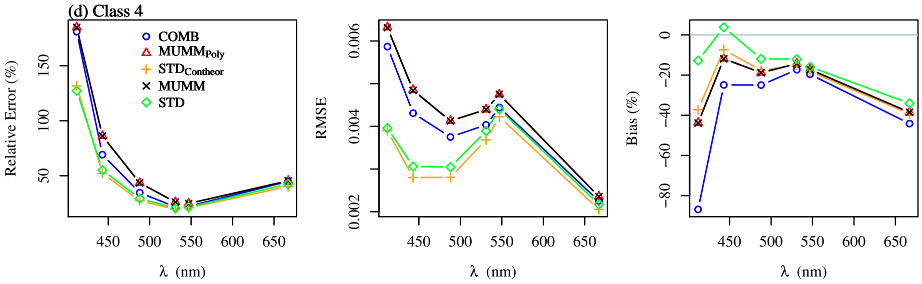

Figure 6.4: *RE, RMSE and bias for all data (772, 783, 771, 783 and 761 for the COMB, $MUMM_{Poly}$, $STD_{Contheor}$, MUMM and STD approaches, respectively) (a) and per class (b, c and d) as a function of wavelength.*

the polynomial NIR spectral relationship in moderately turbid waters, Fig. 6.5 indicates that the constant NIR reflectance ratio may however be more appropriate for certain water types (e.g., dark waters optically dominated by high concentrations of CDOM). Note however that this is less evident in Fig. 6.4.

According to Goyens et al. (2013c), the MUMM NIR-modelling schemes provide lower RE compared to the STD approach over Class 1 waters (waters dominated by detrital and mineral material). Here, Fig. 6.5 shows that the STD$_{\text{Contheor}}$ approach provides very similar or even better results compared to the MUMM-based NIR modelling schemes, even for Class 1 waters. Hence, these results suggest that the spectral relationship constraints, recommended to extent the STD approach to optically more complex waters, are appropriate to improve $\rho_w(\lambda)$ retrievals over all optical water types. However, the large negative bias (up to $\sim$ 45%), the significant

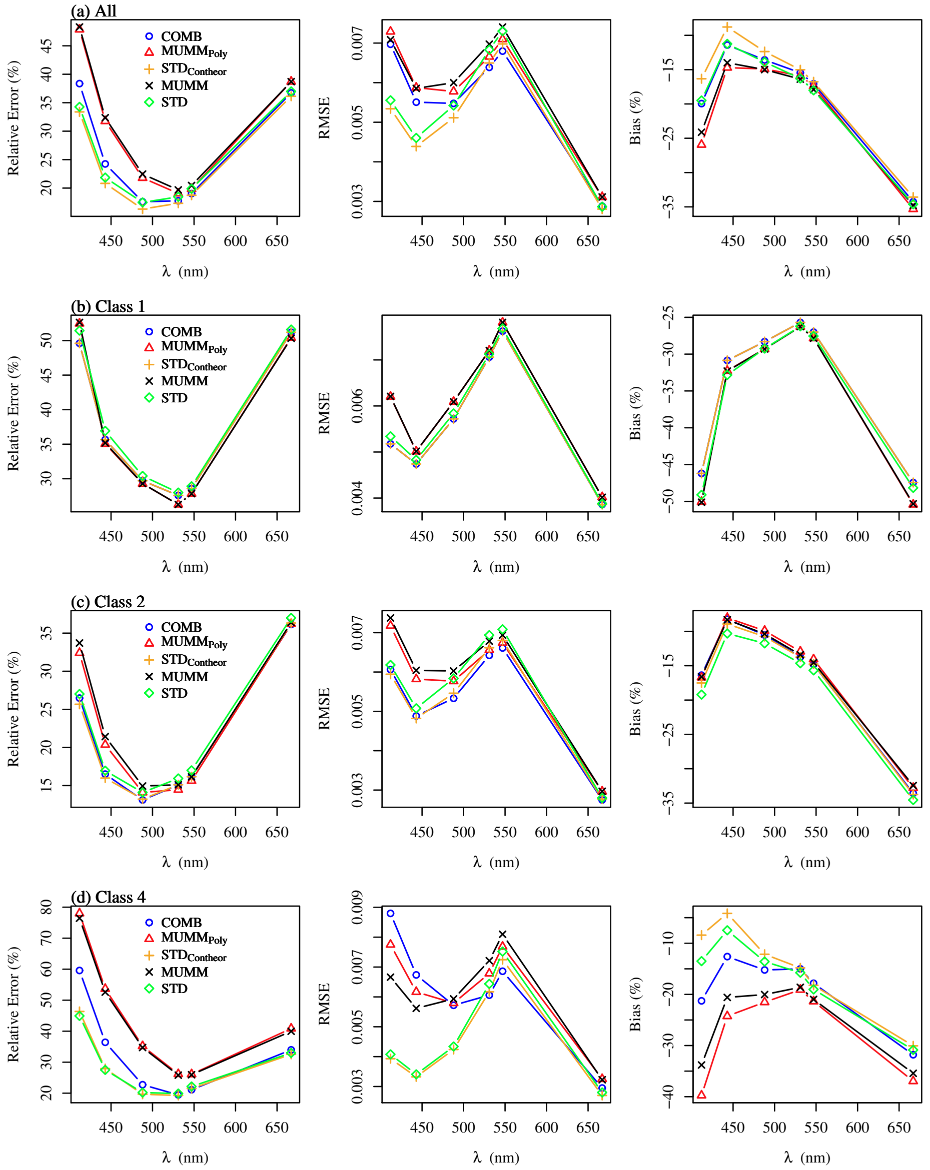

Figure 6.5: *RE, RMSE and bias for the 211 match-up pairs for the COMB, $MUMM_{Poly}$, $STD_{Contheor}$, MUMM and STD approaches (a) and per class (b, c and d) as a function of wavelength.*

relative errors (up to ∼ 50%), and the percentage of negative $\rho_w(\lambda)$ retrievals (15%), indicate that further improvement is still required.

Results shown in Fig. 6.5 (when considering the 211 common match-ups) are similar to the results obtained previously by Goyens et al. (2013c). However, for Class 4 water masses, the STD AC method retrieved positive biases in the blue spectral region according to the study of Goyens et al. (2013c), while in the present study this method results in negative biases. A possible explanation for these differences may be due to the modified vicarious calibration gains suggested with the reprocessing of 2012 (R2012) to correct for anomalies encountered with the MODIS Aqua bands at 412 and 433 nm. As shown in Table 3.1 the gain factors slightly decreased between the Reprocessing of 2010 and 2012. According to the OBPG, a difference of 1% in the AC or sensor calibration, results in approximately 10% difference in the derived $\rho_w(\lambda)$ (Franz et al., 2012). Hence, a small change in the gain factors may result in more differences in $\rho_w(\lambda)$ retrievals. This is noticeable in Fig. 6.6 showing the 211 common match-up pairs for different visible MODIS bands processed with SeaDAS version 6.4 with the gain factors suggested by the Reprocessing of 2010 and with the gain factors suggested by the Reprocessing of 2012 (all other parameters being equal). Nevertheless, overall differences remain very small.

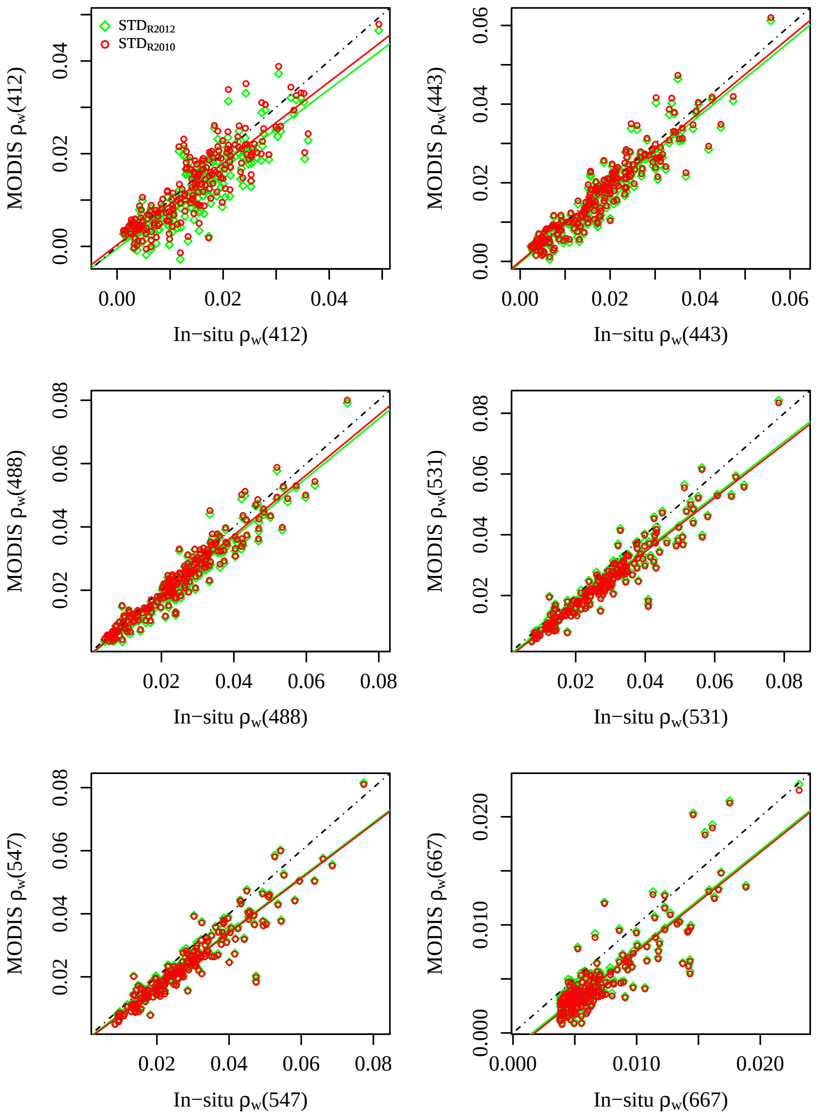

Figure 6.6: *STD MODIS Aqua estimated $\rho_w(\lambda)$ values versus in situ $\rho_w(\lambda)$ at six visible wavelengths processed with SeaDAS 6.4 once with the default gain factors suggested by the Reprocessing of 2010 (STD_{R2010}) and once by the Reprocessing of 2012 (STD_{R2012}).*

6.2 IMPROVING AC METHODS IN EXTREMELY TURBID WATERS: CASE STUDIES OVER THE NORTH-SEA ENGLISH CHANNEL AND THE COAST OF FRENCH GUIANA

6.2.1 Data and Methods

For 52 data points, out of the 210 *in situ* above water $\rho_w(\lambda)$ measurements from the LOG dataset (Section 3.3.2.1, Chapter 3), coincident satellite images are obtained. Each satellite image is processed with the modified STD$_{\text{Contheor}}$, COMB and MUMM$_{\text{Poly}}$ AC methods and the initial STD and MUMM AC methods. Note that the low number of retrieved coincident satellite images relative to the total number of *in situ* $\rho_w(\lambda)$ LOG data, is partially due to the measurements protocols which were not always meant for satellite validation exercises and hence the time interval between measurements and satellite overpass often exceeded 2 hours.

To avoid the erroneous flagging of extremely turbid waters and to ensure a greater number of match-up pairs, the default L2-processing flags are slightly modified. The standard cloud masking approach at 869 nm, which flags any pixel with a Rayleigh-corrected reflectance exceeding 0.027, was shown to mask highly reflective water bodies even in clear atmospheric conditions (Wang and Shi, 2006). For cloud detection over MODIS Aqua images, the use of the 2130 nm SWIR band was therefore suggested with a threshold of 0.0018 (Franz et al., 2006; Dogliotti et al., 2011). This SWIR-based cloud detection mask is applied here.

A second L2 default mask is also omitted for image processing, the high total radiance flag (HILT) resulting from sensor saturation in the red and NIR bands. This flag is meant to exclude pixels where the sensor saturates and, subsequently, does not ensure sufficient precision to correctly characterize aerosols. However, high NIR radiance values may be encountered in coastal areas and may therefore be erroneously masked. Note however, that the exclusion of this flag needs to be taken with care since band saturation may lead to the failure of NIR-modelling schemes for the AC.

To further characterize the *in situ* data, the classification scheme of Vantrepotte et al. (2012) is used to allocate each spectrum to a water optical type. According to the $\rho_w(\lambda)$ value in the NIR spectral region, a turbidity level is also assigned to each spectrum.

6.2.2 Results and discussion

6.2.2.1 Match-up selection

Among the 52 coincident satellite-*in situ* data pairs, 42 pairs presented less than 6 valid pixels within the 3 by 3 pixels windows and, except for the STD AC approach, for 1 pair the variation coefficient exceeded 25% and was thus excluded for further data analysis. Hence, only 9 match-up pairs were retained. The *in situ* $\rho_w(\lambda)$ spectra for these 9 pairs are shown in Fig. 6.7. The selected spectra show moderate to very turbid waters (according to the turbidity levels previously described in Chapter 5). Unfortunately, none of the 9 spectra showed extremely turbid waters. Indeed, the *in situ*-satellite pairs presenting extremely turbid water cases were all excluded because the 3 by 3 pixel windows including the *in situ* data point showed less than 6 valid pixels (possibly due to glint contamination, cloud mask or proximity of the coast).

Among the 9 match-up pairs, different optical water types are encountered (according to the classification scheme of Vantrepotte et al. (2012)). Water optical type and turbidity classes assigned to each spectrum are given in Table 6.6. As shown in Fig. 6.7, the water mass optically dominated by detrital and mineral material (Class 1 'Guyane-A20092881710' spectra, Table 6.6) shows a gradual slope, relative to the other spectra, from the blue to the green with a large peak in the 550-600 nm spectral range followed by a lower peak around 700 nm. Mixed water masses optically dominated by phytoplankton and significant CDOM concentrations (Class 4 'Belcolor',

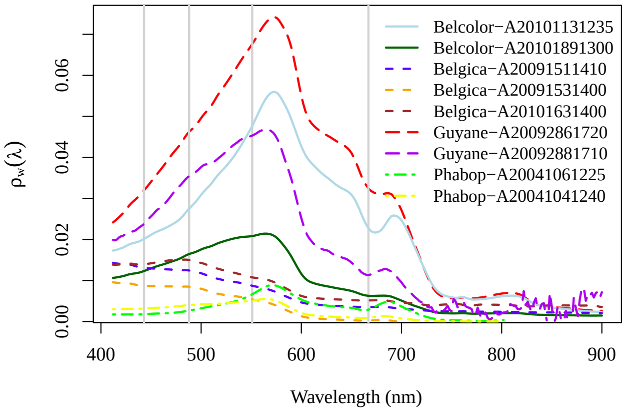

Figure 6.7: *Selected in situ $\rho_w(\lambda)$ spectra from the LOG dataset used in the present study.*

'Guyane' and 'Phabop' spectra, Table 6.6) also show these two peaks in the red-green and NIR spectral regions but exhibit a much steeper slope from the blue to the green spectral domain. The spectra classified as optically dominated by phytoplankton (Class 2 'Belcolor-A20101891300' spectra) shows a gentle slope in the blue and peaks are less pronounced compared to the spectra of Class 1 and 4.

Table 6.6: *$\rho_w(\lambda)$ in the NIR spectral domain for MODIS Aqua bands of the selected spectra and assigned turbidity level and water optical type according to the classification scheme of Vantrepotte et al. (2012).*

Station	Image ID	$\rho_w(748)$	$\rho_w(869)$	Turbidity level	Water optical class
Belcolor	A20101131235	0.0019	0.0009	moderate/very	4
	A20101891300	0.0006	0.0005	moderate	2
Belgica	A20091511410	0.0008	0.0007	moderate	unclassified
	A20091531400	0.0000	0.0000	non-turbid	unclassified
	A20101631400	0.0013	0.0012	moderate/very	unclassified
Guyane	A20092861720	0.0018	0.0010	moderate/very	4
	A20092881710	0.0009	0.0018	moderate/very	1
Phabop	A20041061225	0.0001	0.0001	moderate	4
	A20041041240	0.0000	0.0000	non-turbid	unclassified

Four spectra remained unclassified, the 3 spectra from the 'Belgica' field campaign and 1 spectra from the 'Phabop' campaign. These 4 spectra show a greater signal in the blue spectral region which decreases with wavelength and exhibits very low or no signal in the red and NIR spectral domain (> 600 nm). Such spectral shapes indicate rather clear water masses. Subsequently, since the classification scheme of Vantrepotte et al. (2012) focuses on contrasted coastal waters, it is not surprising that these spectra remain unclassified. Although our objective is to improve $\rho_w(\lambda)$ in turbid waters, these spectra are maintained for further data analysis to evaluate the performance of the NIR-modelling schemes in less turbid waters too.

6.2.2.2 Qualitative and quantitative satellite $\rho_w(\lambda)$ validation

The MODIS Aqua retrieved $\rho_w(\lambda)$ from the selected spectra are plotted together with the *in situ* data in Fig. 6.8. According to this figure, differences in NIR-modelling schemes mainly affect $\rho_w(\lambda)$ retrievals over Class 4 waters (Table 6.6). Indeed, in Figs. 6.8(a), (f) and (h), more important discrepancies are observed between the satellite $\rho_w(\lambda)$ values retrieved from the STD and MUMM-based NIR modelling schemes. For the two first 'Class 4' cases (Figs. 6.8(a) and (f)), the $\mathrm{STD}_{\mathrm{Contheor}}$ NIR-modelling scheme gives the best results followed by the initial STD approach. The MUMM-NIR modelling schemes, which gives the best results for the last Class 4 case (Fig. 6.8(h)), can not be differentiated from each other, indicating that both the MUMM and $\mathrm{MUMM}_{\mathrm{Poly}}$ approaches retrieve the same $\rho_w(\lambda_{NIR})$ values. Results shown in Figs. 6.8(b) and (g) show that satellite $\rho_w(\lambda)$ values retrieved over Class 1 water masses were slightly closer to ground truth when using the MUMM NIR-modelling scheme while in Class 2 water masses the STD approach performed better. This is in agreement with the observations of Goyens et al. (2013c).

For the unclassified spectra, both MUMM and STD-based NIR-modelling schemes lead to similar results, except in Fig. 6.8(e), where the MUMM-based approaches perform slightly better.

Hence, overall, these 9 case studies confirm the conclusion made in Section 6.1 and by Goyens et al. (2013c), namely, that in Class 4 waters the STD-based NIR-modelling schemes perform better while in Class 1 waters the MUMM-based NIR-modelling schemes tend to perform slightly better. Moreover, as concluded from the global evaluation in Section 6.1, the $\mathrm{STD}_{\mathrm{Contheor}}$ NIR-modelling generally better estimates $\rho_w(\lambda)$ compared to the initial scheme, in particular in the blue spectral region (see Table 6.3).

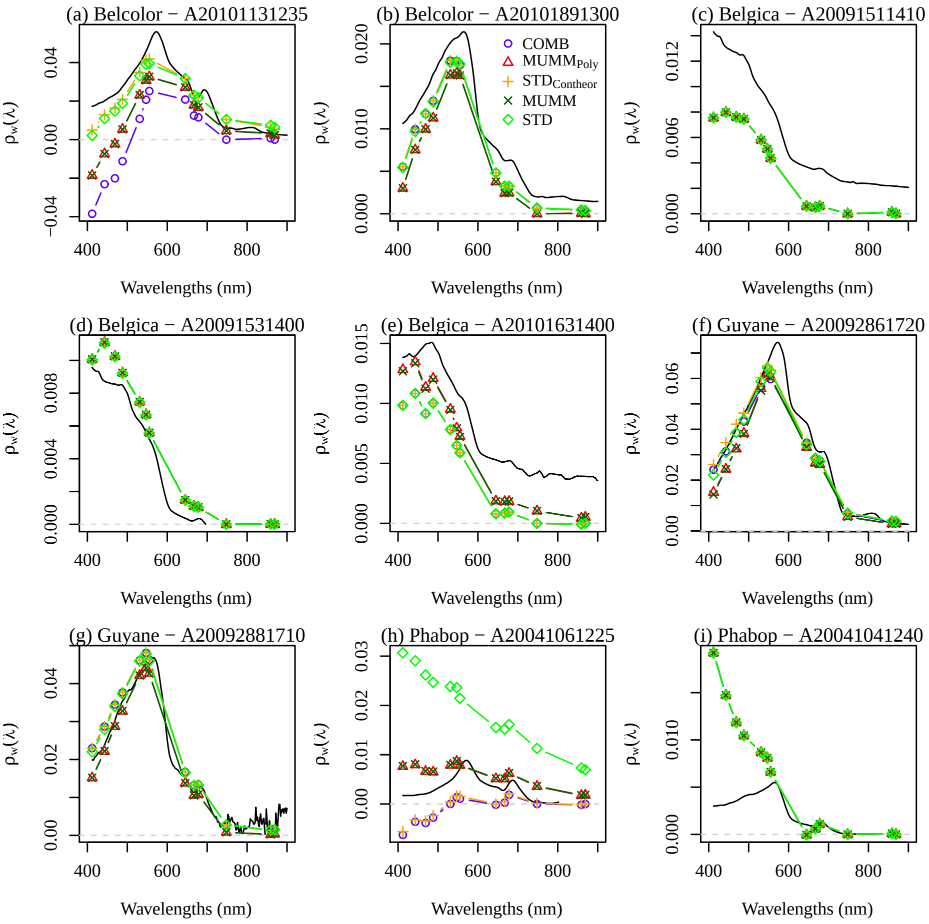

Figure 6.8: *Selected in situ $\rho_w(\lambda)$ spectra together with MODIS Aqua retrieved $\rho_w(\lambda)$ spectra using the COMB, $STD_{Contheor}$, $MUMM_{Poly}$, MUMM and STD NIR-modelling schemes for AC.*

To evaluate the NIR-modelling schemes according to the resulting spatial patterns in $\rho_w(\lambda)$, $\tau(869)$ and $\alpha(531, 869)$, MODIS Aqua images processed with the initial STD and MUMM NIR-modelling schemes are compared with the images processed with the modified $\mathrm{STD}_{\mathrm{Contheor}}$ and $\mathrm{MUMM}_{\mathrm{Poly}}$ schemes. The COMB NIR-modelling scheme is not included for further evaluation since, according to previous results, more work is needed such that a combined MUMM-STD NIR-modelling scheme provides satisfactory results.

Here the generated MODIS Aqua images are shown for the Class 1 and Class 4 waters (see Table 6.6) for the 'Belcolor', 'Guyane' and 'Phabop' field campaigns.

Images corresponding to the unclassified and Class 2 spectra (i.e., all spectra from the 'Belgica' field campaign and the 'Belcolor-A20101891300' and 'Phabop-A20041041240' spectra) showed very similar $\rho_w(\lambda)$ retrievals for all NIR-modelling schemes. These water masses also exhibit lower $\rho_w(\lambda)$ values and subsequently lower turbidity levels. Hence, the different NIR-modelling schemes do not significantly impact the AC and consequently the satellite $\rho_w(\lambda)$ patterns over these images. It was therefore chosen to not include them in the present chapter.

The next paragraphs describe four MODIS Aqua images associated with the following spectra, the 'Belcolor-A20101131235' (Fig. 6.8(a)), 'Guyane-A20092861720' (Fig. 6.8(f)) and 'Phabop-A20041061225' (Fig. 6.8(h)) optical water Class 4 spectra and the 'Guyane-A20092881710' (Fig. 6.8(g)) optical water Class 1 spectra. The true colour images distributed by the OBPG are shown in Fig. 6.9 for these 4 cases.

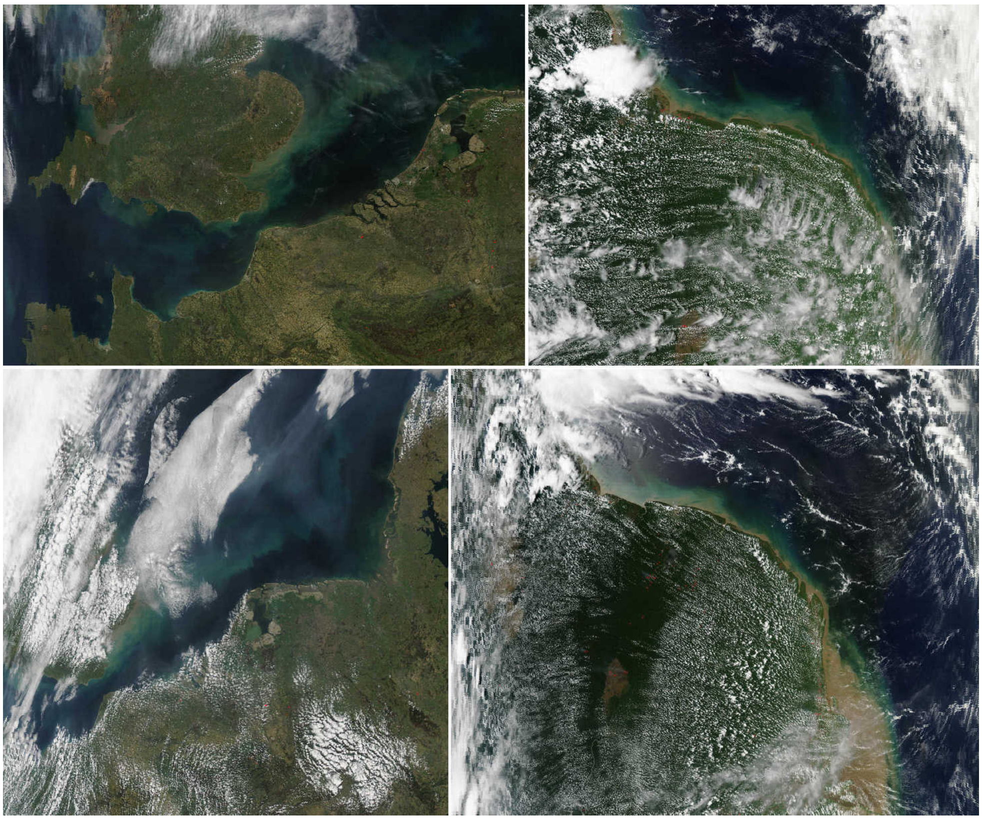

Figure 6.9: *True colour images associated with the in situ data 'Belcolor-A20101131235' (top left), 'Guyane-A20092861720' (top right), 'Phabop-A20041061225' (bottom left) and 'Guyane-A20092881710' (bottom right).*

Figures 6.10, 6.11, 6.14, 6.15, 6.17 and 6.18 show the resulting MODIS Aqua images for the Class 4 waters (see Table 6.6) for $\rho_w(\lambda)$ when processed with the initial STD and MUMM NIR-modelling schemes and when processed with the modified $\mathrm{STD}_{\mathrm{Contheor}}$ and $\mathrm{MUMM}_{\mathrm{Poly}}$ NIR-modelling schemes. Figures 6.12, 6.16 and 6.19 show the retrieved aerosol products, $\tau(869)$

and $\alpha(531, 869)$. When relevant, the estimated $\rho_{am}(\lambda)$ is also shown (Fig. 6.13). Similarly, Figs. 6.20 and 6.21 show the resulting MODIS Aqua images for the Class 1 waters and Fig. 6.22 the associated aerosol parameters, $\tau(869)$ and $\alpha(531, 869)$.

a. Belcolor - A20101131235

In Figs. 6.10 and 6.11, important differences are observed between the MUMM and STD-based AC methods. The STD-based approaches retrieve higher $\rho_w(\lambda)$ values relative to the MUMM-based approaches especially along the British coasts. As observed in Fig. 6.8(a) for the match-up pair 'Belcolor-A2010113123500', the STD-based AC methods tend to better approximate the *in situ* marine signal, while the MUMM-based AC methods retrieve negative $\rho_w(\lambda)$ values in the blue spectral domain. The corresponding true-colour image in Fig. 6.9 also shows a brownish ocean colour patch along the British coast nearby the Thames Estuary, indicating more reflective waters as retrieved by the STD-based NIR-modelling schemes (black square in Fig.6.10). Hence, the MUMM-based AC approaches seem to underestimate the water signal. However, compared to initial MUMM NIR-modelling scheme, the $\mathrm{MUMM_{Poly}}$ approach resulted in some improvement. Indeed, as observed in Fig. 6.11, the modified scheme retrieved slightly higher $\rho_w(\lambda)$ values compared to the standard MUMM approach. This is easily noticeable in the region of the Bristol Channel (black square in Fig. 6.11) for the blue and green bands. Differences between the initial STD and $\mathrm{STD_{Contheor}}$ approaches are also noticeable (Fig. 6.10), in particular nearby the Thames estuary where the $\mathrm{STD_{Contheor}}$ approaches results in more reflective water (black square in Fig. 6.10).

According to Fig. 6.12, the MUMM-based and STD-based approaches show important differences in terms of aerosol properties, especially in the Bristol Channel and nearby Cherbourg in the English Channel. Higher values for $\alpha(531, 869)$ may be expected given the proximity of human activities at both locations. For this region, the STD-based approaches seem thus to provide better aerosol parameters. Spatial heterogeneity in $\alpha(531, 869)$ is also more pronounced with the STD-based AC approaches compared to the MUMM-AC approaches (Fig. 6.12), suggesting the non-valid spatial homogeneity assumption for aerosol reflectance adopted by the MUMM-based NIR-modelling schemes. In contrast, nearby the Thames Estuary, smaller $\alpha(531, 869)$ values are encountered with the STD-based NIR-modelling schemes. The $\mathrm{STD_{Contheor}}$ approach even retrieved negative $\alpha(531, 869)$ over this region, indicating rather maritime aerosols. Hence, both STD-AC approaches seemed to erroneously retrieve the aerosol properties in this coastal region. However, although the STD-based approaches may result in erroneous aerosol products, both approaches provided realistic images for $\rho_w(\lambda)$. Moreover, as observed when comparing Figs. 6.10, 6.12 and 6.13, beside some patterns near Bristol and the Thames Estuary, oceanic and aerosol parameters do not seem to be spatially correlated. This is coherent since the aerosol parameters should not affect spatial patterns in $\rho_w(\lambda)$ estimations.

b. Guyane - A20092861720

Similarly to the previous case, the MUMM-based AC methods retrieve lower $\rho_w(\lambda)$ values in the blue and green spectral region relative to the STD-based approaches, for the MODIS Aqua images associated with the 'Guyane - A20092861720' spectra (Figs. 6.14 and 6.15). The $\mathrm{STD_{Contheor}}$ NIR-modelling scheme exhibits the highest values, in particular along the coast of Suriname (black box in Fig.6.14). In the red and NIR spectral region, differences resulting from the distinctive NIR-modelling schemes are not as pronounced. Figures 6.14, 6.15 and 6.16 also confirm the added value of the MUMM-based approaches in terms of spatial coverage. Indeed, nearby the coast, in Fig. 6.14, small patches of negative $\rho_w(\lambda)$ values are observed with both STD-AC methods. These approaches also failed to retrieve $\alpha(531, 869)$ values in this region (Fig. 6.16). Both approaches show indeed very small $\tau(869)$ and $\alpha(531, 869)$ estimations along the coast. Hence, similarly to the previous case (see above for 'Belcolor - A20101131235'), the STD-based AC approaches still retrieve valuable $\rho_w(\lambda)$ values, although unlikely aerosol parameters are retrieved.

c. Phabop - A20041061225

As observed on the true color image in Fig. 6.9, this case study shows sudden transitions in water masses with darker waters in the English Channel along the French and Belgian coast, rather blue-green water masses nearby the Thames Estuary and more turbid brownish waters along the English coast.

According to the match-up exercise in Fig. 6.8(h), the STD NIR-modelling scheme appears to significantly overestimate $\rho_w(\lambda)$ at all wavelengths compared to the other NIR-modellings schemes and relative to the *in situ* data. This is in agreement with Figs. 6.17 and 6.18. Indeed, along the French coast, this AC approach retrieves a band of high reflective water (in the visible and NIR spectral region, stretching from the Belgian coast to the French "Baie de Somme") which is not or less observable on the images processed with the other NIR-modelling schemes. However on the true colour image this band exhibits rather darker blue colours relative to the surrounding waters (Fig. 6.9). Hence, the initial STD NIR-modelling scheme probably greatly overestimates $\rho_w(\lambda_{NIR})$ in this region, while the $\text{STD}_{\text{Contheor}}$ NIR-modelling scheme seems to retrieve more realistic results (lower $\rho_w(\lambda)$ values) relative to the true colour image. This observation is promising indicating that the $\text{STD}_{\text{Contheor}}$ approach does not systematically tend to retrieve higher $\rho_w(\lambda)$ values compared to the initial STD approach (as observed for the other cases).

In the Thames Estuary (black box in Fig. 6.17), the modified STD NIR-modelling scheme results in some questionable speckle patterns for $\rho_w(\lambda)$. This is also observable on the MODIS Aqua images for $\tau(869)$ and $\alpha(531, 869)$ (Fig. 6.19). Indeed, in the north of the Thames Estuary, discontinuous patterns of negative or near-zero $\tau(869)$ and $\alpha(531, 869)$ values are observed nearby extremely high values for both aerosol parameters ($\tau(869) > 0.5$ and $\alpha(531, 869) > 1.8$). The initial STD approach also seems to fail over this coastal region. Abrupt changes in both $\tau(869)$ and $\alpha(531, 869)$ are observed for this NIR-modelling scheme. Moreover, Figs. 6.17 and 6.19 show similar spatial patterns for the images processed with the STD NIR-modelling scheme, indicating a non-physical correlation between the aerosol and marine parameters. These questionable results obtained with the STD-based AC methods, may arise from two imperfections in the image processing. First, the non-systematic application of the red-bounding or blue-green spectral relationship constraints in the NIR-modelling scheme may lead to abrupt changes in neighbouring $\rho_w(\lambda_{NIR})$ values explaining the speckle patterns observed in Fig. 6.17 (black box). The NIR-modelling scheme could therefore be modified (e.g., including smoothing techniques within or after the iteration model) to prevent sudden changes in the modelled $\rho_w(\lambda_{NIR})$. Secondly, the abrupt changes in both $\tau(869)$ and $\alpha(531, 869)$ coincide with an area where the red band sensor saturates ($\rho_w(\lambda_{red}) \sim 0.03$ in Fig. 6.17 and Fig. 6.18, Table 3.1 in Chapter 3). To increase the spatial coverage in extremely turbid waters, this flag was omitted for image processing. However, as mentioned previously, when the ocean bands reach their saturation limits, sufficient precision to correctly characterize aerosols and estimate $\rho_w(\lambda)$, is not guaranteed.

As observed previously, the MUMM-based approaches result in less spatial variations in $\alpha(531, 869)$, compared to the STD-based approaches (Fig. 6.19). However, it provides a better coverage for both marine and aerosol parameters. Important differences in $\rho_w(\lambda)$ retrievals are also observed between the STD and MUMM-based approaches, with lower $\rho_w(\lambda)$ values along the coasts of Belgium and the Netherlands when processed with the MUMM-based approaches (Figs. 6.17 and Fig. 6.18). The suspicious speckle patterns observed with the STD-based approaches are not present when the MUMM-based NIR-modelling schemes are used for the AC (black box Figs. 6.17 and 6.19), possibly due to the spatial homogeneity assumption in aerosol reflectance and the application of the constant NIR water reflectance ratio. According to Fig. 6.8(h), the MUMM-based AC methods also resulted in $\rho_w(\lambda)$ values closer to ground truth, while the $\text{STD}_{\text{Contheor}}$ NIR-modelling scheme led to negative $\rho_w(\lambda)$ retrievals. According to Fig. 6.18, the $\text{MUMM}_{\text{Poly}}$ NIR-modelling scheme also present more reflective waters compared to the initial MUMM AC method, especially North of the Thames Estuary (black box in Fig. 6.18). Hence, for this particular case, the $\text{MUMM}_{\text{Poly}}$ AC method seems to perform better than the other AC approaches.

d. Guyane - A20092861710

Figure 6.20 shows the MODIS Aqua images associated with the Class 1 water spectra of French Guiana. When comparing the two MUMM-based approaches with each other, only small differences are encountered. This is also true when comparing the STD and MUMM-based approaches with each other. However, the STD-based approaches still result in overall more reflective waters and, as observed for previous cases (a, b and C), the marine signal with the $\text{STD}_{\text{Contheor}}$ NIR-modelling scheme is slightly higher relative to the initial STD approach. When looking at the aerosol properties the algorithms retrieve relatively high $\tau(869)$ values for pixels along the coast (> 0.5, Fig. 6.22). These pixels are also flagged in Figs. 6.20 and 6.21, due to negative $\rho_w(\lambda)$ retrievals. For the STD approach, we also observe a thin band of higher $\tau(869)$ values in the South-Eastern corner of the image along the coasts of Brazil. This thin band is not as pronounced on the images processed with the other NIR-modelling schemes. On the corresponding true colour image (Fig. 6.9, bottom right picture), variations are observed from brown to blue-green water colours in this area, probably concurring with sediment-rich waters. Hence, the STD modelling scheme may have detected these variations. However, these seem to correspond to variations in aerosol parameters. Additional research should be done to verify this fact.

Similarly to the previously discussed case over French Guiana ('Guyane - A20092861720', Figs. 6.14, 6.15, and 6.16), $\alpha(531, 869)$ appeared to be better retrieved with the MUMM-based AC methods (Fig. 6.22). Indeed, Fig. 6.22 shows a small increase in $\alpha(531, 869)$ values when approaching the coast while with the STD based AC methods we observe a rather abrupt change in $\alpha(531, 869)$ which could possibly result from glint contamination.

6.3 CONCLUSION

The present chapter evaluates, based on MODIS Aqua satellite-*in situ* match-ups for $\rho_w(\lambda)$, $\tau(869)$ and $\alpha(531, 869)$, three modified NIR-modelling schemes suggested to improve $\rho_w(\lambda)$ retrievals, the $\text{MUMM}_{\text{Poly}}$, $\text{STD}_{\text{Contheor}}$ and COMB NIR-modelling schemes (all detailed in the Chapter 5). Similarly to the MUMM and STD AC approach, these NIR-modelling schemes are implemented in the GW94 AC algorithm to extent the algorithm to turbid waters where the black pixel assumption is invalid. The $\text{STD}_{\text{Contheor}}$ and COMB approaches are STD-based NIR-modelling schemes, while the $\text{MUMM}_{\text{Poly}}$ approach is a MUMM-based NIR-modelling scheme. The newly suggested NIR-modelling schemes are evaluated based on a match-up exercise performed with AERONET-OC and LOG data and a visual inspection of processed MODIS Aqua images over the turbid waters of French Guiana and the North Sea-English Channel.

According to the sensitivity studies outlined in Chapter 5, the suggested modified NIR-modelling schemes should mainly improve $\rho_w(\lambda)$ retrievals in very and extremely turbid waters. However, improvements in $\rho_w(\lambda)$ were also noticeable with the validation exercise performed with the AERONET-OC and LOG data, containing mainly moderately turbid waters spectra (Section 6.1), in particular for Class 1 and 4 spectra (defined as water masses optically dominated by detrital and mineral material and by phytoplankton and high loads of CDOM, respectively). Relative errors and biases slightly decreased with the $\text{STD}_{\text{Contheor}}$ approach compared to the initial STD AC method (by about 1%). Improvements with the $\text{MUMM}_{\text{Poly}}$ approach, relative to the initial MUMM AC method, was not as pronounced ($< 1\%$ differences in RE and bias). For the unclassified spectra (mostly showing open ocean water spectral shapes) and Class 2 waters (defined as water masses mainly dominated by phytoplankton), the differences in NIR-modelling schemes did not significantly affect the AC method.

A first advantage encountered with the $\mathrm{STD}_{\mathrm{Contheor}}$ and COMB NIR-modelling schemes is the number of retrieved match-up pairs. Indeed, for the global validation, both the $\mathrm{STD}_{\mathrm{Contheor}}$ and COMB AC methods retrieved more valid match-ups compared to the STD AC method (771, 772, and 762, respectively). However, both modified approaches also retrieved more negative $\rho_w(\lambda)$ values relative to the initial STD approach (12%, 15% and 16%, with the STD, $\mathrm{STD}_{\mathrm{Contheor}}$ and COMB NIR-modelling schemes, respectively).

Overall, the modified NIR-modelling schemes provided improved $\rho_w(\lambda)$ estimations compared to the initial schemes. Only, the COMB AC method, which was meant to combine the $\mathrm{MUMM}_{\mathrm{Poly}}$ and $\mathrm{STD}_{\mathrm{Contheor}}$ NIR-modelling schemes to increase the spatial coverage of the initial AC methods, resulted in greater overall errors compared to the initial schemes. Hence, more work is needed such that a combined MUMM-STD NIR-modelling scheme provides satisfactory results. The COMB AC approach was therefore not further investigated.

According to the visual inspection of MODIS Aqua images from the North Sea-English Channel and the French Guiana waters, the $\mathrm{MUMM}_{\mathrm{Poly}}$ and $\mathrm{STD}_{\mathrm{Contheor}}$ AC approaches showed more reflective $\rho_w(\lambda)$ values in turbid waters, relative to the initial MUMM and STD AC methods, respectively. Compared to the initial STD AC approach, the $\mathrm{STD}_{\mathrm{Contheor}}$ also better separated the marine and aerosol contributions. Indeed, the STD AC approach often showed similar spatial patterns between aerosol and ocean colour products.

Although the constrained AC methods resulted in some improvements, limitations and inaccuracies were still noticed. Indeed, non-physical speckle patterns were observed on the MODIS Aqua $\rho_w(\lambda)$ images processed with the $\mathrm{STD}_{\mathrm{Contheor}}$ NIR-modelling scheme. This scheme should also be further improved to ensure a better spatial coverage. Similarly, the $\mathrm{MUMM}_{\mathrm{Poly}}$ NIR-modelling scheme still tended to underestimate $\rho_w(\lambda)$ values. More work should also be done such that this AC approach accounts for spatial heterogeneity in aerosol properties.

Improvements in satellite $\rho_w(\lambda)$ retrievals have thus been achieved with these spectral relationship-forced NIR-modelling schemes, but more work is still required to further improve $\rho_w(\lambda)$ values.

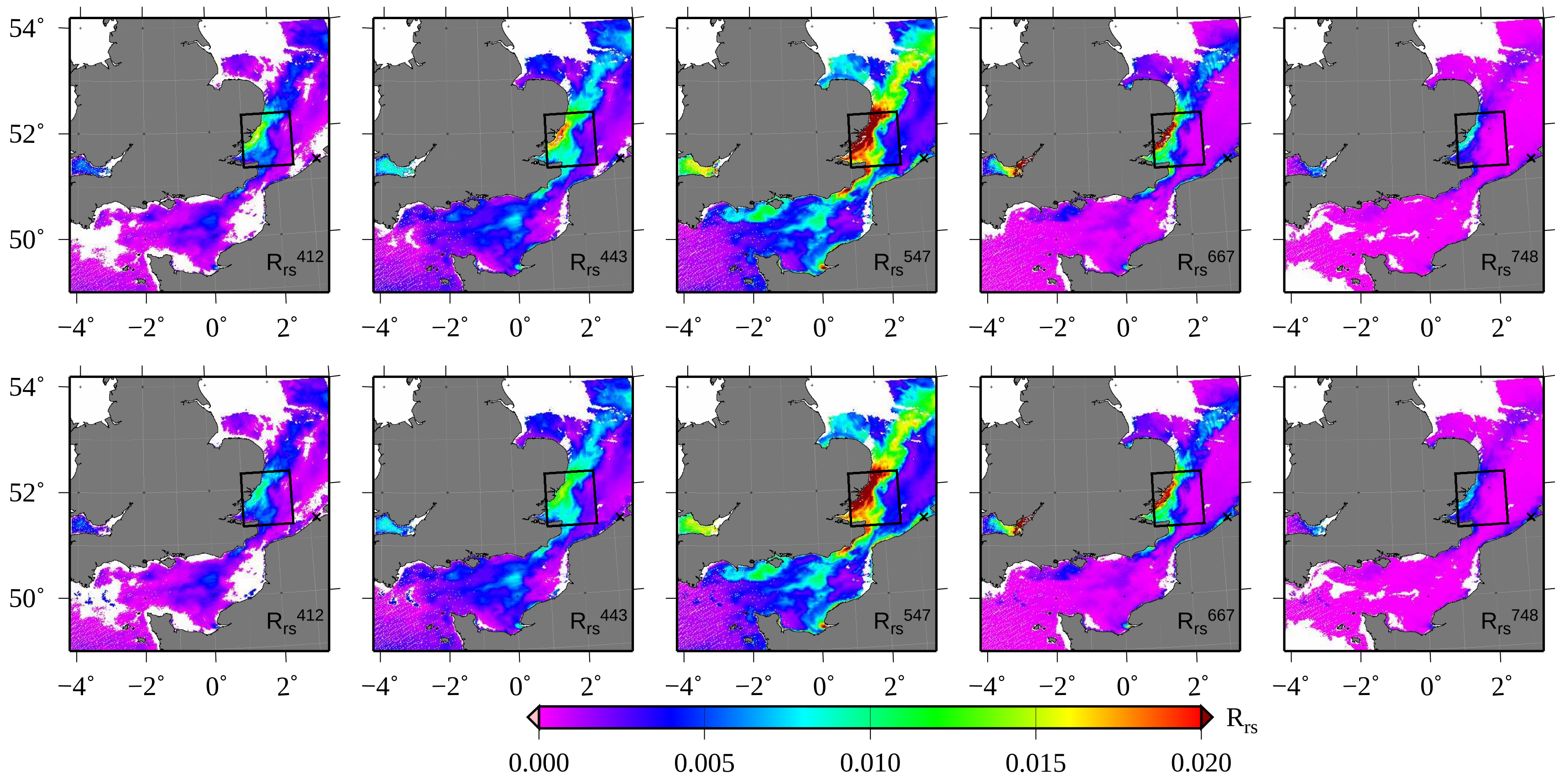

Figure 6.10: *MODIS Aqua* $R_{rs}(\lambda)$ *images associated with 'Belcolor-A2010113126500' spectra (black cross) retrieved using the* $STD_{Contheor}$ *(upper row) and STD (bottom row) NIR-modelling schemes for the AC. The black box corresponds to the Thames Estuary where the* $STD_{Contheor}$ *NIR-modelling scheme shows more reflective waters compared to the initial STD scheme.*

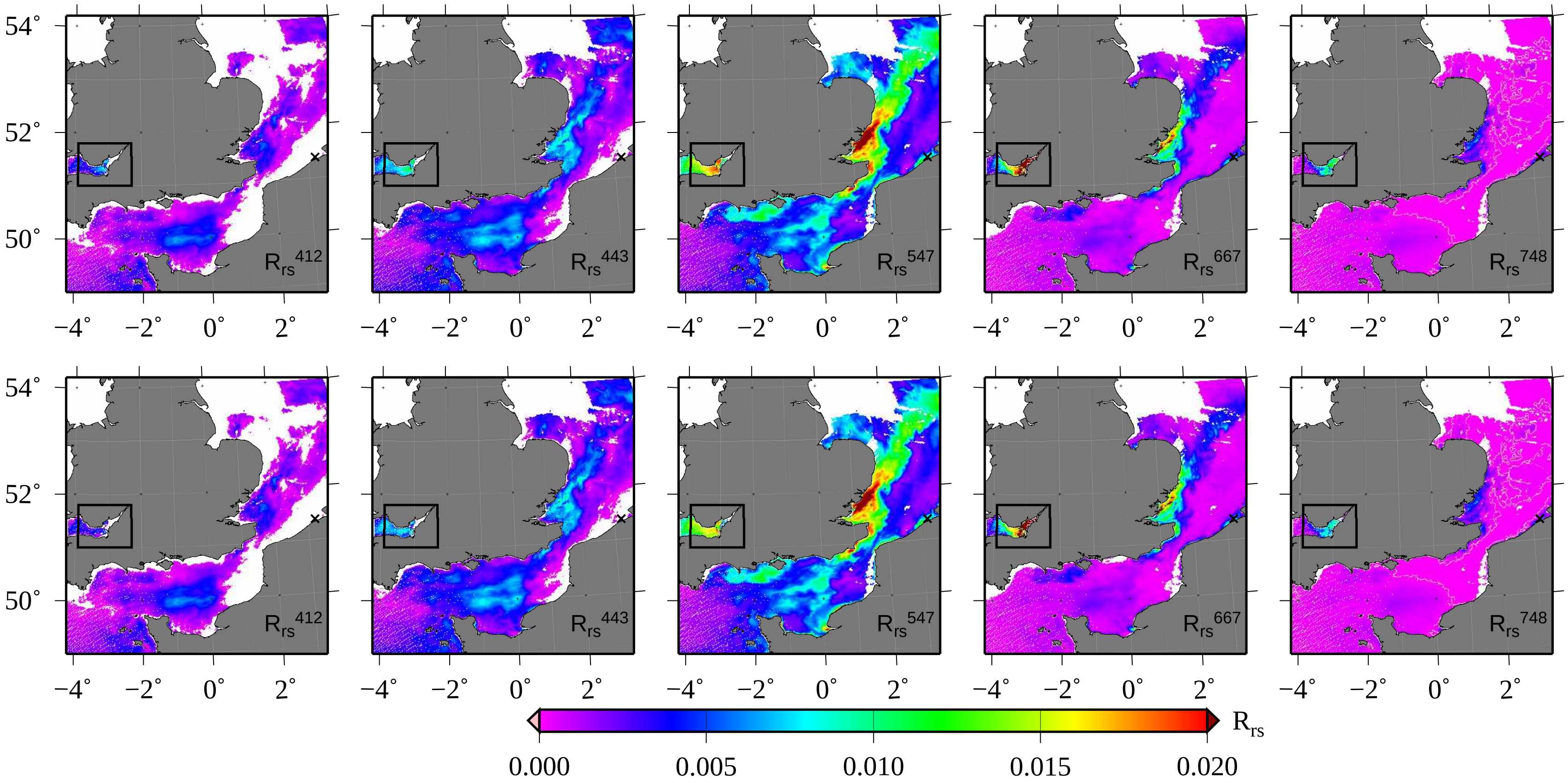

Figure 6.11: *MODIS Aqua* $R_{rs}(\lambda)$ *images associated with 'Belcolor-A2010113126500' spectra (black cross) retrieved using the* $MUMM_{Poly}$ *(upper row) and MUMM (bottom row) NIR-modelling schemes for the AC. The black box corresponds to the Bristol Channel where the* $MUMM_{Poly}$ *NIR-modelling scheme shows more reflective waters compared to the initial MUMM scheme.*

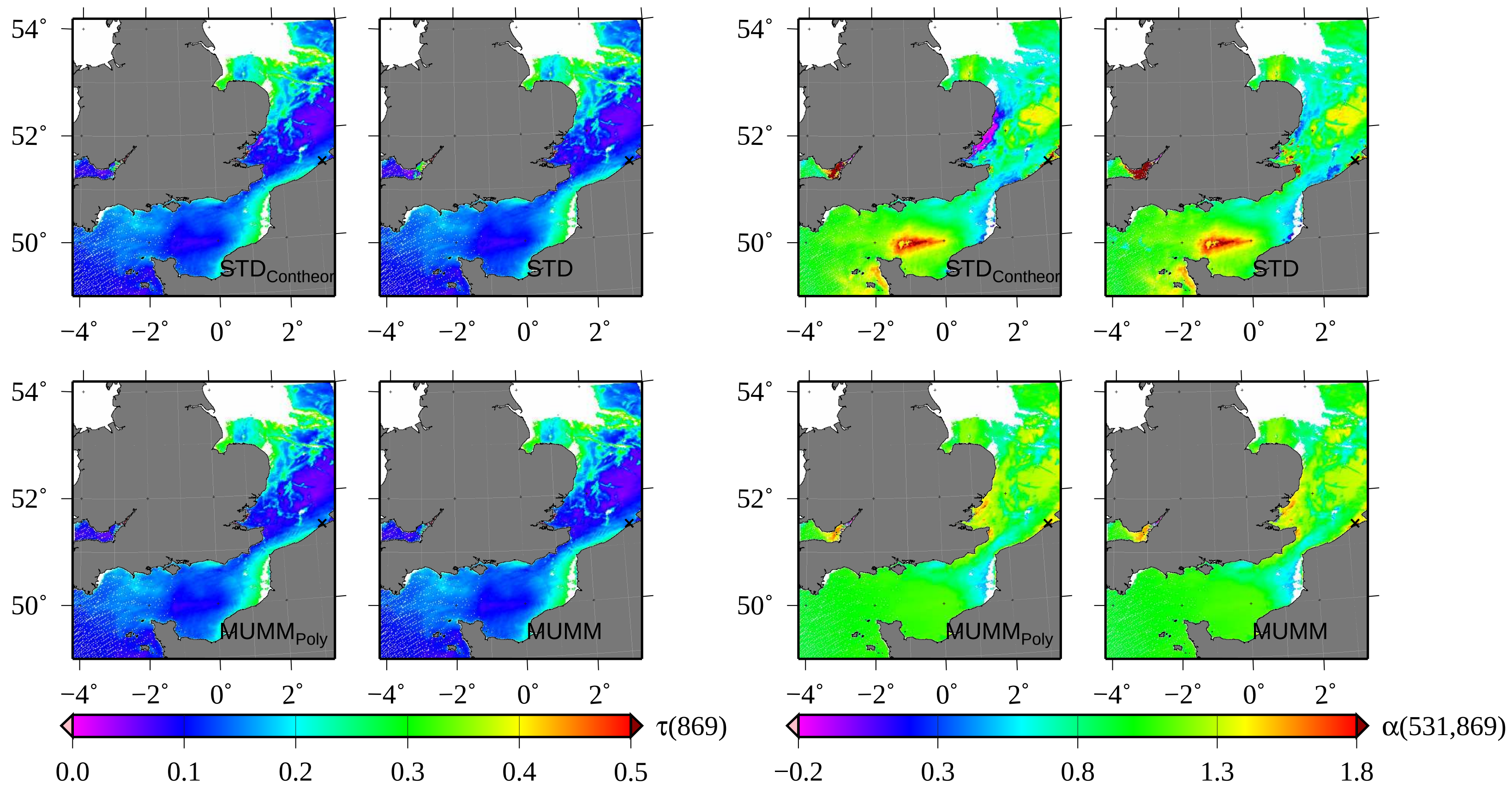

Figure 6.12: *MODIS Aqua aerosol products,* $\tau(869)$ *and* $\alpha(531, 869)$*, associated with 'Belcolor-A2010113126500' spectra (black cross) retrieved using the* $STD_{Contheor}$*, STD,* $MUMM_{Poly}$ *and MUMM NIR-modelling schemes for the AC.*

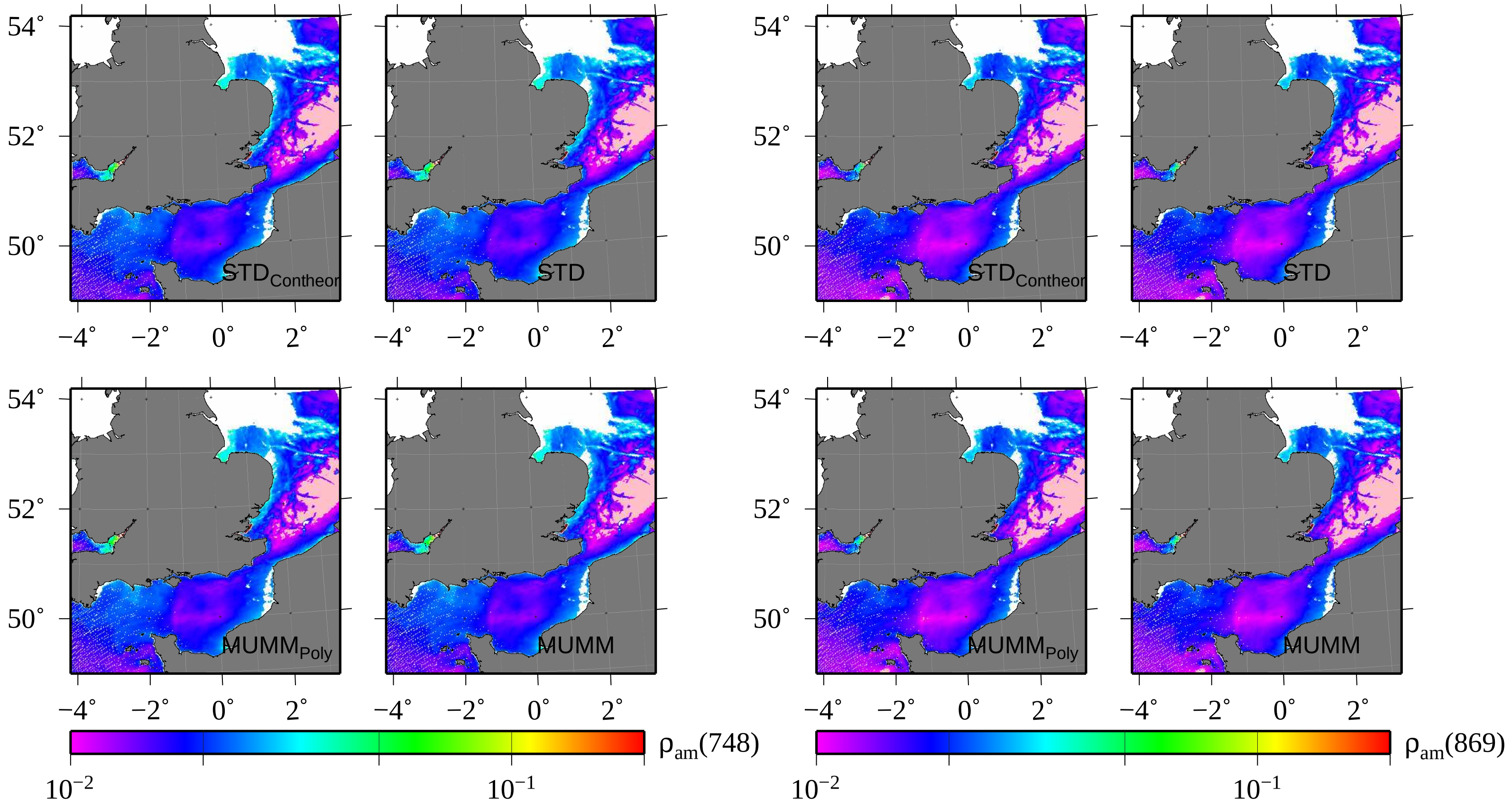

Figure 6.13: *MODIS Aqua $\rho_{am}(\lambda)$ images at 748 and 869 nm associated with 'Belcolor-A2010113126500' spectra (black cross) retrieved using the $STD_{Contheor}$, STD, $MUMM_{Poly}$, and MUMM NIR-modelling schemes for the AC.*

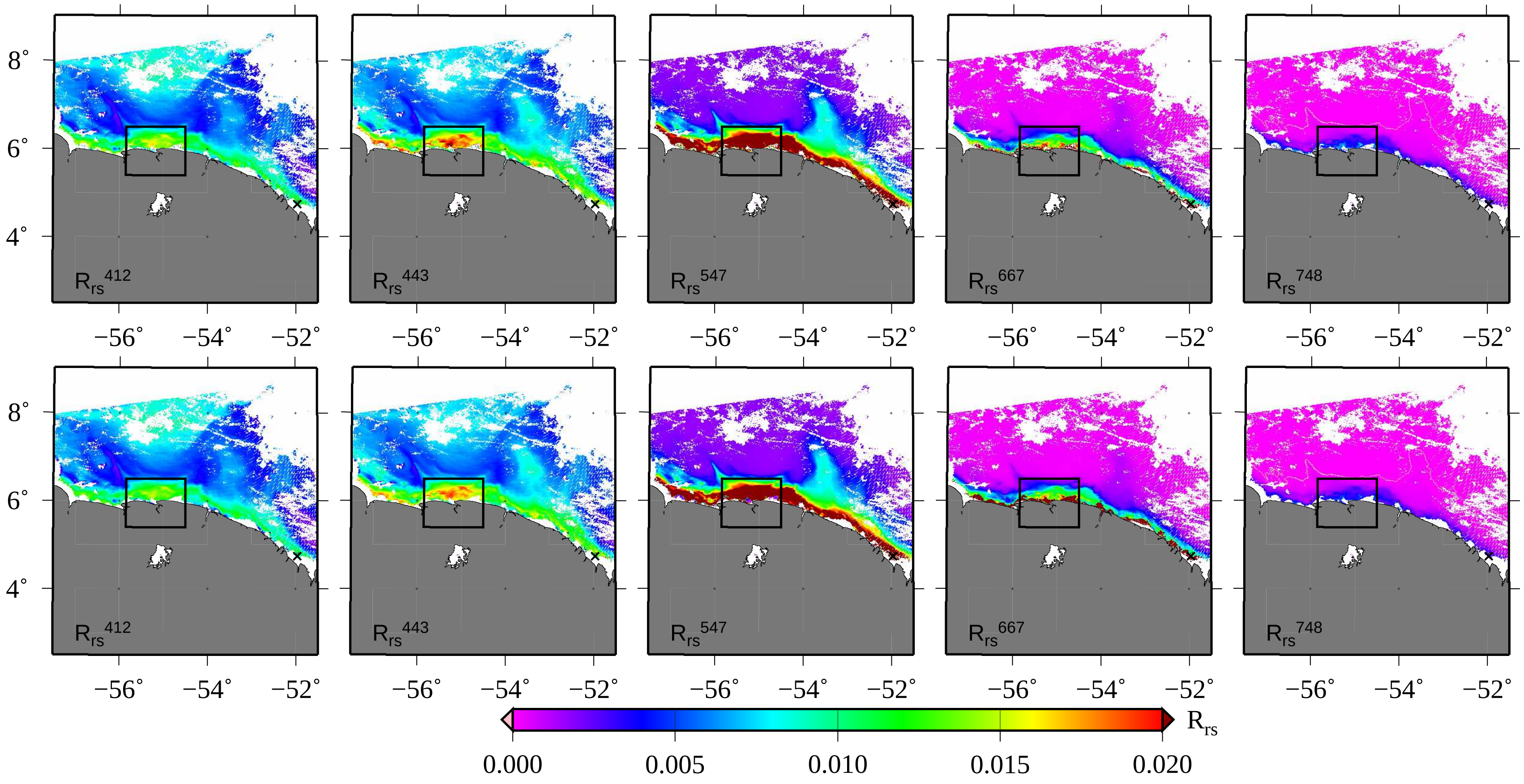

Figure 6.14: *MODIS Aqua $R_{rs}(\lambda)$ images associated with 'Guyane-A2009286172000' spectra (black cross) retrieved using the $STD_{Contheor}$ (upper row) and STD (bottom row) NIR-modelling schemes for the AC. The black box indicates the region where the $STD_{Contheor}$ NIR-modelling scheme results in more reflective waters compared to the initial STD scheme.*

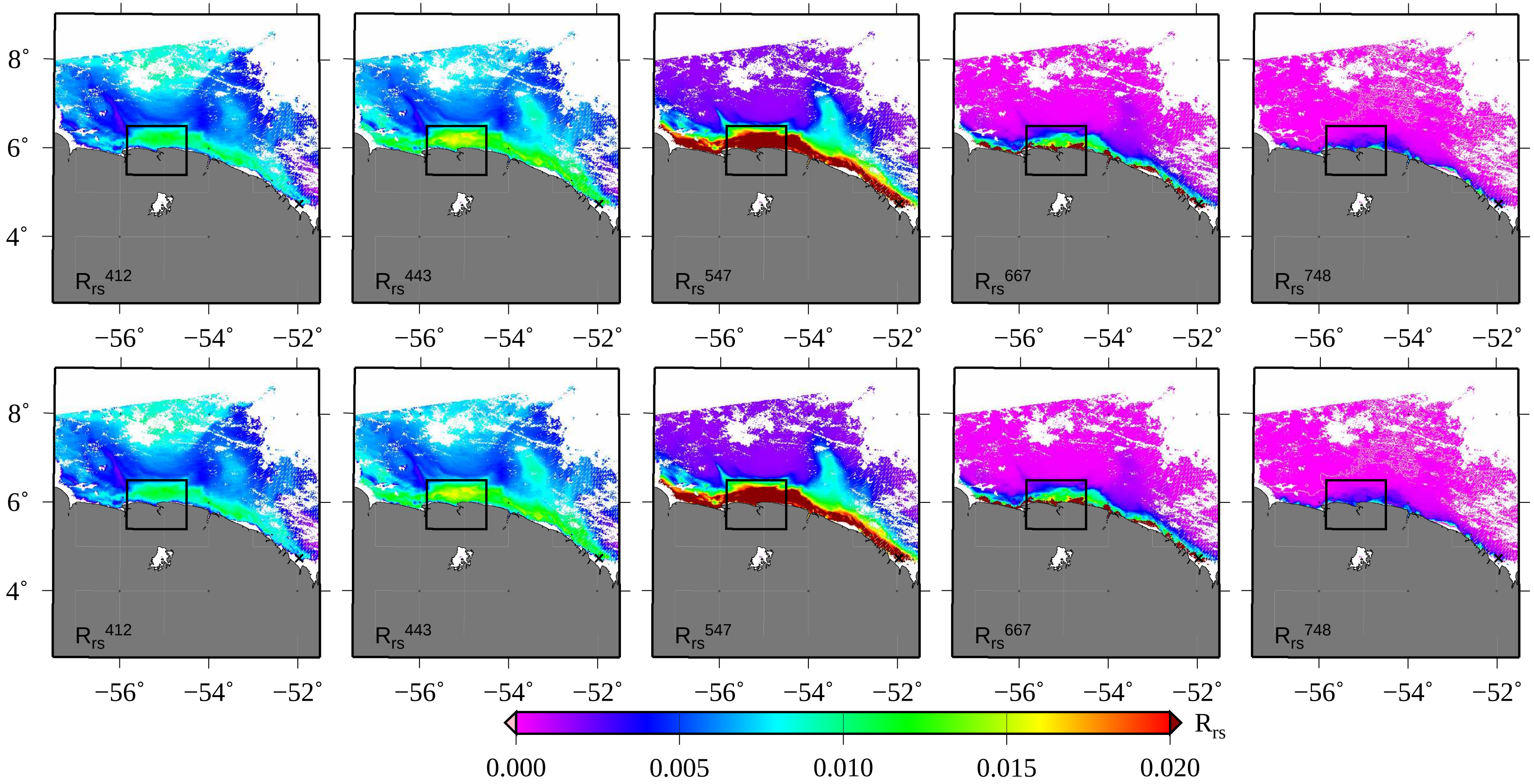

Figure 6.15: *MODIS Aqua $R_{rs}(\lambda)$ images associated with 'Guyane-A2009286172000' spectra (black cross) retrieved using the $MUMM_{Poly}$ (upper row) and MUMM (bottom row) NIR-modelling schemes for the AC.*

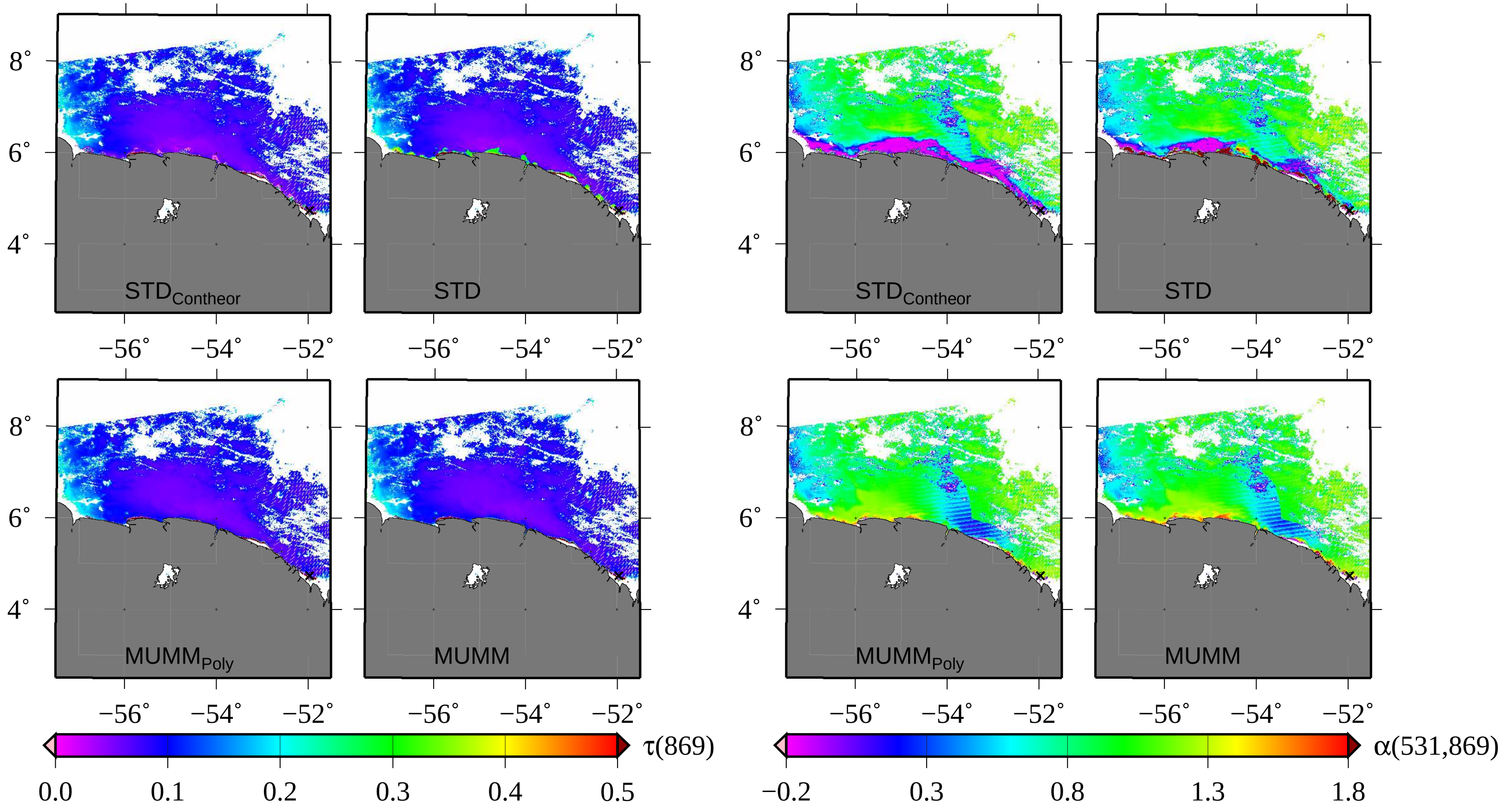

Figure 6.16: *MODIS Aqua aerosol products, $\tau(869)$ and $\alpha(531, 869)$, associated with 'Guyane-A2009286172000' spectra (black cross) retrieved using the $STD_{Contheor}$, STD, $MUMM_{Poly}$ and MUMM NIR-modelling schemes for the AC.*

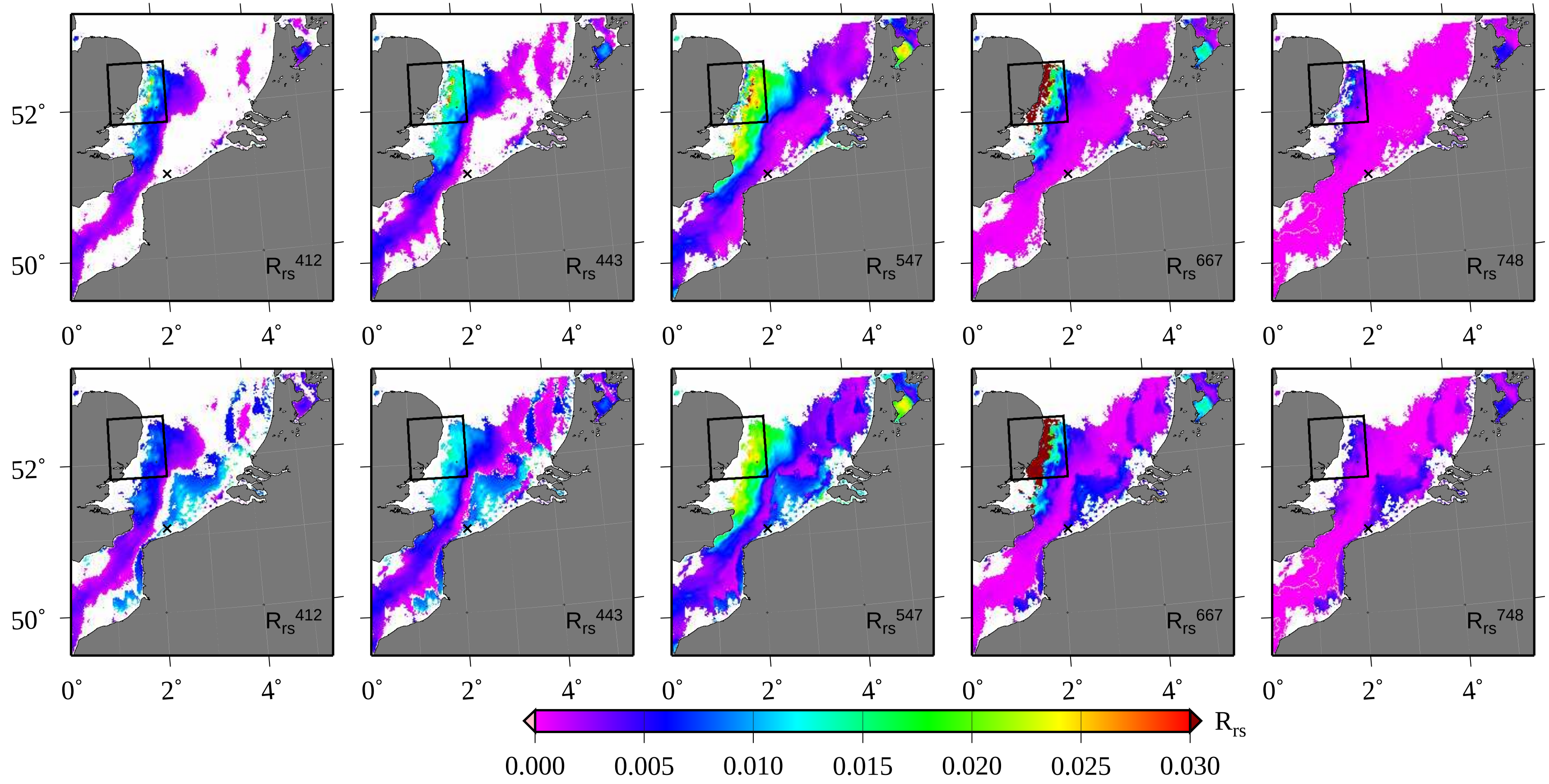

Figure 6.17: *MODIS Aqua $R_{rs}(\lambda)$ images associated with 'Phabop-A2004106122500' spectra (black cross) retrieved using the $STD_{Contheor}$ (upper row) and STD (bottom row) NIR-modelling schemes for the AC. The black box indicates the region where questionable speckle patterns are observed.*

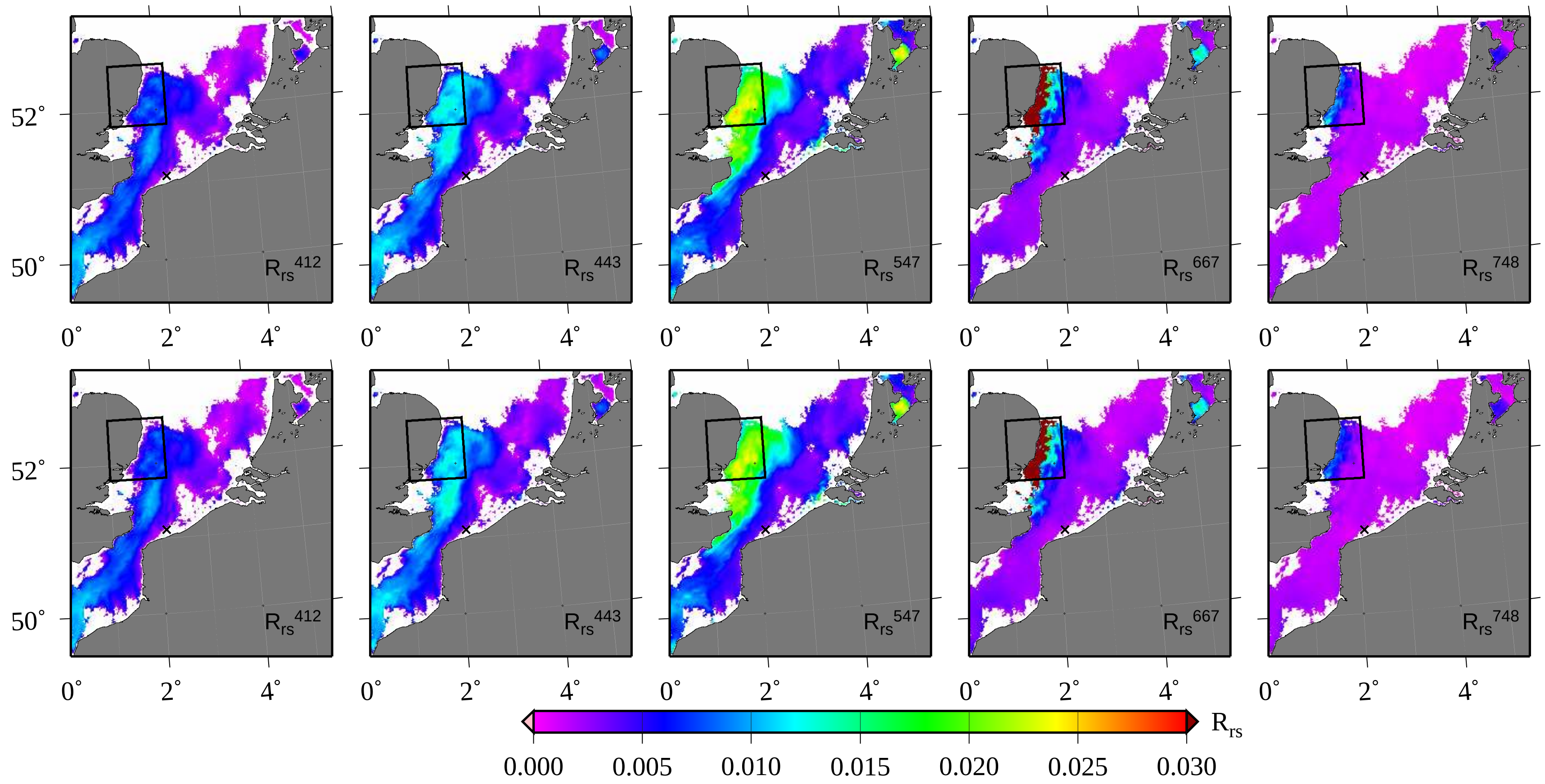

Figure 6.18: *MODIS Aqua* $R_{rs}(\lambda)$ *images associated with 'Phabop-A2004106122500' spectra (black cross) retrieved using the* $MUMM_{Poly}$ *(upper row) and MUMM (bottom row) NIR-modelling schemes for the AC. The black box indicates the region where the* $MUMM_{Poly}$ *NIR-modelling scheme results in more reflective waters compared to the other AC approaches.*

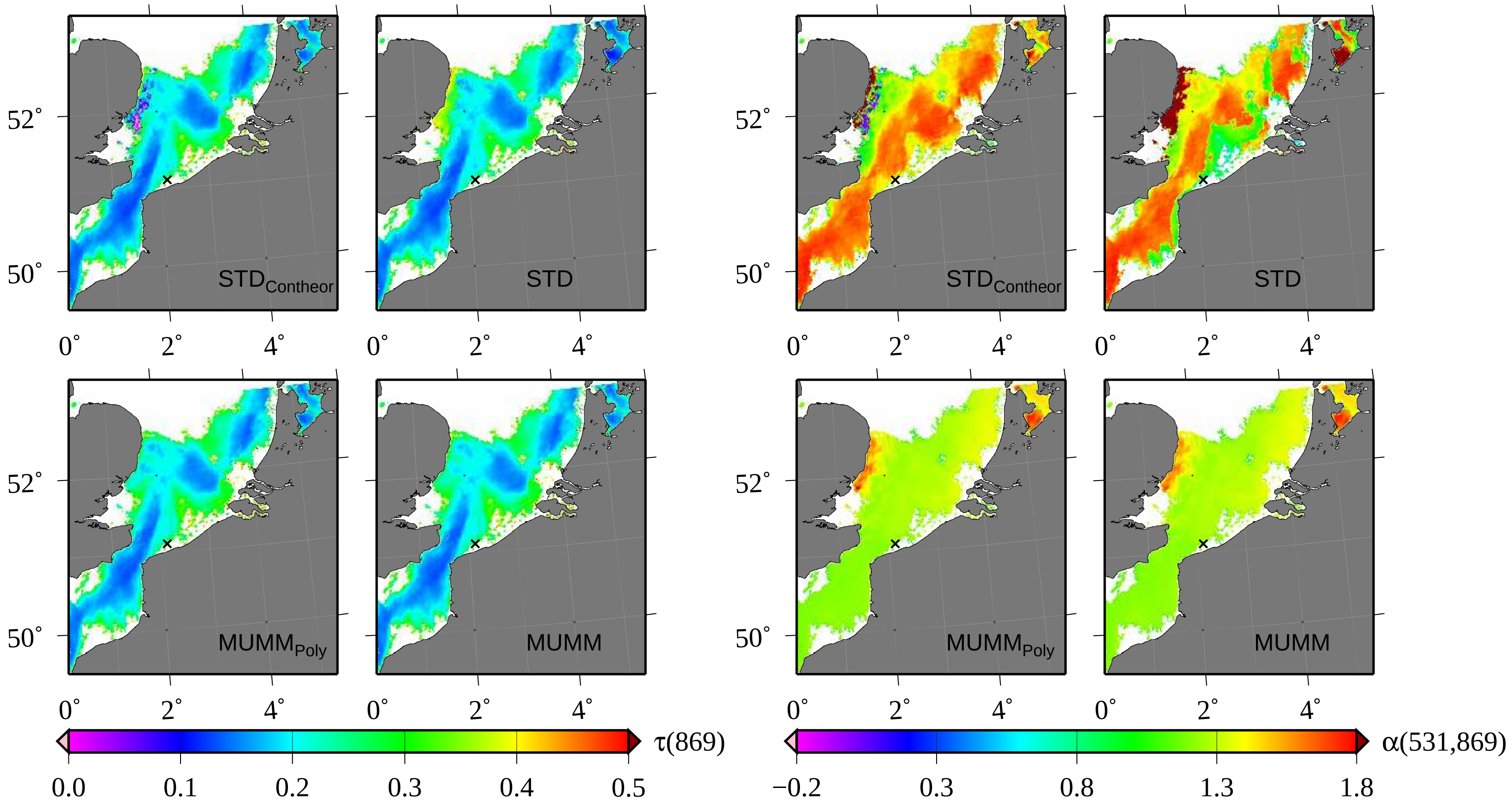

Figure 6.19: *MODIS Aqua aerosol products,* $\tau(869)$ *and* $\alpha(531, 869)$*, associated with 'Phabop-A2004106122500' spectra (black cross) retrieved using the* $STD_{Contheor}$*, STD,* $MUMM_{Poly}$ *and MUMM NIR-modelling schemes for the AC.*

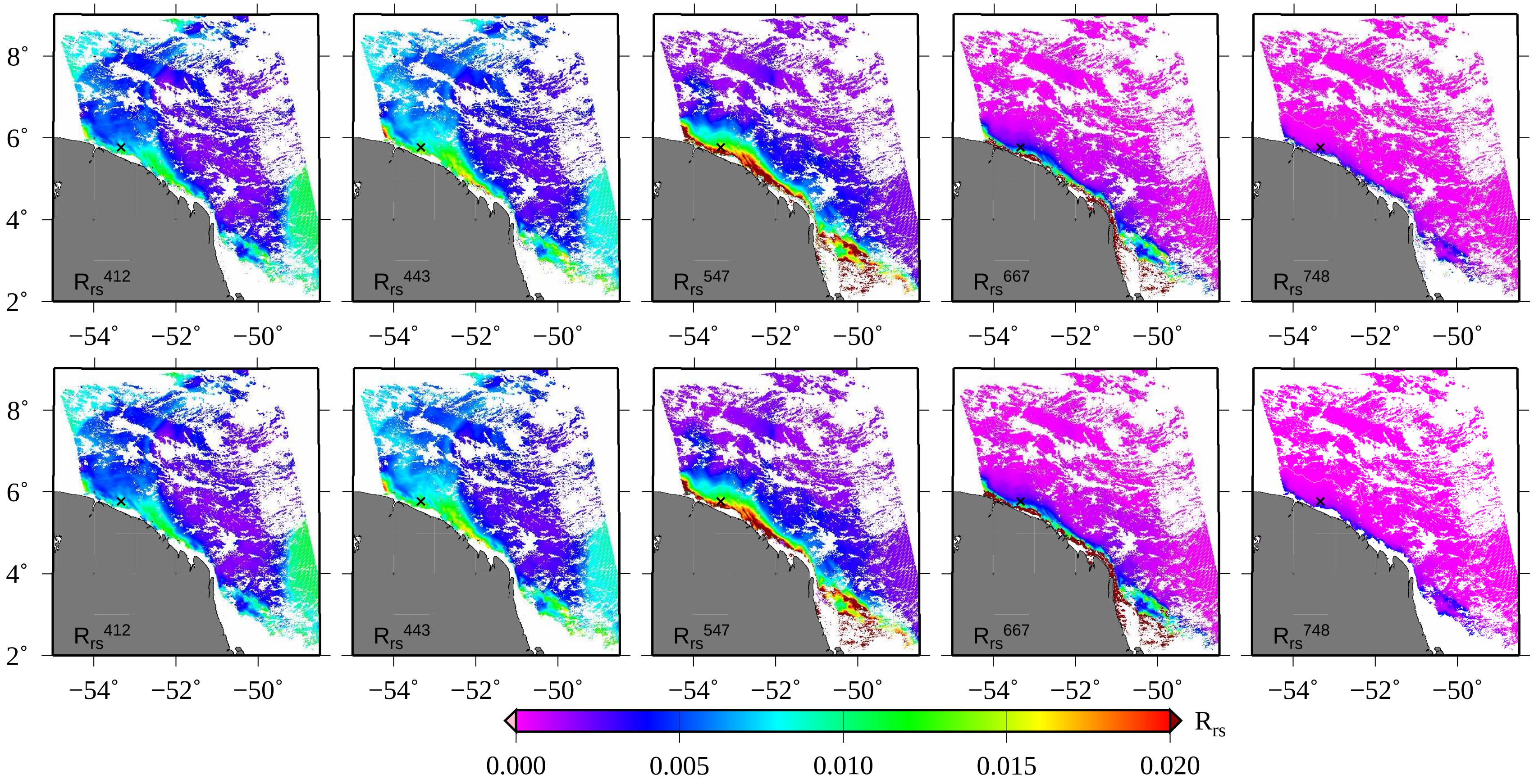

Figure 6.20: *MODIS Aqua $R_{rs}(\lambda)$ images associated with 'Guyane-A2009288171000' spectra (black cross) retrieved using the $STD_{Contheor}$ (upper row) and STD (bottom row) NIR-modelling schemes for the AC.*

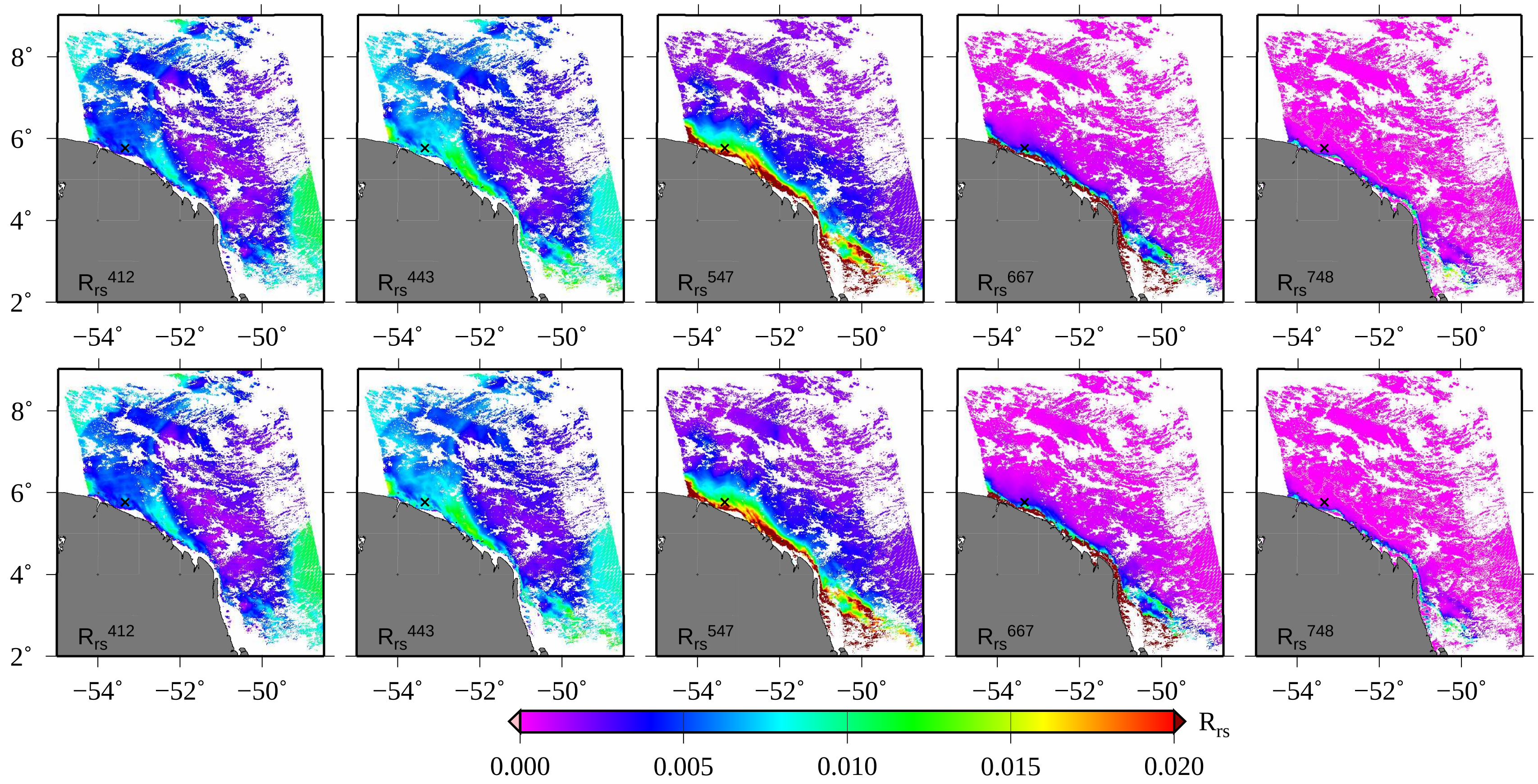

Figure 6.21: *MODIS Aqua $R_{rs}(\lambda)$ images associated with 'Guyane-A2009288171000' spectra (black cross) retrieved using the $MUMM_{Poly}$ (upper row) and MUMM (bottom row) NIR-modelling schemes for the AC.*

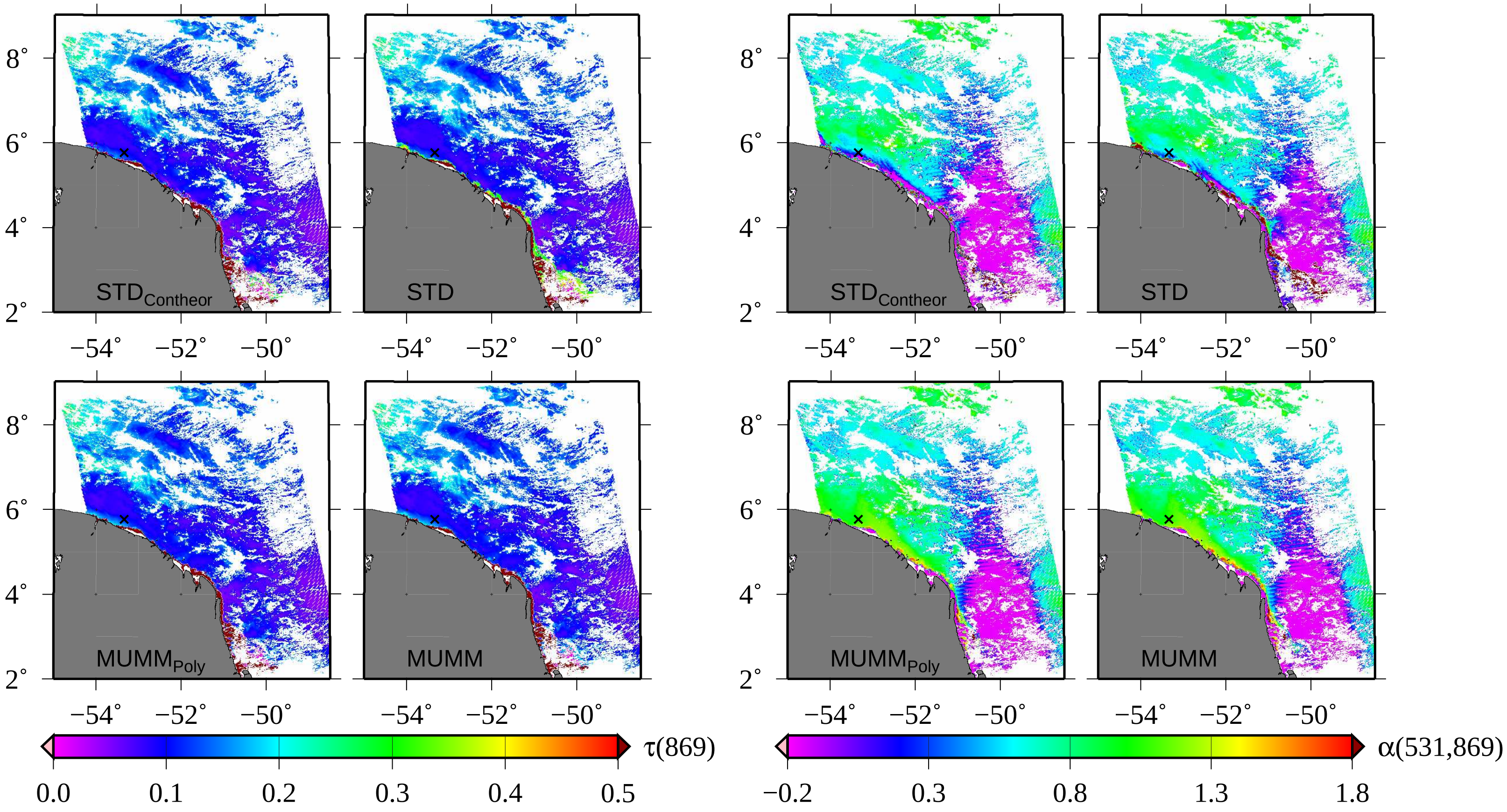

Figure 6.22: *MODIS Aqua aerosol products,* $\tau(869)$ *and* $\alpha(531, 869)$*, associated with 'Guyane-A2009288171000' spectra (black cross) retrieved using the* $STD_{Contheor}$*, STD,* $MUMM_{Poly}$ *and MUMM NIR-modelling schemes for the AC.*

General conclusion and perspectives

Atmospheric correction (AC) in ocean colour remote sensing is intended to remove the contribution of the atmosphere from the sensor measured signal to estimate the ocean colour and, subsequently, to retrieve marine parameters. However AC processes remain a challenge in optically complex and highly productive waters. Indeed, in such waters, the classic black pixel assumption, referred as the GW94 AC method (Gordon and Wang, 1994), is not valid (Siegel et al., 2000), and the complexity of the water optical properties makes it difficult to accurately quantify the atmospheric contribution. To solve these issues, multiple alternative AC methods have been suggested for turbid waters (e.g., Arnone et al., 1998; Moore et al., 1999; Siegel et al., 2000; Ruddick et al., 2000; Stumpf et al., 2003; Ruddick et al., 2006; Bailey et al., 2010; Wang and Shi, 2005, 2007; Wang et al., 2009; Gordon et al., 1997; Chomko and Gordon, 1998; Chomko et al., 2003; Kuchinke et al., 2009a,b; Jamet et al., 2005; Brajard et al., 2006a; Doerffer and Schiller, 2007; Schroeder et al., 2007; Doeffer and Schiller, 2008; IOCCG, 2010; Brajard et al., 2012). However, the significant contribution of the atmosphere and the radiometric accuracy specifications determined by a large diversity of ocean colour applications (Hooker et al., 1992, 2002; Franz et al., 2007), requires further improvement in AC for ocean colour remote sensing images. This brings us to the main objectives of my Ph.D. thesis consisted in (1) validating existing AC methods developed for optically complex waters, with a focus on MODIS Aqua ocean colour images, and (2) suggesting further improvements in the aim to provide accurate remote sensing derived water properties.

First a global validation of four common AC methods developed for turbid waters was carried out with *in situ* water-leaving reflectance ($\rho_w(\lambda)$) data from the AERONET-OC and LOG databases. The four methods are (1) the NASA official GW-94 based algorithm including an iterative NIR-modelling scheme with a bio-optical model (Stumpf et al., 2003; Bailey et al., 2010) (referred to as 'STD'), (2) the GW94-based algorithm assuming spatial homogeneity of the atmosphere over the region of interest in the NIR and a constant NIR water-leaving reflectance ratio (Ruddick et al., 2000, 2006) (referred to as 'SIMIL' or 'MUMM'), (3) the GW94-based algorithm using the Short-Wave-Infra-Red (SWIR) bands in very turbid waters (Wang et al., 2009) (referred to as 'NIR-SWIR') and (4) the direct inversion approach based on an artificial neural network suggested by Schroeder et al. (2007) (referred to as 'NN'). This global validation exercise also included an evaluation of the performances of the algorithms as a function of the optical water type (Vantrepotte et al., 2012). Results from this validation exercise suggested that, overall, the STD AC method performed the best. However, it failed to retrieve accurate $\rho_w(\lambda)$ estimations in water masses optically dominated by detrital and mineral material. For these water masses, the MUMM AC method provided slightly better results. The latter also ensured a greater spatial coverage. Results also showed that the performances of all AC methods were significantly reduced in water masses optically dominated by high CDOM concentrations. The NN AC method presented better performances compared to the GW94-based algorithms in the blue and red spectral regions. However, the sensitivity of this AC approach to the used training dataset, for the development of the neural-network inversion method, significantly affected the number of valid retrieved match-up pairs. The NIR-SWIR AC method provided similar results to the STD AC approach, possibly because the AERONET-OC and LOG datasets presented only low to moderate turbidity levels. Nonetheless, for some match-up pairs, where switching between NIR and SWIR AC components occurred, abrupt changes in satellite $\rho_w(\lambda)$ retrievals were observed between neighbouring pixels. Hence, this switching AC approach should be improved to avoid non-physical spatial heterogeneity in $\rho_w(\lambda)$.

Following the global and class-specific evaluation of the turbid waters AC methods, several areas of improvements were defined to enhance AC methods for optically complex waters. This work focussed on improving the STD and MUMM AC methods and attempted to extent both NIR-modelling schemes to a wider range of contrasted coastal waters. Indeed, it was found that the bio-optical model within the STD NIR-modelling scheme, relying largely on Chl_a estimations to model $\rho_w(\lambda_{NIR})$, was inappropriate for mineral and detrital sediment rich waters or waters optically dominated by important loads of CDOM. Similarly, the class-specific validation exercise demonstrated that the MUMM AC approach should be revised to avoid underestimations in $\rho_w(\lambda)$.

To extend these existing NIR-modelling schemes, validated spectral relationship constraints were added in the NIR-modelling schemes. Spectral relationships allow to retrieve $\rho_w(\lambda)$ values at a given wavelength according to the water signal at one or more other bands. Hence, such relationships encompass the spectral dependency of the absorption and backscattering coefficients simultaneously and, subsequently, do not require any information on these properties. Such relationships have already been suggested by numerous authors to constrain AC methods of past and present sensors. In this work an extensive overview and validation of these red and NIR spectral relationships found in the literature was performed and led to the selection of globally valid spectral relationships, the red bounding equations suggested by Lee et al. (2009) to delineate red $\rho_w(\lambda)$ values according to the water signal in the green, and a polynomial NIR spectral relationship, suggested by Wang et al. (2012) for the NIR-modelling scheme of the AC method of GOCI.

To improve the initial MUMM NIR-modelling scheme, the constant NIR reflectance ratio (Ruddick et al., 2000, 2006), observed as non-valid for extremely turbid waters (Shi and Wang, 2009; Doron et al., 2011; Goyens et al., 2013a), was replaced by the polynomial NIR spectral relationship (referred to as the $\text{MUMM}_{\text{Poly}}$ AC method), and, both red and NIR spectral relationships, were used to constrain the STD NIR-modelling scheme (referred to as the $\text{STD}_{\text{Contheor}}$ AC method).

The potential of these spectral relationships to improve satellite retrieved $\rho_w(\lambda)$ was first investigated based on a sensitivity study conducted with *in situ* $\rho_w(\lambda)$ and simulated $\rho_{rc}(\lambda)$ data. Results of this study showed that the constrained STD and polynomial based MUMM NIR-modelling schemes (referred to as STD_{Con} and $\text{MUMM}_{\text{Poly}}$, respectively), performed better than the initial approaches, in particular in very turbid waters and in the blue spectral region. These results were promising since the global validation exercise concluded that the greatest errors in $\rho_w(\lambda)$ were observed in this spectral range. However, for both algorithms, the added value of the spectral relationships was slightly reduced. Indeed, the number of valid retrieved $\rho_w(\lambda)$ spectra with the STD_{Con} NIR-modelling scheme slightly decreased compared to the initial STD NIR-modelling scheme, and the sensitivity to erroneously retrieved aerosol properties with the $\text{MUMM}_{\text{Poly}}$ NIR-modelling scheme slightly increased compared to the MUMM NIR-modelling scheme.

To further improve $\rho_w(\lambda)$ retrievals, two additional spectral relationships were also suggested showing relatively good performances, a red-NIR hyperbolic function (relating $\rho_w(667)$ and $\rho_w(748)$) and a blue-green linear relationship (relating $\rho_w(\lambda)$ at 443 and 547 nm). To evaluate if the empirical spectral relationships were globally valid, I also attempted to confirm the spectral relationships with a theoretical basis and concluded that the empirically retrieved parameters of the red-NIR spectral relationship appeared to be appropriate only for a certain range of turbidity. However, it was found that the hyperbolic form of the relation was globally valid. These findings led to an additional modified STD NIR-modelling scheme, referred to as the $\mathrm{STD_{Contheor}}$ NIR-modelling scheme. Modifications in the $\mathrm{STD_{Contheor}}$ NIR-modelling scheme were the following;(1) the interpolation of $b_b(\lambda)$ from the red to the NIR spectral domain was replaced by the theoretical red-NIR hyperbolic (with parameters varying according to the estimated inherent optical properties) and the empirical NIR polynomial spectral relationship, and, (2) erroneous estimations of blue and red $\rho_w(\lambda)$ within the bio-optical model were corrected with the blue-green and red bounding equations.

A combined $\mathrm{MUMM_{Poly}}$-$\mathrm{STD_{Contheor}}$ NIR-modelling scheme was also suggested to retrieve more valid $\rho_w(\lambda)$ spectra by using the $\mathrm{MUMM_{Poly}}$ NIR-modelling scheme when $\mathrm{STD_{Contheor}}$ method failed to retrieve physical $\rho_w(\lambda)$ values. However, this combined NIR-modelling scheme showed some large inconsistencies and was therefore not further investigated.

An evaluation exercise based on *in situ*-satellite match-up pairs for $\rho_w(\lambda)$, $\tau(869)$ and $\alpha(531, 869)$, confirmed the results of the sensitivity studies. Indeed, both $\mathrm{STD_{Contheor}}$ and $\mathrm{MUMM_{Poly}}$ NIR-modelling schemes resulted in improved satellite $\rho_w(\lambda)$ retrievals compared to the initial STD and MUMM AC approaches, respectively. In turbid coastal waters, the $\mathrm{MUMM_{Poly}}$ NIR-modelling scheme resulted in more reflective waters compared to the initial scheme. This is also true for the $\mathrm{STD_{Contheor}}$ approach. Moreover, a better separation was found between aerosol and marine parameters with the $\mathrm{STD_{Contheor}}$ approach. Some inconsistencies encountered with the initial STD NIR-modelling scheme were also corrected with the $\mathrm{STD_{Contheor}}$ NIR-modelling.

This study provided thus a comprehensive evaluation of the different turbid water AC approaches and resulted in important findings and suggestions improving $\rho_w(\lambda)$ retrievals in optically complex waters. However, imperfections in the AC are still encountered. Indeed, non-physical negative $\rho_w(\lambda)$ retrievals are still retrieved. Questionable speckle patterns of $\rho_w(\lambda)$ were also observed on the MODIS Aqua images processed with the $\mathrm{STD_{Contheor}}$ NIR-modelling, and, the $\mathrm{MUMM_{Poly}}$ NIR-modelling scheme was still affected by non-homogeneity in aerosol properties. Hence, perspectives to further improve $\rho_w(\lambda)$ retrievals are multiple and this study could be continued to further investigate and enhance the suggested NIR-modelling schemes. Ideas of possible improvements may be:

- How to avoid non-physical negative $\rho_w(\lambda)$ retrievals?

  Negative $\rho_w(\lambda)$ are non-physical and should be avoided. A possible way to reduce the number of negative $\rho_w(\lambda)$ retrievals, may consist to force the iteration in the STD-based NIR-modelling schemes until $\rho_w(\lambda)$ estimations are positive over the entire spectrum. The use of an offset to correct for negative $\rho_w(\lambda)$ retrievals may also be examined. Such an offset could be implemented in both STD and MUMM-based AC methods. As observed by Goyens et al. (2013a), the NIR polynomial spectral relationship also slightly underestimated low and extreme $\rho_w(\lambda_{NIR})$ values. Hence, a rectification of this spectral relationship may eventually reduce the number of negative $\rho_w(\lambda)$ retrievals with the modified NIR-modelling schemes. Future ocean colour sensors may also provide more spectral bands and better spectral resolutions whereby spectral relationships may be further improved.

- Should the speckle patterns in $\rho_w(\lambda)$ be smoothed?

  Non-physical speckle patterns, observed with the $\mathrm{STD_{Contheor}}$, were partially due to the non-systematic application of the red and blue-green constraints. This may be rectified by including a smoothing technique within the NIR-modelling scheme (e.g., using weighting functions throughout the iteration process) or by including class-specific constraints and thus including a classification scheme within the iterative process.

- Spectral relationship constraints to improve both marine and aerosol parameters?

As demonstrated with the sensitivity studies in Chapter 5, although the NIR-modelling scheme may perfectly retrieve $\rho_w(\lambda_{NIR})$, the AC method may still fail to match the *in situ* data because of inaccuracies in the retrieved aerosol parameters. Hence, rather than forcing the NIR-modelling scheme solely (as suggested in this work), constraints could be applied to the entire AC method and, subsequently, also correct for imperfections in the aerosol component of the AC approach. Spectral relationships should thus encompass correction for errors on marine and aerosol reflectances. Accordingly, it may be worth evaluating if spectral relationships could be developed based on Rayleigh corrected reflectances rather than on $\rho_w(\lambda)$ solely (e.g., using aerosol-model-specific spectral relationships). The use of bounding equations to constrain either top of atmosphere or Rayleigh corrected reflectances may also be investigated. In this case both the aerosol model selection component and the NIR-modelling scheme will be constrained simultaneously. Note however that such method may lead to unlikely spatially correlated marine and aerosol parameters.

- Could we use aerosol products from other sources?

  The aerosol models used by the ocean colour community (e.g., Shettle and Fenn, 1979; Ahmad et al., 2010) are an oversimplified representation of the atmospheric aerosols. Moreover, deriving aerosol properties from ocean colour bands may result in significant inaccuracies. Including data from external sources to determine the aerosol reflectance may reduce such inaccuracies and, subsequently, improve $\rho_w(\lambda)$ retrievals (Julie Letertre at LOA, personal communication). For the MODIS Aqua images, for instance, one should investigate if MODIS Atmosphere products may be used (`http://modis-atmos.gsfc.nasa.gov/`) for the AC.

- Should the level-2 flags and masks be modified?

  In this work, the difficulty to ensure reliable Rayleigh-corrected $\rho(\lambda)$ retrievals was briefly illustrated in the last chapter. Indeed, to avoid pixel flagging over extremely turbid waters, the default cloud mask was modified (i.e., a SWIR-based cloud mask was used) and the ‘sensor saturation’ flag was not considered. However, this also includes the possible consideration of pixels where the precision of the sensor signal is not sufficient to ensure accurate AC. Hence, to further improve satellite $\rho_w(\lambda)$ retrievals over very and extremely turbid waters, more work is required to investigate the L2-processing flags and masks and to improve the accuracy of Rayleigh-corrected $\rho(\lambda)$ spectra.

If this Ph.D. project could be drawn out, these perspectives will be further investigated.

To conclude, I hope that the results of the validation exercises, class-specific evaluations and sensitivity studies conducted in this studies as well as the suggested improvements for the STD and MUMM NIR-modelling schemes will be helpful for the ocean optics community to aid movements towards better radiometric accuracy and to provide global marine parameters for the scientific community.

List of Figures

List of Tables

Bibliography

Ahmad, Z., F., B., McClain, C. R., Kwiatkowska, E. J., Werdell, P. J., Shettle, E. P., Shettle, E. P., and Holben, B. N. (2010). New aerosol models for the retrieval of aerosol optical thickness and normalized water-leaving radiances from the SeaWiFS and MODIS sensors over coastal regions and open oceans. *Applied Optics*, 49:5545–5560. 18, 25, 53, 162

Ahn, J., Park, Y., Ryu, J., Lee, B., and Oh, I. S. (2012). Development of Atmospheric Correction Algorithm for Geostationary Ocean Color Imager (GOCI). *Ocean Science Journal*, 47(3):247–259. 75

Aiken, J. and Moore, G. (2000). ATBD Case 2 bright pixel atmospheric correction. In *Report PO-TN-MEL-GS-0005, Vol. 4*, page 14, Centre for coastal and marine sciences, Plymouth Marine Laboratory, U.K. 22, 54

Arellano, A., Cao, N. B. F., Chase, A., Chen, H., Dave, A., Freitas, F. H., Goyens, C., Kearney, C., Kheireddine, M., Mishra, S., Neeley, A., Omand, M., Powers, L., Reisinger, A., Rivero, S., Russell, B., Seegers, B., Vandermeulen, R., and Zhu, W. (2011). *Portfolio of Measurement, Processing, and Analysis Techniques for Optical Oceanography Data*. Ocean Optics Summer School, Calibration and Validation for Ocean Color Remote Sensing, University of Maine Darling Marine Center, 11-29 July 2011. `ftp://misclab.umeoce.maine.edu/users/optics/classFTP/Portfolio/`. 3, 31, 49

Arnone, R. A., Matinolich, P., Gould, R. W., Stumpf, R., and Ladner, S. (1998). Coastal optical properties using SeaWiFS. In *SPIE proceedings Ocean Optics XIV*, Kailua-Kona, Hawaii. 3, 22, 159

Austin, R. W. (1980). Gulf of Mexico, ocean-colour surface-truth measurements. *Boundary-Layer Meteorology*, 18:269–285. 9

Austin, R. W. and Petzold, T. (1980). The determination of the diffuse attenuation coefficient of sea water using the coastal zone color scanner. In Gower, J. F. R., editor, *Oceanography from Space*, pages 239–256, Plenum Publishing Corporation, New York. 75, 77

Babin, M. (2000). COAstal Surveillance Through Observation of Ocean Colour (COAST-LOOC). In *Final Report, Project ENV4-CT96-0310*, Laboratoire de Physique et Chimie Marines, Villefranche-sur-mer, France. 30

Babin, M. and Stramski, D. (2002). Light absorption by aquatic particles in the near-infrared spectral region. *Limnology and Oceanography*, 47(3):911–915. 82

Bailey, S. and Wang, M. (2001). Satellite aerosol optical thickness match-up procedures. In Fargion, G. S., Barnes, R., and McClain, C., editors, *NASA/TM-2001-209982*, pages 70–73, NASA Goddard Space Flight Center, Greenbelt, Maryland. 52

Bailey, S. W., Franz, B. A., and Werdell, P. J. (2010). Estimations of near-infrared water-leaving reflectance for satellite ocean color data processing. *Optics Express*, 18(7):7521–7527. 3, 20, 22, 24, 25, 26, 53, 75, 88, 159, 163

Bailey, S. W. and Werdell, P. J. (2006). A multi-sensor approach for the on-orbit validation of ocean color satellite data products. *Remote Sensing of Environment*, 102:12–23. 43, 51, 52

Banzon, V. F., Evans, R. E., Gordon, H. R., and Chomko, R. M. (2004). SeaWiFS observation of the Arabian Sea southwest monsoon bloom for the year 2000. *Dea-Sea Research*, 51:189–208. 24

Banzon, V. F., Gordon, H. R., Kuchinke, C. P., Antoine, D., Voss, K. J., and Evans, R. E. (2009). Validation of SeaWiFS dust-correction methodology in the Mediterranean Sea: Identification of an algorithm-switching criterion. *Remote Sensing of Environments*, 113:2689–2700. 3, 54

Behrenfeld, M. J., O'Malley, R. T., Siegel, D. A., McClain, C. R., Sarmiento, J. L., Feldman, G. C., Milligan, A. J., Falkowski, P. G., Letelier, R. M., and Boss, E. S. (2006). Climate-driven trends in contemporary ocean productivity. *Nature*, 444:752–755. 1

Berthon, J.-F. and Zibordi, G. (2004). Bio-optical relationships for the northern Adriatic Sea. *International Journal of Remote Sensing*, 25:1527–1532. 36

Berwald, J., Stramski, D., Mobley, C. D., and Kiefer, D. A. (1998). Effect of Raman scattering on the average cosine and diffuse attenuation coefficient of irradiance in the ocean. *Limnology and Oceanography*, 43(4):564–576. 47

Brajard, J., Jamet, C., Moulin, C., and Thiria, S. (2006a). Use of neuro-variational inversion for retrieving oceanic and atmospheric constituents from satellite ocean color sensors: Application to absorbing aerosols. *Neural Networks*, 19:178–185. 3, 24, 159

Brajard, J., Jamet, C., Moulin, C., and Thiria, S. (2006b). Validation of a neuro-variational inversion of ocean colour images. *Advances in Space Research*, 38(10):2169–2175. 24

Brajard, J., Santer, R., Crépon, M., and Thiria, S. (2012). Atmospheric correction of MERIS data for case-2 waters using a neuro-variational inversion. *Remote Sensing of Environment*, 126:52–61. 3, 20, 24, 159

Bricaud, A. and Morel, A. (1987). Atmospheric corrections and interpretation of marine radiances in CZCS imagery: Use of a reflectance model. *Oceanologica Acta*, pages 33–50. 12, 75, 77

Bricaud, A., Morel, A., Babin, M., Allali, K., and Claustre, H. (1998). Variations of light absorption by suspended particles with chlorophyll a concentration in oceanic (case 1) waters: analysis and implications for bio-optical models. *Journal of Geophysical Research*, 103:31 033–31 044. 30

Briggs, N., Chen, H., Dave, A., Freitas, F. H., Goyens, C., Kearney, C., Powers, L., Rivero, S., and Vandermeulen, R. (2011). Hyperspectral radiometers. In *Arellano et al., Portfolio of Measurement, Processing, and Analysis Techniques for Optical Oceanography Data*, pages 116–161, Ocean Optics Summer School, Calibration and Validation for Ocean Color Remote Sensing, University of Maine Darling Marine Center, 11-29 July 2011. `ftp://misclab.umeoce.maine.edu/users/optics/classFTP/Portfolio/`. 49

Chomko, R. M. and Gordon, H. R. (1998). Atmospheric correction of ocean color imagery: use of Junge power-law aerosol size distribution with variable refractive index to handle aerosol absorption. *Applied Optics*, 37:5560–5572. 3, 24, 159

Chomko, R. M., Gordon, H. R., Maritorena, S., and Siegel, D. A. (2003). Simultaneous retrieval of oceanic and atmospheric parameters for ocean color imagery by spectral optimization: A validation. *Remote Sensing of Environment*, 84:208–220. 3, 24, 159

Cox, C. and Munk, W. (1954). Measurements of the roughness of the sea surface from photographs of the sun's glitter. *Journal of Optical Society of America*, 44:838–850. 16

Cui, T. W., Song, Q. J., Tang, J. W., and Zhang, J. (2013). Spectra variability of sea surface skylight reflectance in its effect on ocean color. *Optics Express*, 21(21):24929–24941. 34

D'Alimonte, D., Mélin, F., Zibordi, G., and Berthon, J.-F. (2003). Use of the novelty detection technique to identify the range of applicability of the empirical ocean color algorithms. *IEEE Transactions on Geoscience and Remote Sensing*, 41:2833–2843. 12, 13, 58

Doeffer, R. and Schiller, H. (2008). MERIS lake water algorithm for BEAM. In *Algorithm Technical Basis Document*, page 17, GKSS Forschungszentrum, Geesthacht, Germany. 3, 24, 159

Doerffer, R. and Schiller, H. (2007). The MERIS case 2 water algorithm. *International Journal of Remote Sensing*, 28(3):517–535. 3, 20, 24, 159

Dogliotti, A. I., Ruddick, K., Nechad, B., and Lasta, C. (2011). Improving water reflectance retrieval from MODIS imagery in the highly turbid waters of la plata river. In *Proceedings of VI International Conference 'Current Problems in Optics of Natural Waters*, St. Petersburg, Russia. 3, 29, 34, 54, 137

Doron, M., Bélanger, S., Doxoran, D., and Babin, M. (2011). Spectral variations in the near-infrared ocean reflectance. *Remote Sensing of Environment*, 115:1617–1631. 39, 54, 75, 80, 131, 160

Doxaran, D., Froidefond, J. M., and Castaing, P. (2003). Remote-Sensing reflectance of turbid sediment-dominated waters. Reduction of sediment type variations and changing illumination conditions effects by use of reflectance ratios. *Applied Optics*, 42(15):2623–2634. 11, 41, 80

Doxaran, D., Froidefond, J. M., Lavender, S. J., and Castaing, P. (2002). Spectral signature of highly turbid waters. Application with SPOT data to quantify suspended particulate matter concentrations. *Remote Sensing of Environment*, 81:149–161. 10, 80

Doyle, J. P. and Zibordi, G. (2002). Optical propagation within a three-dimensional shadowed atmosphere-ocean field: Application to large deployement structures. *Applied Optics*, 41:4283–4306. 34

Feng, H., Vandemark, D., Campbell, J. W., and Holben, B. N. (2008). Evaluation of MODIS ocean color products at a northeast United States coast site near the Martha's Vineyard Coastal Observatory. *International of Remote Sensing*, 29:4479–4497. 3, 36, 52, 53

Field, C. B., Behrenfeld, M. J., Randerson, J. T., and Falkowski, P. (1998). Primary production of the biosphere: Integrating terrestrial and oceanic components. *Science*, 281:237–240. 1

Franz, B. A., Bailey, S. W., Meister, G., and Werdell, P. J. (2012). Consistency of the NASA Ocean Color Data Record. In *Proceedings Ocean Optics 2012*, Glasgow, Scotland. 33, 53, 135

Franz, B. A., Bailey, S. W., Werdell, P. J., and McClain, C. R. (2007). Sensor-independent approach to the vicarious calibration of satellite ocean color radiometry. *Applied Optics*, 46(22):5068–5082. 33, 159

Franz, B. A., Werdell, P. J., Meister, G., Bailey, S. W., Eplee, R. E., Feldman, G. C., Kwiatkowska, E., McClain, C. R., Patt, F. S., and Thomas, D. (2005). The continuity of ocean color measurements from SeaWiFS to MODIS. In *Proceedings of SPIE. Earth Observing Systems X*, San Diego, US. 53

Franz, B. A., Werdell, P. J., Meister, G., Kwiatkowska, E. J., Bailey, S. W., Ahmad, Z., and McClain, C. R. (2006). MODIS land bands for ocean remote sensing applications. In *Proceedings Ocean Optics XVIII*, Montreal, Canada. 32, 34, 137, 169

Frouin, R., Schwindling, M., and Deschamps, P.-Y. (1996). Spectral reflectance of sea foam in the visible and near-infrared: In situ measurements and remote sensing implications. *Journal of Geophysical Research*, 101:14361–14371. 16

Fu, G., Baith, K. S., and McClain, C. R. (1998). SeaDAS: The SeaWiFS Data Analysis System. In *Proceedings of 'The 4th Pacific Ocean Remote Sensing Conference'*. 33

Garaba, S. P. and Zielinski, O. (2013). Comparison of remote sensing reflectance from above-water and in-water measurements west of Greenland, Labrador Sea, Denmark Strait, and west of Iceland. *Optics Express*, 21(13):15938–15950. 49

Gordon, H., Brown, O. J., and Jacobs, M. M. (1975). Computed relationships between the inherent and apparent optical properties of a flat, homogeneous ocean. *Applied Optics*, 14:417–427. 11

Gordon, H. R. (1978). Removal of atmospheric effects from satellite imagery of the oceans. *Applied Optics*, 17:1631–1636. 20

Gordon, H. R. (1997). Atmospheric correction of ocean color imagery in the Earth Observing System era. *Journal of Geophysical Research*, 102:17081–17106. 15, 16, 20, 21

Gordon, H. R., Brown, O. B., Evans, R. H., Brown, J. W., Smith, R. C., Baker, K. S., and Clark, D. K. (1988). A semi-analytical radiance model of ocean color. *Journal of Geophysical Research*, 93(10):909–924. 11, 24, 81

Gordon, H. R. and Clark, D. K. (1981). Clear water radiances for atmospheric correction of Coastal Zone Color Scanner imagery. *Applied Optics*, 20:4175–4180. 9

Gordon, H. R., Clark, D. K., Brown, J. W., Brown, O. B., Evans, R. H., and Broenkow, W. W. (1983). Phytoplankton pigment concentrations in the Middle Atlantic Bight: comparison between ship detreminations and Coastal Zone Color Scanner estimates. *Applied Optics*, 22:20–36. 20

Gordon, H. R. and Ding, K. (1992). Self-shading of in-water optical instruments. *Limnology and Oceanography*, 37:491–500. 45

Gordon, H. R., Ding, K., and Gong, W. (1993). Radiative transfer in the ocean: Computations relating to the asymptotic and near-asymptotic daylight field. *Applied Optics*, 32:1606–1619. 47

Gordon, H. R., Du, T., and Zhang, T. (1997). Remote sensing of ocean color and aerosol properties resolving the issue of aerosol absorption. *Applied Optics*, 36(33):8670–8684. 3, 24, 54, 159

Gordon, H. R. and Morel, A. (1983). *Remote Assessment of Ocean Color for Interpretation of Satellite Visible Imagery: A Review. Lecture Notes on Coastal and Estuarine Studies*, volume 4. Springer Verlag, New York, USA. 9, 11

Gordon, H. R. and Wang, M. (1994). Retrieval of water-leaving radiance and aerosol optical thickness over the oceans with SeaWiFS: A preliminary algorithm. *Applied Optics*, 33:443–452. 15, 18, 19, 20, 21, 22, 23, 27, 77, 94, 130, 159, 163, 169

Gould, R. W., Arnone, R. A., and Sydor, M. (2001). Absorption, scattering and remote-sensing reflectance relationships in coastal waters: Testing a new inversion algorithm. *Journal of Coastal Research*, 17:328–341. 34

Goyens, C., Jamet, C., and Ruddick, K. (2013a). Spectral relationship for atmospheric correction. I. validation of red and near infra-red spectral relationships. *Optics Express*, 21(18):21162–21175. 4, 75, 76, 77, 79, 80, 84, 94, 95, 128, 131, 133, 160, 161

Goyens, C., Jamet, C., and Ruddick, K. (2013b). Spectral relationship for atmospheric correction. II. improving the nasa standard and mumm atmospheric correction algorithms. *Optics Express*, 21(18):21176–21187. 4, 76, 77, 88, 92, 93, 94, 95, 96

Goyens, C., Jamet, C., and Schroeder, T. (2013c). Evaluation of four atmospheric correction algorithms for MODIS-Aqua images over contrasted coastal waters. *Remote Sensing of Environment*, 131:63–75. 3, 22, 53, 54, 55, 58, 59, 88, 125, 126, 127, 128, 132, 134, 135, 139

Hale, G. M. and Querry, M. R. (1973). Optical constants of water in the 200 nm to 200 mm wavelength region. *Applied Optics*, 12:555–563. 30

Holben, B. N., Eck, T. F., Slutsker, I., Tanré, D., Buis, J. P., Setzer, A., Vermote, E., Reagan, J. A., Kaufman, Y. J., Nakajima, T., Lavenu, F., Jankowiak, I., and Smirnov, A. (1998). AERONET - a federated instrument network and data archive for aerosol characterization. *Remote Sensing of Environment*, 66(1):1–16. 18, 35

Hooker, S. B., Esaias, W. E., Feldman, G. C., Gregg, W. W., and McClain, C. R. (1992). An overview of SeaWiFS and ocean color. In Hooker, S. B. and Firestone, E. R., editors, *NASA/TM-1992-104566*, page 24, NASA Goddard Space Flight Centre, Greenbelt, Maryland. 159

Hooker, S. B., Lazin, G., Zibordi, G., and McLean, S. (2002). An evaluation of above- and in-water methods for determining water-leaving radiances. *Journal of Atmospheric and Oceanic Technology*, 19:486–515. 34, 35, 159

Hooker, S. B. and Maritorena, S. (2000). An evaluation of oceanographic radiometers and deployment methodologies. *Journal of Atmospheric and Oceanic Technology*, 17(6):811–830. 49

Hooker, S. B., McClain, C. R., and Mannino, A. (2007). NASA Strategic Planning Document: A comprehensive plan for the long-term calibration and validation of oceanic biogeochemical satellite data. In *NASA Special Pub. 2007-214152*, page 31, NASA Goddard Space Flight Center, Greenbelt, Maryland. 34

Hooker, S. B. and Morel, A. (2003). Platform and environmental effects on above- and in-water determinations of water-leaving radiances. *Journal of Atmospheric and Oceanic Technology*, 20:187–205. 34

Hu, C., Carder, K. L., and Muller-Krager, F. E. (2000). Atmospheric correction of SeaWiFS imagery over turbid coastal waters: A practical method. *Remote Sensing of Environment*, 74:195–206. 22, 29

IOCCG (2000). Remote sensing of ocean colour in coastal, and other optically-complex waters. In Sathyendranath, S., editor, *Reports of the International Ocean-Colour Coordinating Group, No. 5, IOCCG*, page 140, Dartmouth, Canada. 20

IOCCG (2006). Remote Sensing of Inherent Optical Properties: Fundamentals, Tests of Algorithms, and Applications. In Lee, Z., editor, *Reports of the International Ocean-Colour Coordinating Group, No. 5, IOCCG*, page 128, Dartmouth, Canada. 83, 86, 94, 96

IOCCG (2010). Atmospheric correction for remotely-sensed ocean-colour products. In Wang, M., editor, *Reports of the International Ocean-Colour Coordinating Group, No. 10, IOCCG*, page 83, Dartmouth, Canada. 16, 159

Jamet, C., Loisel, H., Kuchinke, C. P., Ruddick, K., Zibordi, G., and Feng, H. (2011). Comparison of three SeaWiFS atmospheric correction algorithms for turbid waters using AERONET-OC measurements. *Remote Sensing of Environment*, 115(8):1955–1965. 3, 51, 52, 54

Jamet, C., Thiria, S., Moulin, C., and Crépon, M. (2005). Use of a neurovariational inversion for retrieving oceanic and atmospheric constituents from ocean color imagery: A feasibility study. *Journal of Atmospheric and Oceanic Technology*, 22:460–475. 3, 24, 159

Jerlov, N. G. (1951). Optical studies of ocean water. *Rep. Swedish Deep-Sea Expedition*, 3:1–59. 12

Knaeps, E., Raymaekers, D., Sterckx, S., Ruddick, K., and Dogliotti, A. I. (2012). In-situ evidence of non-zero reflectance in the OCLI 1020 nm band for a turbid estuary. *Remote Sensing of Environment*, 120:133–144. 30

Kou, L., Labrie, D., and Chylek, P. (1993). Refractive indices of water and ice in the 0.65 mm to 2.5 mm spectral range. *Applied Optics*, 32:3531–3540. 25, 83

Kuchinke, C. P., Gordon, H. R., and Franz, B. A. (2009a). Spectral optimization for constituent retrieval in Case 2 waters I: Implementation and performance. *Remote Sensing of Environment*, 113(3):571–587. 3, 20, 24, 54, 159

Kuchinke, C. P., Gordon, H. R., Harding, L. W., and Voss, K. J. (2009b). Spectral optimization for constituent retrieval in Case 2 waters II: Validation study in the Chesapeake Bay. *Remote Sensing of Environment*, 113:610–621. 3, 159

Lavender, S. J., Pinkerton, M. H., Moore, G. F., Aiken, J., and Blondeau-Patissier, D. (2005). Modification to the atmospheric correction of SeaWiFS ocean colour images over turbid waters. *Continental Shelf Research*, 25:539–555. 22

Leathers, R. A. and Downes, T. V. (2004). Self-shading correction for oceanographic upwelling radiometers. *Optics Express*, 12:4709–4718. 45

Lee, Z., Ahn, Y.-H., Mobley, C., and Arnone, R. A. (2010a). Removal of surface-reflected light for the measurement of remote sensing reflectance from an above-surface platform. *Optics Express*, 18(25):26313–26324. 34

Lee, Z., Carder, K. L., and Arnone, R. A. (2002). Deriving inherent optical properties from water color: a multiband quasi-analytical algorithm for optically deep waters. *Applied Optics*, 41(27):5755–5772. 11

Lee, Z., Lubac, B., Werdell, J., and Arnone, R. (2009). An update of the Quasi-Analytical Algorithm, QAA v.5. `http://www.ioccg.org/groups/Software_OCA/QAA_v5.pdf`. 77, 84, 95, 160

Lee, Z., R. A. Arnone, C. H., Werdell, P. J., and Lubac, B. (2010b). Uncertainties of optical parameters and their propagations in an analytical ocean color inversion algorithm. *Applied Optics*, 49(3):369–381. 25, 27, 80

Lee, Z. P., Carder, K. L., Mobley, C. D., Steward, R. G., and Patch, J. S. (1998a). Hyperspectral remote sensing for shallow waters: 1. A semianalytical model. *Applied Optics*, 37(27):6329–6338. 10, 11

Lee, Z. P., Carder, K. L., Mobley, C. D., Steward, R. G., and Patch, J. S. (1998b). Hyperspectral remote sensing for shallow waters: 2. Deriving bottom depths and water properties by optimization. *Applied Optics*, 38(18):3831–3843. 11

Loisel, H., Lubac, B., Dessailly, D., Duforet-Gaurier, L., and Vantrepotte, V. (2010). Effect of inherent optical properties variability on the chlorophyll retrieval from ocean color remote sensing: an in situ approach. *Optics Express*, 18(20):20949–20952. 12

Loisel, H., Mériaux, X., Poteau, A., Artigas, L., Lubac, B., Gardel, A., Caillaud, J., and Lesourd, S. (2009). Analyze of inherent optical properties of French Guiana coastal waters for remote sensing applications. *Journal of Coastal Research*, SI 56:1532–1536. 37, 45

Loisel, H. and Morel, A. (2001). Non-isotropy of the upward radiance field in typical coastal (Case 2) waters. *International Journal of Remote Sensing*, 22(2-3):275–295. 11, 12, 80, 81

Loisel, H., Nicolas, J.-M., Sciandra, A., Stramski, D., and Poteau, A. (2006). Spectral dependency of optical backscattering by marine particles from satellite remote sensing of the global ocean. *Journal of Geophysical Research*, 111:C09024:1–14. 25, 80

Loisel, H. and Stramski, D. (2000). Estimation of the inherent optical properties of natural waters from the irradiance attenuation coefficient and reflectance in the presence of Raman scattering. *Applied Optics*, 39(18):3001–3011. 7

Lubac, B. and Loisel, H. (2007). Variability and classification of remote sensing reflectance spectra in the eastern English Channel and southern North Sea. *Remote Sensing of Environment*, 110:45–58. 6, 12, 45, 59

McClain, C. R., Ainsworth, E. J., Barnes, R. A., Eplee, R. E., Patt, F. S., Robinson, W. D., Wang, M., and Bailey, S. W. (2000). SeaWiFS Postlaunch Technical Report Series. In *NASA/TM-2000-206892*, volume 11, page 82, Greenbelt, Maryland, NASA Goddard Space Flight Center. 18, 22, 163

Meister, G., Franz, B. A., Kwiatkozska, E. J., and McClain, C. R. (2012). Corrections to the calibration of MODIS Aqua Ocean Color Bands Derived from SeaWiFS data. *IEEE Transactions on Geoscience and Remote Sensing*, 50(1):310–319. 32

Mélin, F., Berthon, J. F., and Zibordi, G. (2005). Assessment of apparent and inherent optical properties derived from SeaWiFS with field data. *Remote Sensing of the Environment*, 97:540–553. 3

Mélin, F., Vantrepotte, V., Clerici, M., D'Alimonte, D., Zibordi, G., Berthon, J. F., and Canuti, E. (2011). Multi-sensor satellite time series of optical properties and chlorophyll-a concentration in the Adriatic Sea. *Progress in Oceanography*, 91:229–244. 3, 13, 52, 53, 58

Mélin, F., Zibordi, G., and Berthon, J. F. (2007). Assessment of satellite ocean color products at a coastal site. *Remote Sensing of Environment*, 110:192–215. 3, 36, 53

Mélin, F., Zibordi, G., Carlund, T., Holben, B. N., and Stefan, S. (2013). Validation of SeaWiFS and MODIS Aqua/Terra aerosol products in coastal regions of European marginal seas. *Oceanologia*, 55(1):27–51. 3, 53

Mie, G. (1908). Beiträge zur optik trüber medien, speziell kolloidalre metallösungen. *Annalen der Physik, (Leipzig)*, 330:377–445. 18

Mobley, C. D. (1989). A numerical model for the computation of radiance distributions in natural waters with wind-roughened surfaces. *Limnology and Oceanography*, 34(8):1473–1483. 10, 12, 50

Mobley, C. D. (1994). *Light and Water: Radiative Transfer in Natural Waters*. Academic Press, San Diego, California, USA. 6, 18

Mobley, C. D. (1999). Estimation of remote-sensing reflectance from above-surface measurements. *Applied Optics*, 38:7442–7455. 9, 34, 38, 39, 41

Mobley, C. D., Boss, E., and Roesler, C. (2011). Ocean optics web book. `http://www.oceanopticsbook.info/`. 6, 7, 8, 18, 19, 163

Mobley, C. D., Stramski, D., Bissett, W. P., and Boss, E. (2004). Optical modeling of ocean waters: Is the case 1-case 2 classification still useful? *Oceanography*, 17(2):60–67. 12

Mobley, C. D. and Sundman, L. K. (2008). HydroLight 5 - EcoLight 5 Users Guide (2008). 10, 12, 50

Moore, G. F., Aiken, J., and Lavender, S. J. (1999). The atmospheric correction of water colour and the quantitative retrieval of suspended particulate matter in Case II waters: Application to MERIS. *International Journal of Remote Sensing*, 20:1713–1733. 3, 20, 22, 159

Moore, T. S., Campbell, J., and Dowell, M. D. (2009). A class-based approach for characterizing the uncertainty of the MODIS chlorophyll product. *Remote Sensing of Environment*, 113:2424–2430. 6, 12

Moore, T. S., Campbell, J. W., and Feng, H. (2001). A fuzzy logic classification scheme for selecting and blending satellite ocean color algorithms. *IEEE Transactions on Geoscience and Remote Sensing*, 39(8):1764–1776. 6, 12

Morel, A. (1974). Optical properties of pure water and sea water. In Jerlov, N. G. and Nielsen, E. S., editors, *Optical Aspects of Oceanography*, pages 1–24, New York, Academic Press. 30

Morel, A., Antoine, D., and Gentili, B. (2002). Bidirectional reflectance of oceanic waters: Accounting for Raman emission and varying particle phase function. *Applied Optics*, 41:6289–6306. 9, 11, 35, 80, 81, 83

Morel, A. and Belanger, S. (2006). Improved detection of turbid waters from ocean color sensors information. *Remote Sensing of Environment*, 102:237–249. 12

Morel, A. and Gentili, B. (1996). Diffuse reflectance of oceanic waters. III: Implication of bidirectionality for the remote-sensing problem. *Applied Optics*, 35:4850–4862. 9, 10, 11, 25, 35, 80, 81

Morel, A. and Gentili, B. (2004). Radiation transport within oceanic (case 1) water. *Journal of Geophysical Research*, 109:C06008:1–22. 47

Morel, A. and Maritorena, S. (2001). Bio-optical properties of oceanic waters : a reappraisal. *Journal of Geophysiscal Research*, 106(C4):7163–7180. 48

Morel, A. and Prieur, L. (1977). Analysis of variations in Ocean Color. *Limnology and Oceanography*, 22(4):709–722. 11, 12

Moses, W. J., Gitelson, A. A., Berdnikov, S., and Povazhnny, V. (2009). Estimation of chlorophyll-a concentration in case II waters using MODIS and MERIS data. Successes and challenges. *Environmental Research Letters*, 4:045005. 54

Moulin, C., Gordon, H. R., Banzon, V. F., and Evans, R. H. (2001a). Assessment of Saharan dust absorption in the visible from SeaWiFS imagery. *Journal of Geophysical Research*, 106:18239–18249. 24

Moulin, C., Gordon, H. R., Banzon, V. F., and Evans, R. H. (2001b). Assessment of Saharan dust absorption in the visible from SeaWiFS imagery. *Journal of Geophysical Research*, 106(18):239–249. 24

Moulin, C., Gordon, H. R., Chomko, R. M., Banzon, V. F., and Evans, R. H. (2001c). Atmospheric correction of ocean color imagery through thick layers of Saharan dust. *Geophysical Research Letters*, 28:5–8. 24

Mueller, J. and Austin, R. W. (2003). Characterization of oceanographic and atmospheric radiometers. In Mueller, J. L., Fargion, G. S., and McClain, C. R., editors, *NASA/TM-2003-21621, rev4-vol2*, pages 17–33, Greenbelt, Maryland, NASA Goddard Space Flight Center. 44

Mueller, J. L. (2003). In-water radiometric profile measurements and data analysis protocols. In Mueller, J. L., Fargion, G. S., and McClain, C. R., editors, *NASA/TM-2003-211621, Rev4-vol3*, pages 87–97, NASA Goddard Space Flight Center, Greenbelt, Maryland. 45

Mueller, J. L. and Austin, R. W. (1995). Volume 25 of Ocean Optics Protocols for SeaWiFS validation, Revision 1. In Hooker, S. B., Firestone, E., and Acker, J. G., editors, *NASA/TM-1995-104566*, Greenbelt, Maryland, NASA Goddard Space Flight Center. 39

Mueller, J. L., Johnson, B. C., Cromer, C. L., Hooker, S., McLean, J., and Biggar, S. F. (1996). The Third SeaWiFS Intercalibration Round-Robin Experiment (SIRREX-3), 19-30 September 1994. In Hooker, S. B., Firestone, E. R., and Acker, J. G., editors, *NASA/TM-1996-104566, vol34*. 43, 49

Mueller, J. L., Morel, A., Frouin, R., Davis, C., Arnone, R., Carder, K., Lee, Z. P., Steward, R., Hooker, S., Mobley, C. D., McLean, S., Holben, B., Miller, M., Pietras, C., Knobelspiesse, K. D., Fargion, G. S., Porter, J., and Voss, K. (2003). Ocean Optics Protocols For Satellite Ocean Color Sensor Validation: Instrument Specifications, Characterization and Calibration. In Mueller, J. L., Fargion, G. S., and McClain, C. R., editors, *NASA/TM-2003-211621, Rev4-vol3*, page 84. 34, 43

Nechad, B., Ruddick, K., and Park, Y. (2010). Calibration and validation of a generic multi-sensor algorithm for mapping of total suspended matter in turbid waters. *Remote Sensing of Environment*, 114:854–866. 37

Nellemann, C., Corcoran, E., Duarte, C. M., Valdes, L., Young, C. D., Fonseca, L., and Grimsditch, G. (2009). Blue carbon. A Rapid Response Assessment. `www.grida.no/files/publications/blue-carbon/BlueCarbon_screen.pdf`. 1

Neukermans, G., Ruddick, K., Bernard, E., Ramon, D., Nechad, B., and Deschamps, P.-Y. (2009). Mapping total suspended matter from geostationary satellites: a feasibility study with SEVIRI in the Southern North Sea. *Optics Express*, 17(16):14029–14052. 54

Nicolas, J. M., Deschamps, P. Y., Loisel, H., and Moulin, C. (2005). POLDER-2:Ocean Color Atmospheric Correction Algorithms. In *Algorithm Theoretical Basis Document*, page 17, Laboratoire d'Optique Atmosphérique (LOA), Lille, France. 75

Nobileau, D. and Antoine, D. (2005). Detection of blue-absorbing aerosols using near infrared and visible (ocean color) remote sensing observations. *Remote Sensing of Environment*, 95:368–387. 24

Nordkvist, K., Loisel, H., and Duforêt-Gaurier, L. (2009). Cloud masking of SeaWiFS images over coastal waters using spectral variability. *Optics Express*, 17(15):12246–12258. 34

Ohde, T. and Siegel, H. (2003). Derivation of immersion factors for the hyperspectral TriOS radiance sensor. *Journal of Optics, Pure and Applied Optics*, 5:12–14. 44

O'Reilly, J. E., Maritorena, S., O'Brien, M. C., Siegel, D., Toole, D., Menzies, D., Smith, R. C., Mueller, J. L., Mitchell, B. G., Kahru, M., Chavez, F. P., Strutton, P., Cota, G. E., Hooker, S. B., McClain, C. R., Carder, K. L., and et al. (2000). Ocean color chlorophyll a algorithms for SeaWiFS, OC2, and OC4: Version 4. In O'Reilly, J. E., editor, *NASA/TM-2000-206892*, volume 11, pages 9–23, Greenbelt, Maryland, NASA Goddard Space Flight Center. 25

Pegau, W. S., Gray, D., and Zaneveld, J. R. V. (1997). Absorption and attenuation of visible and near-infrared light in water: dependence on temperature and salinity. *Applied Optics*, 36(24):6035–6046. 27

Pope, R. M. and Fry, E. S. (1997). Absorption spectrum (380:700 nm) of pure water. II. Integrating cavity measurements. *Applied Optics*, 36(33):8710–8723. 25, 30, 50, 83

Preisendorfer, R. W. (1961). Application of radiative transfer theory to light measurements in the sea. *IUGG Monography, Paris*, 10:11–30. 6

Reynolds, R. A., Stramski, D., and Mitchell, B. G. (2001). A chlorophyll dependent semi analytical reflectance model derived from field measurements of absorption and backscattering coefficients within the Southern Ocean. *Journal of Geophysical Research*, 106:C4:7125–7138. 80

Robinson, W. D., Franz, B. A., Patt, F. S., Bailey, S. W., and Werdell, P. J. (2003). Masks and flags updates. In *S. B. Hooker and E. R. Firestone (Eds.), SeaWiFS Postlaunch Technical Report Series, Chap.6, NASA/TM-2003-206892*, volume 22, pages 34–40, Greenbelt, Maryland, NASA Goddard Space Flight Center. 52, 55, 126

Ruddick, K., Cauwer, V. D., and Mol, B. V. (2005). Use of the near infrared similarity relfectance spectrum for the quality control of remote sensing data. *Proc. SPIE 5885, 588501*. 39

Ruddick, K., Cauwer, V. D., Park, Y., and Moore, G. (2006). Seaborne measurements of near infrared water-leaving reflectance: The similarity spectrum for turbid waters. *Limnology and Oceanography*, 51(2):1167–1179. 3, 11, 20, 22, 27, 28, 29, 34, 37, 38, 39, 40, 54, 75, 77, 80, 83, 93, 159, 160, 163

Ruddick, K., Ovidio, F., and Rijkeboer, M. (2000). Atmospheric correction of SeaWiFS imagery for turbid coastal and inland waters. *Applied Optics*, 39:897–912. 3, 20, 22, 27, 28, 39, 53, 75, 77, 80, 93, 159, 160, 163

Rudorff, N. D. M., Frouin, R., Kampel, M., Goyens, C., Meriaux, X., and Schieber, B. (2013). Assesing accurate ocean colour in situ radiometry across the southern Atlantic and southeastern Pacific. *Submitted to Remote Sensing of Environment*. 3, 31, 34, 35, 39, 43, 44, 45, 47, 48, 49

Sayer, A. M., Smirnov, A., Hsu, N. C., and Holben, B. N. (2012). A pure marine aerosol model, for use in remote sensing applications. *Journal of Geophysical Research*, 117:D05213. 17, 163

Schroeder, T., Behnert, I., Schaale, M., Fischer, J., and Doerffer, R. (2007). Atmospheric correction algorithm for MERIS above case-2 waters. *International Journal of Remote Sensing*, 28(7):1469–1486. 3, 20, 24, 30, 52, 53, 54, 159

Shanmugam, P. (2012). CAAS: An atmospheric correction algorithm for the remote sensing of complex waters. *Annales Geophysicae*, 30:203–220. 20

Shettle, E. P. and Fenn, R. W. (1979). Models for the aerosols of the lower atmosphere and the effects of humidity variations on their optical properties. AFGL-TR 790214, U. S. Air Force Laboratory, Hanscom Air Force Base, Mass. 17, 18, 21, 30, 77, 94, 162, 169

Shi, W. and Wang, M. (2007). Detection of turbid waters and absorbing aerosols for the MODIS ocean color data processing. *Remote Sensing of Environment*, 110:149–161. 29

Shi, W. and Wang, M. (2009). An assessment of the black ocean pixel assumption for MODIS SWIR bands. *Remote Sensing of Environment*, 113:1587–1597. 30, 53, 80, 160

Siegel, D. A., Maritorena, S., Nelson, N. B., and Behrenfeld, M. J. (2005a). Independence and interdependencies of global ocean color properties: Reassessing the bio-optical assumption. *Journal of Geophysical Research*, 110:C07011. 12

Siegel, D. A., Maritorena, S., Nelson, N. B., and McClain, M. J. B. C. R. (2005b). Colored dissoleved organic matter and its influence on the satellite-based characterization of the ocean biosphere. *Geophysical Research Letters*, 32:L20605. 12

Siegel, D. A., Wang, M., Maritorena, S., and Robinson, W. (2000). Atmospheric correction of satellite ocean color imagery: The black pixel assumption. *Applied Optics*, 39(21):3582–3591. 2, 3, 20, 22, 37, 76, 159

Smith, R. C. and Baker, K. S. (1981). Optical properties of the clearest natural waters (200-800 nm). *Applied Optics*, 20(2):177–184. 25, 45

Smith, R. C. and Wilson, W. H. (1980). Ship and satellite bio-optical research in the Calofornia Bight. In Gower, J. F. R., editor, *Oceanography from Space*, pages 281–294, Plenum Publishing Corporation, New York. 75, 76

Stramska, M., Stramski, D., Hapter, R., Kaczmarek, S., and Ston, J. (2003). Bio-optical relationships and ocean color algorithms for the north polar region of the Atlantic. *Journal of Geophysical Research*, 108:C73239: 1–17. 80

Stumpf, R. P., Arnone, R. A., Gould, R. W., and Ransibrahmanakul, V. (2003). A partially coupled ocean-atmosphere model for retrieval of water-leaving radiance from SeaWiFS in coastal waters. In Hooker, S. B. and Firestone, E. R., editors, *NASA/TM-2003-206892*, volume 22, pages 51–59, Greenbelt, Maryland, NASA Goddard Space Flight Center. 3, 20, 22, 24, 53, 75, 159

Sturm, B. (1981). The atmospheric correction of remotely sensed data and the quantitative determination of suspended matter in marine water surface layers. In Cracknel, A. P., editor, *Remote Sensing in Meteorology, Oceanography and Hydrology*, pages 163–197, Chister, UK: Ellis Horwood. 75, 77

Sturm, B. (1983). Selected topics of coastal zone color scanner (CZCS) data evaluation. In Cracknel, A. P., editor, *Remote Sensing in Meteorology, Oceanography and Hydrology*, pages 137–168, Dordrecht, The Netherlands: D. Reidel. 75, 77

Sturm, B., Barale, V., Larkin, D., Andersen, J. H., and Turner, M. (1999). OCEANcode: the complete set of algorithms and models for the level 2 processing of European CZCS historical data. *International Journal of Remote Sensing*, (20(7)):1219–1248. 77

Sun, J., Xiong, X., Barnes, W. L., and Guenther, B. (2007). MODIS reflective solar bands on-orbit lunar calibration. *IEEE Transactions on Geoscience and Remote Sensing*, 45(7):2383–2393. 32

Sydor, M., Gould, R. W., Arnone, R. A., Haltrin, V. I., and Goode, W. (2004). Uniqueness in remote sensing of the inherent optical properties of ocean water. *Applied Optics*, 43(10):2156–2162. 29

Thieuleux, F., Moulin, C., Bréon, F. M., Maignan, F., Poitou, J., and Tanré, D. (2005). Remote Sensing of aerosols over oceans using MSG/SEVIRI. *Annales Geophysicae*, 23:1–8. 21

Toole, D. A., Siegel, D. A., Menzies, D. W., Neumann, M. J., and Smith, R. C. (2000). Remote-sensing reflectance determinations in the coastal ocean environment: impact of instrumental characteristics and environmental variability. *Applied Optics*, 39:456–469. 34, 39, 41, 43, 49

Vantrepotte, V., Loisel, H., Dessailly, D., and Mériaux, X. (2012). Optical classification of contrasted coastal waters. *Remote Sensing of Environment*, 123:306–323. 3, 6, 12, 13, 14, 54, 55, 56, 58, 59, 60, 125, 126, 137, 138, 159, 163, 170

Vantrepotte, V., Loisel, H., Mériaux, X., Neukermans, G., Dessailly, D., Jamet, C., Gensac, E., and Gardel, A. (2011). Seasonal and inter-annual (2002-2010) variability of the suspended particulate matter as retrieved from satellite ocean color sensors over the French Guiana coastal waters. *Journal of Coastal Research*, SI64:1750–1754. 37, 45

Viollier, M. and Sturm, B. (1984). CZCS data analysis in turbid coastal water. *Journal of Geophysical Research*, 89:4977–4985. 75, 77

Wang, M. (1999). Atmospheric correction of ocean color sensors: computing atmospheric diffuse transmittance. *Applied Optics*, 38(3):451–455. 15

Wang, M. (2007). Remote sensing of the ocean contributions from ultraviolet to near infrared using shortwave infrared bands: simulations. *Applied Optics*, 46:1535–1547. 22, 29

Wang, M. and Shi, W. (2005). Estimation of ocean contribution at the MODIS near infrared wavelengths along the east coast of the U.S.: Two case studies. *Geophysical Research Letters*, 32:L13606. 3, 22, 159

Wang, M. and Shi, W. (2006). Cloud masking for ocean color data processing in the coastal regions. *IEEE Transactions on Geoscience and Remote Sensing*, 44(11):3196–3205. 34, 137

Wang, M. and Shi, W. (2007). The NIR-SWIR combined atmospheric correction approach for MODIS ocean color data processing. *Optics Express*, 15:15722–15733. 3, 22, 29, 53, 159

Wang, M., Shi, W., and Jiang, L. (2012). Atmospheric correction using near-infrared bands for satellite ocean color data processing in the turbid western Pacific region. *Optics Express*, 20(2):741–753. 20, 22, 75, 76, 77, 79, 82, 83, 84, 93, 94, 95, 96, 125, 160, 165

Wang, M., Son, S., and Shi, W. (2009). Evaluation of MODIS SWIR and NIR-SWIR atmospheric correction algorithms using SeaBASS data. *Remote Sensing of Environment*, 113:635–644. 3, 20, 24, 29, 53, 54, 76, 159

Werdell, P. J. and Bailey, S. W. (2005). An improved in-situ bio-optical data set for ocean color algorithm development and satellite data product validation. *Remote Sensing of Environment*, 98(1):122–140. 25, 27, 53

Werdell, P. J., Franz, B. A., and Bailey, S. W. (2010). Evaluation of shortwave infrared atmospheric correction for ocean color remote sensing of Chesapeake bay. *Remote Sensing of Environment*, 114:2238–2247. 30, 53, 54, 57

Wolfe, R. E., Nishihama, M., Fleig, A., Kuyper, J. A., Roy, D. P., Storey, J. C., and et al. (2002). Achieving sub-pixel geolocation accuracy in support of MODIS land pixel. *Remote Sensing of Environment*, 83:31–49. 51

Wozniak, S. B., Stramski, D., Stramska, M., Reynolds, R., Wright, V., Miksic, E., Cichocka, M., and Cieplak, A. (2010). Optical variability in relation to particle concentration composition and size distribution in the near-shore marine environment at Imperial Beach California. *Journal of Geophysical Research*, 115(C08027):doi:10.1029/2009JC005554. 12

Xiong, X., Sun, J., Xie, X., Barnes, W. L., and Salomonson, V. V. (2010). On-orbit calibration and performance of Aqua MODIS reflective solar bands. *IEEE Transactions on Geoscience and Remote Sensing*, 48(1):535–546. 32

Yang, H. and Gordon, H. R. (1997). Remote sensing of ocean color: assessment of water-leaving radiance bidirectional effects on atmospheric diffuse transmittance. *Applied Optics*, 36:7887–7897. 16

Zhang, T., Fell, F., and Fisher, J. (2002). Modelling the backscattering ratio of marine particles in case-2 waters. In *Proceedings of the Ocean Optics XVI*, Santa Fe, USA. 30

Zibordi, G., Berthon, J.-F., and D'Alimonte, D. (2009a). An evaluation of radiometric products from fixed-depth and continuous in-water profile data from moderately complex waters. *Journal of Atmospheric and Oceanic Technology*, 26(1):91–106. 35, 52

Zibordi, G., Berthon, J.-F., Mélin, F., D'Alimonte, D., and Kaitala, S. (2009b). Validation of satellite ocean color primary producs at optically complex coastal sites: Northern Adriatic Sea, Northern Baltic Proper and Gulf of Finland. *Remote Sensing of Environment*, 113:2574–2591. 3, 35, 36, 53

Zibordi, G., D'Alimonte, D., and Berthon, J. (2004a). An evaluation of depth resolution requirements for optical profiling in coastal waters. *Journal of Atmospheric and oceanec technology*, 21:1059–1073. 44

Zibordi, G., Holben, B., Hooker, S. B., Mélin, F., Berthon, J.-F., Slutsker, I., Giles, D., Vandemark, D., Feng, H., Rutledge, K., Schuster, G., and Mandoos, A. A. (2006a). A Network for Standardized Ocean Color Validation Measurements. *EOS Transactions*, 87(30):293–297. 53

Zibordi, G., Mélin, F., Berthon, J.-F., Holben, B., Slutsker, I., Giles, D., D'Alimonte, D., Vandemark, D., Feng, H., Schuster, G., Fabbri, B., Kaitala, S., and Seppala, J. (2009c). AERONET-OC: A network for the validation of ocean color primary products. *Journal of the Atmospheric and Oceanic Technology*, 26(8):1634–1651. 36, 49

Zibordi, G., Mélin, F., Hooker, S. B., D'Alimonte, D., and Holben, B. (2004b). An autonomous above-water system for the validation of ocean color radiance data. *IEEE Transactions on Geoscience and Remote Sensing*, 42(2):401–415. 3, 53

Zibordi, G., Ruddick, K., Ansko, I., Moore, G., Kratzer, S., Icely, J., and Reinart, A. (2012). In situ determination of the remote sensing reflectance: an inter-comparison. *Ocean Sciences*, 8:567–586. 36, 49

Zibordi, G., Stroembeck, N., Mélin, F., and Berthon, J.-F. (2006b). Tower-based radiometric observations at a coastal site in the Baltic Proper. *Estuarine, Coastal and Shelf Science*, 69:649–654. 3, 36

Zibordi, G. and Voss, K. J. (2010). Field Radiometry and Ocean Color Remote Sensing. In Barale, V., Gower, J., and Alberotanza, L., editors, *Oceanography from space, revisited.* 43